Doctoral Dissertation (Censored)

博士論文（要約）

Method and practice of broadband ocean bottom seismology: case studies in the western Pacific

（広帯域海底地震学の手法と実践：西太平洋域アレイ観測への適用）

A Dissertation Submitted for the Degree of Doctor of Philosophy
December 2021

令和３年１２月博士（理学）申請

Department of Earth and Planetary Science, Graduate School of Science,
The University of Tokyo

東京大学大学院理学系研究科地球惑星科学専攻

Yuki Kawano

川野　由貴

Abstract

This thesis developed methods to overcome three technical challenges in broadband surface-wave array analysis. I applied the improved method to the in situ seismograms recorded in the oldest Pacific Ocean and measured Rayleigh-wave phase velocity at a period range of 5–200 s and Love-wave phase velocity at a period range of 5–100 s. The measured phase velocities are inverted to one-dimensional isotropic, radially and azimuthally anisotropic shear-wave velocity structures.

With the short thermo-chemical evolution history and a simple crustal structure, imaging of the oceanic mantle is essential to elucidate the nature of the lithosphere-asthenosphere system (LAS), which is the most representative system of plate tectonics. Broadband surface-wave array analysis provides continuous imaging of the LAS from the seafloor to a depth within the asthenosphere. The method was previously applied to various oceanic basins, and the obtained high-resolution imaging led to an awareness of the variable dynamics within the asthenosphere.

There, however, still exists technical challenges in broadband surface-wave array analysis, which hamper our investigation into the LAS. In this thesis, I developed methods to overcome three challenges and analyzed the seafloor records obtained by an array of broadband ocean bottom seismometers (BBOBSs) deployed along the 170-Ma isochrone, the Oldest-1 Array, where the eastern edge of the array overlaps an ancient ridge-ridge-ridge (RRR) triple junction.

The first challenge is the high noise level of the long-period oceanic seismograms. Long-period data (>10 s) at seafloor stations tends to have higher noise levels than at land stations due to tilt noise and compliance noise, which originated from seawater. Noise reduction processing is essential to maximize the use of data. I established a noise reduction method for the vertical component seismograms of the BBOBS by modifying pre-existing method and applied it to the Oldest-1 Array data set. Using noise-reduced data, I measured Rayleigh-wave phase velocities up to a period of 200 s, and structures in a depth of 200–300 km were successfully constrained by the direct observation.

The second challenge is the measurement of short-period (<30 s) phase velocities. It is difficult to achieve a stable measurement in a seafloor array due to the long interstation distances and small numbers of stations. Therefore, I improved pre-existing ambient-noise analysis and realized a more stable and physically more appropriate measurement with smaller uncertainties. I measured Rayleigh- and Love-wave phase velocities at a period range of 5–25 s and 5–10 s, respectively.

The third challenge is measuring long-period (>30 s) Love-wave phase velocities. Although

Love waves are crucial to understanding the LAS, the measurement of Love-wave phase velocities has been rare because of technical difficulties. Due to the characteristics of the oceanic structure (thin crust and mantle low-velocity zone), several different modes of Love waves have close or even overlapped arrival times, resulting in mode interference. Therefore, if Love waves are analyzed without any special care, the measured phase velocities are potentially biased. In order to measure less-biased fundamental-mode love-wave phase velocity, I devised a method to measure phase velocity by treating the Love waves as a superposition of the fundamental and first higher modes. I measured the fundamental-mode Love-wave phase velocities in a period range of 33–100 s.

I then inverted the measured phase velocities and obtained one-dimensional radially and azimuthally anisotropic structure beneath the Oldest-1 Array, which involve both horizontally propagating vertically and horizontally polarized shear waves (V_{SV} and V_{SH}). I compared the obtained isotropic shear-wave velocity (V_{SV}=V_{SH}) structure with that of the other two ocean basins of different ages (130 and 140 Ma). There is no significant difference in the high-velocity Lid (Moho–60 km) among the three regions, whereas it is difficult to explain the velocity difference within the low-velocity zone (80–150 km) only by cooling associated with the age difference.

The azimuthal anisotropy at shallow depths (<50 km) differs between the eastern and western areas of the array. The intensity of azimuthal anisotropy is ∼3.7 % and the fastest direction is quasi-perpendicular to the predicted past seafloor spreading direction in the western area of the array, while the intensity is ∼1.6 % and the fastest direction largely deviates from the predicted past seafloor spreading direction in the eastern area of the array. The intensity of the azimuthal anisotropy at depths deeper than 50 km is weak (∼1 %), and the direction of the fast axis is in the east-west direction, which is different from the absolute plate motion. The radial anisotropy is estimated in two layers (Moho–60 km and 60–240 km). The shallow radial anisotropy in the eastern area is $V_{SH} > V_{SV}$ by 7.5±1.0 % while it is 3.4±1.1 % in the western area. The deep radial anisotropy is estimated to be $V_{SH} > V_{SV}$ by 2–8 %.

Both azimuthal and radial anisotropy are significantly different between the eastern and western areas within the Oldest-1 Array, which may reflect the complication of the evolution of the early Pacific plate, which involves the RRR triple junction. Radial anisotropy is stronger than azimuthal anisotropy and likely to be consistent with a conventional notion of the olivine fabric type (A-type olivine).

This thesis improved broadband surface-wave array analysis by overcoming three technical

challenges and estimated the isotropic, azimuthally and radially anisotropic shear-wave velocity structures, which are all crucial to discuss the structure and mantle flow in the oceanic lithosphere-asthenosphere system. The realization of obtaining all three types of structures means that seismic observations are ready to be compared to rheological studies and to constrain various hypothesized structures by direct observations in the future.

Contents

Chapter 1

Introduction

1.1 Oceanic lithosphere-asthenosphere system

1.1.1 Plate tectonics in oceanic regions

Plate tectonics is the most fundamental theory to describe the motions of the solid Earth. Under its framework, the Earth's surface is covered by a number of rigid plates, the lithosphere, which consists of the crust and the uppermost mantle, and moves slowly and horizontally over the asthenosphere, the softer and weaker mantle beneath it. The basic form of plate tectonics exists in the oceanic region: The oceanic lithosphere emerges at the mid-oceanic ridge, and as it moves away horizontally, the plate cools and thickens eventually sinking back into the mantle at the subduction zone. Thus, while plate tectonics started billions of years ago, the age of the seafloor and the oceanic lithosphere is relatively young. The oldest remaining seafloor in the Pacific Ocean is 0.18 billion years old. In contrast to the oceanic lithosphere, the continental lithosphere is typically older and much more complex. It does not subduct nor recycle due to its stable and buoyant nature. The continental lithosphere contains time-integrated records of undergone modifications such as subduction zone processes, volcanic activities, and plate collisions and/or breakups.

With the short thermo-chemical evolution history and a simple crustal structure, the oceanic mantle provides an excellent observation window into mantle dynamics. To first order, oceanic structures can be explained by a simple thermal model. At ages younger than 70 Ma, the age dependence of heat flow and bathymetry data can be explained by a half-space cooling (HSC) model, which assumes that the plate is thickened and cooled by heat conduction in the depth direction and subsides due to its own weights (e.g., Parker and Oldenburg, 1973). At ages greater than 70 Ma, however, it is known that the depth of seafloor is anomalously shallower (seafloor flattening), and heat flow measurement is anomalously higher than that of the HSC model prediction (e.g., Parsons and Sclater 1977; Stein and Stein 1992). Empirical models with thermal boundary at depth, the plate model, can explain bathymetry and heat flow data (e.g., Parsons and Sclater 1977; Stein and Stein, 1992). However, what kind of structure the thermal boundary corresponds

to is ambiguous and has long been under debate. Localized sub-lithospheric convection is proposed to explain the difference between the observations and the HSC model prediction (e.g., Richter and Parsons, 1975; Parsons and McKenzie, 1978). In recent, this has been one of the hottest topics in broadband ocean seismology (e.g., Eilon et al., 2021).

1.1.2 Implications from seismic studies

Surface-wave analysis

Surface waves are typically the most prominent wave trains in the teleseismic seismograms and are a key source of information to understand upper mantle structure. Surface waves propagate two-dimensionally along the Earth's surface. Their energy reaches deep into the upper mantle, resulting in its dispersion nature and sensitivity to the upper mantle shear-wave (S-wave) velocity structure. Most studies of surface waves measure the dispersion (frequency dependence of wave velocity) and invert it to the S-wave velocity depth profile.

There are two types of surface waves, Rayleigh waves and Love waves, which are sensitive to the velocities of horizontally propagating vertically and horizontally polarized S-waves, V_{SV} and V_{SH}, respectively. They can be represented as a summation of normal modes, the free oscillations of spherical Earth (Takeuchi and Saito, 1972). Surface waves generally consist of a fundamental mode with the largest amplitude and overtones with relatively small amplitude. The fundamental mode is sensitive to shallow S-wave velocity structure and typically arrives independently from overtones, whereas overtones are sensitive to deeper structures and have similar arrival times.

As well as isotropic structures, anisotropic structures can also be investigated via surface-wave analysis. There are two types of seismic anisotropy: azimuthal anisotropy and radial anisotropy. Azimuthal anisotropy is the difference in wave velocity depending on the direction of propagation in a horizontal plane, which can be inferred from either Rayleigh- or Love-wave dispersion curves but using Rayleigh waves in most of the cases because of better signal-to-noise ratios. Radial anisotropy is the inconsistency between azimuthally averaged Rayleigh- and Love-wave dispersion curves.

Azimuthal anisotropy is linked to flow-induced olivine alignment and thus indicates mantle deformation (e.g., Becker et al., 2014). Olivines, which are the most common minerals in the upper mantle, are intrinsically anisotropic. Elastic waves propagate faster along olivine's a-axis than along its b- and c-axes. Shearing due to the plate motion aligns olivines in a particular direction, the a-axis direction (the lattice preferred orientation; LPO). This orientation occurs over length scales of hundreds of kilometers which are comparable to length scales of the Fresnel zone of surface waves. Consequently, Rayleigh waves propagate faster along the direction of mantle shearing, and thus observations of seismic azimuthal anisotropy can directly infer current and/or past mantle flow dynamics.

Radial anisotropy, as well as azimuthal anisotropy, ubiquitously exists within the upper mantle. It has long been known that Rayleigh- and Love-wave dispersion curves cannot be explained by

isotropic S-wave velocity models, i.e., $V_{SH}/V_{SV} \neq 1$ (e.g., Aki and Kaminuma, 1963). Based on this discrepancy, the existence of radial anisotropy is conclusively established and imposed in the one-dimensional reference Earth model at the depth range of 24.4–220 km with $V_{SH} > V_{SV}$ (Dziewonski and Anderson, 1981). Radial anisotropy can be linked to both flow-induced LPO (e.g., Karato et al., 2008) and structural layering (e.g., Backus, 1962).

1.1.3 Seismologically inferred oceanic mantle structure

The typical oceanic upper mantle consists of a thin crust with a thickness of ∼7 km (White et al., 1992), a high-velocity layer (Lid), and an underlying low-velocity zone (LVZ) (Gutenberg and Richter, 1939; Gutenberg, 1948; Dorman et al., 1960; Nishimura and Forsyth, 1989). Global tomography illuminates the lateral and vertical variation in the upper mantle structures (e.g., Tanimoto and Anderson, 1984; Montagner and Tanimoto, 1991; Maggi et al., 2006ab; Nettles and Dziewonski, 2008; Burgos et al., 2014; Debayle et al., 2020). To first order, the Lid gets thicker and the seismic velocities in the LVZ get faster at older seafloor, indicating that the change in thermal structure due to cooling with age is a primary factor controlling the seismic velocity structure (e.g., Maggi et al., 2006a). Due to the observed strong correlation between the seafloor age and the Lid/LVZ structure, the Lid is typically interpreted as the lithosphere, and the LVZ is typically interpreted as the asthenosphere.

Global tomography also provides anisotropic imaging. At shallow depths, the fast direction of azimuthal anisotropy is found to be parallel to the past seafloor spreading direction (e.g., Tanimoto and Anderson, 1984; Montagner and Tanimoto, 1991; Maggi et al., 2006b; Burgos et al., 2014) and at the depths range at 100–200 km, the fast direction of azimuthal anisotropy is found to be coherent with the absolute plate motion (e.g., Maggi et al., 2006b; Burgos et al., 2014). At a similar depth range, strong radial anisotropy ($V_{SH} > V_{SV}$) is observed beneath the Pacific basin (Nettles and Dizewonski, 2008). Those coherent relationships are interpreted as flow-induced LPO alignment, resulting from shearing associated with the plate motions.

Although global tomography is a strong tool to investigate the oceanic mantle structures, there are also limitations due to the lack of in situ observations in the ocean. For example, due to the lack of short-period dispersion curves, shallow structures are not well constrained by the data but are mostly fixed to assumed structures. This might result in some trade-offs between the shallow and deep structures. Also, while isotropic components are correlated among different tomographic imaging, anisotropic components result in poor correlations (Schaeffer et al., 2016). In order to investigate the details of the oceanic mantle structure, in situ observations and higher-resolution imaging are required.

More focused studies revealed that within the lithosphere, there exist quasi-laminated heterogeneities (Furumura and Kennett, 2005; Shito et al., 2013). Observations on high-amplitude, high-frequency, and long-duration coda waves generated by deep earthquakes in the subducting slabs suggest the existence of multiple laterally elongated heterogeneities within the subducted and

old lithosphere (Shito et al., 2013). The existence of those small-scale heterogeneities will result in the lithospheric radial anisotropy with $V_{SH} > V_{SV}$ (Kennett and Furumura, 2015). In addition, from an active source experiment on the old Pacific seafloor (128–148 Ma), quasi-laminated heterogeneous structures are also observed and interpreted as the frozen-in melt pockets within the lithosphere (Ohira et al., 2017). Whether or not those quasi-laminated heterogeneities are ubiquitous within the lithosphere is unknown. Estimation in radial anisotropy within the lithosphere at various seafloor ages may answer this question.

Beneath the lithosphere, localized small-scale thermal convection (SSC) is proposed to explain the seafloor flattening phenomena (Richter and Parsons, 1975; Parsons and McKenzie 1978; Buck and Parmentier, 1986; Huang and Zhong, 2005). SSC results from gravitational instability occurred at the bottom of the lithosphere whereby cold and dense lithospheric material sinks and is replaced by warm asthenospheric upwelling. In the Pacific Ocean, both basin-wide studies and more high-resolution locally estimated S-wave velocity vertical profiles on mid to old ages support the occurrence of SSC (e.g., Lin et al., 2016; Takeo et al., 2018; Ma and Dalton, 2019). Not only for old ages, but SSC is also predicted for younger ages (e.g., Buck and Parmentier, 1986), and recent surface-wave studies on 40-Ma Pacific and the mid-Atlantic ridge (0–80 Ma) support the occurrence of SSC (Harmon et al., 2020; Russell, 2021). The key to constrain the sub-lithospheric convection is to obtain all three types of S-wave velocity structures that are isotropic, azimuthally and radially anisotropic structures till the depth of ∼300 km where correspond to the bottom of the LVZ. With all of these structures, we can discuss the mantle flow field and temperature variations associated with the sub-lithospheric convection.

A limitation of surface waves is that their sensitivity is broad in depth and it cannot distinguish a sharp and a gradual velocity contrast. Contrarily, body waves are sensitive to the velocity contrast and provide us with complementary information. Many studies utilize converted and reflected body waves to image G-discontinuity, where seismic velocity drops abruptly from the Lid to the LVZ (Gutenberg and Richter, 1939), and interpret it as seismic lithosphere-asthenosphere boundary in the oceanic mantle (e.g., Kawakatsu et al., 2009; Schmerr, 2012; Kawakatsu and Utada, 2017; Tharimena et al., 2017; Fischer et al., 2020; Mark et al., 2021). The velocity contrast is sharp and abrupt, for instance in the Pacific Ocean, velocity drops by 7–8 % over 10–15 km (Kawakatsu et al., 2009). Global compilations of the detected velocity discontinuities show that, if only observations at normal oceanic seafloor are considered, the depth of the discontinuities roughly follow the 1100 °C isotherm until the age of ∼36–64 Myr and centered around 60 km depth (e.g., Fischer et al., 2020). Temperature only changes gradually and hence only results in a gradual change in seismic velocities. The observations of sharp velocity contrasts suggest the existence of other mechanisms, such as shear-induced partial melts embedded within the asthenosphere, which qualitatively explains the strong radial anisotropy observed from global tomography (Kawakatsu et al., 2009).

1.2 Broadband surface-wave array analysis

In situ observation using focused arrays of ocean bottom seismometers (OBSs) is essential to obtain high-resolution models to investigate the local scale structure. In the early array observations, the shallow structure was estimated by seismic interferometry (Harmon et al., 2007), and the deep structure was estimated by teleseismic waveform analysis (Forsyth et al., 1998; Weeraratne et al., 2007). Seismic interferometry is a method to extract elastic waves propagating between stations from ambient noise records by calculating noise cross-correlation functions (NCFs) between a station pair, and measuring the interstation phase difference of extracted waves (Shapiro and Campillo, 2004). In teleseismic waveform analysis, the structure at depth is estimated by measuring the interstation phase difference of incoming surface waves. Typically, phase velocities of 30–100 s or 30–150 s have been measured, yielding structures to depths of 150–400 km.

Seismic interferometry and teleseismic waveform analysis are complementary. At short periods ($<\sim$30 s), due to the strong heterogeneities within the shallow structure outside the array, multipath and ray bending occurs, which complicates the waveforms and makes phase velocity measurement difficult. On the other hand, in seismic interferometry, since the sensitivities are confined within the array, the extracted elastic waves are simpler than that of the teleseismic waveforms. At long periods ($>\sim$30 s), while the signal-to-noise ratio of NCFs gets lower since ambient noise is excited by microseisms, teleseismic waveforms typically provide a high signal-to-noise ratio. In terms of depth profile, the two data sets have sensitivities at different depths, indicating that a combination of two methods can enable us to image the lithosphere-asthenosphere system continuously from shallow to deep and hence reduce the trade-off between the shallow and deep structures, which is a problem for global tomography.

The broadband surface-wave array analysis combined the two methods and obtained broadband dispersion curves to constrain the Lid/LVZ structure (Takeo et al., 2013). The inversion of the broadband dispersion curve provides a quantitative estimation on the structure beneath the array footprint from the crust to the deep mantle, whereas the global tomography is only able to constrain the deep structures and the refraction exploration is only effective to constrain the shallow structures. The broadband surface-wave array analyses are performed on the various seafloor ages of the Pacific plate: 20–30, 40, 60, 70, 130, and 140 Ma seafloor (Takeo et al., 2013, 2016, 2018; Lin et al., 2016; Russell et al., 2019; Yang et al., 2020; Russell, 2021). Results in these studies differ from global tomography, suggesting the importance of in situ observations in understanding local dynamics that are not detectable on a global scale.

For example, Takeo et al. (2018) estimated the V_{SV} structure including azimuthal anisotropy in two arrays (130 and 140 Ma) $\sim$1000 km apart. Although global tomography obtained azimuthal anisotropy that was parallel to the absolute plate motion within the LVZ, in situ analysis by Takeo et al. (2018) obtained azimuthal anisotropy that significantly deviated from the absolute plate motions. Since the azimuthal anisotropy averaged over the two arrays is parallel to the absolute plate motion, the local scale pattern is likely to be averaged out in the lower resolution

analysis (Takeo et al., 2018). They also reported a significant difference in the shear-wave velocity of the LVZ between the two arrays, which could not be explained by simple thermal cooling models. Furthermore, in other seafloor ages, observed azimuthal anisotropy in the LVZ was also not parallel to the absolute plate motion, largely changing our conventional view of the oceanic azimuthal anisotropy. Lin et al. (2016) proposed the occurrence of the local asthenospheric convections beneath the 70-Ma seafloor. Based on those in situ high-resolution imaging, it turns out that the asthenosphere is more dynamic than conventionally thought. Further quantitative constraints are required to elucidate the nature of the lithosphere-asthenosphere system.

1.3 Technical challenges of the broadband surface-wave array analysis

The previously listed studies have continued to improve and expand the applicability of broadband surface-wave array analysis after Takeo et al. (2013) first proposed it. The analysis of short-period dispersion curves via ambient noise has been improved by Takeo et al. (2014), allowing multiple modes to be analyzed simultaneously. Analysis of azimuthal anisotropy is included by Takeo et al. (2016) and Lin et al. (2016) to infer the past and current mantle flow dynamics. Lin et al. (2016) is the first study to incorporate noise reduction of seismograms before array analysis and measured up to 150 s. Although Takeo et al. (2016) measured up to 200 s under good source-station geometry, without noise reduction, the typical measurement limitation is 100 s. Russell et al. (2019) intensively investigated the crust and uppermost mantle structures including both radial and azimuthal anisotropy, and first reported the existence of strong radial anisotropy within the lower crust. Yang et al. (2020) measured the fundamental-mode Love waves at a period range of 28–48 s by teleseismic waveform analysis and estimated radial anisotropy at a depth range from the seafloor to 150 km.

There, however, still exists technical challenges in the broadband surface-wave array analysis. In this thesis, I focus on three challenges: (1) high-noise levels at low-frequency broadband OBS (BBOBS) records, (2) unstable high-frequency phase velocity measurement via seismic interferometry, and (3) mode interference in low-frequency Love waves. I improve the surface-wave array analysis to overcome those problems. Then, I apply the improved method to the seismic data recorded at the oldest ever Pacific seafloor.

The first challenge is the high noise levels of the seafloor records. There exist two types of long-period noise caused by the seawater, which overwhelm the earthquake-generated signals. Crawford and Webb (2000) and Bell et al. (2015) developed noise reduction methods and more and more overseas studies perform noise reduction before the surface-wave dispersion measurement (Lin et al., 2016; Russell et al., 2019; Yang et al., 2020; Russell, 2021). However, noise reduction has not yet been applied to the OBSs developed in Japan until recently (Isse et al., 2021). Due to the lack of long-period measurements (>100 s), broadband surface-wave array analysis conducted

by Japanese groups has only been able to constrain structures down to a depth of 150 km (or 225 km). In order to image the bottom of the LVZ, structure to depths of 300 km has to be constrained, meaning that measurement of dispersion curves at a period range of 100–200 s is required. Therefore, noise reduction processing should also be established for the OBSs developed in Japan to extract as much data as possible.

In Chapter 2, the noise reduction procedure is established and applied to OBS records. By removing two sorts of long-period noise caused by the seawater, up to ∼20 dB of noise reduction is achieved, and long-period (>100 s) Rayleigh waves become available for the array analysis. I also discuss the differences observed between the OBSs developed by the Japanese and the U.S. groups that appeared in the previous study and modify the method based on the observations in this study.

The second challenge is the measurement of short-period phase velocities. When the interstation distance is long and the number of stations is small, which is a typical case for an OBS array, it is difficult to perform a stable measurement. A multi-mode measurement method was developed by Takeo et al. (2014), but the method needs to be finely tuned depending on the modes and frequencies to avoid the appearance of unrealistic peaks and troughs on the dispersion curves. Thus, it is not suitable for applying the method to a large number of observations and comparing the results.

Furthermore, since seismic interferometry is a method of extracting correlated signals between stations, it potentially extracts not only the desired signals but also signals that cannot be explained by the interstation propagations. If the signal source is not well understood and if one used the NCFs containing the unexpected signals to measure dispersion curves, the obtained results may be biased (e.g., Seydoux et al., 2017).

In Chapter 3, seismic interferometry is applied to two OBS arrays in the western Pacific Ocean. This chapter consists of two parts. I first introduce the unexpected volcanic signals observed in the NCFs and identify the signal source as well as discuss the excitation mechanism of the volcanic signals. In the later part, I develop a short-period phase-velocity measurement technique. The new approach achieves a more stable and physically more appropriate measurement than that of the previous study. I measure Rayleigh- and Love-wave phase velocities at a period range of 5–25 s.

The third challenge is the measurement of Love-wave phase velocities at periods longer than ∼10–20 s. The fundamental-mode Love waves are subjected to the contamination of the overtones due to their closeness of arrival times at a broad period range of about 20–100 s or even longer, resulting in particularly severe model interference in seafloor records. The measurement of the Love-wave phase velocity is, therefore, a challenge that has always been avoided, and not only is there no effective solution, but it is not even well understood what and how difficult it is. In spite of the difficulties, since Love-wave phase velocities are essential for the estimation of radial anisotropy, a comprehensive understanding of the lithosphere-asthenosphere system is not possible without Love waves.

In Chapters 4 and 5, I obtain the long-period Rayleigh- and Love-wave phase-velocities. In Chapter 4, I summarize the measurement of Rayleigh-wave phase velocity at a period range of 25–200 s. In Chapter 5, I propose a method for measuring long-period Love-wave phase velocity (30–100 s) via the teleseismic waveform analysis. I treat the observed Love waves as a superposition of two different modes and measure the fundamental-mode phase velocity. Different from what has been previously thought, from a series of analyses, I found that not only the first higher mode contaminates the fundamental-mode phase-velocity measurement but also the second and higher modes introduce significant biases. The proposed method only considers the contamination due to the first higher modes. These limitations are also discussed.

In Chapter 6, I invert the estimated broadband phase velocity into the one-dimensional depth profile and obtain the isotropic, azimuthally and radially anisotropic structures. Based on those structures, I discuss the LVZ structure and its implications on the asthenospheric dynamics, as well as the implications of the Lid on the early evolution dynamics of the Pacific plate.

1.4 Technical introduction: surface-wave sensitivity to the crust and mantle structure

Throughout this study, I measure surface-wave phase velocities as a function of frequency (dispersion curves) and intensively utilize their sensitivity nature to shear-wave (S-wave) velocity. To simplify the subsequent analyses, I demonstrate the dispersion nature in surface waves by showing phase and group velocities in an oceanic setting. Then I summarize their sensitivity to the crust and mantle structure. This study will measure three modes of surface waves in oceanic regions: the fundamental mode Rayleigh waves (0S modes), the first higher-mode Rayleigh waves (1S mode), and the fundamental-mode Love waves (0T modes). I assume an S-wave velocity structure (Figure 1.1) which has two features in a typical oceanic structure for demonstration: a thin crust (7 km) and a well-developed LVZ. Phase and group velocities and corresponding sensitivity kernels are calculated by a Fortran package DISPER80 (Saito, 1988).

Rayleigh waves are sensitive to S waves and also have small sensitivity to compressional waves (P waves) at shallow depths. Figure 1.2 shows phase velocities of Rayleigh waves. At frequencies close to 0.2 Hz, the phase velocity of the 0S mode mainly reflects the velocity of seawater (1.5 km/s). At the frequency range of 0.05–0.1 Hz, the phase velocity of the 0S mode increases dramatically. This is associated with the transition of modal energy from the ocean to the solid (crust and mantle), and hence the velocity increase reflects that Rayleigh waves start to be sensitive to the solid. The velocity change of the 1S mode at a frequency of $\sim$0.07 Hz has occurred in the same manner. At frequencies lower than 0.05 Hz, the phase velocity is dominated by mantle S-wave velocity structure. The 1S mode has higher values of phase velocities than the 0S mode at the same frequency because the 1S mode is sensitive to a deeper structure than the 0S mode is. Figure 1.2 also shows group velocities of Rayleigh waves which reflect energy arrival. The group velocity of the

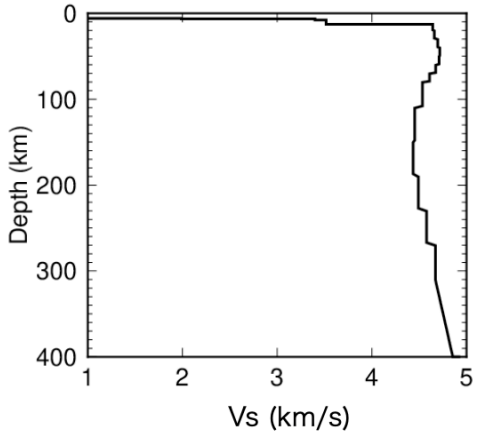

Figure 1.1: An oceanic isotropic shear-wave velocity model used for demonstration. The model is taken from Kawano et al. (2020, AGU), which is an isotropic shear-wave velocity model estimated in the Oldest-1 Array (will be detailed in section 1.5) by measuring phase velocities at a frequency range of 0.005–0.2 Hz following the method of Takeo et al. (2013, 2018).

0S and 1S modes are well-separated from each other, meaning that they are observable as isolated wave trains. The large velocity drops are observable at a frequency of 0.07 Hz, corresponding to the frequency of the modal energy transition from the ocean to the solid.

The perturbation in phase velocities is due to the perturbation in the shear-wave velocity structure. The sensitivity of phase velocity (c) at a frequency ω to a parameter p at a depth of z is called sensitivity kernel, $K_p(z, \omega)$ (Figure 1.3). The linearly approximated relationship between the perturbation in model parameter (Δp) and the associated perturbation in phase velocity (Δc) is defined as

$$\frac{\Delta c(\omega)}{c(\omega)} = \int \left[K_p(z, \omega) \frac{\Delta p(z)}{p(z)} \right] dz. \tag{1.1}$$

Figure 1.3 shows the sensitivity kernels of Rayleigh waves to three different parameters: S-wave velocity (β), P-wave velocity (α), and density (ρ). The 0S mode at frequencies higher than 0.1 Hz (Figure 1.3a) and the 1S mode at 0.2 Hz (Figure 1.3c) have a strong sensitivity to the seawater, resulting in the phase velocities at the corresponding frequencies being about 1.5 km/s (Figure 1.2). The 1S mode at 0.1 and 0.15 Hz is sensitive to S-wave velocities in the crust and the uppermost mantle (Figure 1.3c). At a frequency range of 0.005–0.03 Hz, Rayleigh waves are dominantly sensitive to S-wave velocity structures (Figures 1.3b and d). The 1S mode is sensitive to a deeper structure than the 0S mode at the same frequency. The peak of the 0.01-Hz sensitivity kernel is in a depth range of 100–150 km, which is the depth range of the LVZ (Figure 1.1). In order to investigate the bottom of the LVZ which exists in a depth range of 200–300 km (Figure 1.1), I need to measure the phase velocities to a frequency of 0.005 Hz, which has a peak of sensitivities in the depth range of 200–300 km (Figure 1.3b).

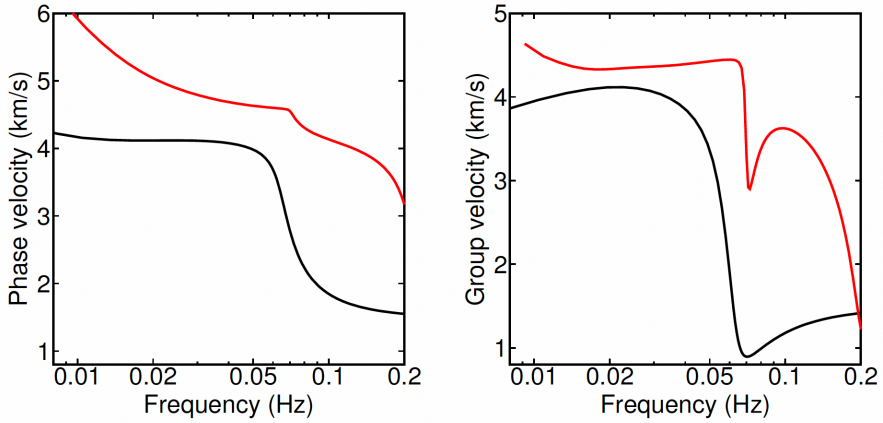

Figure 1.2: Phase and group velocities of Rayleigh waves calculated on the structure in Figure 1.1. The black and red solid lines represent the 0S and 1S modes, respectively.

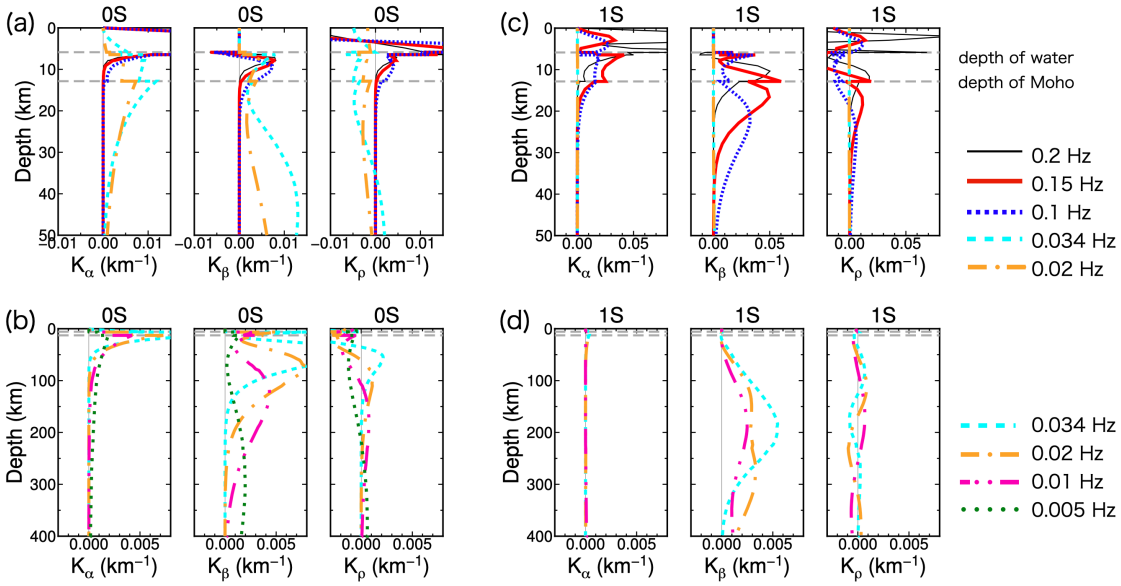

Figure 1.3: Sensitivity kernels of Rayleigh-wave phase velocity to S-wave velocity (K_β), P-wave velocity (K_α), and density (K_ρ) at different frequencies. (a, b) The sensitivity kernels of the 0S mode. (c, d) The sensitivity kernels of the 1S mode. The gray dashed lines are the depth of seafloor and Moho.

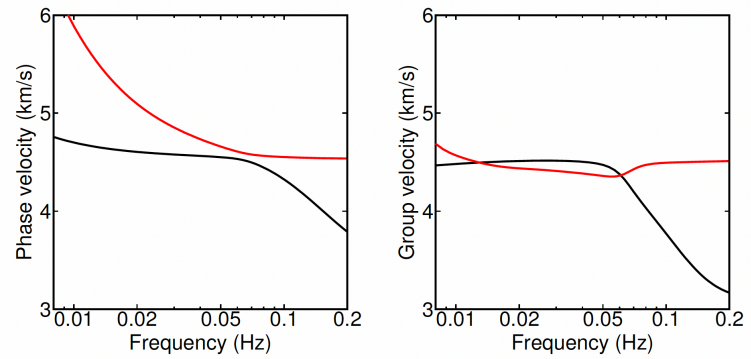

Figure 1.4: Same as Figure 1.2 but for Love waves.

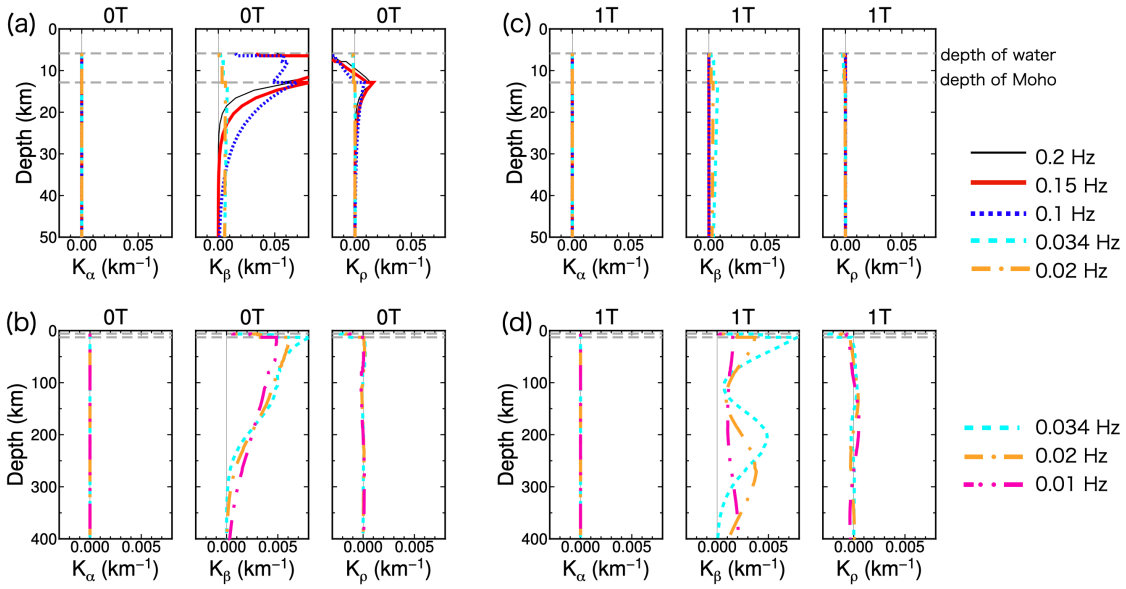

Figure 1.5: Same as Figure 1.3 but for Love waves.

Next, I summarize the Love-wave phase and group velocities in Figure 1.4. Phase velocities gradually increase as the frequency gets lower because Love waves become more sensitive to deeper structures. The phase velocities of the 0T and 1T modes at a frequency range of 0.05 to 0.08 Hz are close to each other. Group velocities of 0T and 1T modes are close to each other at frequencies lower than 0.06 Hz, meaning that the arrival times of the two modes are close to or overlap with each other. Love-wave sensitivity kernels to S- and P-wave velocity and density are shown in Figure 1.5. Love waves are dominantly sensitive to S-wave velocity, slightly sensitive to density, and insensitive to P-wave velocities. The 0T mode at frequencies higher than 0.1 Hz is strongly sensitive to crust and uppermost mantle. The 0T mode at a frequency range from 0.01–0.03 Hz (Figure 1.5b) has broad sensitivity in mantle structure from Moho to a depth of 400 km. Compared to Rayleigh waves at the same frequency, the 0T mode is more sensitive to the shallow structure.

Both Rayleigh and Love waves are sensitive to S-wave velocity, and in detail, they are sensitive to two differently polarized S waves. Rayleigh waves are sensitive to the velocity of horizontally

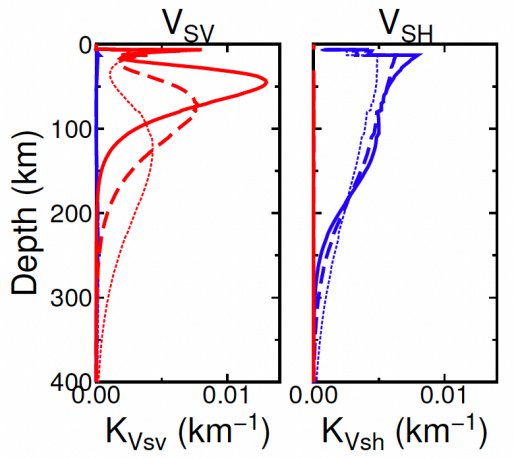

Figure 1.6: Sensitivities of the 0S- (red lines) and 0T-mode (blue lines) phase velocity to V_{SV} and V_{SH} at frequencies of 0.034 Hz (solid lines), 0.02 Hz(broken lines), and 0.01 Hz (thin dotted lines).

propagating and vertically polarized S waves, V_{SV}, whereas Love waves are sensitive to the velocity of horizontally propagating and horizontally polarized S waves, V_{SH}. Figure 1.6 shows their sensitivities to V_{SV} and V_{SH}, and their sensitivities are clearly different.

Phase velocities at different frequencies are controlled by S-wave velocities at different depths. I, therefore, can investigate the S-wave velocity structure by inverting the measured phase velocities. To investigate crustal and uppermost mantle structure, phase velocities of the 0T and 1S modes at frequencies higher than 0.1 Hz are needed. To elucidate the Lid/LVZ structure down to the bottom of the LVZ, phase velocities at frequencies lower than 0.01 Hz are required. Both Rayleigh and Love waves are needed to fully describe the S-wave velocity structure.

1.5 Study area and data: Oldest-1 Array

1.5.1 Scientific scopes

This study uses the seismic data recorded at the Oldest-1 Array (Figure 1.7) as a place to practice solving the problems in the broadband surface-wave array analysis described in Section 1.3. The Oldest-1 Array belongs to the international collaborative initiative, the Pacific Array[1], which aims to advance our knowledge of the oceanic lithosphere-asthenosphere system using multiple temporary ($\sim$1 year) focused arrays of broadband ocean bottom seismometers and ocean bottom electromagnetometers span across the Pacific basin. The arrays that comprise the Pacific Array are expected to reveal the detail of the oceanic mantle directly beneath each array and increase the trans-Pacific ray paths and enhance the spatial resolution of the global tomography.

The Oldest-1 Array is designed to unravel the lithosphere-asthenosphere system beneath the oldest Pacific seafloor, with particular focuses on the evolution process of the Pacific plate and

[1]http://eri-ndc.eri.u-tokyo.ac.jp/PacificArray/index.html

Table 1.1: Summary of the stations in the Oldest-1 Array

Station code	On date (yyyy/mm/dd)	Off date (yyyy/mm/dd)	Latitude (°)	Longitude (°)	Depth (m)		
OL01	2018/10/31	2019/11/02	13.992	152.993	5960	OBS	DPG
OL02	2018/11/07	2019/10/28	12.098	153.211	5934	OBS	DPG
OL03	2018/11/01	2019/11/03	15.999	154.499	5687	OBS	DPG
OL04	2018/11/06	2019/10/29	14.001	155.099	6033	OBS	DPG
OL05	2018/11/06	2019/10/28	12.498	156.000	5942	OBS	DPG
OL06	2018/11/03	2019/11/04	17.201	157.749	5790	OBS	DPG
OL07	2018/11/02	2019/11/01	15.599	156.799	5974	OBS	DPG
OL08	2018/11/05	2019/10/30	14.517	158.598	5765	OBS	DPG
OL09	2018/11/02	2019/11/04	17.400	156.601	5755	OBS	DPG
OL10	2018/11/03	2019/11/04	18.199	157.998	5684	OBS	DPG
OL11	2018/11/04	2019/11/03	16.219	159.495	5766	OBS	DPG
OL12	2018/11/04	2019/11/03	17.699	159.998	5609		DPG

the sub-lithospheric dynamics. Mesozoic magnetic lineations are identified in the old Pacific basin surrounding the array: Japanese, Hawaiian, Mid-Pacific Mountains, Phoenix, and Magellan Lineation Sets (e.g., Nakanishi et al., 1992; Stadler and Tominaga, 2015; Figure 1.8). Those marine magnetic lineations indicate that the oldest seafloor lies in the western-central Pacific (Larson and Chase, 1972), currently enclosed by Chron M29 ($\sim$160 Ma). The area surrounded by Chron M29 is known as the Jurassic magnetic quiet zone (JQZ), characterized by low-amplitude and uncorrelated magnetic anomalies. Whether or not the Jurassic magnetic polarity was constant is still under debate (e.g., Tominaga et al., 2021). Partly because magnetic lineations are not observable at older seafloor (>160–170 Ma), the early evolutionary process of the Pacific plate remains poorly understood. The azimuthal and radial anisotropy within the lithosphere ($<\sim$100 km) may visualize the past mantle flow field and constrain the early Pacific plate evolution dynamics. The constraint on the birth process of the Pacific plate may make global plate reconstruction more accurate and thus may have an impact on other fields.

The presence of thermal disturbance, such as small-scale convection, has been predicted to explain the seafloor flattening on the old ($>\sim$70 Ma) oceanic basin (Richter and Parsons, 1975). Its existence remains a hypothesis and needs to be verified. The oceanic mantle structure beneath the oldest seafloor is an essential place to constrain the existence of thermal disturbance. Azimuthally and radially anisotropic shear-wave velocity structure within the asthenosphere ($\sim$100–300 km) constrain the current mantle flow field and temperature structure, allowing for a more quantitative assessment of the thermal disturbance. Combined with the results of previous studies at younger seafloors, the age dependence of the lithosphere-asthenosphere system is also expected to be unraveled.

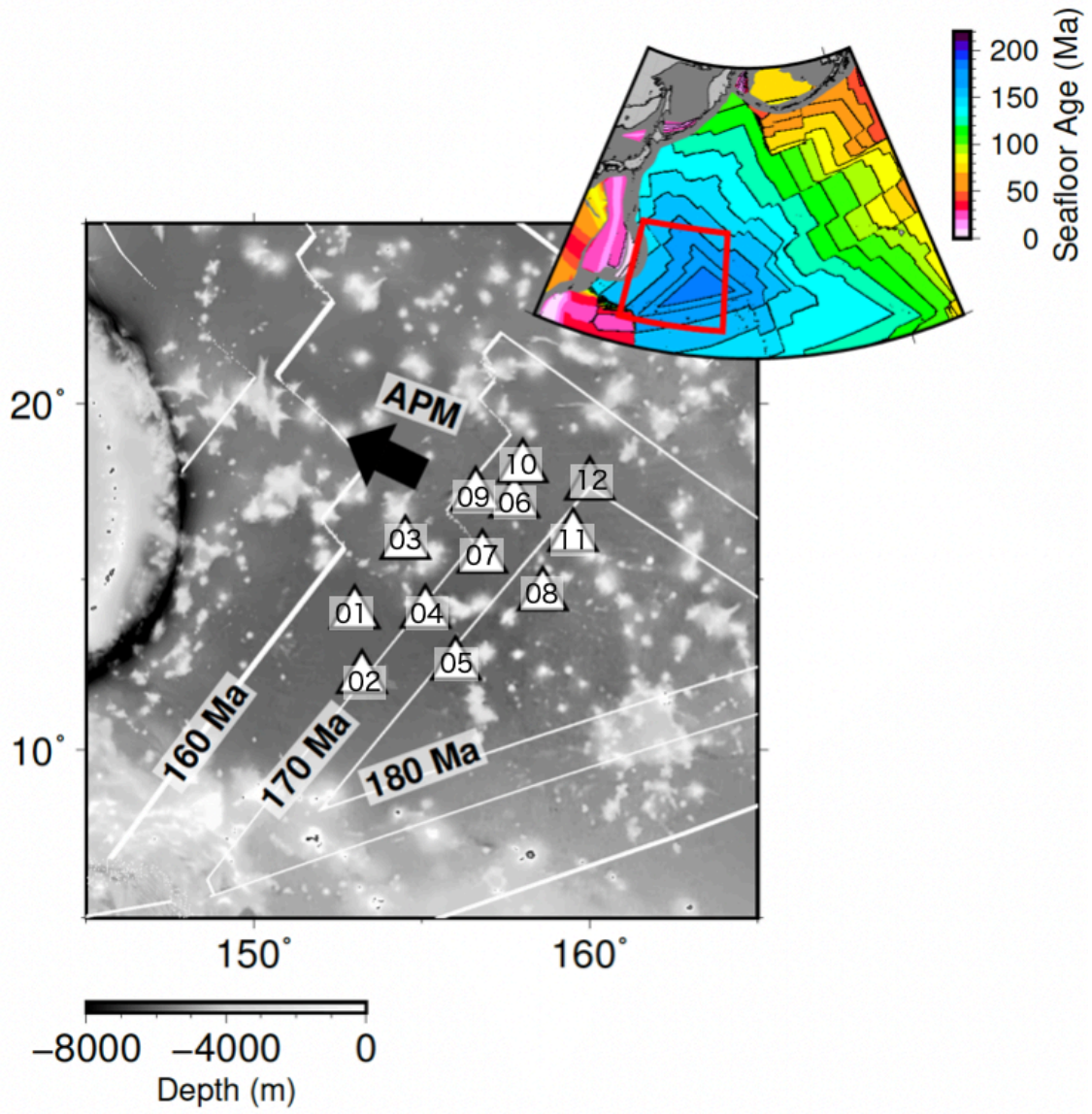

Figure 1.7: Map showing the location of the Oldest-1 Array. The white-filled triangles represent the stations of BBOBSs with DPGs, and the open triangle represents the station of DPG only. The numbers on the triangles denote station codes (Table 1.1). The black arrow shows present-day absolute plate motion (APM). The background white lines represent isochrones (Seton et al., 2020). The area of the large map is shown by a red rectangle in the smaller map on the right top. The seafloor age is taken from Seton et al. (2020).

1.5.2 Deployments

The Oldest-1 Array situates on the oldest Pacific seafloor (170 Ma) ∼1000 km off the Marian trench (Figure 1.7). The array occupies one side (the ancient Pacific-Izanagi plate boundary) of the so-called Pacific triangle where three magnetic lineation sets (Japanese, Hawaiian, and Phoenix lineations) intersect (more details will be described in the next section), recording the birth of the Pacific plate. The array is comprised of 12 broadband ocean-bottom seismometers (BBOBSs) with differential pressure gauges (DPGs) (Cox et al., 1984; Araki and Sugioka, 2009) attached and seven ocean bottom electromagnetometers deployed from November 2018 to November 2019 by Japan-South Korean joint teams using R/V ISABU for deployment and R/V ONNURI for recovery. The locations of stations in the array are given in Table 1.1. All BBOBSs were equipped with Guralp CMG-3T seismic sensors with a sampling frequency of 100 Hz and were successfully recovered with continuous seismic and pressure data except for OL12, whose tilt-meter could not operate well, and only the DPG had operated. The array footprint is an ellipse across ∼500×1000 km region with the long major axis set along the 170–180 Ma isochrone (Seton et al., 2020). The shortest interstation interval is ∼110 km. The specific sites are chosen so as to avoid the seamounts and cover the flat area of the oldest oceanic basin to sample the unblemished oceanic mantle (Figure 1.7).

1.5.3 Tectonic settings

Birth of Pacific plate

In spite of the lack of available magnetic lineation sequences in the oldest Pacific, it is widely accepted that the Pacific plate has emerged at a ridge-ridge-ridge triple junction within the vast Panthalassa Ocean at about 190 Ma (e.g., Seton et al., 2012; Boschman and van Hinsbergen, 2016; Figure 1.9). Constraints are mainly given by extrapolating the identified younger magnetic lineation sets in the western Pacific to the oldest seafloor (e.g., Handschumacher et al., 1988). The ridge-ridge-ridge triple junction had been surrounded by three oceanic plates: Farallon, Izanagi, and Phoenix plates, which are now extinct. The birthplace of the Pacific plate is thought to be about in the south-central of the current Pacific plate and has moved westward since 140 Ma (e.g., Seton et al., 2012; Boschman and van Hinsbergen, 2016). The estimated ancient spreading rate is quite fast. Abrams et al. (1993) estimated the constant half spreading rate is 80 mm/yr between an ODP site (Site 801) where recovered 166.8±4.5 Ma basalt and Chron M25 (∼154 Ma). In the relatively younger western Pacific (123–160 Ma; Japanese, Hawaiian, and Phoenix lineation sets; Figure 1.8a), where the marine magnetic lineations are more clearly observed, the spreading rate is estimated to be 30–80 mm/yr, which is comparable to those of the current East Pacific Rise (40–90 mm/yr) (Nakanishi et al., 1992).

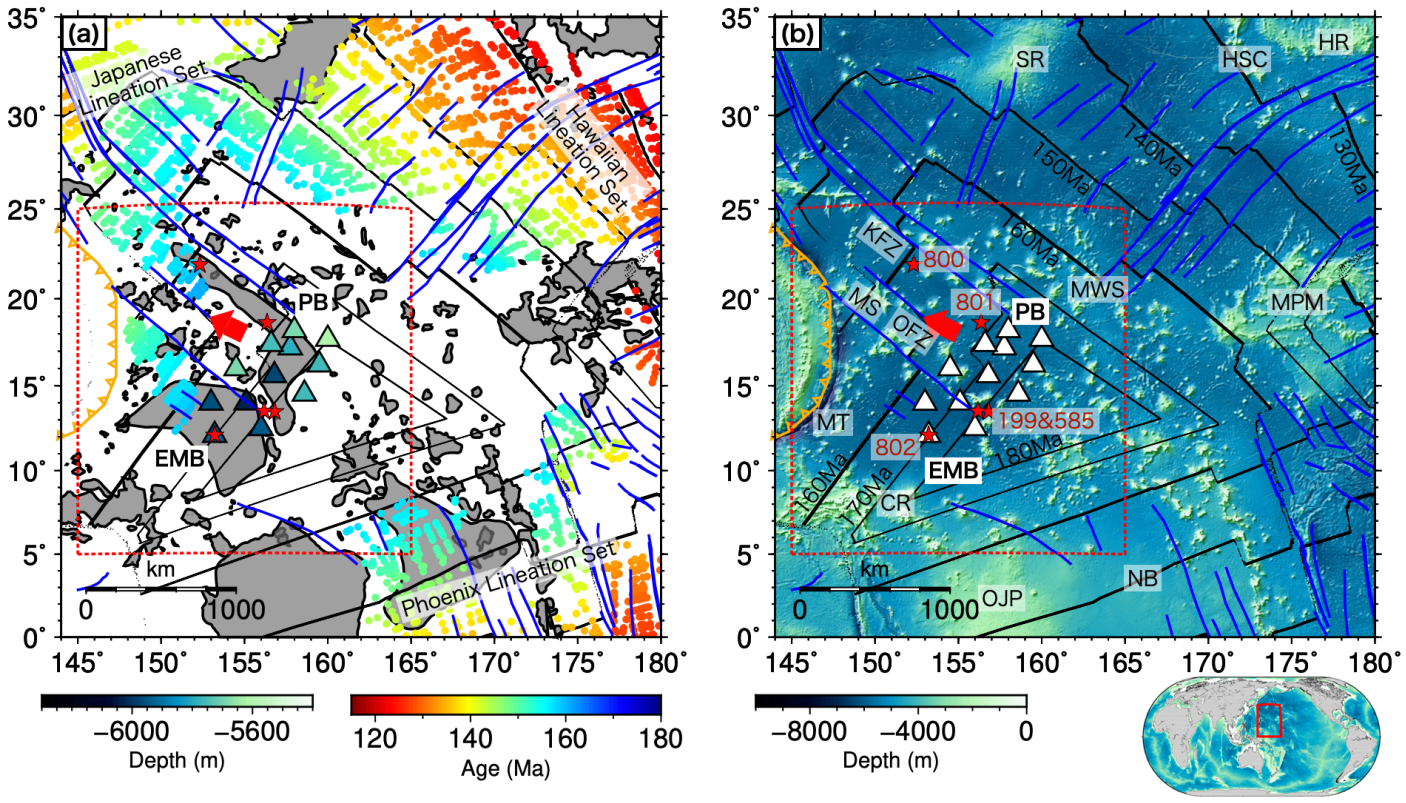

Figure 1.8: Tectonic settings around the Oldest-1 Array. (a): triangles represent the stations in the Oldest-1 Array colored by water depths at each station, gray shades represent the Large Igneous Provinces (LIP) products (Coffin et al., 2006), blue lines represent Fracture zones (Matthews et al., 2011; Wessel et al., 2015), colored small circles represent the magnetic anomalies identified by Nakanishi et al. (1992), Tivey et al. (2006), and Tominaga et al. (2008) and compiled by Seton et al. (2014), the red arrow indicates the current absolute plate motion, the thin black lines represent isochrones by Seton et al. (2020), the orange line represents plate boundary, the red stars denote the drilling sites (800, 801, and 802) of ODP Leg 129 and DSDP Sites 585 and 199 (see also Figure b), and the red dashed box shows the area of Figure 1.7. (b): topography around the Oldest-1 stations. The area of (a) and (b) is shown by a red box in the small global topography map on the right bottom. Legend abbreviations are: CR=Caroline Ridge, EMB=East Mariana Basin, HR=Hess Rise, HSC=Hawaiian Seamount Chain, KFZ=Kashima Fracture Zone, MPM=Mid-Pacific Seamounts, MS=Magellan Seamounts, MT=Mariana Trench, MWS=Marcus-Wake Seamounts, NB=Nauru Basin, OFZ=Ogasawara Fracture Zone, OJP=Ontong Java Plateau, PB=Pigafetta Basin, and SR=Shatsky Rise.

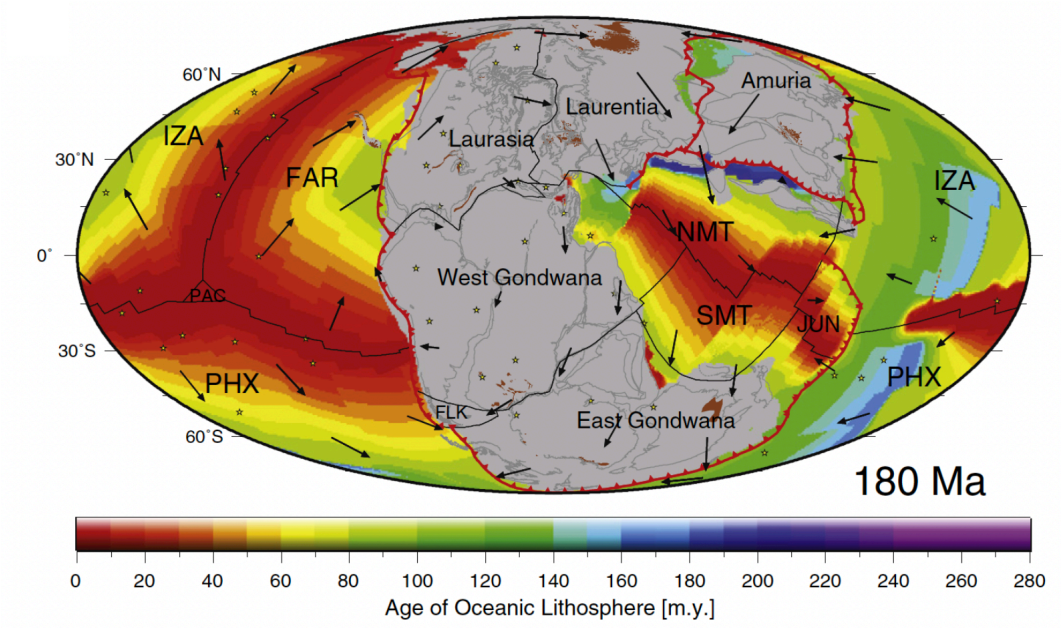

Figure 1.9: Age-plate distribution at the time of 180 Ma. Figure is taken from Seton et al. (2012). Red lines represent subduction zones, black lines represent mid-ocean ridges and transform faults, yellow stars are present-day hotspot locations, brown shaded areas indicate the products of plume-related excessive volcanism, and black arrows represent absolute plate velocity. Legend abbreviations are FAR=Farallon plate, FLK=Falkland, IZA=Izanagi plate, JUN=Junction plate, NMT=North Meso-Tethys, PAC=Pacific plate, PHX: Phoenix plate, and SMT=South Meso-Tethys.

Rock samplings and age identifications in the oldest seafloor

Pacific plate had experienced volcanic activity during the Cretaceous, which emplaced many LIP products, and the Oldest-1 Array is deployed on the LIP products (Coffin et al., 2006; Figure 1.8a). Therefore, to interpret the structure beneath the Oldest-1 Array, it is necessary to recognize the presence of LIP products formed by Cretaceous igneous activity. There were many drilling and dredging experiments on the northwestern Pacific seafloor to sample and analyze the Jurassic (about 140–200 Ma) rocks. Except for ODP Site 801, however, all the sampled rocks showed the age of Cretaceous, although the ages are variable (e.g., Abrams et al., 1993; Winterer et al., 1993; Kopper et al., 2003; Figure 1.10). ODP Site 801 of Leg 129 is the only example of sampling Jurassic oceanic crust. Site 801 sampled 166.8±4.5 Ma Jurassic oceanic basalt at ∼590 meters below seafloor (mbsf) as well as Jurassic sediments dated ∼157–166 Ma, although it is overlain by Middle Jurassic to Lower Cretaceous pelagic sediments and volcanic turbidites dated about 97–135 Ma (Abrams et al., 1992). ODP Site 800 of Leg 129, which reached 545 mbsf, sampled dolerite sills dated at 126.1±0.6 Ma and ODP Site 802 of Leg 129, which reached 560 mbsf, sampled basalt flows and pillows dated at 114.6±3.2 Ma (Abrams et al., 1992, 1993). DSDP Sites 585 and 199 penetrated the anomalously deep trough of the Ogasawara Fracture Zone (Figure 1.10). Site 585 reached volcanic turbidites dated at about 110–120 Ma at 893 mbsf, but it could not reach the high-velocity igneous basement at about 260 m deeper. Site 199 terminated at 456 mbsf within the volcanic turbidites, and it also could not sample the high-velocity basement.

The results of these rocks in the Oldest-1 array are evidence that a large portion of the western Pacific Ocean was affected by igneous activity during the Cretaceous. Although Cretaceous igneous materials overprinted Jurassic oceanic crust, no clear correlations between the magnetic anomaly and the location of sills/flows and between the magnetic anomaly amplitude and the gravity anomaly are observed at least in the Pigaffeta Basin (Figure 1.8a) (Stadler and Tominaga, 2015). It is worth noting that JQZ is unlikely the result of subsequent igneous disturbance but rather the small amplitude nature of the magnetic anomaly in the Jurassic oceanic crust (Stadler and Tominaga, 2015).

Cretaceous volcanic activities within the Oldest-1 Array

Based on the topographic features (Figure 1.8b), Abrams et al. (1992, 1993) defined East Mariana Basin (EMB) and Pigafetta Basin (PB) in the northwestern Pacific. Both basins locate at depths deeper than 5500 m (Figure 1.10), covering the area of 1×10^6 km^2. The EMB is about 250 m deeper than the PB (Figure 1.10). The EMB is surrounded by the Mariana Trench, Caroline Ridge, the Ogasawara Fracture Zone, and Magellan Seamounts (Figure 1.8b). The PB is surrounded by the Kashima Fracture Zone, Marcus-Wake Seamounts, the Ogasawara Fracture Zone, and Magellan Seamounts (Figure 1.8b). The relatively large LIP products that cover the EMB and PB (Figure 1.8a) are formed by ocean basin flood basalt (Coffin and Eldholm, 1994), which less alters the pre-existing crust compared to the formation of off-axis oceanic plateaus

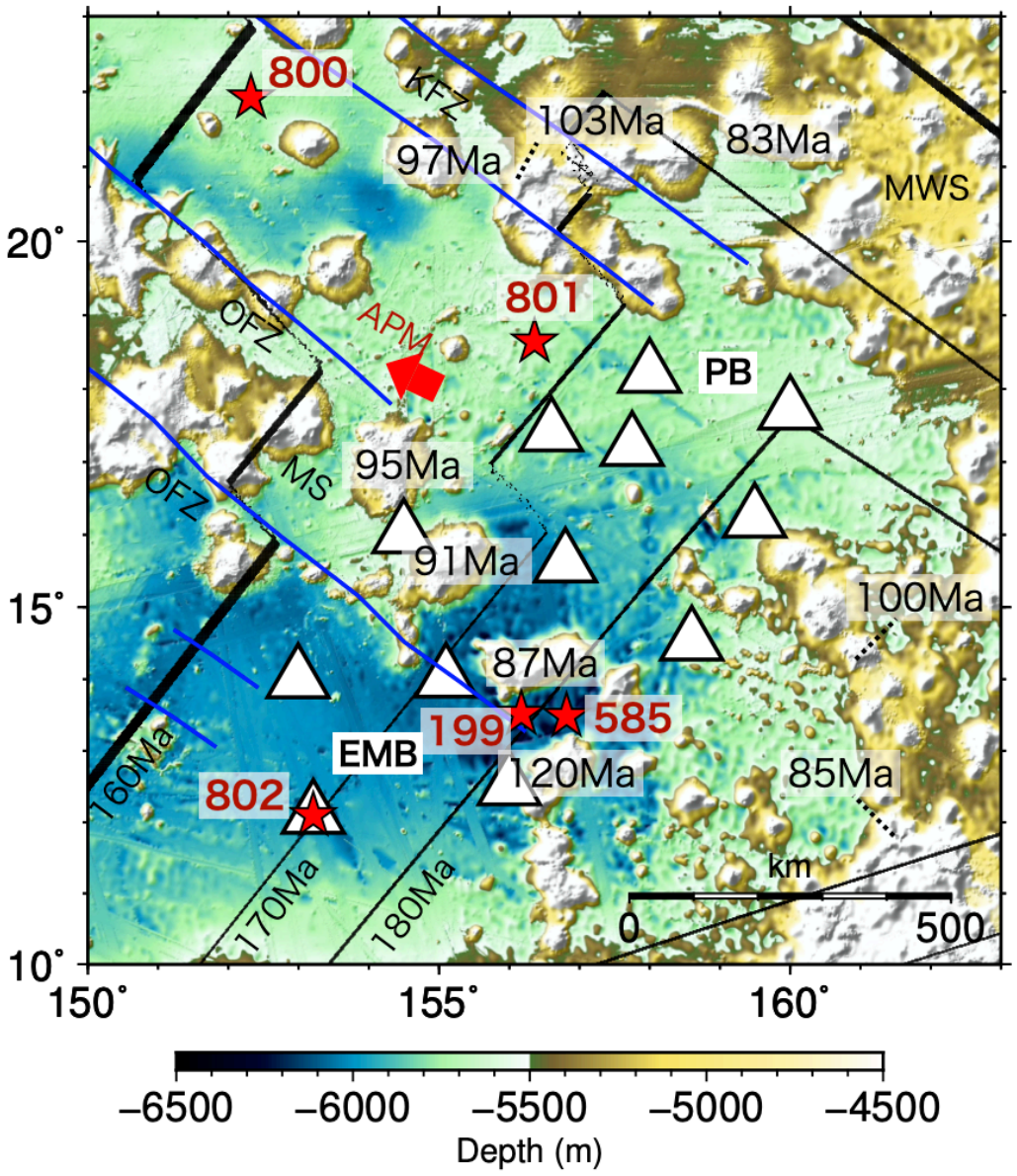

Figure 1.10: The topography around the Oldest-1 Array with selected seamount ages being labeled (Koppers et al., 2003). The color scale is saturated. The red stars represent the ODP Sites 800, 801, and 802 during Leg 129 and selected DSDP Sites 199 and 585, the red arrow indicates the absolute plate motions (APM), blue lines represent Fracture zones (Matthews et al., 2011; Wessel et al., 2015), and thin black lines represent isochrones by Seton et al. (2020). See caption of Figure 1.8 for legend abbreviations.

(Coffin et al., 2006).

Abrams et al. (1993) reported the first multi-channel seismic study in the EMB and PB. They analyzed data of MESOPAC 2[2] and FM35-12[3] seismic surveys, which well cover the Oldest-1 Array. They observed reflections called Horizon B throughout the EMB and PB. Horizon B is an onset of underlying high velocity (>3.6 km/s), characterized by two end-members: (1) a flat-lying, high reflection amplitude, nondiffractive (smooth) semicontinuous surface, which is interpreted as the top of Cretaceous sills/flows overlying the true Jurassic oceanic crust or (2) a relatively high-relief, lower reflection amplitude, and diffractive (rough) surface which is interpreted as the top of the Jurassic oceanic crust without Cretaceous igneous overburden (Abrams et al., 1993).

In a large portion of the EMB, the observed Horizon B had the character of end-member (1) and was categorized as sills/flows, which formed during 110–130 Ma, with Horizon B extending to the Caroline Ridge (Abrams et al., 1993). In the PB, Abrams et al. (1993) observed a boundary of rough/smooth (diffractive/nondiffractive) Horizon B located about 100 km southeast of Site 801, which intersects OL09 and OL10 (Figure 1.7). In areas covered by OL06–OL12, Horizon B was semicontinuous, flat-lying, and shallow, which had the character of end-member (1), whereas it became diffractive, higher-relief, and lower in reflection amplitude in the vicinity of Site 801, which had the character of end-member (2). They reported that the high-relief Horizon B extended between Sites 800 and 801. Around Site 800, however, Horizon B showed a variety of characters and could be categorized as neither end-member (1) nor (2). Throughout the EMB and PB, they identified middle Cretaceous sills/flows along more than 4000 km of the survey line. The volume of those sills/flows was estimated to be $\sim 0.25 \times 10^6$ km^3, which is small compared to large oceanic plateaus such as Ontong Java Plateau (50×10^6 km^3) (Abrams et al., 1993).

They also found the coincidence of their rough/smooth boundary to a previously reported magnetic boundary of high/low field amplitude anomalies. They further pointed out that MORBs in the EMB shared similar age and chemical characteristics to those collected in the Nauru Basin and the Ontong Java Plateau. Considering their results that the flat-lying Horizon B (end-member 2) in the EMB extended to the Caroline Ridge, they suggested that deep-sea volcanism in the EMB and the southeast PB was associated with the rapid formation of the Ontong Java Plateau and the rough/smooth boundary is the edge of distributed sills/flows. However, recently, Stadler and Tominaga (2015) cast a question on Abrams et al.'s interpretation of the smooth/rough boundary and argue the smooth/rough 'boundary' is more likely to be a volcanic feature that ubiquitously exists within the PB.

Abrams et al. (1993) further obtained one-dimensional depth profiles of P-wave velocity derived from seismic records of each of 13 sonobuoys in the relatively flat areas of the EMB and PB, overlapping the Oldest-1 Array. The total crustal thickness was between ∼7–8 km, and subsequent studies in the PB obtained consistent results (Kaneda et al., 2010; Stadler and Tominaga, 2015). According to the gravity modeling of Stadler and Tominaga (2015), seamounts distributed in their

[2]https://campagnes.flotteoceanographique.fr/campagnes/89001511/

[3]https://www.marine-geo.org/tools/search/Files.php?data_set_uid=28269#datasets

survey area produce downward flexure of Moho about 1–3 km. Abrams et al. (1993) observed no seismically resolvable systematic differences in either crustal thickness or velocity between the EMB and PB. Furthermore, the depth profiles were consistent with the normal oceanic crustal structure (Abrams et al., 1993), except at a sonobuoy covering the DSDP Site 585 (Figure 1.10) surveyed in the vicinity of the seamounts, where the sediments were estimated to be 1150 m thick underlain by igneous basement. The thickness of middle Cretaceous igneous sills/flows that overlay the Jurassic oceanic crust is estimated to be 400 m in maximum.

Cretaceous volcanic activities surrounding the Oldest-1 Array

Although the Oldest-1 Array has been deployed at the flat areas in the EMB and PB and seems to have less altered crustal structures, numerous Cretaceous seamounts exist surrounding the Oldest-1 Array, potentially contaminating the desired oldest (Jurassic) mantle Lid. Understanding their origin may be important for interpreting the mantle structure.

Radiometric observations of rocks sampled at seamounts spread over the western Pacific show various ages (69–134 Ma). No clear systematic age distribution pattern on a basin-wide scale has been observed (Kopper et al., 2003), indicating repetitive volcanic episodes and overprinting. Their geochemical analysis suggested that seamounts are formed by multiple closely-spaced short-lived (<40 Ma) mantle plumelets that originated within the upper mantle and stemmed from the top of the superplume in the South Pacific mantle, which was driven by the regional extension of the lithosphere. Stadler and Tominaga (2015), who investigated gravity, magnetic, and seismic data collected in the PB around the ODP Site 801, also support the plumelets scenario.

The Magellan Seamounts traverse the Oldest-1 Array. The crustal and uppermost mantle structures are potentially altered at and around the seamounts. Although the Oldest-1 Array locates on the flat seafloor, considering the basin-wide activity of the mantle plumelets, the underlying mantle structures are also potentially altered.

1.6 Outline of this study

This study first focuses on improving the broadband surface-wave array analysis by solving three technical challenges (Section 1.3): (1) high-noise levels at low-frequency BBOBS records, (2) unstable high-frequency phase velocity measurement via seismic interferometry, and (3) mode interference in low-frequency Love waves. In Chapters 2–5, I improve and develop the methods of measuring surface-wave phase velocities. I measure Rayleigh- and Love-wave phase velocities at a broad frequency range (Table 1.2). Then, in Chapter 6, I apply the improved method to the seismic data recorded by the Oldest-1 Array and invert phase velocity to radially and azimuthally anisotropic shear-wave (S-wave) velocity depth profiles to discuss the lithosphere-asthenosphere system beneath the oldest Pacific seafloor. The continuous high-resolution depth profiles are expected to reveal the past and current mantle flow field as well as mantle temperature profile,

which are the key to achieving the scientific goals of the Oldest-1 Array.

In Chapter 2, the procedure to reduce tilt and compliance noise from vertical component BBOBS records is established. This method is particularly effective in reducing noise at frequencies lower than ∼0.03 Hz, and drastically reducing the noise level at frequencies around 0.01 Hz, making it possible to extract usable low-frequency (0.005–0.01 Hz) teleseismic waveforms.

In Chapter 3, I improve the method of measuring multi-mode surface-wave phase velocities via ambient noise cross-correlation functions (NCFs) and measure Rayleigh- and Love-wave phase velocities at a frequency range of 0.04–0.2 Hz and 0.1–0.2 Hz, respectively. The improved method realizes a more physically appropriate and stable measurement for arrays with relatively long interstation distances and a small number of stations, which is the case of this study. In this chapter, vertical, radial, transverse, and pressure component records are analyzed (Table 1.2). Although the vertical component records are noise-reduced data, since the noise reduction does not result in significant changes in the high-frequency (>0.04 Hz) data, it does not provide much benefit in this chapter (Table 1.2).

In Chapter 3, I also show an example of anomalous wave packets observed in NCFs obtained in another BBOBS array. Phase velocity measurement using NCFs typically assumes a homogeneous distribution of ambient noise sources around stations. The existence of a spatially localized source that persistently generates seismic waves, such as a volcano, may bias the measurements and thus it is important to identify and understand such a source. Therefore, I will describe how to locate a signal source that generates persistent signals which contaminate the measurement.

In Chapters 4 and 5, I measure low-frequency phase velocities via teleseismic waveform analysis (Table 1.2). In Chapter 4, by using the noise-reduced seismograms, I measure the phase velocity up to a frequency of 0.005 Hz, whereas the measurement was limited up to a frequency of 0.01 Hz in the previous study which did not apply noise reduction (e.g., Takeo et al., 2018). In Chapter 5, I develop the method to measure low-frequency (0.01–0.03 Hz) Love-wave phase velocities using BBOBS records. The developed method can reduce the bias in the fundamental-mode phase-velocity measurement caused by higher-mode contamination (Thatcher and Brune, 1969).

As a result of Chapters 3–5, I obtain Rayleigh-wave phase velocity at a frequency range of 0.005–0.2 Hz and Love-wave phase velocity at a frequency range of 0.1–0.2 Hz and 0.01–0.03 Hz.

The Oldest-1 Array is a suitable place to tackle the technical challenges mentioned above and in Section 1.3. The Oldest-1 Array has DPGs equipped on BBOBSs at every observation site, whereas previous OBS arrays deployed by the Japanese group typically did not have DPGs. DPGs are required to reduce low-frequency noise recorded on seafloor seismograms (Chapter 2). In addition, the Oldest-1 Array is larger in size (∼1000 km) than typical OBS arrays (∼500 km), and with the stations distributed sparsely, improvement of the high-frequency dispersion measurement method is needed (Chapter 3). On the other hand, the larger array size is more suitable for the analysis of teleseismic waveforms (Chapters 4 and 5).

In Chapter 6, the broadband surface-wave phase-velocities are inverted to isotropic and radially and azimuthally anisotropic S-wave velocity structures. The isotropic V_{SV} structure ($V_{SV} = V_{SH}$)

Table 1.2: Summary of phase velocity measurements

	Ambient noise analysis				Teleseismiv waveform analysis	
Component	Z	R	P	T	Z	T
Wave type	0S and 1S	0S and 1S	0S and 1S	0T	0S	0T
Frequency (Hz)	0.04–0.2	0.1–0.2	0.04–0.2	0.1–0.2	0.005–0.04	0.01–0.03
Effectiveness of noise reduction	×	–	–	–	◯	–

Z, R, P, and T represent vertical, radial, pressure, and transverse components, respectively.
0S and 1S represent the fundamental- and first higher-mode Rayleigh waves, respectively, and 0T represents the fundamental-mode Love waves.
◯: Noise reduction in Chapter 2 is effective
×: Noise reduction is performed but not much effective
–: Noise reduction is not performed

from Moho to a depth of 300 km will be first constrained using only Rayleigh-wave phase velocities. Since I extracted teleseismic waveforms at a frequency range of 0.005–0.01 Hz in Chapter 2, the structure down to a greater depth is constrained compared to the previous study, which resolved only down to a depth of 150 km (Takeo et al., 2018). The azimuthally anisotropic V_{SV} structure is also constrained using only the Rayleigh-wave phase velocities. In particular, the differences between the eastern and western areas within the array at shallow depths (<50 km), which is mainly constrained by the high-frequency (0.04–0.2 Hz) phase velocities in Chapter 3, will be discussed. The radial anisotropy will be constrained using Rayleigh- and Love-wave phase velocities measured in Chapters 3–5 as a two-layered structure from Moho to a depth of 240 km. In particular, the radial anisotropy at depths deeper than 60 km can be constrained because the Love-wave phase velocities become available at a frequency range of 0.01–0.03 Hz in Chapter 5, which were previously not measured (Takeo et al., 2016, 2018; Lin et al., 2016; Russell et al., 2019; Russell, 2021).

Chapter 2

Noise reduction for low-frequency vertical component seismograms recorded by ocean bottom seismometers

2.1 Introduction

Great innovations of seismic instruments allow us to obtain long-term, broadband, and high-quality oceanic data (e.g., Beauduin and Montagner, 1997; Kanazawa et al., 2001; Shinohara et al., 2006; Shinohara et al., 2011; Shiobara et al., 2012; Suetsugu and Shiobara, 2014). However, analyses of low-frequency data recorded on ocean bottom seismometers (OBSs) still tend to be more difficult than that of land data due to the high noise level originating from seawater. Crawford and Webb (2000) developed a method to reduce low-frequency noise on vertical component seismograms. They removed two sorts of noise, which are originated from seafloor current and seafloor pressure perturbation and called tilt noise and compliance noise, respectively. The former also highly depends on the accuracy of the sensor's leveling, i.e., the more precisely leveled sensor shows the lower tilt-noise level. As a result of noise reduction, Crawford and Webb (2000) achieved up to 25 dB noise reduction on vertical component seismograms. Deen et al. (2017) applied a similar analysis to data collected in the Indian Ocean and observed the Earth's hum in noise-reduced vertical component seismograms.

Japanese-type BBOBS

Although the noise reduction method has been established in the U.S., there have been no attempts to perform the noise-reduction analysis on the seismograms recorded by the broadband OBS (BBOBS) developed by Japanese groups till the recent (Isse et al., 2021). One of the reasons that there are fewer attempts to conduct noise reduction analysis is that the design of the common BBOBSs developed in Japan (Japanese-type BBOBS) is different from that of the common type in the U.S (U.S.-type BBOBS). For example, the U.S.-type BBOBS has an external seismic sensor

sphere that is separated from the batteries, the recorder, and the anchor unit. The separated system can make the sensor's height shorter and thus keep the sensor sphere less exposed to the seafloor current (Webb et al., 2001). However, since the seismic sensor sphere is light in weight, the sensor might be less coupled to the seafloor, which might not be resistant to the seafloor current. In the case of the Japanese-type BBOBS, all units, including the batteries, the recorders, and the seismic sensors, are installed in a titanium sphere attached with an anchor (Kanazawa et al., 2001; Shinohara et al., 2011). This heavy but compact design can realize a good coupling between a BBOBS and sediments, making the mass center of the BBOBS unit lower, which can be expected to be resistant to the seafloor current. Since the Japanese-type BBOBSs somehow keep to provide a high signal-to-noise ratio and substantial data set for analyses, noise reduction has rarely been attempted. However, considering the more and more importance of noise reduction for the BBOBSs developed overseas (e.g., Lin et al., 2016; Deen et al., 2017; Tian and Ritswoller, 2017; Janiszewski et al., 2019; Yang et al., 2020), it is time to establish a noise reduction method for the data recorded by the Japanese-type BBOBSs.

In this chapter, I first summarize the low-frequency noise typically observed on the BBOBSs and then describe a noise reduction method developed based on Crawford and Webb (2000) and Bell et al. (2015) but is modified to suit the case of the Japanese-type BBOBSs. Finally, I demonstrate some examples of noise-reduced spectra and seismograms.

2.2 Low-frequency noise on BBOBS

2.2.1 Tilt noise

The three components of BBOBS have been subjected to seawater noise originated from seafloor currents and seafloor pressure perturbations, and the noise level is much higher than that on land. In particular, the seafloor current is known to cause significant noise in the horizontal component seismograms. The noise generated by the seafloor current which flows past a BBOBS is called tilt noise (Crawford and Webb, 2000). The time variations of the noise seismograms recorded by a BBOBS are coherent to that of the current flow speed (e.g., Shiobara et al., 2012). Figure 2.1 shows a comparison between the daily power-spectral densities (PSD) of the current-flow speed, horizontal and vertical component seismograms recorded on the BBOBS deployed at offshore Miyagi where water depth is about 3400 m and the current meter was deployed about 300 m away from the BBOBS (Appendix A). The daily PSD is calculated as follows: I first divided the 24-h time series into 2000-s sections with a 50-% overlap between adjacent sections. Then, I obtained a median value of power at each frequency from the PSD of each section. Comparison between Figures 2.1a and b clearly shows that the time variations of the horizontal component seismograms correlate with that of the current flow speed (e.g., days highlighted by the black arrows). The seafloor current is a dominant noise source for the horizontal component seismograms at a frequency lower

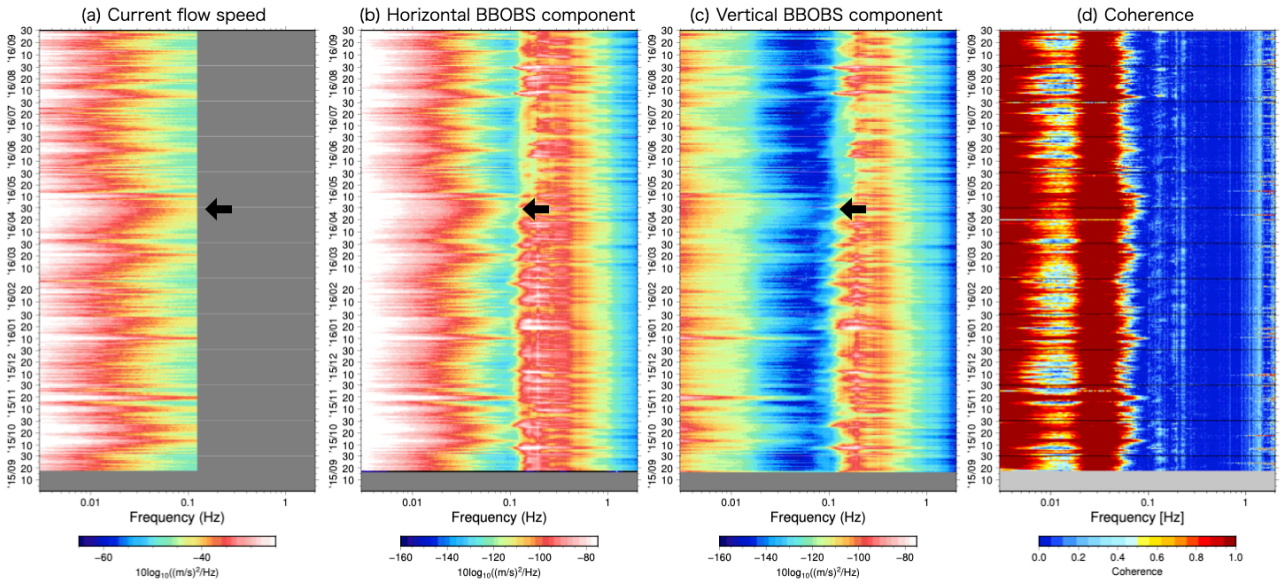

Figure 2.1: Power spectral density (PSD) as a function of time and frequency recorded at offshore Miyagi (Figure A.1 in Appendix A). Results obtained for (a) current flow speed, (b) horizontal component BBOBS data, (c) vertical component BBOBS data, and (d) squared-coherence between the horizontal and vertical component BBOBS data are shown. The horizontal component is taken along the direction that maximizes the squared coherence between the horizontal and vertical components at a frequency range of 0.02–0.06 Hz. There is no data for the gray shaded area either due to sampling rate or observation period. The black arrows indicate an example of coherent relationships among (a)–(c). The value outside the range of the color scales is saturated in (a)–(c).

than 0.1 Hz.

Tilt noise is also observable on vertical component seismograms of the BBOBS, showing a coherent time variation with the current flow speed (e.g., black arrows in Figures 2.1a,c) but with much lower noise levels than that of the horizontal component seismograms (Figures 2.1b,c). Tilt noise on vertical component seismograms is dominantly a result of the misalignment between the sensor's vertical axis and the gravitational direction (Crawford and Webb, 2000). Since it is extremely difficult to exactly align the sensor's vertical axis to the gravitational direction, the discrepancy (θ) between the two axes remains. Hence, the noisy horizontal component seismograms are projected on the vertical component seismograms. Due to the difference in noise levels between the two components, even if θ is small, it causes significant noise in the vertical component seismograms, resulting in a coherent relationship between the two components (Crawford and Webb, 2000). Crawford and Webb (2000) compared the noise level of the vertical component seismograms recorded by a poorly leveled (θ=0.2°) seismometer to the nearby well-leveled (θ=0.0006°) gravimeter. They find that the low-frequency background noise level of the gravimeter is up to 20 dB quieter than that of the seismometers. Bell et al. (2015) removed tilt and compliance noise from the vertical component seismograms recorded on the Cascadia Initiative and showed that the estimated θ is in the range of 0.1°–1.5°.

In order to illustrate the coherent relationship between the horizontal and vertical component

seismograms, I estimate the time variation of the coherent orientation, which maximizes coherence between the horizontal and vertical components (Bell et al., 2015). I simply call this orientation the coherent orientation. I first divide the 24-h time series into 2000-s sections with a 50-% overlap between neighboring sections and discard any sections containing electrical glitches and earthquake-generated signals. Using the remnant noise sections, I calculate the daily-average cross and power spectra as

$$G_{HZ}(\omega) = \frac{1}{n_d}\sum_{i=1}^{n_d} H_i^*(\omega)Z_i(\omega), \tag{2.1}$$

$$G_{HH}(\omega) = \frac{1}{n_d}\sum_{i=1}^{n_d} H_i^*(\omega)H_i(\omega), \tag{2.2}$$

$$G_{ZZ}(\omega) = \frac{1}{n_d}\sum_{i=1}^{n_d} Z_i^*(\omega)Z_i(\omega), \tag{2.3}$$

where n_d is the number of 2000-s-long noise sections included in a 24-h time series, $H_i(\omega)$ and $Z_i(\omega)$ are the Fourier-transformed horizontal and vertical component seismograms of i^{th} section, respectively. Using those spectra, the squared coherence between the horizontal and vertical components on day d is given by

$$\gamma_d^2(\omega) = \frac{|G_{HZ}(\omega)|^2}{G_{HH}(\omega)G_{ZZ}(\omega)}. \tag{2.4}$$

The coherent orientation, which maximizes the squared coherence (equation 2.4) averaged over a frequency range of 0.02–0.06 Hz, is searched for by rotating and composing the two horizontal components at a one-degree interval clockwise from the H1-component axis. The daily coherence between the horizontal and vertical components is large ($\sim$1) at frequencies below 0.1 Hz (Figure 2.1d). When the seafloor current has energy up to high frequencies, the coherence also increases up to high frequencies. The low coherence at a frequency range between 0.01–0.02 Hz is due to the dominance of compliance noise in this band (more details in later descriptions).

Figure 2.2a shows the time variation of the flow direction of the seafloor current. The daily average of the flow direction fluctuates between 90–180°. The one-minute sampled data largely fluctuates throughout the day. The annual average value of the flow direction is about 118° (toward the ESE), and the seafloor current flows in the direction along the slope of the Japan Trench (Figure A.1 in Appendix A). In contrast, the coherent orientation is time-invariant (Figure 2.2b) and points about -8° (north), which is significantly different from the flow direction (Figure A.1). The observed stable coherent orientation indicates that the orientation which maximizes the coherence between the vertical and horizontal components is most likely not affected by the seafloor current and supports the dominance of the θ, which is time-invariant.

This study analyzes seismic data recorded by the Oldest-1 Array, which has about 20 dB

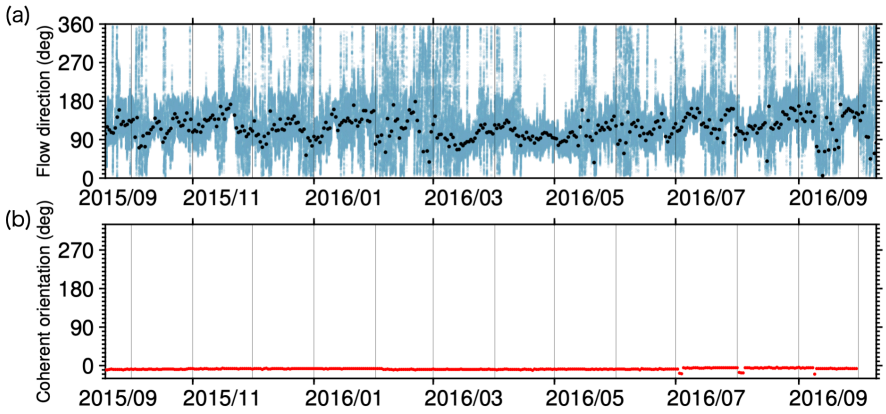

Figure 2.2: (a) Time variation of the flow direction of the seafloor current. Blue dots are data sampled at the one-minute interval, and black dots are the one-day average of the blue dots. The direction is measured clockwise from the north. (b) Time variation of the observed coherent orientation that maximizes the squared coherence between the horizontal and vertical component seismograms. The coherent orientation is measured from the north. The data set is the same as that in Figure 2.1, which is collected at offshore Miyagi.

lower noise level in both horizontal and vertical components than the station at offshore Miyagi (Figure A.2 in Appendix A). The different noise levels may reflect the difference in the installation location of the Oldest-1 Array and the station at offshore Miyagi. For example, the topography is more variable in offshore Miyagi, with the seafloor current flowing along the slope of the trench (Figure A.1). Contrarily, the Oldest-1 Array has a flatter topography (Figure 1.7) and may have a simpler current flow field than the steep topography in offshore Miyagi. The water depth and the distance to the shore are also different: the station at offshore Miyagi is 3400 m depth and only 100–200 km away from the coast, while the Oldest-1 Array is 5600–6000 m depth and much far away from the coast. The noise level also suggests the difference in the noise level of compliance noise, indicating the potential difference in the sediment thickness (see more details in the next section). These environmental factors might be responsible for the lower noise level in the horizontal component recorded at the Oldest-1 Array compared to the station in offshore Miyagi. Although the noise levels are low for both horizontal and vertical component seismograms, the squared coherence between the horizontal and vertical components observed in the Oldest-1 Array is still high (Figure A.3). Furthermore, the coherent orientation is time-invariant and stable throughout the observation period (about a year) (Figure 2.3a), with the peak of the most frequent value being significant in the histogram (Figure 2.3b). These observations suggest the existence of tilt noise in the vertical component, which has been induced by the seafloor current and the misalignment θ of the sensor's vertical axis relative to the gravitational direction.

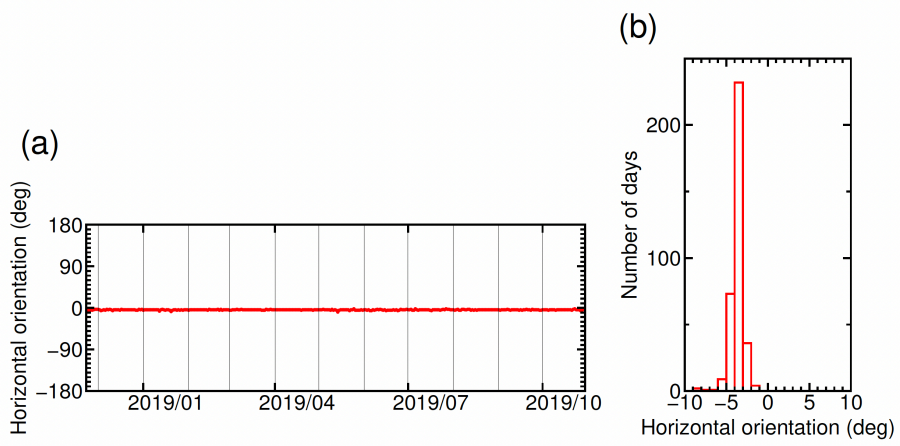

Figure 2.3: Observed coherent orientation that maximized the squared coherence between the horizontal and vertical component seismograms. The coherent orientation is measured clockwise from the H1-axis. (a) Time variation of the measured coherent orientation. The red dots are measurements. (b) A histogram of the measured coherent orientations in (a). The measurement is from OL08 in the Oldest-1 Array.

2.2.2 Compliance noise

The compliance noise originated from the long-period seafloor deformation under the seafloor pressure perturbation caused by the long-period ocean surface gravity waves (infragravity waves) that have longer periods than wind-driven waves and swells (e.g., Crawford et al., 1991). The infragravity-wave energy is generated at coastlines and propagates into the deep water as free surface waves and ubiquitously exists in the ocean (e.g., Webb et al., 1991). The seafloor deformation signals due to the infragravity waves depend on the amplitude of the seafloor pressure perturbations, the water depth, and the elastic properties of the underlying structure.

The dispersion relationship of an ocean surface gravity wave is given by

$$\omega^2 = gk\tanh(kH), \tag{2.5}$$

where ω is the angular frequency of the waves, k is the wavenumber, g is the gravitational acceleration, and H is the water depth of the observation point. By rearranging the equation (2.5) and assuming the wavelength of the wave is equal to the water depth, the cutoff frequency (f_c) of the infragravity wave, which can exert pressure on the seafloor, can be approximated as

$$f_c \approx \sqrt{\frac{g}{2\pi H}}. \tag{2.6}$$

From equation (2.6), the f_c is inversely proportional to the square root of the water depth, thus the compliance noise observed under the deeper water appears at the lower frequency band than that observed at the shallow water. For example, f_c is 0.016 Hz for $H = 6000$ m and is 0.021 Hz for $H = 3500$ m. Thus, compliance noise is typically observable as a gentle peak in noise spectra of pressure and vertical components at low frequencies and the peak is at a frequency of about 0.009 Hz in the Oldest-1 Array.

The transfer function between the seafloor displacement and the seafloor pressure is called seafloor compliance. Because the deformation is approximately inversely proportional to the structural shear modulus for a given pressure signal at the seafloor, the soft sediment site shows stronger compliance noise (e.g., Crawford et al., 1991). The pressure-to-displacement transfer function thus can be used in two ways: (1) estimation of the shallow structure (crust and uppermost mantle) and (2) noise reduction from the vertical component seismograms (e.g., Webb and Crawford, 1999). This study focuses on the later use.

2.3 Method: Tilt-noise removal

In this section, I describe the procedure to remove tilt noise from the vertical component BBOBS seismograms. I first summarize the noise transfer function between the horizontal and vertical component BBOBS seismograms in previous studies which used the U.S.-type BBOBSs. Then, I describe the modification and calculation of the transfer function for the Japanese-type

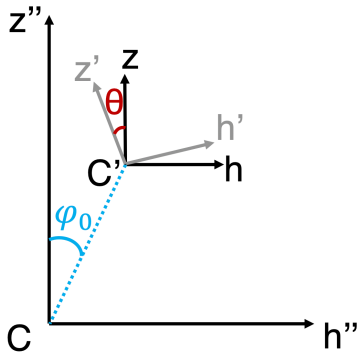

Figure 2.4: A schematic figure shows the two-dimensional coordinate system of BBOBS defined by Crawford and Webb (2000). The origin of the C-z”h” coordinate system is the center of mass of the BBOBS, where the z-axis is along the gravitational direction. The origin of the C’-zh coordinate system is the center of mass of the seismic sensor, where the z- and h-axes are parallel to z”- and h”-axes, respectively. C’ is offset from C by some distance and an angle φ_0. C’-z’h’ is the coordinate system of the seismic sensor, which is rotated by an angle of θ around C’.

BBOBSs. Finally, I remove tilt noise using the modified transfer function.

2.3.1 Horizontal-to-vertical noise transfer functions of previous studies

Horizontal and vertical component seismograms in the time domain

I first summarize the coherent relationship between the horizontal and vertical component seismograms in the time domain demonstrated by Crawford and Webb (2000). They formulated the generation of low-frequency tilt noise on the vertical and horizontal component seismograms as a change in the gravitational acceleration felt by the sensor by assuming the seafloor current rotates the seismic sensor around the center of mass of the entire BBOBS package by $\varphi = \varphi_0 + \epsilon(\omega)\cos(\omega t)$ (Figure 2.4), where φ_0 is the offset of the two mass center, $\epsilon(\omega)\cos(\omega t)$ is the fluctuation around the mass center C' due to the seafloor current, ω is an angular frequency, and t is time. The change in the gravitational acceleration felt by the sensor on horizontal and vertical components ($h'_g(t)$ and $z'_g(t)$, respectively) are given by

$$\begin{aligned} h'_g(t) &= g\,[\,\sin(\theta + \epsilon(\omega)\cos(\omega t)) - \sin\theta\,] \qquad (2.7)\\ &= g\epsilon(\omega)[\cos\theta\cos(\omega t) - \frac{\epsilon(\omega)}{2}\sin\theta\cos^2(\omega t)] + O(\epsilon(\omega)^2),\\ z'_g(t) &= g\,[\,\cos(\theta + \epsilon(\omega)\cos(\omega t)) - \cos\theta\,] \qquad (2.8)\\ &= -g\epsilon(\omega)[\sin\theta\cos(\omega t) + \frac{\epsilon(\omega)}{2}\cos\theta\cos^2(\omega t)] + O(\epsilon(\omega)^2), \end{aligned}$$

where g is the gravitational acceleration. They further simplified equations (2.7–2.8) under the assumption that θ, $\epsilon \ll 1$ and obtain

$$h'_g(t) \approx g\epsilon(\omega)\cos\theta\cos(\omega t), \tag{2.9}$$

$$z'_g(t) \approx -g\epsilon(\omega)\left[\sin\theta\cos(\omega t) + \frac{\epsilon(\omega)}{2}\cos\theta\cos^2(\omega t)\right]. \tag{2.10}$$

Thus, $z'_g(t)$ is approximately $(\epsilon(\omega)\cos(\omega t)/2 + \sin\theta)$ times $h'_g(t)$, indicating a coherent relationship between the vertical and horizontal component seismograms (Crawford and Webb, 2000).

Calculation of the noise transfer function

Following previous studies (Crawford and Webb, 2000; Bell et al., 2015), I calculate the noise transfer function between the horizontal and vertical component seismograms (H-to-Z transfer function). Using the calculated spectra (equations 2.1–2.3), I obtain H-to-Z transfer function of day d, $D_d(\omega)$, as

$$D_d(\omega) = \frac{G_{HZ}(\omega)}{G_{HH}(\omega)}, \tag{2.11}$$

$$A_d(\omega) = \frac{|G_{HZ}(\omega)|}{G_{HH}(\omega)}, \tag{2.12}$$

$$\phi_d(\omega) = \arctan\left[\frac{\mathfrak{Im}[G_{HZ}(\omega)]}{\mathfrak{Re}[G_{HZ}(\omega)]}\right], \tag{2.13}$$

where $A_d(\omega)$ is the admittance of the H-to-Z transfer function, $\phi_d(\omega)$ is the phase of the H-to-Z transfer function. Horizontal component is taken along the daily calculated coherent orientation, which is the orientation that maximize the squared coherence (equation 2.4) between the vertical and horizontal components (Figure 2.3).

The normalized standard errors of the admittance($\Delta A_d(\omega)$) and the squared coherence ($\Delta\gamma_d^2(\omega)$), and the normalized standard deviation of the phase($\Delta\phi_d(\omega)$) are given as (Bendat and Piersol, 2011)

$$\Delta A_d(\omega) = \frac{\sqrt{1-\gamma_d^2(\omega)}}{\sqrt{2n_d}|\gamma_d(\omega)|}, \tag{2.14}$$

$$\Delta\phi_d(\omega) = \frac{\sqrt{1-\gamma_d^2(\omega)}}{\sqrt{2n_d}|\gamma_d(\omega)|}, \tag{2.15}$$

$$\Delta\gamma_d^2(\omega) = \frac{\sqrt{2}(1-\gamma_d^2(\omega))}{\sqrt{n_d}|\gamma_d(\omega)|}, \tag{2.16}$$

where n_d is number of noise sections in a 24-h time series defined in equations (2.1–2.3). Figure 2.5 shows an example of the daily H-to-Z transfer function. The squared coherence is close to one at frequencies lower than 0.04 Hz (Figure 2.5a). It drops at around 0.01 Hz because of the presence

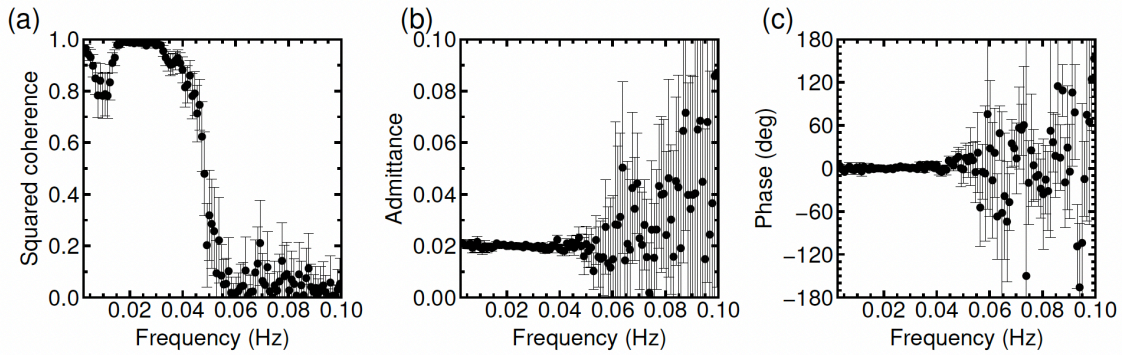

Figure 2.5: The squared coherence and the H-to-Z transfer function recorded at OL08 on November 10, 2018. (a) Squared coherence (equation 2.4), (b) Admittance (equation 2.12), (c) Phase (equation 2.13). Error bars represent 95 % confidence intervals.

of compliance noise, which "contaminates" the tilt noise. The squared coherence also drops at around 0.05 Hz because of the presence of microseisms and the amplitude of the tilt noise becomes relatively small. At frequencies where coherence is stable and high (<0.04 Hz), both admittance and phase of the H-to-Z transfer function are stable and almost have no frequency dependence. The admittance is ∼0.02 (Figure 2.5b). The phase is ∼zero, indicating that the horizontal and vertical component seismograms are in-phase (Figure 2.5c).

The H-to-Z transfer function is calculated every day throughout the observation period. Figures 2.6 and 2.7 show the time variation of the admittance and phase of the H-to-Z transfer function. Both admittance and phase are stable at frequencies lower than 38 mHz, especially at 13–33 mHz. The admittance is about 0.02 and the phase is zero throughout the observation period.

Noise reduction procedure in previous studies

To perform noise reduction, Crawford and Webb (2000) first estimated the H-to-Z transfer function and then subtracted the signal showing high coherence between the horizontal and vertical components from the vertical component. There are two horizontal components, and the transfer functions between the vertical and each horizontal component are calculated and subtracted one by one. Bell et al. (2015) modified the procedure of Crawford and Webb (2000) and performed noise reduction to the Cascadia Initiative data set. They first estimated the coherent orientation that maximizes the squared coherence between the vertical and horizontal components, then calculated the H-to-Z transfer function. Their observations showed that both the coherent orientation and the H-to-Z transfer function drifted systematically during the observation period, concluding that the H-to-Z transfer function should be estimated daily to account for those systematic changes. They further estimated the frequency-dependent transfer function to account for the unknown mismatch in the response functions among different components.

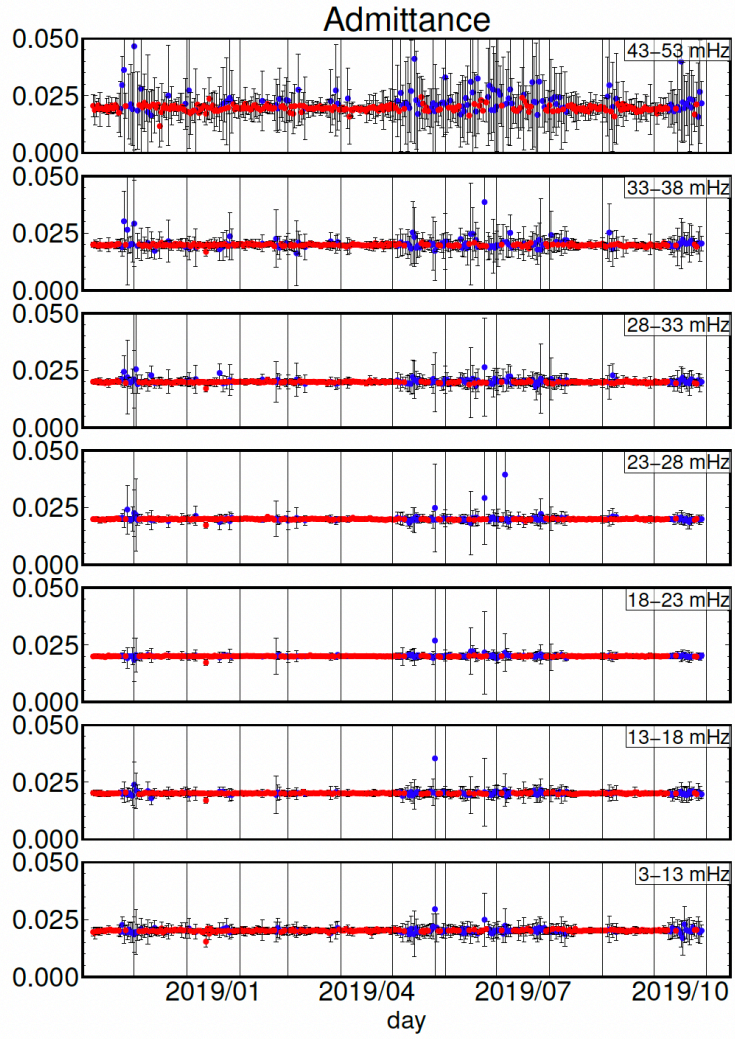

Figure 2.6: The admittance of the noise transfer function between the horizontal and vertical component seismograms (equation 2.12). Each panel shows average values in the frequency band written in the top right box. The dots are measurement and the error bars represent 95 % confidence intervals. The red and blue dots indicate the days whose squared coherence (equation 2.4) (averaged over a frequency range of 0.003-0.05 Hz) is larger or less than 0.6, respectively.

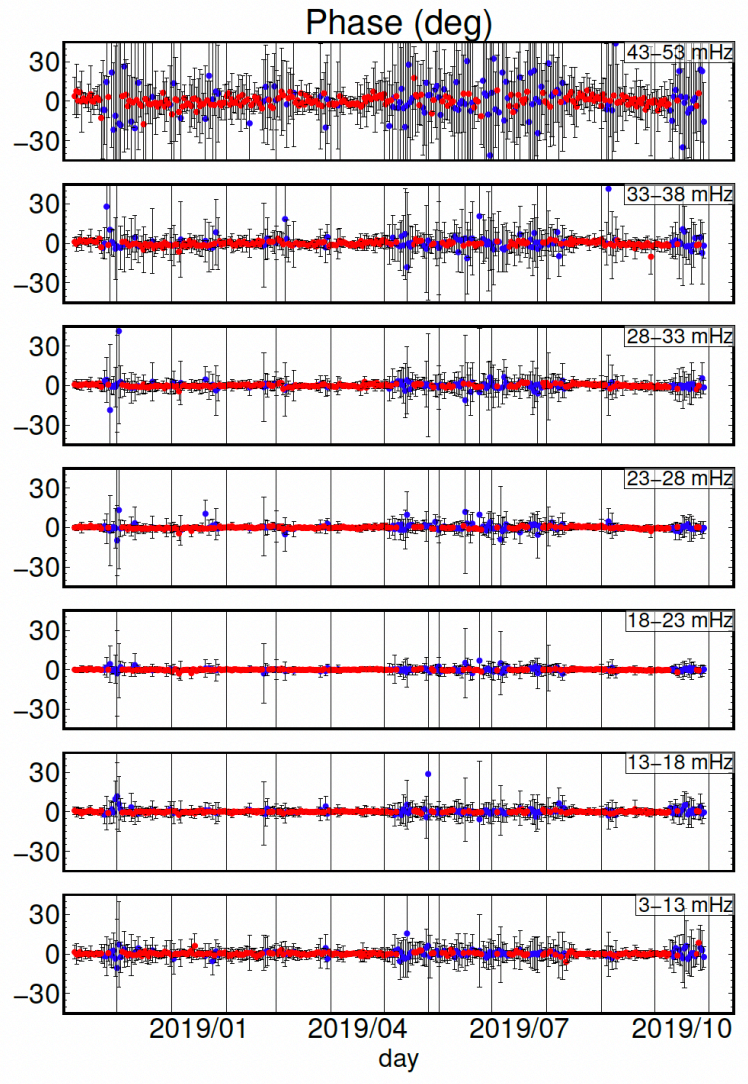

Figure 2.7: Same as Figure 2.6 but for the phase (equation 2.13).

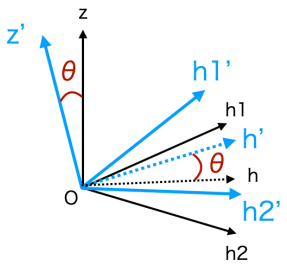

Figure 2.8: Definition of the coordinate system.

2.3.2 Tilt-noise removal procedure for the Japanese-type BBOBS

Although a lot of studies follow the method of Crawford and Webb (2000), there are two approximations in their formulations. First, to simplify the setting, they defined that the plane in which the seafloor current fluctuates the OBS around its mass center coincides with the plane in which the θ exists (Figure 2.4). Since the flow direction of the seafloor current is essentially independent from the plane where the θ exists, the problem should be formulated in a 3D space rather than the 2D space. Second, the static term due to the existence of the θ is ignored. If the θ exists, then all horizontal component signals should be projected to the vertical component, regardless of the presence or absence of the seafloor current, whereas in their formulation (equations 2.7–2.10), tilt noise is zero if $\epsilon(\omega) = 0$.

The coherent orientations which maximize the coherence between the vertical and horizontal component and H-to-Z transfer functions measured in this study using the Japanese-type BBOBS are stable throughout the observation period (Figures 2.3 and 2.6–2.7), and the H-to-Z transfer function is stable at low frequencies (Figures 2.5–2.7). These characteristics of transfer functions and coherent orientations in the Japanese-type BBOBS are different from those observed in the U.S.-type BBOBS. Time-invariant and frequency-independent transfer functions indicate that the transfer function is dominantly controlled by the static tilt angle, θ, and $\epsilon(\omega)$-induced tilt noise is ignorably small. The difference may arise from the difference in designs of BBOBSs as summarized in Section and/or differences in observation environment. The above characteristics are robust using the Japanese-type BBOBSs at different observation locations such as in the Oldest-1 Array (this study), northwestern Pacific Ocean (Kawano et al., 2019a, JpGU), and on voluminous oceanic plateaus (Isse et al., 2021). Therefore, the difference in the observed transfer functions is more likely attributed to the difference in the designs of BBOBSs. Based on the discussions about the formulations of Crawford and Webb (2000) and the difference in the results between Bell et al. (2015) and this study, I aim to estimate the θ, the misalignment between the sensor's vertical axis and the gravitational direction and remove the tilt noise on the vertical component seismograms by rotating the coordinate system to align the sensor's vertical axis to the gravitational direction.

Tilt-noise generation due to the θ

I assume a coordinate system (O-zh1h2; Figure 2.8) whose z-axis is along the gravitational direction and the h1- and h2-axes are orthogonal to the z-axis, and a coordinate system O-z'h1'h2' which is tilted by an angle of θ with respect to the z-axis of O-zh1h2 system. h'- and h-axes are taken in the plane where θ exists. The horizontal and vertical component seismograms ($h'(t)$ and $z'(t)$) in the tilted coordinate system can be given by

$$\begin{pmatrix} h'(t) \\ z'(t) \end{pmatrix} = \begin{pmatrix} \cos\theta & -\sin\theta \\ \sin\theta & \cos\theta \end{pmatrix} \begin{pmatrix} h(t) \\ z(t) \end{pmatrix}, \tag{2.17}$$

where $h(t)$ and $z(t)$ are horizontal and vertical component seismograms in the O-zh1h2 system.

The Japanese-type BBOBSs analyzed in this study have equipped the Guralp CMG-3T sensors [1]. In the CMG-3T sensor, the h1'- and h2'-axes are expected to be more precisely confined in the true horizontal plane that is orthogonal to gravitation direction compared to the accuracy of the alignment of the sensor's vertical axis (z'-axis) along the gravitational direction (z-axis) (Text A.4 and Figure A.4 in Appendix A). Therefore, equation (2.17) can be rewritten as

$$h'(t) = h(t), \tag{2.18}$$

$$z'(t) = \sin\theta\, h(t) + \cos\theta\, z(t). \tag{2.19}$$

As the above equation, while the horizontal component channels record the motions in the true horizontal plane, the vertical component seismogram is contaminated by the horizontal component seismograms multiplied by $\sin\theta$.

Estimating the θ

I estimate the coherent orientation and θ such that they are representative of the observation period. I first measure the coherent orientation on a daily basis (Section 2.2.1). The vertical component and the horizontal component taken along the coherent orientation are then used to calculate the daily H-to-Z transfer function. I then extract the most frequent value of the coherent orientation during the observation period at each station (Figure 2.3b) and define it as the representative coherent orientation, α^{rep}. I estimate the θ using the measured admittance in a frequency range where the uncertainty is small (18–23 mHz, Figure 2.6). The representative admittance is obtained by averaging all daily calculated admittances at the frequency range of 18–23 mHz with only using the measurements whose fractional uncertainties are 5 % or less: $A = \sum_d \sum_{f=0.018}^{f=0.023} A_d(f)/N$, where N is the number of measurements. Since the obtained representative admittance is $\sin\theta$ (equation 2.19), I obtain the representative θ (θ^{rep}) as $\arcsin(A)$. The accuracy of the obtained θ should be higher than that in the previous studies since I estimated the θ based

[1] Accessed on December 03, 2021: https://www.guralp.com/documents/MAN-030-0001.pdf

on a larger data set that contains measurements of all usable days while the previous studies estimated transfer functions on a daily basis.

The above method is more favorable than that of previous studies (Crawforad and Webb, 2000; Bell et al., 2015) in terms of how the noise-reduction procedure distorts the earthquake-generated signals. Previous studies used frequency-dependent transfer functions to subtract tilt noise. This procedure not only removes tilt noise but also distorts the earthquake-generated signals because the signals are equally subjected to the transfer function (although previous studies concluded that the distortion is sufficiently small). On the other hand, in this study, I only correct the tilt angle θ by rotating the coordinate system to align the sensor's vertical axis to the gravitational direction. Thus, the distortion of the earthquake-generated signals will not occur since in the tilted system (equations 2.18–2.19), not only the noise associated with the seafloor current but also the horizontal motions of the earthquake-generated signals are projected onto the vertical component. Note that although the formulation in this study (equations 2.18–2.19) differs from that of Crawford and Webb (2000) (equations 2.9–2.10), practically, there should be no significant difference in the tilt-noise estimation because Crawford and Webb (2000) formulated in a 2D plane where θ exist, and if we replace $g\epsilon(\omega)\cos(\omega t)$ in equations (2.7–2.8) to the horizontal component, the formulation will be similar to that of this study.

Figure 2.9 shows the estimated θ^{rep} and the α^{rep}. Since the BBOBSs were deployed by free fall from the sea surface, the coherent orientations, which maximize the coherence between the horizontal and vertical components, are expected to orient randomly and thus differ among the BBOBSs. Nevertheless, a bias in the direction along the H1-axis is observable (Figure 2.9). This can be understood by considering the architecture of seismic sensors as follows. The CMG-3T requires to set the three components independently on a common base (Figure A.4). The mass of the vertical component is attached to the end of a boom, and the boom is parallel to the H1-axis (Figure A.4). Thus, it tends to tilt along the H1-axis, not in the H2-axis direction, which is the direction orthogonal to the boom. I believe that this structure is reflected in the results. Bell et al. (2015) analyzed three types of OBSs and observed the same bias with similar values of θ at WHOI-Keck stations whose seismic sensors are also CMG-3Ts [2]. It is worth noting that the other types of OBSs used in Bell et al. (2015) equipped with different seismic sensors (Nanometrics Compact Trillium seismometer) do not have bias along the H1-axis.

Estimation and removal of tilt noise

Tilt noise recorded on the vertical component seismograms is estimated by using the parameters (θ^{rep} and α^{rep}) that I estimated above (Figure 2.9). I proceeded in the time domain as

$$Z_{-t}(t) = Z'(t) - \sin\theta^{rep}\ H'(t), \tag{2.20}$$

[2]Accessed on December 04, 2021: http://ds.iris.edu/mda/7D/?starttime=2011-01-01T00:00:00&endtime=2017-12-31T23:59:59

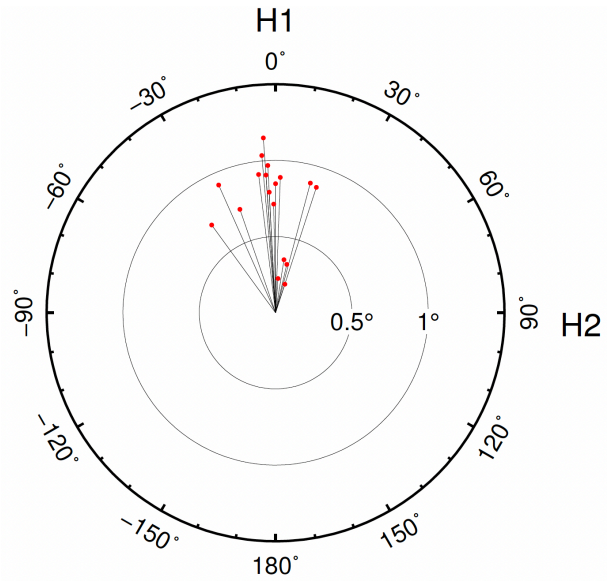

Figure 2.9: A polar figure of the estimated θ^{rep} and α^{rep} (red dots) for all BBOBSs deployed in the Oldest-1 Array. The magnitude of θ is shown as the diameter of the circle. The α^{rep} are shown as the black solid lines. The number of red dots is larger than the number of stations because some stations experienced releveling (readjustment of the horizontal plane of the seismic sensor) during the observation period, which has resulted in a change of the magnitude of θ^{rep}, so the observation period is divided for stations that have been releveled.

where $Z_{-t}(t)$ and $Z'(t)$ are tilt-noise reduced and original vertical component seismograms, respectively, and $H'(t)$ is the horizontal component signals taken along the α^{rep}. The results will be shown in Section 2.5.

2.4 Method: Compliance-noise removal

After the tilt-noise reduction, the compliance noise on the vertical component seismograms is subtracted in the same manner as that of the tilt-noise reduction. As summarized in Section 2.2.2, the transfer function between the vertical and the pressure component signals (P-to-Z transfer function), the seafloor compliance, depends on the shallow elastic structure. Thus, the seafloor compliance is time-invariant but frequency-dependent. Therefore, I estimate a representative P-to-Z transfer function by averaging the daily calculated transfer functions over the observation period.

2.4.1 Pressure-to-vertical transfer functions

I calculate the daily P-to-Z transfer function using equations (2.1–2.4) and (2.11–2.16). Here, H (horizontal component records) which appeared in those equations should be regarded as P (pressure component records). Figure 2.10 shows an example of a daily P-to-Z transfer function. At frequencies where the squared coherence is high, both admittance and phase are stable. At

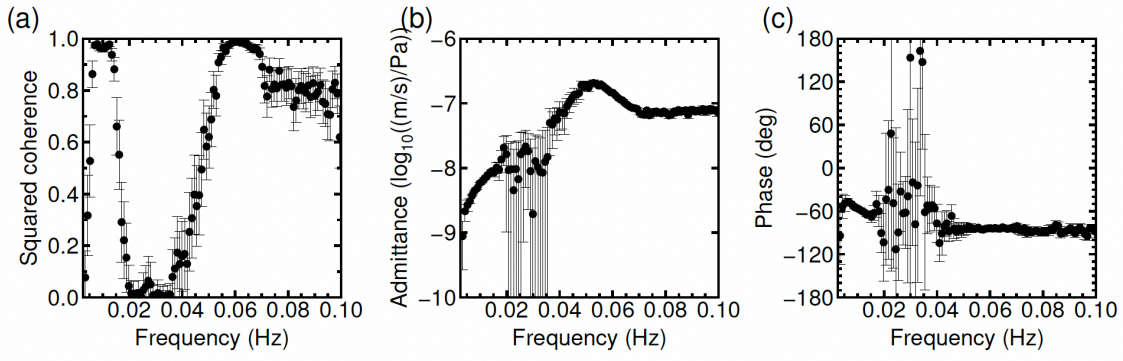

Figure 2.10: Same as Figure 2.5 but for the P-to-Z transfer function.

a frequency of 0.02 Hz or lower, significant compliance noise is recorded on both pressure and vertical component records, resulting in the high (∼1) squared coherence. The coherence is also high at a frequency of 0.06 Hz or higher because the two components record the common signal, microseisms.

Figure 2.11 summarizes the process of estimation of the representative P-to-Z transfer function. First, I obtain daily P-to-Z transfer function ($D_d(f)$) throughout the observation period (light pink dots in Figure 2.11). Second, I extract admittances whose fractional uncertainties are smaller than 5 % and phases whose uncertainties are smaller than five degrees (red dots in Figure 2.11). If there are more than 30 of such data points at a frequency, I calculate a transfer function averaged over the data points at that frequency (gray open circles in Figure 2.11): $A(\omega) = \sum_d^N A_d(\omega)/N$ and $\phi(f) = \sum_d^N \phi_d(\omega)/N$, where d is a day and N is the number of days and other notations follow equations (2.12) and (2.13). Third, I fit the average P-to-Z transfer function ($A(\omega)$ and $\phi(\omega)$) using cubic functions (Black solid and dashed lines in Figure 2.11, the difference of the line types will be mentioned later) and obtain the representative P-to-Z transfer function as $D^{rep}(\omega) = A^{rep}(\omega)\exp[\phi^{rep}(\omega)]$. $A^{ref}(\omega)$ and $\phi^{rep}(\omega)$ do not change significantly when the average of the real and imaginary parts is taken and fitted (Figure A.5 in Appendix A.5) instead of using amplitudes and phases.

Compliance-noise removal is performed at a frequency range of 0.002–0.02 Hz where compliance noise is observable. I apply a cosine taper at frequency ranges of 0.0018–0.002 Hz and 0.02–0.03 Hz to avoid abruptly cutting the frequency of noise reduction. In Figure 2.11, the representative P-to-Z transfer function in the cosine-tapered frequency band is shown by the dashed lines, and that in the 0.002–0.02 Hz is shown by the solid lines. At a frequency higher than 0.02 Hz, the representative admittance is estimated to be a few factors larger than the centroid of the daily calculated values. This would not distort seismograms significantly because the cosine taper is applied and the magnitude of the pressure signals is small in this frequency band.

I remove the compliance noise in the frequency domain as follows

$$Z_{-tc}(\omega) = Z_{-t}(\omega) - D^{rep}(\omega)P(\omega), \tag{2.21}$$

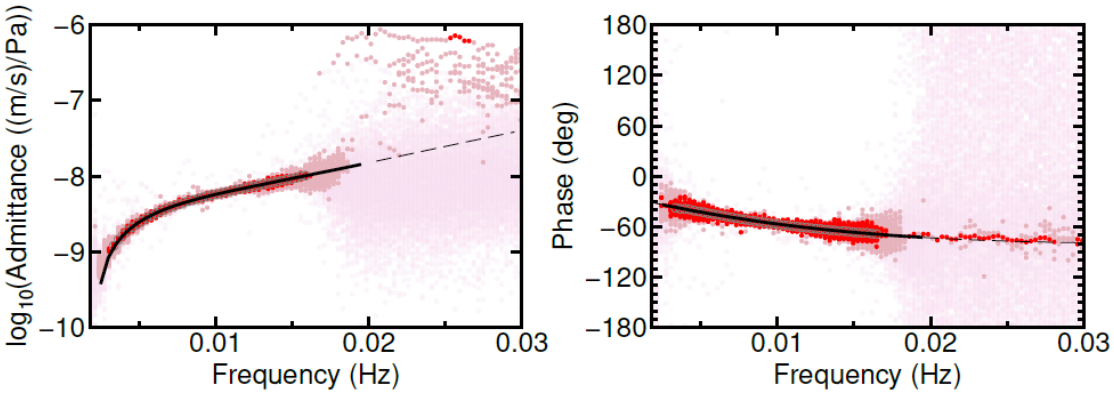

Figure 2.11: An example of the P-to-Z transfer function at OL08. The left panel is the admittance and the right panel is the phase of the P-to-Z transfer function, respectively. The dots represent the daily P-to-Z transfer functions. The light pink dots represent all data points. The deep pink and red dots represent the data points whose fractional uncertainties are smaller than 20 % and 5 % for admittances, respectively, or whose uncertainties are smaller than 10° and 5 ° for phases, respectively. The gray open circles represent the average transfer functions at that frequency (see also the main text). The black solid and dashed lines are the fitted P-to-Z transfer function using cubic functions.

where $Z_{-tc}(\omega)$ is the Fourier transform of the tilt- and compliance-noise removed vertical component seismograms, $Z_{-t}(\omega)$ is the Fourier transform of the tilt-noise removed vertical component seismograms, and $P(\omega)$ is the Fourier transform of the pressure signal.

2.5 Results: Noise-reduced spectra and seismograms

At frequencies lower than ∼0.04 Hz, there is a noticeable difference between the original and tilt-noise removed vertical component spectra (Figure 2.12). The tilt-noise removed vertical component spectra are about 10–20 dB lower than that of the original ones. The compliance-noise peak becomes more pronounced in the spectrum after the tilt-noise reduction. The power of the compliance noise increases at a frequency of ∼0.02 Hz, peaks at 0.009 Hz, and is overwhelmed by other background noise at 0.005 Hz or lower. After removing the compliance noise, the noise level at a frequency range of 0.005–0.02 Hz is successfully reduced by 10–20 dB.

Rayleigh waves at this frequency range are sensitive to the S-wave velocity of the mantle low-velocity zone, suggesting the importance of noise reduction to investigate the Lid/LVZ structure and discuss the lithosphere-asthenosphere system. The amount of noise-reduction levels differ among the stations, and this variation might be due to the presence of noise other than tilt noise, such as instrumental noise. At frequencies higher than 0.1 Hz, microseisms become dominant and the energies of the tilt noise become relatively small, so the original and tilt-noise removed vertical spectrum does not have any significant changes.

Figure 2.13 shows an example of noise-reduced Rayleigh-wave signals band-pass filtered from 0.005 to 0.015 Hz. In the original vertical records, it is difficult to recognize the propagation of

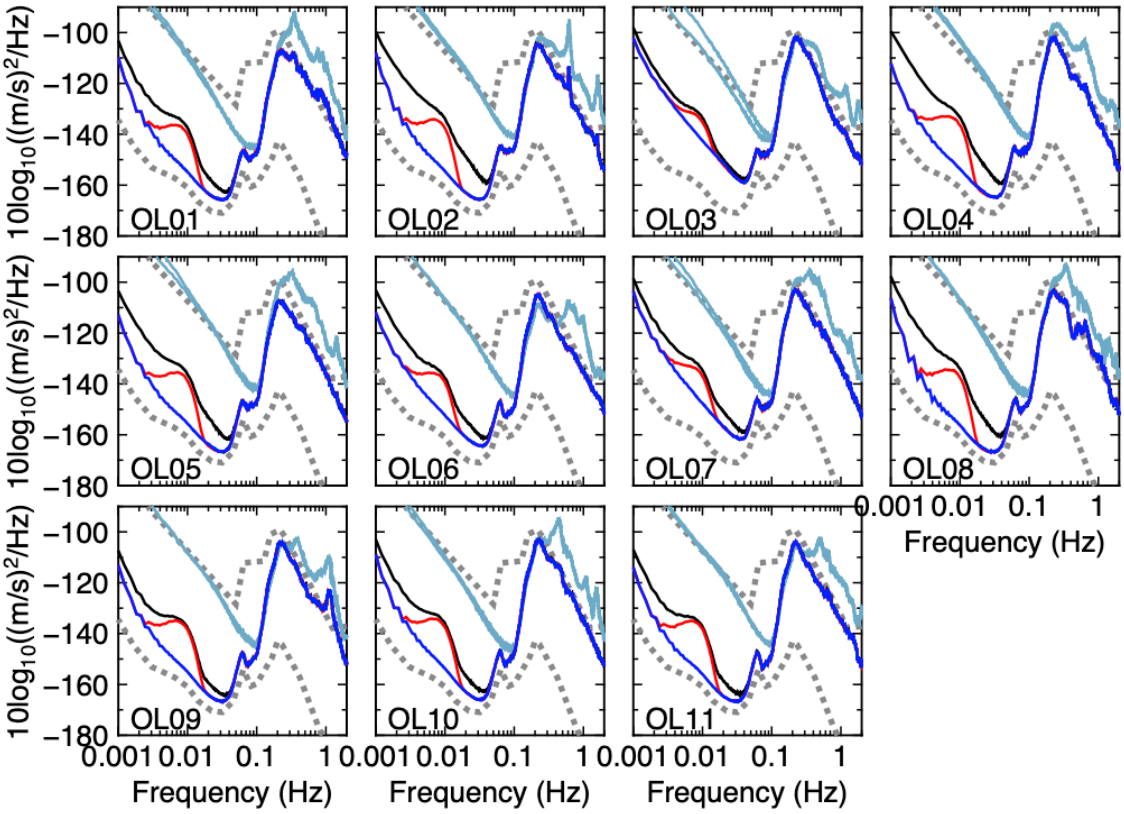

Figure 2.12: Noise power-spectral densities of each station. In each panel, the light blue lines represent two horizontal component spectra, the black line represents the original, the red line represents the tilt-noise removed, and the blue line represents the tilt- and compliance-noise removed vertical component spectrum. The dashed gray lines are new high and low noise models that represent the upper and lower bound of noise levels recorded on the terrestrial regions (Peterson, 1993). The spectra are calculated in the same manner as Figure A.2.

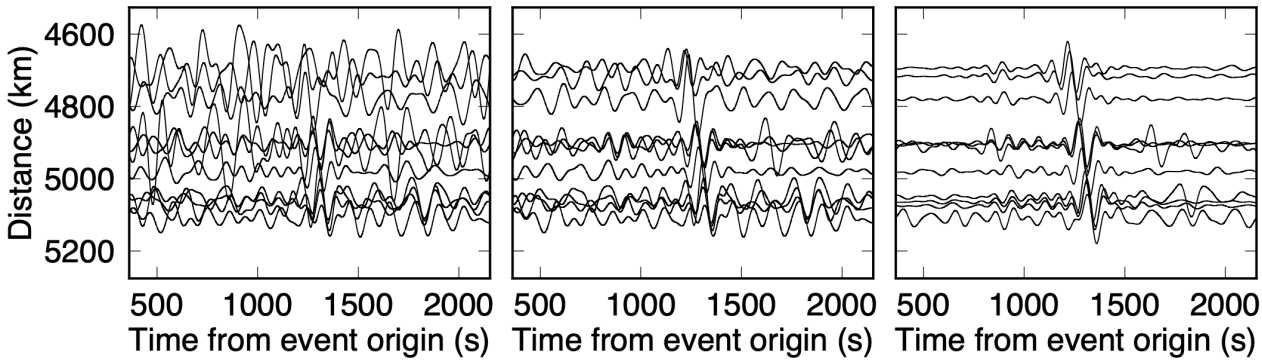

Figure 2.13: An example of Rayleigh-wave propagation in noise-reduced records at the Oldest-1 Array. From left to right; the original, tilt-noise removed, tilt- and compliance-noise removed vertical component seismograms, respectively. Each waveform has been band-pass filtered from 0.005 to 0.015 Hz. The seismic event occurred in Tonga island at 9:01:12.6 GMT on Aug. 5th, 2019 with a moment magnitude of 5.7 and a focal depth of 12 km.

Rayleigh waves. In the tilt-noise removed but compliance-noise not removed records, although the propagation of Rayleigh waves becomes clearer compared to that in the original ones, the signals still have no sufficiently high signal-to-noise ratio. In the tilt- and compliance-noise-removed records, the fundamental-mode Rayleigh-wave propagation becomes very clear at about 1300 s after the event origin time. In addition, even the small-amplitude S-wave propagation becomes visible at about 980 s after the event origin time. This means that by noise reduction, usable body waves are also increased and might be useful for full-wave inversions. The noise reduction contributes not only to surface-wave studies but has a broader impact on seismic waveform analysis.

Chapter 3

Array analysis of ambient noise cross-correlation functions recorded at BBOBS arrays

3.1 Introduction

Seismic interferometry is a method to extract deterministic signals from the random ambient seismic wavefield (e.g., Wapenaar et al., 2010ab) which has been early explored by Aki (1957). Assuming homogeneously distributed random noise sources around a station pair, the interstation ambient noise cross-correlation function (NCF) can be approximated as Green's function between the two stations. Therefore, NCFs can be used to infer the subsurface structure (Aki, 1957). With long digitally recorded seismograms being available, noise-based structural imagings become more and more common after Shapiro et al. (2005) published the first ambient noise tomography. The method is powerful to investigate the crustal and uppermost mantle seismic structure (e.g., Shapiro et al., 2005; Nishida et al., 2008; Takeo et al., 2013).

Since the analysis typically assumes homogeneously and randomly distributed noise sources around stations, the existence of a spatially localized source that persistently generates seismic waves, such as a volcano, may bias the surface wave dispersion measurements essential to investigate the structure (e.g., Shapiro et al., 2006). For example, Aso volcano in Japan has been known to generate persistent long-period tremors dominant in a period range of 3–15 s that had been observed locally and regionally (e.g., Kawakatsu et al., 1994; Kaneshima et al., 1996; Kawakatsu et al., 2000) that are recently observed by stations in East Asia via NCFs (Zeng and Ni, 2010, 2011). As such localized sources may result in anomalous signals in NCFs which contaminate surface waves propagating between station pairs, it is necessary to understand the origin of the signals.

This chapter contains two topics based on seismic interferometry. In Section 3.2, in order to show an example of a localized signal source that may potentially bias the dispersion measurement,

I use seismic interferometry to extract long-period (18 and 25 s) volcanic signals from an OBS array deployed in the western-central Pacific Ocean, which is different from the Oldest-1 Array. I locate the source of the volcanic signals and discuss possible oscillation mechanisms beneath the volcano. In Section 3.3, I perform seismic interferometry on the Oldest-1 Array data set and measure surface-wave phase velocity at a frequency range of 0.04–0.2 Hz. I first introduce the data set used in this study, then I discuss the difficulties in phase-velocity measurement using OBS data set and improve the pre-existing method for phase-velocity measurement.

3.2 Persistent Long-Period Signals Recorded by an OBS Array in the Western-Central Pacific: Activity of Ambrym Volcano in Vanuatu

This section has been published:
Kawano, Y., Isse, T., Takeo, A., Kawakatsu, H., Suetsugu, D., Shiobara, H., et al. (2020). Persistent long-period signals recorded by an OBS array in the western-central Pacific: Activity of Ambrym volcano in Vanuatu. Geophysical Research Letters, 47, e2020GL089108.
https://doi.org/10.1029/2020GL089108

3.2.1 Introduction

A well-known localized signal source is in the Gulf of Guinea that generates 26 s signal (Oliver, 1962, 1963; Holcomb, 1980, 1998). Shapiro et al. (2006) reported that the signal resulted in fast arriving wave-trains in NCFs computed for the North American and European stations. Ambient noise cross-correlation functions (NCFs) observed in East Asia and the Western Pacific also show the existence of fast-arriving signals centered around 26 s (Shapiro et al., 2006), but more recently Zeng and Ni (2014) suggested that this signal was independent from that of the Gulf of Guinea and originated from one of the volcanoes in the Vanuatu Arc region. Until now, however, the exact source origins and the excitation mechanisms of the signals observed at the Gulf of Guinea and the Vanuatu Arc are still poorly understood.

From December 2014 to January 2017, a geophysical network was deployed around the Ontong Java Plateau (OJP). This network, the OJP array, includes 23 broadband ocean bottom seismometers (BBOBSs) together with broadband seismic stations at two nearby islands and is designed to reveal the seismic structure of the Plateau (Suetsugu et al., 2018; Table B.1). During the process of conducting the Rayleigh wave dispersion analysis for regional tomography (Kawano et al., 2019b, AGU), I noticed, in NCFs, the presence of band-limited signals whose apparent travel time is smaller than that of inter-station Rayleigh waves, suggesting the existence of persistent spatially localized signal sources. As such signals might bias the dispersion measurement, the origin of the signals needed to be understood. In this section, based on the analysis of NCFs of the OJP array

data, supplemented by regional and local data (Table B.1), I show conclusively that the signals are emitted from an active volcano, Ambrym in the Vanuatu Arc, and discuss the excitation origin in association with the subsurface magma system therein.

3.2.2 Analysis of persistent long-period signals

OJP array data

The ambient noise cross-correlation functions at the OJP array are computed from vertical component seismograms. I first perform tilt-noise reduction from the BBOBS data (Crawford and Webb, 2000; Bell et al., 2015; see Chapter 2 for details). After dividing whole seismograms into 2000 s-long sections with a 50 % overlap, I discard any sections containing glitches or earthquake-generated signals. Then I stack all the Fourier-transformed sections with spectral whitening (Bensen et al., 2007) and obtain NCFs via the inverse Fourier-transform. The NCFs for July 2015 (Figure 3.1a) and for July 2016 (Figure 3.1b) show a difference in the signal appearance: in July 2015, the NCFs show clearly the propagation of inter-station fundamental-mode Rayleigh waves (0S in Figure 3.1a), whereas, in July 2016, some signals arrive earlier than 0S and the amplitudes of the fast arriving signals are larger compared to those of 0S observed in July 2015 (Figures 3.1a,b). The NCFs for July 2016 show significant peaks centered around 25 s (0.040 Hz) and 18 s (0.057 Hz) in spectra, whereas the NCFs for July 2015 show less significant peaks at those periods (Figures 3.1c,d).

In order to estimate the location of the signal sources, I conduct a grid search employing the NCFs similar to the previous studies (Shapiro et al., 2006). In addition to the OJP array dataset, I incorporate records from regional permanent broadband seismic stations for better spatial coverage (Figure 3.2a). The analysis is done for data recorded from April to September 2016 when the 25 s and 18 s signals have a strong amplitude (note that the data recording ended at the end of September 2016 for most of the OJP stations). I compute NCFs using 4000 s-long sections considering the large inter-station distances (6,184 km for the largest separation) and discard those whose signal to noise ratio is less than two; here, signal and noise levels are measured respectively by average Fourier amplitudes between 0.030–0.050 (0.050–0.070) Hz for the 25 s (18 s) signal and between 0.020–0.030 Hz. After band-pass filtering the NCFs with a Gaussian function centered at 0.040 (0.057) Hz, I take the envelopes of the filtered NCFs in the time domain and normalize each by its maximum value to extract arrival time information but not amplitude.

I search for a source location (x, y), where x and y is longitude and latitude, respectively, that maximizes the stacked amplitude, E, of envelopes having the Rayleigh wave group velocity, U, as a parameter:

$$E(x, y, U) = \sum_{p} H_p(t_p) \tag{3.1}$$

where $H_p(t_p)$ denotes the envelope amplitude for p^{th} station pair (station j and k) and t_p for a

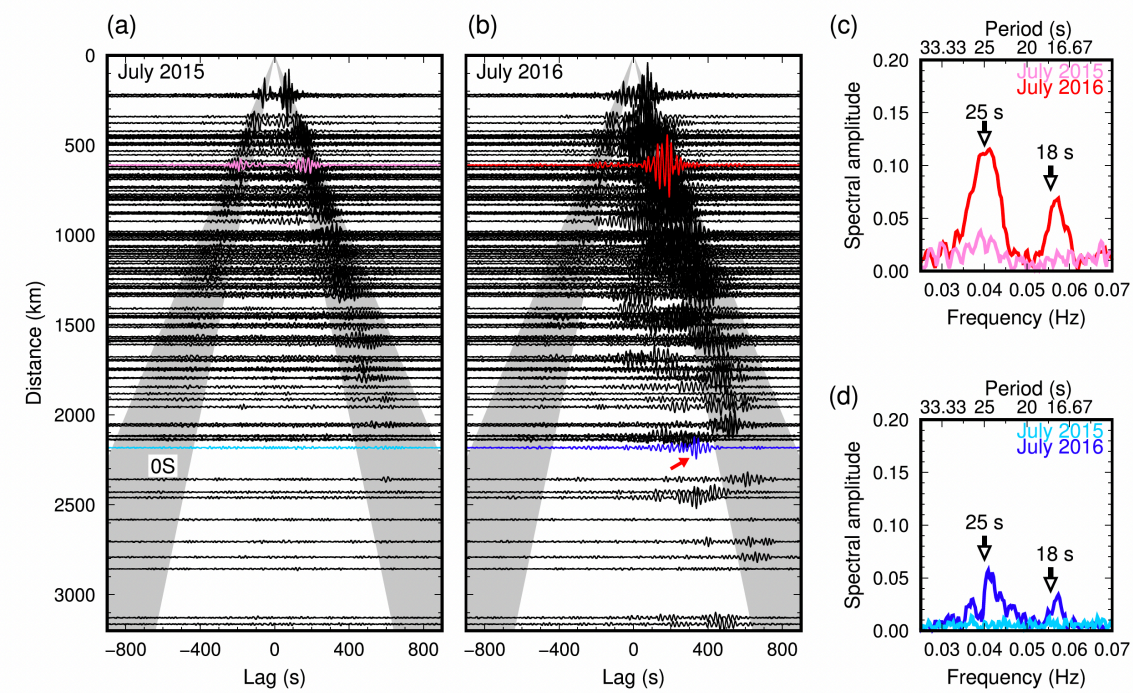

Figure 3.1: Examples of the NCFs of vertical component seismograms recorded by the OJP array (Figure 3.2a). NCFs are computed from 1-month records and band-pass filtered between 0.025 and 0.070 Hz. (a, b) NCFs for July 2015 and July 2016 (only for BBOBS pairs are shown): They are displayed such that the positive lag time corresponds to waves traveling away from the inferred source locations in the Vanuatu Arc (Figure 3.2b). The gray-shaded bands indicate the time interval corresponding to a group velocity window of 2.5–5.0 km/s when interstation fundamental-mode Rayleigh waves (0S) are expected to arrive. The red arrow points a fast arriving signal. (c, d) The Fourier amplitude spectra of the NCFs highlighted in (a) and (b) with the same colors. Black arrows indicate positions of 25 and 18 s.

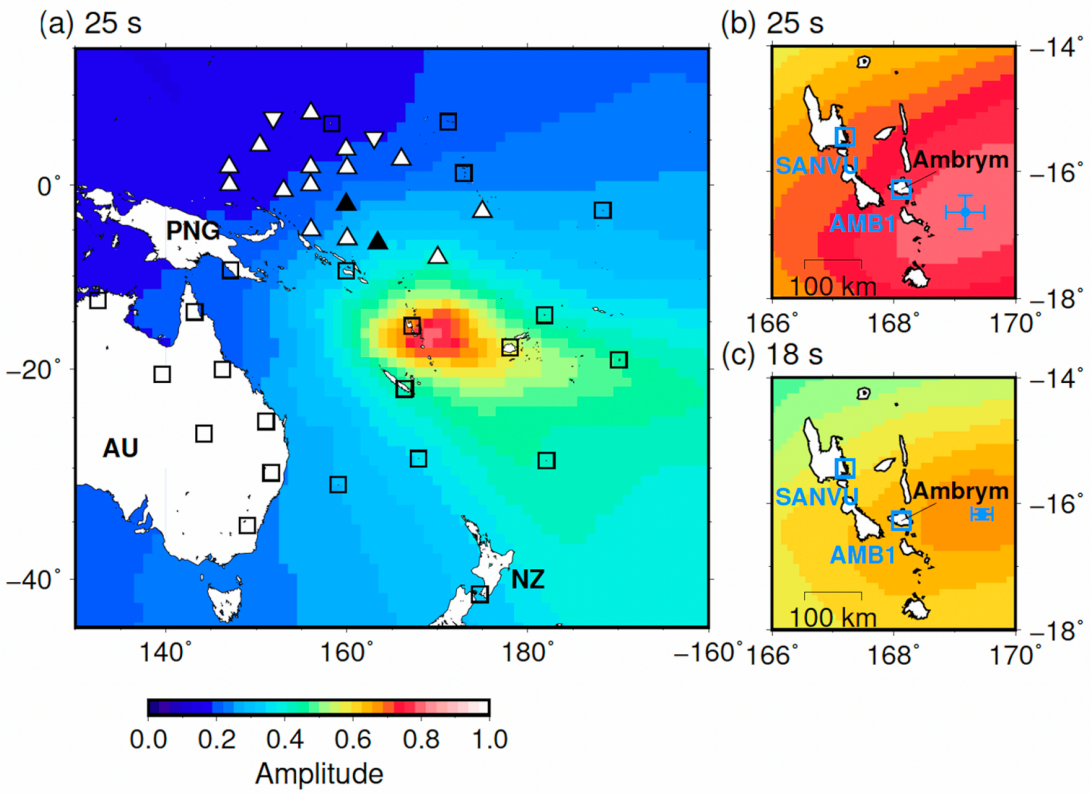

Figure 3.2: Station maps and the results of the grid-search source location. Triangles represent the stations of the OJP array (normal and inverted ones for BBOBS and island stations, respectively), and squares represent permanent land stations employed for the analysis. Two solid triangles denote OJ14 (northern) and OJ16 (southern) stations used in Figure 3.3c. Color contours indicate the amplitude of stacked NCFs (equation 3.1) normalized by the number of station pairs used for stacking. (a) The result of the grid-search source location on a 1° grid for the 25 s signal. (b, c) The close-up of the results of the 0.1° grid-search for the 25 s signal (b) and 18 s signal (c) around the Ambrym island. The blue points with error bars indicate the optimal bootstrap average location with one standard error. Note that AMB1 is not used for the source location estimation. The color scale is common for all results.

group travel time difference between the two stations for a given group velocity; more explicitly, $t_p(x, y, U) = [d_j(x, y) - d_k(x, y)]/U$, where d_j and d_k are great-circle distances connecting the station and a trial source at (x, y).

The grid search is conducted for three parameters, (x, y, U), first on a one-degree grid with a 0.1 km/s step in group velocity U ranging between 3.0–4.3 km/s for the 25 s source and 2.8–3.8 km/s for the 18 s; I then use a 0.1-degree grid in 14°×8° area around the estimated source, and the optimal source location and the standard errors are estimated from one-hundred bootstrap samples: a bootstrap sample consists of randomly selected station pairs of the same data size as the original with duplicates allowed. Both the 25 s and 18 s signal sources are estimated around the Vanuatu Arc: 169.18°E±0.31°, 16.65°S±0.27° with a group velocity of 3.56±0.09 km/s for the 25 s signal (Figure 3.2b), and 169.45°E±0.17°, 16.18°S±0.09° with a group velocity of 3.09±0.03 km/s for the 18 s signal (Figure 3.2c). The estimated source locations for both the 25 s and 18 s signals

are similar to the previous study, where Zeng and Ni (2014) located the source of their 26 s signal in the Vanuatu Arc. They calibrated the source location (168.5°E, 17.5°S assuming homogeneous velocity structure) using local earthquakes and relocated the source at 167.8°E, 16.4°S, suggesting a possible connection with the activity of the Ambrym volcano. I confirm their conclusion by locating a local earthquake near the Ambrym island using our method and observing nearly one-degree bias to the eastern direction (Text B.2 in Appendix B), which is consistent with their result. Here, instead of further relocating the estimated sources, I directly compare the ambient noise cross-correlation functions with seismic records observed around the estimated source area to delineate the source origin. I also note that contamination of the 25 s signal by the 26 s signal originated from the Gulf of Guinea is unlikely (Zeng and Ni, 2014; Figure B.1 in Appendix B).

Regional and Local Observations

I investigate spectrograms recorded by stations SANVU and AMB1 located around the estimated source area (Figures 3.2b,c) and compare them with the cross-spectral density (CSD) observed at the OJP array. SANVU, a part of the GEOSCOPE network, uses a three-component broadband seismometer (STS-2), and AMB1, a part of the Vanuatu seismic network, uses a three-component intermediate-period broadband seismometer (CMG-40T). A comparison of the Fourier amplitude of distant earthquakes recorded at SANVU and AMB1 suggests that the reported instrument response of AMB1 at IRIS DMC is likely incorrect and thus re-estimated (see Figure B.2 and Appendix B for the details). Spectrograms of vertical component velocity seismograms are constructed from daily power-spectral densities (PSDs) that are taken from the median of the Fourier spectra computed for 2000 s-long sections. The CSDs are computed by the same procedure described in Section 3.2.2 but without spectral whitening.

Strong and persistent signal peaks appear at around 25 s and 18 s in the spectrograms at SANVU and AMB1 (Figures 3.3a,b) and in the spectrogram of CSDs between OJ16 and OJ14 (Figure 3.3c). These signals show similar amplitude variations with time, and the dominant periods are stable during the observation period. Although the observation periods do not overlap each other for AMB1 and the OJ16–OJ14 pair, time variations of their signal power are both consistent with that of SANVU. I, therefore, consider that the 25 s and 18 s signals observed at the OJP array and AMB1 have the same origin. AMB1 is the closest to the signal source among these stations because the signal amplitude of AMB1 is about an order larger than the others, which cannot be explained by the site amplification effect (Figure B.3 in Appendix B). These observations strongly indicate that the 25 s and 18 s signals observed by the OJP array originate from the region near the station AMB1. I consider the signals are generated by an active source rather than a passive scatterer of oceanic microseisms (Ma et al., 2013) because no significant correlation between the secondary microseism (5–10 s) and the 25 s and 18 s signals are observed (Figure B.4 in Appendix B).

The station AMB1 is a part of the Vanuatu network operated by the Vanuatu Geoscience Observatory and located in the Ambrym volcanic island. Three-component seismograms at AMB1

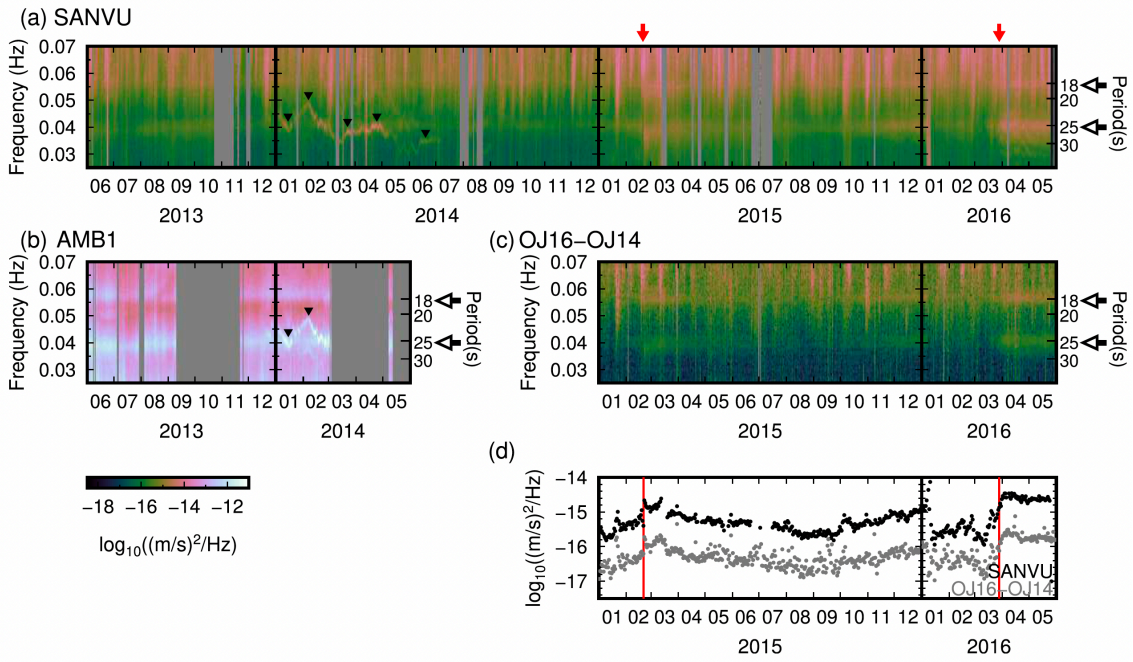

Figure 3.3: Comparison of spectrograms of the vertical component velocity seismograms. (a, b) The power spectral density (PSD) for stations SANVU and AMB1 shown in Figure 3.2b. Black arrows indicate positions of 25 s and 18 s. (a) for SANVU: The red arrows indicate February 20, 2015 and March 28, 2016, when signal intensifications are observed. (b) for AMB1: The black triangles show the fluctuating signal around 25 s (0.04 Hz). (c) The cross-spectral density (CSD) for the OJ16–OJ14 pair computed without spectral whitening. The color scale is common among all spectrograms. (d) A comparison of PSD and CSD for the 25 s signal (averaged in a frequency range of 0.038–0.042 Hz) for SANVU (black) and OJ16–OJ14 pair (gray). The red lines correspond to the dates of red arrows in (a).

are shown in Figure 3.4 for two different pass-bands targeting at the 25 s (0.040 Hz) and 18 s (0.057 Hz) signals. The 25 s signal is coherent between the NS and vertical components (Figure 3.4a), whereas the EW component whose amplitude is smaller than the NS behaves differently; the 18 s signal is coherent among three components (Figure 3.4b). These observations indicate that waveforms are simple enough to investigate the source origin via the polarization analysis (Figures 3.4c,d), which is conducted as follows: (1) time-windows containing earthquakes and/or glitches are discarded, and then three-component seismograms are band-pass filtered at the target frequency windows to make 200 s-long sections with a 50 % overlap, (2) eigenvectors and eigenvalues of a covariance matrix are computed from NS and EW component 200 s sections, and the polarization azimuth is obtained (Jurkevics, 1988), (3) the polarization dip is computed in the same procedure but using radial and vertical component seismograms, where a radial component is computed using the polarization azimuth.

The results show that both the 25 s and 18 s signals are well-polarized, indicating N4°W±11° azimuth with 22°±5° dip and N16°E±4° azimuth with 17°±3° dip, respectively (Figure 3.4e), where the means and the standard deviations are obtained by fitting Gaussian functions to the histograms of all the 200 s window. Azimuths are more variable than dips for the 25 s signal, and both azimuths and dips are poorer polarized than those of the 18 s signal (Figure 3.4e). The fact that the polarizations are quite linear and that the polarization directions of both long-period signals point toward the area right beneath the active cones (Figure 3.4f) make us conclude that the sources of the 25 s and 18 s signals are the volcanic activities of the Ambrym volcano.

3.2.3 Discussion

The Ambrym volcano is one of the most active volcanoes in the Vanuatu Arc. It is characterized by a 12 km-wide caldera hosting two active cones, Marum and Benbow. The volcano recently erupted in February 2015 and in December 2018 (Hamling and Kilgour, 2020; Hamling et al., 2019). The intensification of the 25 s and 18 s signals is observed in the spectral densities (Figure 3.3d), and the one on February 20, 2015, corresponds to the intra-caldera minor eruption (Figure B.5 in Appendix B and Hamling and Kilgour, 2020).

Legrand et al. (2005) installed a three-component broadband seismometer (STS-2) on the southwestern flank of Ambrym volcano (about 9 km from the Benbow crater) from July to November 2000 and observed persistent long-period tremors centered around 18–22 s (Figure 3.4f). Based on the results of the polarization analysis, they concluded that the long-period tremors originate from two sources: one in the central-to-eastern part of the caldera where the 1986 eruption took place, and the other in the western part between Marum and Benbow cones. The estimated depths of the sources are between 2.7–2.9 km below sea level. Although they did not explicitly identify two different spectral peaks for those sources, their observation, in terms of the peak period, is generally similar to ours, except that one of the peak periods of our observation (25 s) is outside of their period range. Also, the inferred source depths and locations may be different as shown

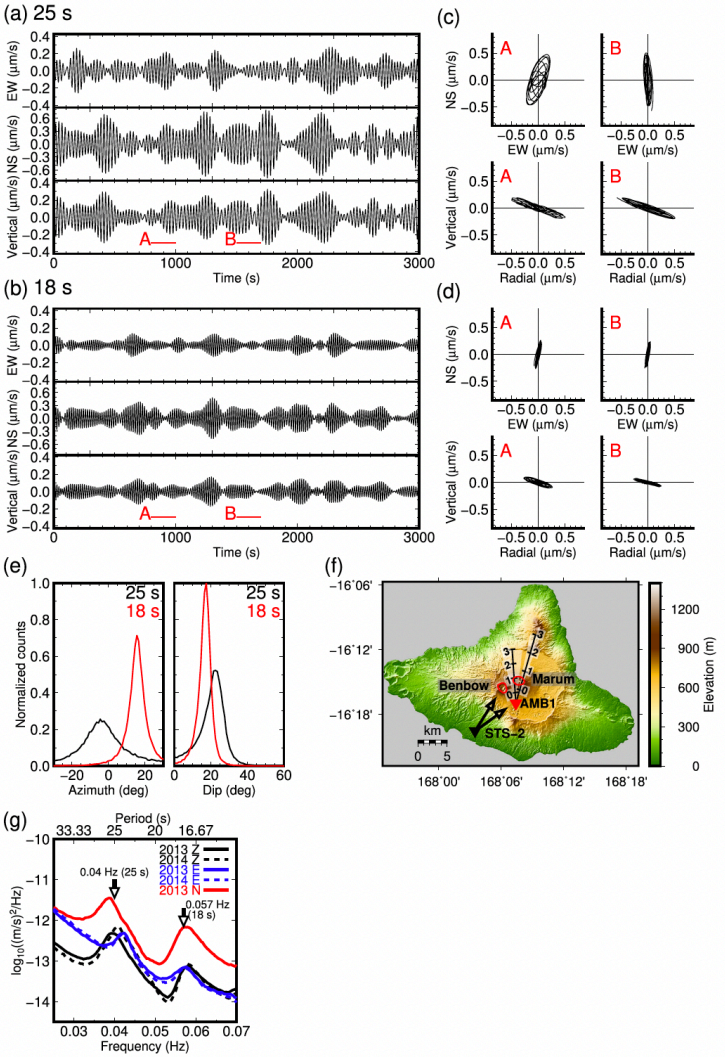

Figure 3.4: Examples of three-component seismograms at AMB1. (a, b) Fifty-minute long seismograms (start at 07:25:00 UTC June 4, 2013) band-pass filtered between 0.035–0.045 Hz targeting for 25 s (a), and 0.052–0.065 Hz for 18 s (b). The scale for the NS component is twice of the other components. (c, d) Particle motions in the horizontal (top) and vertical (bottom) plane for 200 s-long seismograms for the time windows indicated by the red lines in (a, b). (e) Histograms of polarization directions (azimuth: left; dip: right) for 200 s-long sections for the 25 s (red) and 18 s (black) signals recorded from June to August 2013. (f) Topography of the Ambrym volcano with station locations (red triangle for AMB1 and black for the STS-2 seismograph of Legrand et al. (2005)). Black arrows at STS-2 indicate polarization azimuths estimated by Legrand et al. (2005). The two black lines represent the mean polarization azimuths of the long-period signals (with white-shaded areas for one standard deviation ranges) estimated in this study. The numbers along the black lines with ticks indicate the projected source depths below the sea level if the source is there. Red circles show rims of Benbow and Marum cones. (g) A comparison of yearly power-spectral densities of three components of AMB1. Black arrows indicate the position of 0.04 Hz and 0.057 Hz.

below.

The polarization analysis of the 25 s and 18 s signals suggests the existence of multiple signal sources at shallow depth. The consistent time variations between the 25 s and 18 s in the spectrograms (e.g., Figure 3.3c for March-April, 2016) imply that the two sources are physically connected. Recent studies suggest the existence of multiple magma reservoirs beneath the two active cones at depth 1–5 km below sea level (e.g., Hamling et al., 2019). Considering that the wavelengths of the long-period tremors (>∼60 km) are much larger than the distance between the active cones and the station (<5km), AMB1 is likely located within the near-field range from the source (e.g., Aki and Richards, 2002). Near-field seismic records contain various types of waves including static displacement, the near-field terms, and P- and S-waves. If the source is dominated by the isotropic component, as often the case for volcanic volumetric sources, the polarization of filtered seismograms is rectilinear and points to the source centroid (Legrand et al., 2000). Then, I can estimate the source locations using the estimated polarization directions as done in Aso (e.g., Kawakatsu et al., 2000; Legrand et al., 2000; Kawakatsu and Yamamoto, 2015) and in Ambrym (Legrand et al., 2005).

As I have only one observation point here, the best I can do is to infer the range of source locations for presumed depths; Figure 3.4f shows the inferred source locations assuming variable source depths or vice versa. If I assume the signal sources are located beneath Marum, the source depth is 0–1 km below the sea level for both 25 s and 18 s signals, indicating that they are more likely to be associated with the activity of the shallow magma system at depths of 1¬–2 km (Hamling et al., 2019). As like the case of the Aso volcano in Japan, they could be due to vibrations of conduits connecting the magma system to the surface cones, possibly sustained by the hydrothermal reaction at the aquifer. Considering the long-period nature of signals, the temporal deployment of broadband seismometers in the island should allow determining the source geometry better (Yamamoto et al., 1999).

The spectral width of the two signals is similar, but the 25 s signal shows more variable peak frequencies than that of the 18 s signal (Figure 3.4g). The polarization azimuths of the 25 s signal are more variable than those of the 18 s signal (Figure 3.4e). This might suggest that the source for the 25 s signal is distributed wider in the lateral direction compared to that of the 18 s signal; it may be related to a subsurface conduit system that connects Marum and Benbow cones, or the dykes below the cones recently imaged by the analysis of the ALOS-2 InSAR data for the 2015 eruption (Hamling and Kilgour, 2020). From January to June 2014, spectrograms show signals whose peak periods are time-variant and fluctuate around 33 s (0.03 Hz), 25 s (0.04 Hz), and 20 s (0.05 Hz); those signals show a similar time variation, and the one that fluctuates around 25 s is the strongest (Figures 3.3a,b). These may be related to the change of the magmatic fracture system prior to or posterior to the eruptions.

3.2.4 Conclusion

Ambient noise cross-correlation functions observed by the OJP array in the western-central Pacific indicate the existence of spatially localized signal sources that generate long-period seismic waves at periods around 25 s and 18 s. The sources are determined in the Vanuatu Arc where the Ambrym volcano exists that generates the long-period seismic waves whose amplitude variations are consistent with the array observation. Polarization analysis of local seismic records in the Ambrym volcano suggests the existence of multiple sources possibly located at depths of 0–1 km from the sea surface beneath the active cones. This work demonstrates a potential usage of a BBOBS array to discover unknown long-period persistent seismic sources (possible beneath the ocean) via the ambient noise cross-correlation function analysis, and this may, in turn, help our better understanding of the ambient noise seismic field for future structural or monitoring studies.

3.3 Model-based phase velocity measurement

In this section, I detail the method for measuring high-frequency (0.04–0.2 Hz) surface-wave phase velocity. I first summarize the data set of the Oldest-1 Array, and then calculate the ambient noise cross-correlation functions (NCFs) and obtain the interstation cross spectra. I develop a model-based phase-velocity measurement method that provides a more physically appropriate dispersion curve than previous studies did. I apply the method to the Oldest-1 Array and measure both Rayleigh- and Love-wave phase velocities.

3.3.1 Data

Within the Oldest-1 Array, seamounts divide the array into two (The white shaded areas in Figure 3.5). Seamounts are generally known as bodies with thick crusts. To avoid the bias in phase-velocity measurement due to the thick crust of the seamount, I investigate the high-frequency phase velocity using sub-array data sets. Figure 3.5 shows station locations of the two arrays: (a) western array which consists of stations in the western side of the seamounts and (b) eastern array which consists of stations in the eastern side of the seamounts. The western array is located in the East Mariana Basin and the eastern array is located in the Pigafetta Basin (Figure 1.8a). Table 3.1 summarizes numbers of stations and station pairs for calculating NCFs of each component in each array. In the eastern array, since there is a station with only DPG, the numbers are different among components. Additionally, all vertical component seismograms are tilt- and compliance-noise-removed data (See Chapter 2 for the details).

3.3.2 Calculation of noise cross spectra

Noise cross-correlation functions (NCFs) are calculated using ambient noise to extract the background Rayleigh- and Love-wave propagation between the station pairs (Aki, 1957). NCFs

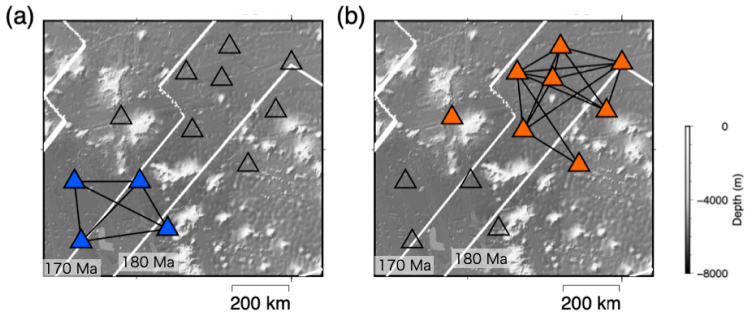

Figure 3.5: Station maps. (a) The western array. (b) The eastern array. The filled triangles represent stations used for the analysis and the open triangles are not. Station pairs used in the analysis are connected with black solid lines. The background white lines represent isochrones (Seton et al., 2020) and the array locates at 170–180 Ma.

Table 3.1: Summary of the data sets used in this study

Data set	Number of stations	Number of station pairs
(a) Western array	4	6
(b) Eastern array	6 (Z and H) 7 (P)	11 (Z and H) 16 (P)

Z, H, and P represent vertical, horizontal, and pressure components, respectively.

are obtained by the same procedure as described in Section 3.2.2 but seismograms are divided into 1600-s-long sections. Figure 3.6 shows NCFs between vertical-vertical (ZZ), pressure-pressure (PP), radial-radial (RR), and transverse-transverse (TT) components for three bandpass filters: 0.025–0.04 Hz, 0.04–0.06 Hz, 0.06–0.1 Hz, and 0.1–0.2 Hz. Multiple modes are recognizable: fundamental-mode and first higher-mode Rayleigh waves (0S and 1S modes, respectively) in ZZ- and RR-component NCFs, 0S modes in PP-component NCFs, fundamental-mode Love waves (0T modes) in TT-component NCFs bandpass filtered at 0.1-0.2 Hz and 0.06–0.1 Hz. Some anomalous fast-arriving signals are observable in RR-component NCFs at 0.06–0.1 Hz. Those signals do not seem to be excited by a volcano at Vanuatu Island reported by Kawano et al. (2020) or Aso volcano reported by Kawakatsu et al. (1994) and Zeng and Ni (2010). The signals might be reflected and/or converted at the seamounts in the middle of the Oldest-1 Array (e.g., Takeo et al., 2014).

Theoretical cross spectra

Phase velocities are measured using the spatial auto-correlation method (Aki, 1957; Haney et al., 2012). Assuming a laterally homogeneous structure and a homogeneous ambient noise source distribution around the stations, theoretical cross spectra for 0S, 1S, and 0T modes in γ-component

NCFs ($\gamma = ZZ, PP, RR$, and TT) observed in p^{th} station pair are given by

$$S_p^{ZZ} = a_{0S}^{ZZ} J_0\left(\frac{\omega c_{0S}}{d_p}\right) + a_{1S}^{ZZ} J_0\left(\frac{\omega c_{1S}}{d_p}\right), \tag{3.2}$$

$$S_p^{PP} = a_{0S}^{PP} J_0\left(\frac{\omega c_{0S}}{d_p}\right) + a_{1S}^{PP} J_0\left(\frac{\omega c_{1S}}{d_p}\right), \tag{3.3}$$

$$S_p^{RR} = a_{0S}^{RR} J_{0-2}\left(\frac{\omega c_{0S}}{d_p}\right) + a_{1S}^{RR} J_{0-2}\left(\frac{\omega c_{1S}}{d_p}\right), \tag{3.4}$$

$$S_p^{TT} = a_{0T}^{TT} J_{0-2}\left(\frac{\omega c_{0T}}{d_p}\right), \tag{3.5}$$

where $a_{0S}^{\gamma}(\omega)$, $a_{1S}^{\gamma}(\omega)$, and $a_{0T}^{\gamma}(\omega)$ represent source intensity for 0S-, 1S-, and 0T-modes observed in γ-component NCFs, respectively, $c_{0S}(\omega), c_{1S}(\omega), c_{0T}(\omega)$ represents phase velocity of 0S, 1S, and 0T modes, respectively, d_p is the distance between the p^{th} station pair, $J_m(x)$ is the m^{th} Bessel function of the first kind, and $J_{0-2}(x) = J_0(x) - J_2(x)$. Transverse component in Rayleigh waves and Radial component in Love waves (Aki, 1957) are ignored by assuming surface-wave wavelength shorter than the interstation distances ($c_n^{\gamma}/\omega \ll d_p$).

3.3.3 Difficulties of phase-velocity measurement using an OBS array

The simplest way to measure phase velocities is to perform a grid search of phase velocity at each frequency while maximizing the variance reduction between the theoretical and observed cross spectra (Figure 3.7). Figure 3.7 shows the variance reduction plots for three different data sets. Variance reduction is defined as $1 - \sum_p [S_p^{\gamma}(\omega) - \Phi_p^{obs}(\omega)]^2 / \sum_p \Phi_p^{obs}(\omega)^2$, where $\Phi_p^{obs}(\omega)$ is the real part of the γ-component cross spectra observed at p^{th} station pair, $S_p^{\gamma}(\omega)$ is defined in equations (3.2–3.5) but a single mode is assumed. To minimize the bias in phase-velocity measurement due to inhomogeneous noise source distribution, I only use the real part of the cross spectra because the imaginary part of the cross spectra mainly results from the inhomogeneous distribution of the noise source (e.g., Harmon et al., 2007; Weaver et al., 2009).

Because the array is divided into two and the number of available station pairs is considerably reduced, compared to the full data set of the Oldest-1 Array (Figure 3.7c), several different curves, which represent 2π ambiguity, can potentially fit the observed data with high variance reduction in both the western and eastern arrays (Figures 3.7a,b). In particular, the 2π ambiguity is strong for all components in the western array (Figure 3.7a). On the other hand, avoidance of the seamounts makes the phase velocities recognizable at a broader frequency range in particular for the 0T and 1S modes whose sensitivities concentrate in the crust and the uppermost mantle: For example, in Figures 3.7a and b, phase velocities of the 0T modes is recognizable at $\sim$0.05–0.2 Hz, whereas in Figure 3.7c, it is only recognizable at $\sim$0.05–0.1 Hz with high variance reduction (>0.5).

Although large variance reduction (>0.9) is obtained by the grid-search method at a certain frequency range (Figure 3.7), due to the difficulties peculiar to the seafloor observation, the circumstances that one can use the grid-search method are still limited. For example, it is difficult

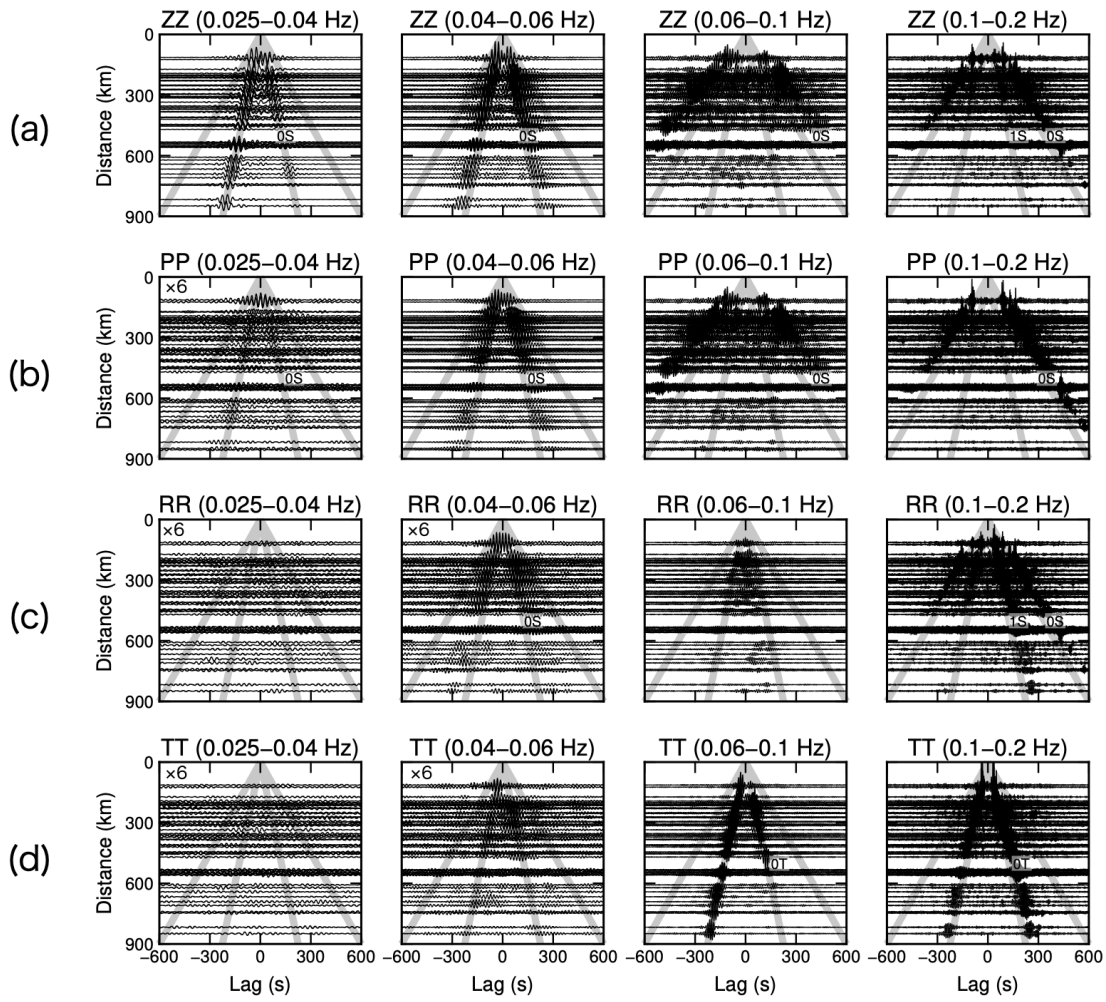

Figure 3.6: NCFs bandpass filtered at 0.025–0.04 Hz, 0.04–0.06 Hz, 0.06–0.1 Hz, and 0.1–0.2 Hz for (a) vertical-vertical (ZZ), (b) pressure-pressure (PP), (c) radial-radial (RR), and (d) transverse-transverse (TT) component pairs. The amplitudes of TT- and RR-component NCFs at 0.025–0.04 Hz and 0.04–0.06 Hz, and PP-component NCFs at 0.025–0.04 Hz are six times exaggerated compared to other NCFs. The gray solid lines indicate arrival times assuming group velocities of 1.5 km/s and 4.0 km/s. All usable station pairs within the Oldest-1 Array are included in the calculations.

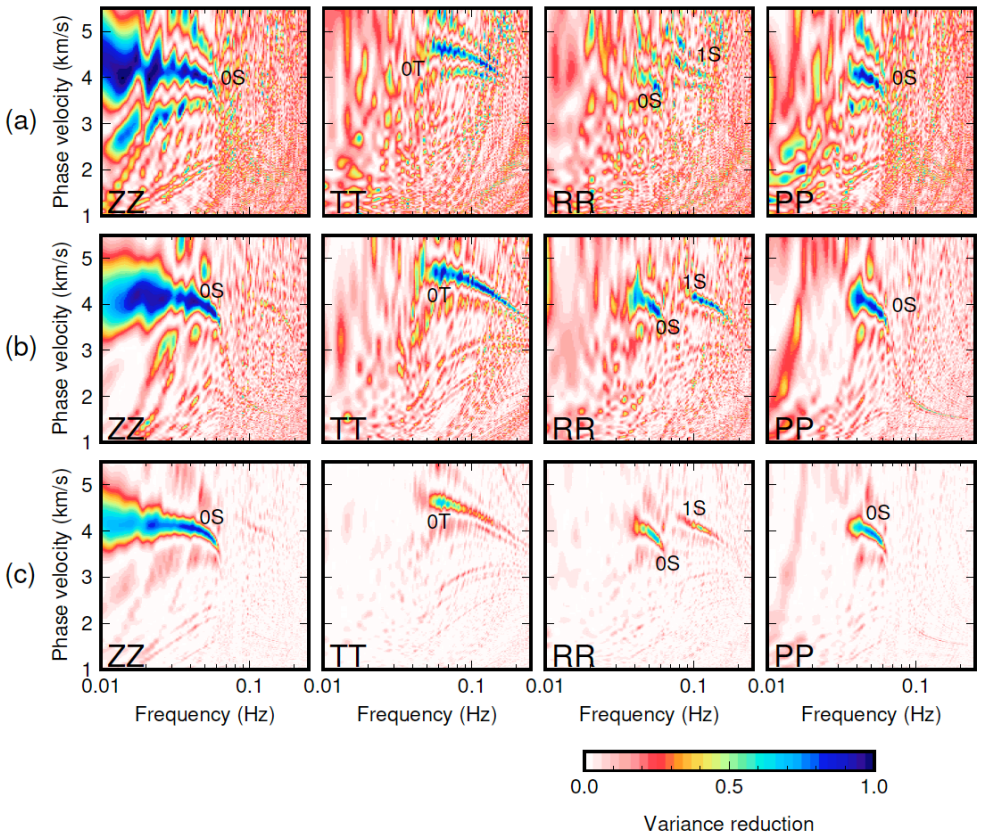

Figure 3.7: Plots of variance reduction against frequency and phase velocity for ZZ-, PP-, RR-, and TT-component NCFs. (a) Variance reduction of data set of the western array (Figure 3.5a and Table 3.1). (b) Variance reduction of the eastern array data set (Figure 3.5b and Table 3.1). (c) Variance reduction calculated by all available station pairs (maximum 66 pairs) in the Oldest-1 Array.

to properly isolate a single mode from the others because short-period surface waves are dispersive and the different modes overlap with each other. If one failed to isolate a mode, the obtained phase velocity might be biased. In particular, for this study, it is also difficult to determine 2π ambiguity (e.g., Figure 3.7a) due to the small number of station pairs and long interstation distances ($>\sim$110 km).

3.3.4 Measurement of phase velocity via multi-mode waveform fitting

To overcome the difficulties described above, Takeo et al. (2014) developed a multi-mode waveform fitting method that simultaneously fits all the observed modes and estimated phase velocities as functions of frequency ($c(\omega)$; dispersion curve), which is constructed by a series of B-spline basis functions: $c(\omega) = \sum_i g_i p_i(\omega)$, where g_i is coefficients and $p_i(\omega)$ is the B-spline function. Unlike the grid search which allows a sudden jump of phase velocity, the B-spline function can provide a smooth dispersion curve, which is more physically appropriate.

What kind of constraints are given to the dispersion curves depends on functions that are

chosen to express the curves. The shape of dispersion curves constructed by the B-spline expansions essentially depends on the knot intervals and potentially introduces unrealistic peaks and/or troughs to the dispersion curves. Therefore, a careful choice of function is needed. In this study, same as Takeo et al. (2014), I estimate phase velocities by fitting the synthetic cross spectra (equations 3.2–3.5) to the observed cross spectra by the multi-mode waveform fitting. Different from Takeo et al. (2014), to give a natural *a priori* constraint on dispersion curves, I calculate the dispersion curves from S-wave velocity structure (e.g., Yoshizawa and Kennett, 2002; Takeo et al., 2018). Even if there are several choices of potential curves to fit the observed cross spectra (e.g., Figure 3.7a), there are limited numbers of curves that are reproducible from a structure. Additionally, unrealistic peaks and/or troughs in the B-spline expansions can be effectively avoided if they are not reproducible from a structure. Therefore, by directly estimating the phase velocities from a structure, the physical feasibility of dispersion curves can be always guaranteed, and thus a more stable measurement can be realized even with a small data size, which is the case of this study.

In what follows, I first describe model parameters, then I introduce a misfit function that measures the difference between the theoretical and observed cross spectra. Finally, I describe how to optimize the phase velocity measurement.

(1) Model parameters: Average and azimuthally anisotropic phase velocities

Due to the limited azimuthal coverage, azimuthal anisotropy potentially introduces bias to the average phase velocity, and the bias can reach up to about 1 % (Takeo et al., 2018). I, therefore, simultaneously search for average (isotropic) phase velocity and their azimuthal anisotropy to avoid unfavorable bias due to the azimuthal anisotropy.

Azimuthally anisotropic phase velocity

The average phase velocity ($c_n^{ave}(\omega)$) of the n^{th} mode (n=0S, 1S, and 0T) and its azimuthal anisotropy can be given by phase velocity ($c_n(\omega,\theta)$) at each wave-propagation azimuth θ as

$$\begin{aligned} c_n(\omega,\theta) &= c_n^{ave}(\omega)\{1 + A_{c2}^n(\omega)\cos(2\theta) + A_{s2}^n(\omega)\sin(2\theta) + A_{c4}^n(\omega)\cos(4\theta) + A_{s4}^n(\omega)\sin(4\theta)\}, \\ &= c_n^{ave}(\omega)\{1 + A_2^n(\omega)\cos2[\theta - \theta_{max2}^n(\omega)] + A_4^n(\omega)\cos4[\theta - \theta_{max4}^n(\omega)]\}, \end{aligned}$$

where $A_{c2}^n(\omega)$ and $A_{s2}^n(\omega)$ are parameters of the 2θ-sinusoidal pattern of azimuthal variation of phase velocity, $A_{c4}^n(\omega)$ and $A_{s4}^n(\omega)$ are parameters of the 4θ-sinusoidal pattern of azimuthal variation of phase velocity (Montagner and Nataf, 1986), $A_2^n(\omega) = \sqrt{[A_{c2}^n(\omega)]^2 + [A_{s2}^n(\omega)]^2}$, $A_4^n(\omega) = \sqrt{[A_{c4}^n(\omega)]^2 + [A_{s4}^n(\omega)]^2}$, $\theta_{max2}^n(\omega) = \frac{1}{2}\arctan[A_{s2}^n(\omega)/A_{c2}^n(\omega)]$, and $\theta_{max4}^n(\omega) = \frac{1}{4}\arctan[A_{s4}^n(\omega)/A_{c4}^n(\omega)]$. $A_2^n(\omega)$ and $A_4^n(\omega)$ are half intensities, and $\theta_{max2}^n(\omega)$ and $\theta_{max4}^n(\omega)$ are the fastest directions of the 2θ and 4θ terms, respectively. For azimuthal anisotropy of the 0S and 1S modes, the 4θ-sinusoidal patterns are theretically ignorable when azimuthal anisotropy is small (Montagner and Nataf,

1986). Thus for the 0S- and 1S-mode phase velocities, azimuthally variable phase velocities are given by

$$\begin{aligned} c_n(\omega,\theta) &= c_n^{ave}(\omega)\{1 + A_{c2}^n(\omega)\cos(2\theta) + A_{s2}^n(\omega)\sin(2\theta)\} && (3.6)\\ &= c_n^{ave}(\omega)\{1 + A_2^n(\omega)\cos 2[\theta - \theta_{max2}^n(\omega)]\}, && (3.7) \end{aligned}$$

where n = 0S and 1S. For azimuthal anisotropy of the 0T-mode phase velocities, the 2θ-sinusoidal pattern is theoretically ignorable although the 2θ-sinusoidal pattern of the 0T mode is observed both in global (Montagner and Tanimoto, 1991) and local scale (Russell et al., 2019). In this study, because the available data sets are small for both regions, I assume that the 4θ-sinusoidal pattern is dominant to avoid adding model parameters. The azimuthally variable phase velocities of the 0T mode are thus given by

$$\begin{aligned} c_{0T}(\omega,\theta) &= c_{0T}^{ave}(\omega)\{1 + A_{c4}^{0T}(\omega)\cos(4\theta) + A_{s4}^{0T}(\omega)\sin(4\theta)\} && (3.8)\\ &= c_{0T}^{ave}(\omega)\{1 + A_4^{0T}(\omega)\cos 4[\theta - \theta_{max4}^n(\omega)]\}. && (3.9) \end{aligned}$$

Model-based calculation

I calculate phase velocities (equations 3.6 and 3.8) from an isotropic S-wave velocity ($V_S = V_{SH} = V_{SV}$, where V_{SH} and V_{SV} are horizontally propagating horizontally and vertically polarized S-waves, respectively) structure which has a water layer, three crustal layers, and 11 mantle layers from Moho to 150 km depth. I calculate average phase velocities ($c_{0S}^{ave}(\omega)$, $c_{1S}^{ave}(\omega)$, and $c_{0T}^{ave}(\omega)$) by a Fortran package DISPER80 (Saito, 1988). I assume a radially isotropic structure and calculate phase velocities of Rayleigh- and Love-waves independently. Therefore, I do not distinguish V_{SV} and V_{SH} but assume that they are independently isotropic. In order to describe the radially isotropic media, at each layer, I need to define P- and S-wave velocities (V_P and V_S), their attenuation coefficients, and density. At each layer, V_S is assigned as a constant value. The crustal density (ρ) and crustal P-wave velocity (V_P) are scaled to V_S with the scaling relationship as follows (Christensen and Salisbury, 1975),

$$\begin{aligned} V_P\ (\mathrm{km/s}) &= 1.75 \times V_S(\mathrm{km/s}) + 0.375\ (\mathrm{km/s}),\\ \rho(\mathrm{kg/m^3}) &= 0.5\ \mathrm{kg/m^3/(km/s)} \times V_S + 1.25\ (\mathrm{kg/m^3}). \end{aligned}$$

Mantle V_P is enforced to be $\sqrt{3}$ times larger than V_S, and the mantle density and attenuation coefficients are fixed to PREM with 1-Hz reference frequency (Dziewonski and Anderson, 1981). The structure deeper than 150 km is fixed to the model of Kawano et al. (2020, AGU), which is an isotropic S-wave velocity model estimated in the Oldest-1 Array (Figure 1.1).

In addition to isotropic V_S for Rayleigh or Love waves, I also estimate anisotropic parameters ($A_p(\omega)$, p=c2 and s2 for Rayleigh waves or p=c4 and s4 for Love waves) by S-wave velocity structure at each layer in the seafloor to 150 km depth, I assign anisotropic parameters: $A_{c2}(z)$

and $A_{s2}(z)$ for Rayleigh waves or $A_{c4}(z)$ and $A_{s4}(z)$ for Love waves. They are converted to the frequency domain using the sensitivity kernels ($K^n_{V_S}(z,\omega)$) as

$$A^n_p(\omega) = \int_z K^n_{V_S}(z,\omega) A_p(z) dz, \tag{3.10}$$

where n = 0S, 1S, and 0T, and $A^n_p(\omega)$ is parameters defined in equations (3.6) and (3.8) (p=c2 and s2 for Rayleigh waves or c4 and s4 for Love waves).

(2) Misfit functions

Using the phase velocities modeled previously, I evaluate the misfit between the synthetic cross spectra (equations 3.2–3.5) and the real part of the observed cross spectra. The misfit function for each γ component (γ =ZZ, PP, RR, and TT) is defined as

$$E_\gamma(\omega) = \frac{1}{\omega} \frac{\sum_p [\Phi^\gamma_p(\omega) - S^\gamma_p(\omega)]^2}{\sum_p [\Phi^\gamma_p(\omega)]^2} / \sum_\omega (1/\omega), \tag{3.11}$$

where $S^\gamma_p(\omega)$ is synthetic cross-spectra in γ-component NCFs in p^{th} station pair, which is defined as the equations (3.2)–(3.5) with azimuthally variable phase velocities (equations 3.6 and 3.8) are substituted, $\Phi^\gamma_p(\omega)$ is the real part of the observed γ-component cross spectra of p^{th} station pair. $a^\gamma_n(\omega)$ in equations (3.2–3.5) is estimated by the least-squares method to minimize the squared misfit ($\sum_p [\Phi^\gamma_p(\omega) - S^\gamma_p(\omega)]^2$) between the synthetic and observed cross spectra. $a^\gamma_n(\omega)$ is constrained to be a non-negative value. Low-frequency misfits are weighted by $1/\omega$.

Because the number of available station pairs is small in this study, to further stabilize the analysis, I introduce narrow-band smoothing on the estimation of the ambient noise source power ($a^\gamma_n(\omega)$). Narrow band is defined as $0.9\omega_0$–$1.1\omega_0$, where ω_0 is a center frequency of the narrow band. I rewrite the misfit function (equation 3.11) for each γ component (γ =ZZ, PP, RR, and TT) as

$$E_\gamma(\omega_0) = \frac{1}{\omega_0} \frac{\sum_p \sum_{\omega=0.9\omega_0}^{1.1\omega_0} [\Phi^\gamma_p(\omega) - \hat{S}^\gamma_p(\omega;\omega_0)]^2}{\sum_p \sum_{\omega=0.9\omega_0}^{1.1\omega_0} [\Phi^\gamma_p(\omega)]^2} / \sum_{\omega_0} (1/\omega_0), \tag{3.12}$$

where

$$\hat{S}^\gamma_p(\omega;\omega_0) = \hat{a}^\gamma_{0S}(\omega_0) J_0(\omega c_{0S}/d_p) + \hat{a}^\gamma_{1S}(\omega_0) J_0(\omega c_{1S}/d_p) \tag{3.13}$$

for γ=ZZ and PP, and

$$\hat{S}^{RR}_p(\omega;\omega_0) = \hat{a}^{RR}_{0S}(\omega_0) J_{0-2}(\omega c_{0S}/d_p) + \hat{a}^{RR}_{1S}(\omega_0) J_{0-2}(\omega c_{1S}/d_p), \tag{3.14}$$

$$\hat{S}^{TT}_p(\omega;\omega_0) = \hat{a}^{TT}_{0T}(\omega_0) J_{0-2}(\omega c_{0T}/d_p) \tag{3.15}$$

for γ=RR and TT, where $\hat{a}_n^\gamma(\omega_0)$ is calculated to minimize the square misfit ($\sum_p \sum_{\omega=0.9\omega_0}^{1.1\omega_0} [\Phi_p^\gamma(\omega) - \hat{S}_p^\gamma(\omega;\omega_0)]^2$) by the least square method.

Using the misfit function (equation 3.12) that is defined at each frequency for each γ-component, the total misfit function E for Rayleigh-wave analysis is given by

$$E = \left[2\sum_{\omega_0} E_{ZZ}(\omega_0) + \sum_{\omega_0} E_{PP}(\omega_0) \right] /3 \qquad \text{at} \leq 0.1\,\text{Hz}, \tag{3.16}$$

$$E = \left[\sum_{\omega_0} E_{ZZ}(\omega_0) + \sum_{\omega_0} E_{PP}(\omega_0) + \sum_{\omega_0} E_{RR}(\omega_0) \right] /3 \qquad \text{at} > 0.1\,\text{Hz}, \tag{3.17}$$

and the misfit function E for Love-wave analysis is defined as

$$E = \sum_{\omega_0} E_{TT}(\omega_0). \tag{3.18}$$

As described in equation (3.16), I avoid using the RR-component NCFs at a frequency lower than 0.1 Hz to avoid unknown anomalously fast-arriving signals (Figure 3.6). In addition, I weight ZZ-component NCFs by a factor of two compared to PP-component NCFs because Rayleigh waves in ZZ-component NCFs have larger amplitudes and hence have a better signal-to-noise ratio (SNR) than the PP-component NCFs at low frequencies (Figures 3.6a,b and 3.7). The difference of SNR for each component is not because of whether noise reduction has been performed or not (Table 1.2), but rather due to the difference in signal amplitude. The energy of Rayleigh waves in PP-component NCFs is concentrated in the oceanic layer, whereas the energy of Rayleigh waves in ZZ-component NCFs exists in both the oceanic and solid layers (e.g., Takeo et al., 2014). Therefore, at a lower frequency where wavelengths become longer, the oceanic layer becomes transparent and the energy in PP-component NCFs dissipates into the solid layer, resulting in small signal amplitudes compared to that in ZZ-component NCFs. The magnitude of the weights was set to two in order to keep the number of components the same as high frequencies.

(3) Optimization of phase velocity measurement

I search for phase velocities (equations 3.6 and 3.8) which minimize the misfit functions (equations 3.16–3.18) by the simulated annealing method (Appendix C; Nam et al., 2004). I prepare 30 000 iterations for the simulated annealing method. At each annealing step, for Rayleigh-wave analysis, I perturb the values of $V_S(z), A_{c2}(z)$, and $A_{s2}(z)$ at each layer of the structure without any vertical smoothing, calculating the phase velocities (equation 3.6), and evaluating the cost functions (equations 3.16 and 3.17). For Love-wave analysis, I search $V_S(z), A_{c4}(z)$, and $A_{s4}(z)$ at each layer, calculating the phase velocities (equation 3.8), and substituting the phase velocities into equation (3.18). Additionally, in a frequency range of 0.04–0.2 Hz, since Rayleigh waves are sensitive to the thickness of the seawater and the crust (Figure 1.3a,c), and Love waves are also sensitive to the crustal structure, the thicknesses of those layers are also searched for at each an-

nealing step. The thickness of the water layer is parameterized in order to model the effect of the slow velocity in the sedimentary layer by treating it as part of the water layer. Phase velocities are calculated by DISPER80 (Saito, 1988) during the first 10 000 iterations. After 10 000 times of iterations, to save the calculation time cost, phase velocities are estimated by linear approximation using the sensitivity kernels (equation 1.1). The sensitivity kernels will be re-calculated every 1000 iterations.

The optimal n^{th}-mode phase velocities and the standard errors are estimated using the bootstrap method (Efron, 1979). A bootstrap sample consists of randomly selected station pairs of the same data size as the original with duplicates allowed. I estimate 100 bootstrapped dispersion curves $(c_n^{ave,1}(\omega), c_n^{ave,2}(\omega), ..., c_n^{ave,100}(\omega))$ of the n^{th} modes. I define the average of those 100 dispersion curves of the n^{th} mode as $\bar{c}_n^{ave}(\omega)$. I further define the measurement error as the standard deviation of those 100 dispersion curves as $\Delta c_n(\omega)$. The estimation of other parameters $(\bar{A}_{c2}^n(\omega) \pm \Delta A_{c2}^n(\omega), \bar{A}_{s2}^n(\omega) \pm \Delta A_{s2}^n(\omega), \bar{A}_{c4}^n(\omega) \pm \Delta A_{c4}^n(\omega)$, and $\bar{A}_{s4}^n(\omega) \pm \Delta A_{s4}^n(\omega))$ are the same as that of $\bar{c}_n^{ave}(\omega)$.

Since the measurement utilizes a one-dimensional structure, I obtain not only phase velocity but also S-wave velocity structures. The S-wave velocity structure is only used for giving natural *a priori* constraints on phase velocities, and the structure has not been optimized through this method. For example, I did not introduce any vertical smoothing between the adjacent layers, so the roughness of the structure is high. Therefore, I discard the S-wave structure after the measurement and only retain phase velocities (Yoshizawa and Kennett, 2002; Takeo et al., 2018).

3.3.5 Results

Comparison to the B-spline expansions

Figure 3.8 is an example showing the effectiveness of the model-based approach. Since the dispersion curve is estimated based on the structure, physical feasibility is guaranteed, and the measurement is more stable than the B-spline expansions. Consequently, the uncertainties of phase velocities via the model-based approach are small compared to the uncertainties obtained by the B-spline expansions, and a peak at 0.03 Hz has been disappeared.

Comparison of theoretical and observed NCFs

I compared synthetic and observed symmetric NCFs (Figures 3.9 and 3.10) to check how well the synthetic waveforms reproduce the observations. The synthetic NCFs are obtained by substituting the average phase velocities into equations (3.2–3.5). Both phases and amplitudes of the observed NCFs are well-reproduced by the synthetic NCFs for all modes in all components. The synthetic RR-component NCFs are not used for phase-velocity measurement at a frequency less than 0.1 Hz as described previously.

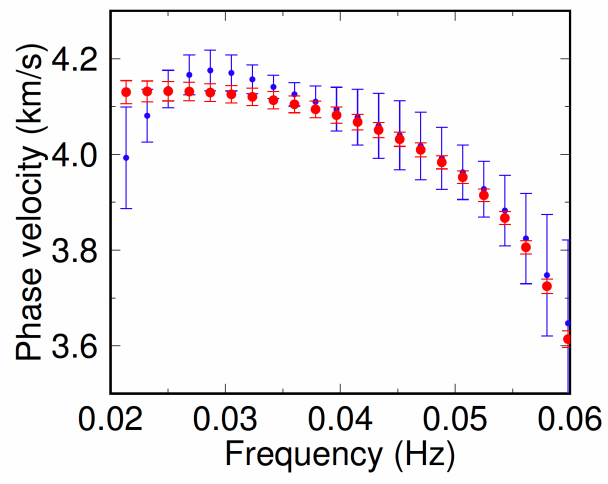

Figure 3.8: A comparison of average fundamental-mode Rayleigh-wave phase velocities via two different methods in the western array. The blue dispersion curve is obtained by using the B-spline expansions (Takeo et al., 2013). Red dispersion curve is obtained by using the model-based measurement developed in this study.

Effects of source heterogeneity

Although the source distribution of ambient noise was assumed to be homogeneous in the measurement, the distribution is not necessarily homogeneous (Weaver et al., 2009). The heterogeneous source distribution can introduce biases in the measurement (Weaver et al., 2009), and it is observable as the asymmetry in the NCFs (Figure 3.6; Section 3.2). For example, at frequencies lower than 0.1 Hz, the amplitude of TT-component NCFs is much larger in the negative time lag than the positive time lag, indicating that the amplitude of the source coming from the western direction is stronger than the eastern direction.

The azimuthal variation in the amplitude of NCF due to source heterogeneity can be expanded into a Fourier Series (Cox, 1973) as

$$a(\theta) = a_0 + \sum_m a_m \cos[m(\theta - \theta_m)], \tag{3.19}$$

where θ represents back-azimuth, and a_n is Fourier coefficients. Thus, for instance, the theoretical cross spectrum for the ZZ-component NCFs can be given as

$$S(\phi) = a_0 J_0\left(\frac{\omega d}{c}\right) + 2\sum_m i^m a_m \cos[m(\theta - \theta_m)] J_m\left(\frac{\omega d}{c}\right), \tag{3.20}$$

where d is the interstation distance, c is phase velocity, and i represents the imaginary unit. The odd-order terms contribute to the imaginary component of the NCFs, and it is removed since only the symmetric NCFs are used in the measurement.

Thus, I estimate the effect of even-order terms on phase velocity measurement. According to Weaver et al. (2009) and Takeo et al. (2016), the apparent phase velocity anomaly (γ_s) can be

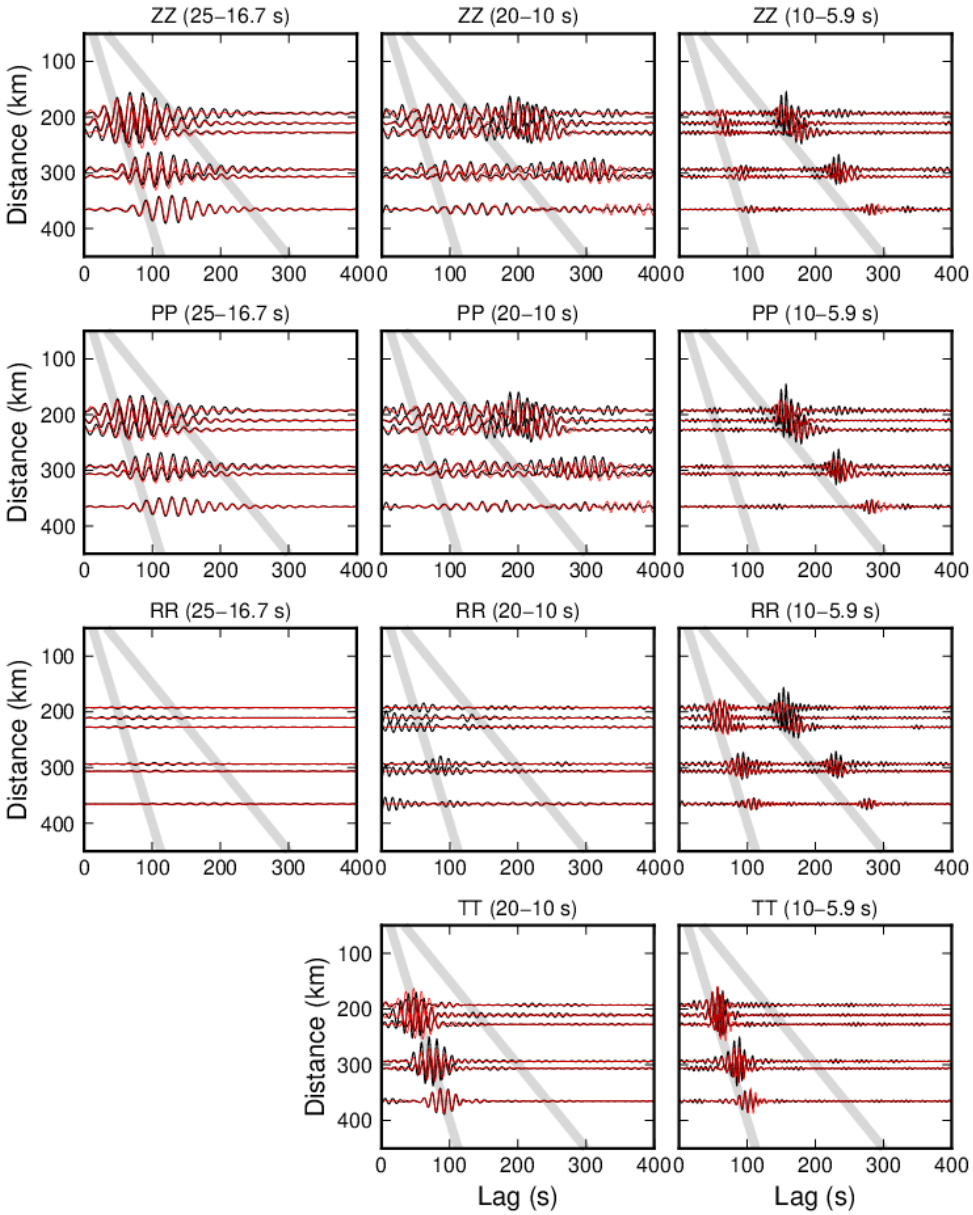

Figure 3.9: Time-symmetric components of observed NCFs (black) and synthetic NCFs (red) for the western Array. Synthetic NCFs are calculated using average phase velocity. The gray solid lines indicate arrival times assuming group velocities of 1.5 km/s and 4.0 km/s.

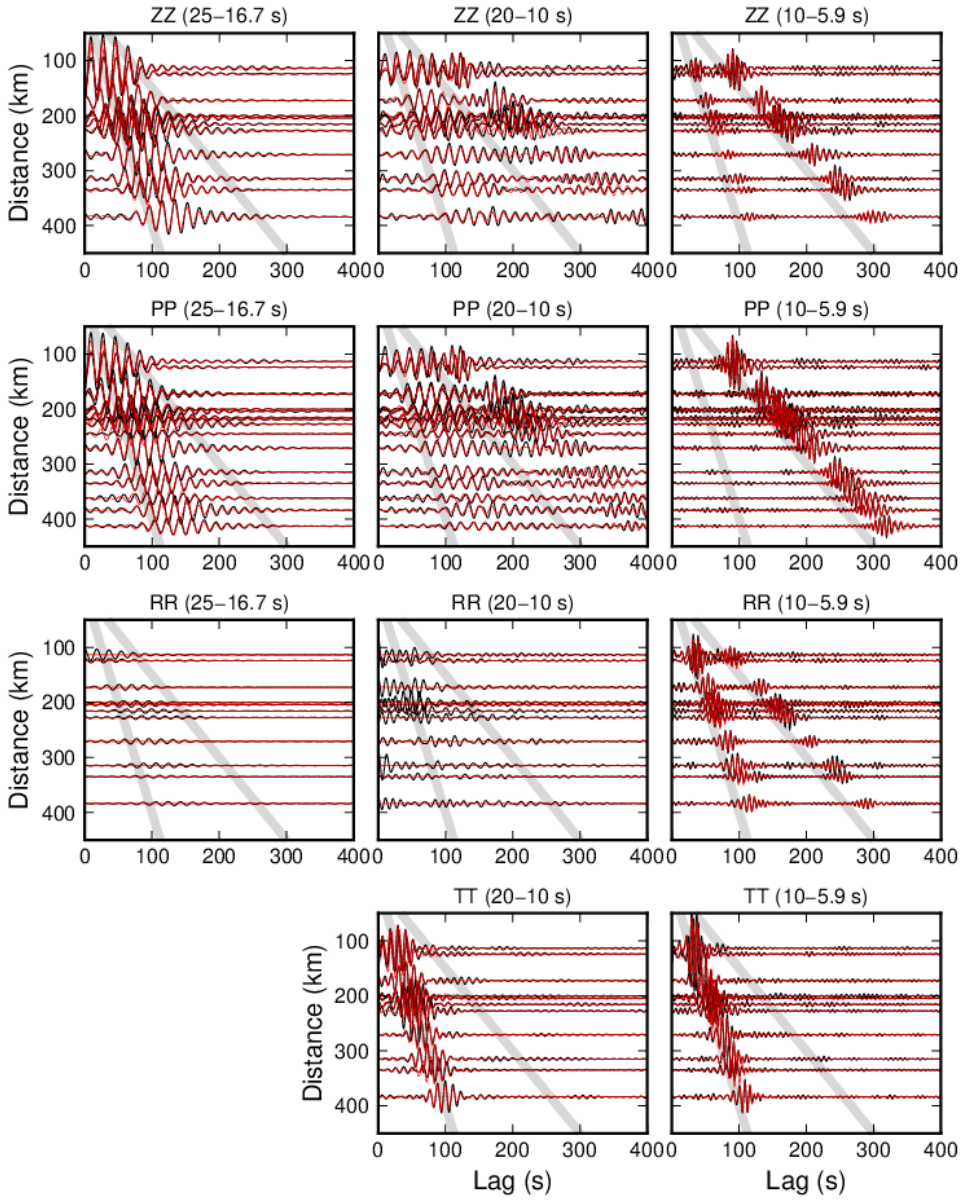

Figure 3.10: Same as Figure 3.9 but for the eastern Array.

calculated by considering the change in the zero-crossing frequency, which is given by

$$\gamma_s = \frac{1}{2\omega^2\tau^2}\frac{a''(\theta)}{a(\theta)} \sim \frac{1}{8\pi^2}\left(\frac{\Lambda}{d}\right)^2 \sum_m m^2 \frac{a_m}{a_0}\cos[n(\theta-\theta_m)], \tag{3.21}$$

where τ is travel time, $\Lambda = u/f$ is approximately equivalent to c/f, where u is group velocity and f is frequency.

Figures 3.11 and 3.12 shows the azimuthal variation of amplitude anomalies, $\zeta_p^n(\omega)$, of each mode observed in each component NCFs. The fitted curve is obtained by assuming $a = a_0 + a_2\cos[2(\theta-\theta_2)] + a_4\cos[4(\theta-\theta_4)]$. On average, the values are $a_2/a_0 =\sim 0.3$ and $a_4/a_0 =\sim 0.2$, comparable to the values observed in the southern Pacific (Takeo et al., 2016). Although source heterogeneity is stronger in the western array than in the eastern array (Figures 3.11 and 3.12), due to the small number of usable station pairs, it is difficult to obtain a reliable $2\theta+4\theta$ azimuthal variation in amplitudes for the western array (Figures 3.11 and 3.12). I believe the results are more reliable in the eastern array than in the western array. γ_s does not exceed 1 % at most at frequencies higher than 0.04 Hz assuming an average interstation distance (∼260 km), and I only retain measurements at frequencies higher than 0.04 Hz.

Average and azimuthally anisotropic phase velocity

Figure 3.13 shows the measured phase velocity, and Figure 3.14 shows the 2θ- and 4θ-sinusoidal patterns of azimuthal anisotropy. To plot the 2θ- and 4θ-sinusoidal patterns, in addition to the measurement using all usable station pairs in each array as described in the previous section, I further measured path-averaged phase velocity using each station pair without assuming azimuthal anisotropy. The analysis is the same as described in Section 3.3.4. Figure 3.13a is the average phase velocities of the 0S, 1S, and 0T modes measured in the eastern and the western arrays. I only retain the measurements that are colored in blue and orange for the structural inversion in Chapter 6 and discard the measurements colored in gray in Figure 3.13a in the following manner.

I discard phase velocities of the 1S mode at frequencies lower than 0.1 Hz. At this frequency range, I did not use RR-component NCFs in order to avoid contamination due to unknown signals (Figure 3.6c). Since the signal-to-noise ratio of the 1S mode in ZZ- and PP-component NCFs is low, the reliability of phase velocities of the 1S mode at frequencies lower than 0.1 Hz is considered to be lower compared to the other measurements. I discard the 0S mode higher than 0.07 Hz because of the strong 2π ambiguity. I also discard phase velocities of the 0T mode at frequencies lower than 0.1 Hz to avoid potential interference between the fundamental- and higher-mode Love waves. Takeo (2020, JpGU) theoretically calculated the bias of the 0T-mode phase velocity due to the presence of the 1T mode assuming various oceanic structures. She showed that the bias is ignorable at >0.1 Hz but increases at a frequency range of 0.05–0.1 Hz, reaching ∼3 % depending on the structure. More practical methods for evaluating the bias due to the presence of second and higher modes will be investigated in the future. The method to reduce bias in the Love-wave

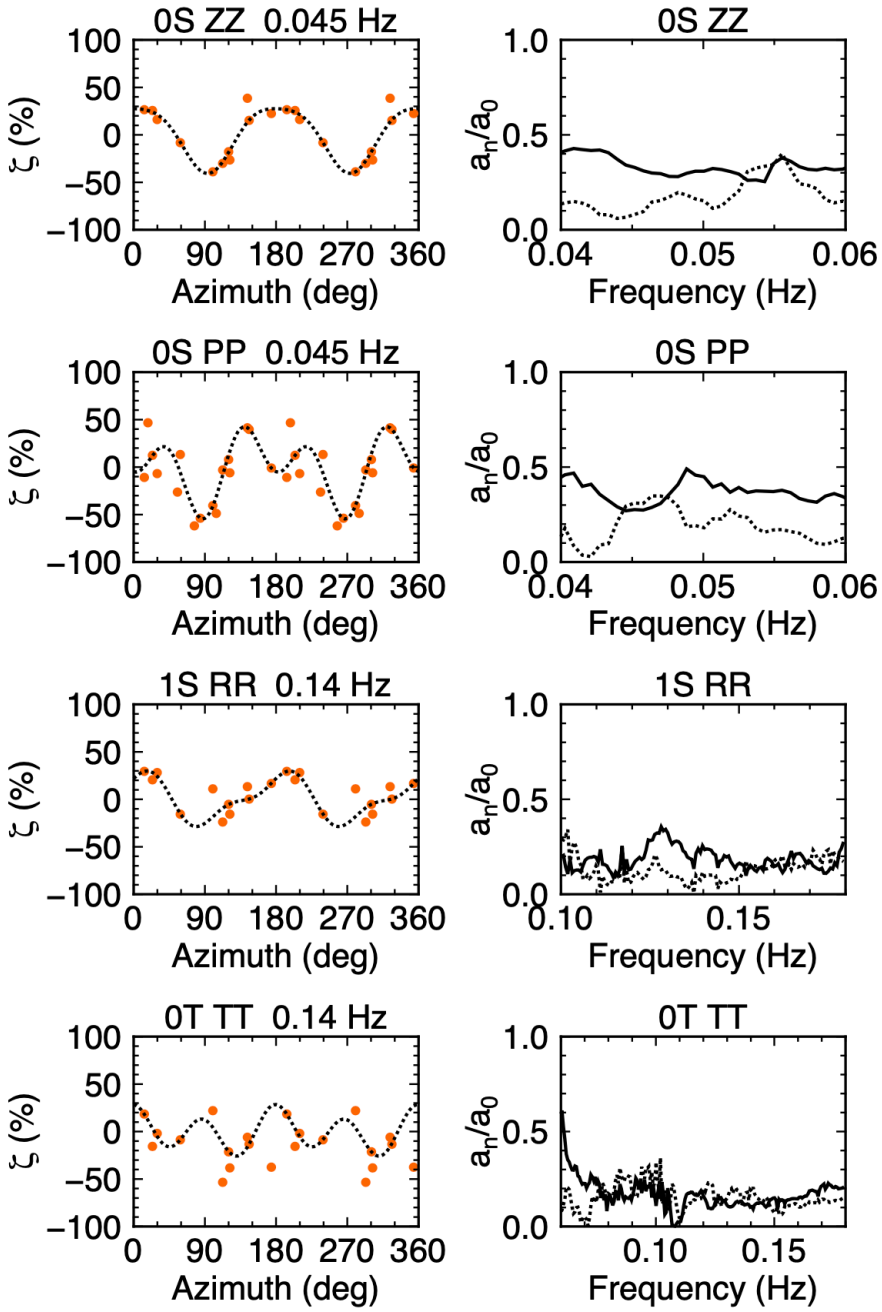

Figure 3.11: Amplitude anomalies, $\zeta_p^n(\omega)$, of the 0S mode in the ZZ-component NCFs as a function of back-azimuth observed by the eastern array. Left column: Orange dots are measurements and the black dotted line is the fitted pattern. Right column: The intensity of the source heterogeneity represented by a_2/a_0 (solid line) and a_4/a_0 (dotted line). From top to bottom: 0S-mode observed in ZZ-component NCFs, 0S-mode observed in PP-component NCFs, 1S-mode observed in RR-component NCFs, and 0T-mode observed in TT-component NCFs.

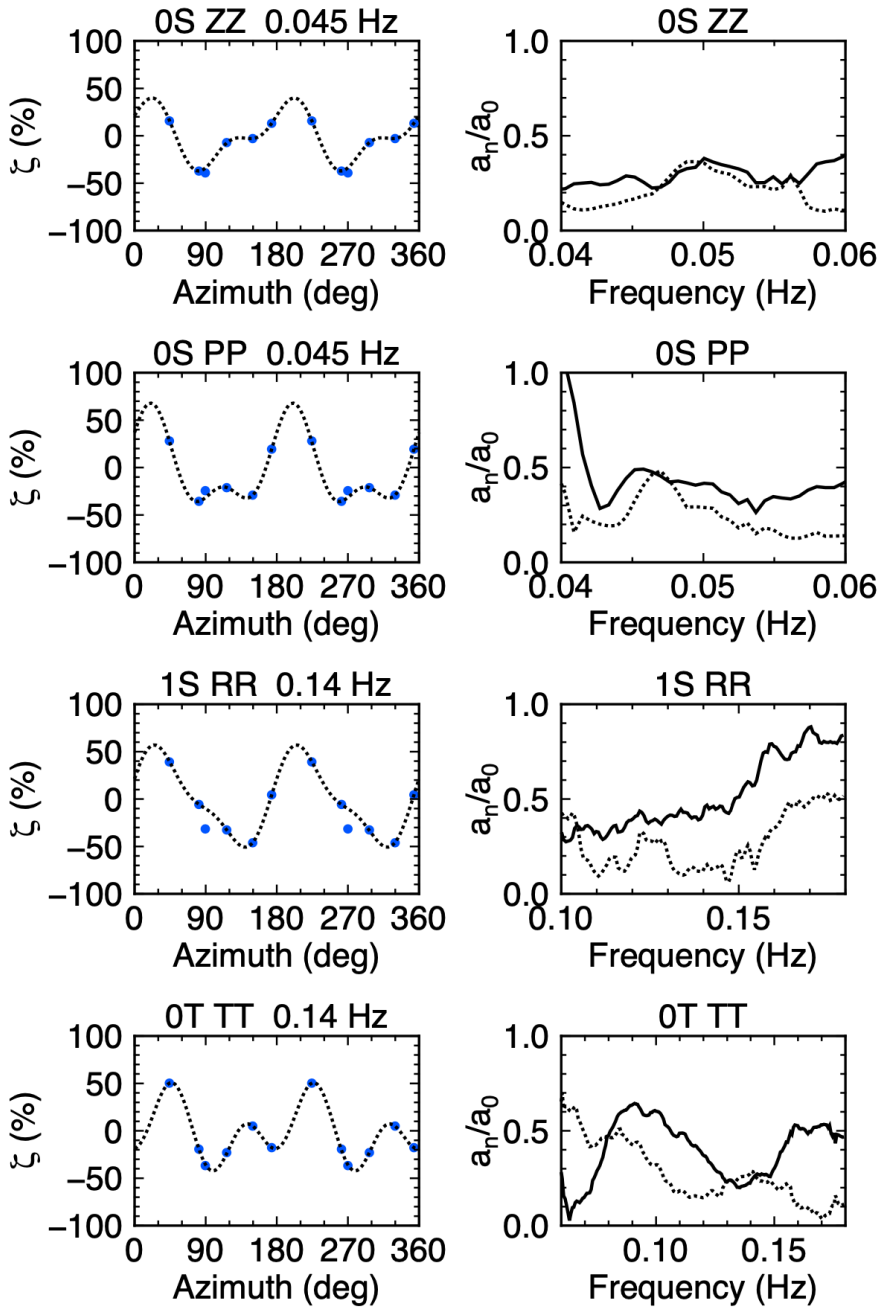

Figure 3.12: Same as Figure 3.11 but for the western array.

dispersion measurement at <0.03 Hz will be discussed in Chapter 5. In addition to the frequency range that I discarded above, I further discard the following measurements for the inversion of azimuthal anisotropy in Chapter 6: (1) I discard phase velocities of the 0S mode at frequencies higher than 0.05 Hz because the 0S-mode phase velocity has a strong sensitivity in the depth of seawater, and thus it is difficult to distinguish whether the variation in phase velocity is due to structural azimuthal anisotropy or differences in depth of water averaged over each interstation path. (2) I discard the measurement of the 0T-mode azimuthal anisotropy because of the large uncertainties in the 4θ-sinusoidal pattern (Figure 3.14) due to the small number of station pairs.

The difference of average phase velocities of the 0S and 1S modes between the western and the eastern arrays is due to the difference of average water depth, where the average water depth in the western array is ∼200 m deeper than that in the eastern array. The average phase velocities of the 0T mode are significantly different in the eastern and western arrays. Since Love waves are sensitive to V_{SH}, the observed difference between the east and west suggests that the shallow V_{SH} structure is significantly different between the two areas.

Azimuthal anisotropy of Rayleigh waves is also different between the eastern and the western arrays (Figures 3.13b,c and 3.14). Peak-to-peak intensities of Rayleigh waves are larger in the western array than that of the eastern array. The fastest directions of azimuthal anisotropy of Rayleigh waves are significantly different between the western and the eastern arrays at all frequencies. The fastest directions are $114^\circ \pm 13^\circ$ in the western and $58^\circ \pm 20^\circ$ in the eastern array averaged at a frequency range of 0.04–0.16 Hz, respectively. The fastest direction is almost perpendicular to the predicted 170-Ma isochrone (∼40°), which may represent the past seafloor spreading direction, in the western array.

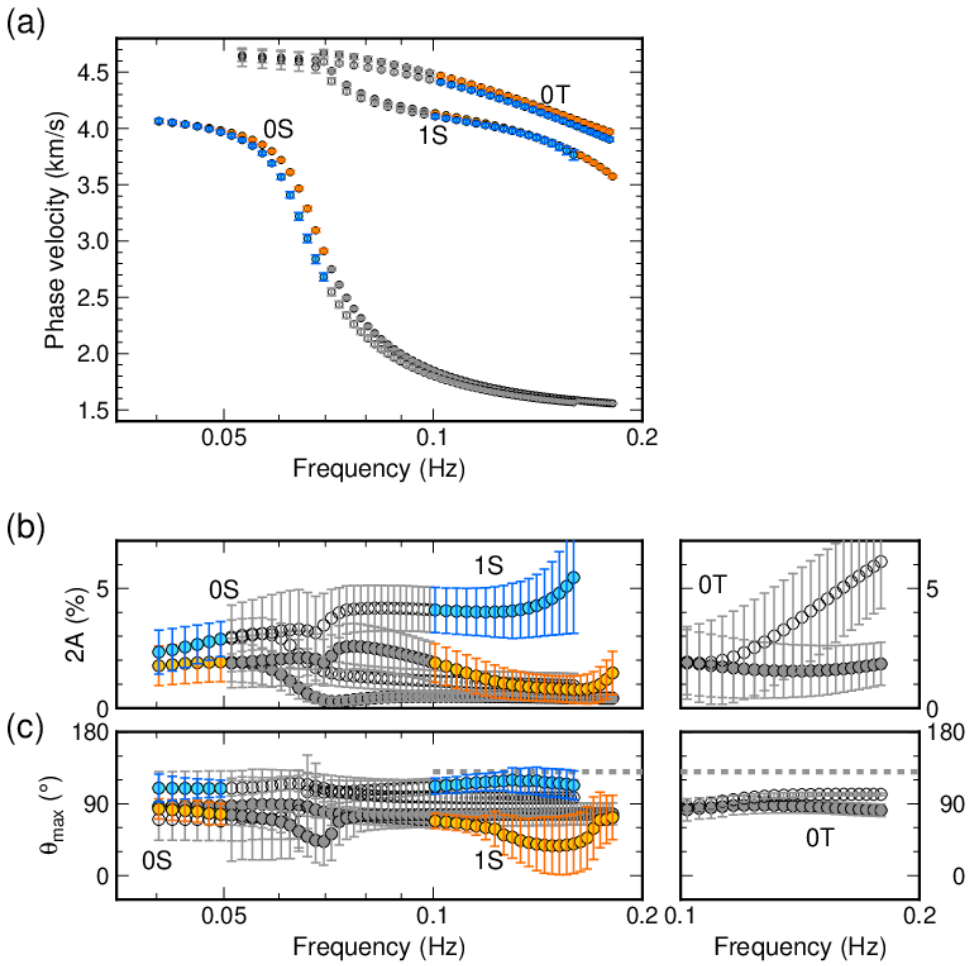

Figure 3.13: The short-period phase velocities of the eastern (orange) and western (blue) arrays. Gray open (western) and filled (eastern) circles represent measurements that are discarded in the inversion in Chapter 6. (a) Average phase velocities. (b) The peak-to-peak intensities of azimuthal anisotropy ($2A = \sqrt{(\bar{A}^n_{c2}(\omega)]^2 + [\bar{A}^n_{s2}(\omega)]^2}$ for Rayleigh waves (n=0S, 1S) and $2A = \sqrt{[\bar{A}^{0T}_{c4}(\omega)]^2 + [\bar{A}^{0T}_{s4}(\omega)]^2}$ for Love waves). (c) The fastest directions of azimuthal anisotropy ($\theta_{max} = \frac{1}{2}\arctan[\bar{A}^n_{s2}(\omega)/\bar{A}^n_{c2}(\omega)]$ for Rayleigh waves and $\theta_{max} = \frac{1}{4}\arctan[\bar{A}^{0T}_{s4}(\omega)/\bar{A}^{0T}_{c4}(\omega)]$ for Love waves). Azimuthal anisotropy of the 0T mode is plotted separately for visual purposes in the small figures on the right in (b) and (c). The gray dashed lines represent the direction perpendicular to the 170-Ma isochrone of Seton et al. (2020).

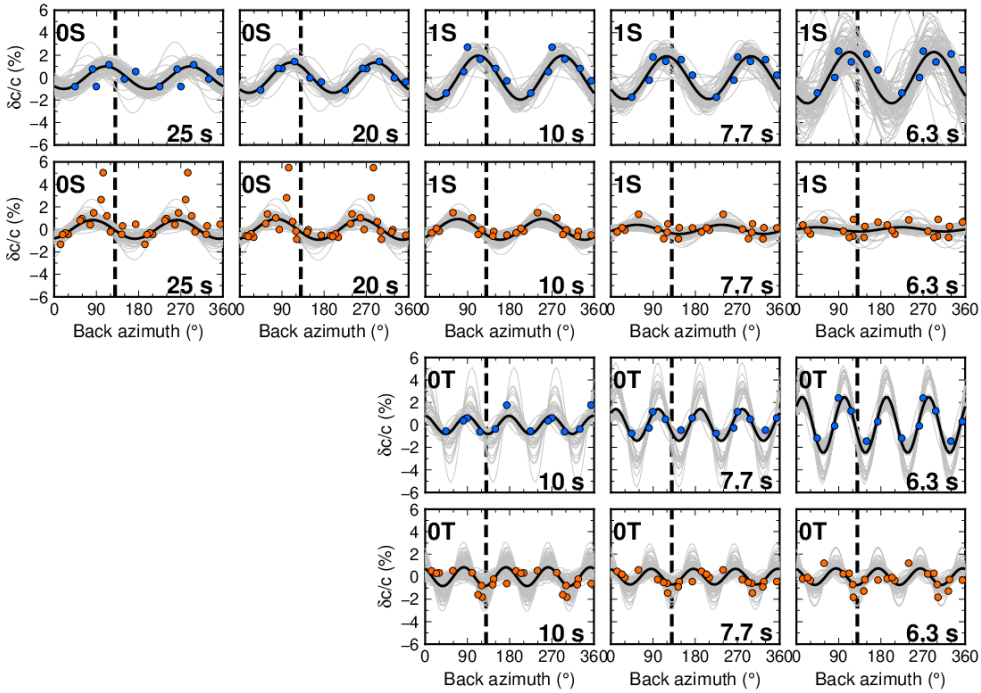

Figure 3.14: Azimuthal variations of phase velocities relative to their average values (see Figure 3.13a for average values). The dots are measurements of the western (blue) and eastern (orange) arrays (Those are obtained by measuring phase velocity using a single station pair without assuming azimuthal anisotropy). The 2θ- and 4θ-sinusoidal fittings are shown in black and gray solid lines. Black solid lines represent the fittings using the anisotropy parameters ($\bar{A}_p^n$, where p=c2, s2, c4, or s4, and n=0S, 1S, and 0T). Gray solid lines represents the fittings obtained from 100 bootstrapped estimations of $A_p^{n,i}$, where i=1,2,...,100. The black dashed lines represent the direction perpendicular to the 170-Ma isochrone of Seton et al. (2020).

Chapter 4

Measurement of Rayleigh-wave phase velocity via teleseismic waveform analysis

4.1 Introduction

In this chapter, I summarize the measurement of fundamental-mode Rayleigh-wave phase velocity including the azimuthal anisotropy at a frequency range of 0.005–0.04 Hz using the teleseismic events recorded at the Oldest-1 Array. I first describe the data set used for the analysis and some special care taken for the measurement (Section 4.2). Then, in Section 4.3, the Rayleigh-wave dispersion analysis will be detailed. Finally, in Section 4.4, the measured azimuthally averaged Rayleigh-wave phase velocity, as well as azimuthal anisotropy, will be shown.

4.2 Data

I use noise-reduced vertical component BBOBS seismograms obtained in Chapter 2. The noise level in the frequency range of 0.005–0.02 Hz was significantly reduced (Figure 2.12) and teleseismic waveforms were extracted (Figure 2.13), allowing us to measure lower frequency (<0.01 Hz) phase velocities compared to the previous study (Takeo et al., 2018). Phase velocities at a frequency range of 0.005–0.01 Hz are essential to resolve the structure at a depth range of 200–300 km where the bottom of the LVZ exists (Figure 1.3b and Chapter 6).

As mentioned in Section 3.3.1, the seamounts in the middle of the array should be avoided (Figure 4.1). The avoidance of the seamounts, however, largely reduces the number of usable station pairs (Table 4.1) and this makes it difficult to measure the phase velocity, especially azimuthal anisotropy. To maximize the number of usable station pairs, I divide the frequency bands and measure the phase velocity at each band. The division of the frequency band is also effective to maximize the number of usable teleseismic events since the observed seismic signal excited by a

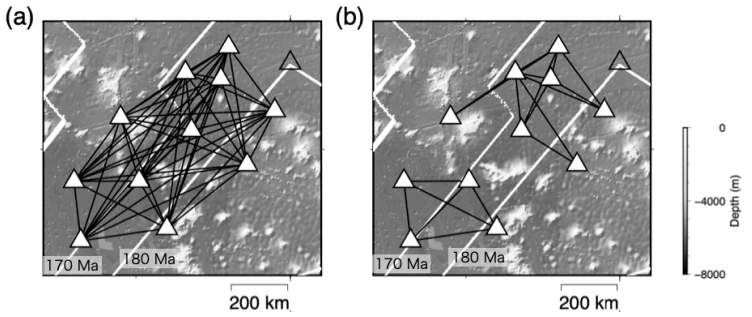

Figure 4.1: The station pairs used for the teleseismic Rayleigh-wave analysis at 0.005-0.025 Hz (a) and 0.025-0.038 Hz (b). The white-filled triangles are stations with BBOBSs, and the open triangle is the station with DPG only. The analyzed station pairs are connected with black solid lines. The background white lines represent the isochrones of Seton et al. (2020).

teleseismic event does not always have large energy at the whole desired frequency band (0.005–0.04 Hz). In total, I divide the frequency band into three (Table 4.1). The numbers of the usable teleseismic event are different depending on the frequency bands to analyze (Table 4.1, D.1–D.3, and Figure 4.2). The higher frequency bands tend to have more usable events even though the number of usable stations is fewer. This is because the noise level at high frequencies (e.g., 0.025–0.038 Hz) is lower than that of low frequencies (Figure 2.12) while the seismic energies are larger at this frequency band.

Table 4.1: Summary of the analyzed frequency bands

Frequency band (Hz)	Number of station pairs	Number of events
(a) 0.005–0.01	55	15
(b) 0.01–0.025	55	24
(c) 0.025–0.038	19	33

4.3 Array analysis of teleseismic Rayleigh waves

I apply the array analysis technique proposed by Takeo et al. (2018) to measure the fundamental-mode Rayleigh-wave phase velocities of the Oldest-1 Array. I assume each of the incoming teleseismic fundamental-mode Rayleigh waves is like a plane wave and estimate phase velocities by measuring the phase delay between station pairs.

I use a local coordinate system proposed by Forsyth and Li (2005) (Figure 4.3). The coordinate system is set up for each teleseismic source, and a reference station in the array is defined as the origin of the coordinate. The $+x$ direction is taken along the great-circle path connecting the epicenter and the reference station, and $+y$ direction is taken along the small circle that is perpendicular to the x direction. The distance between the reference station and an arbitrary

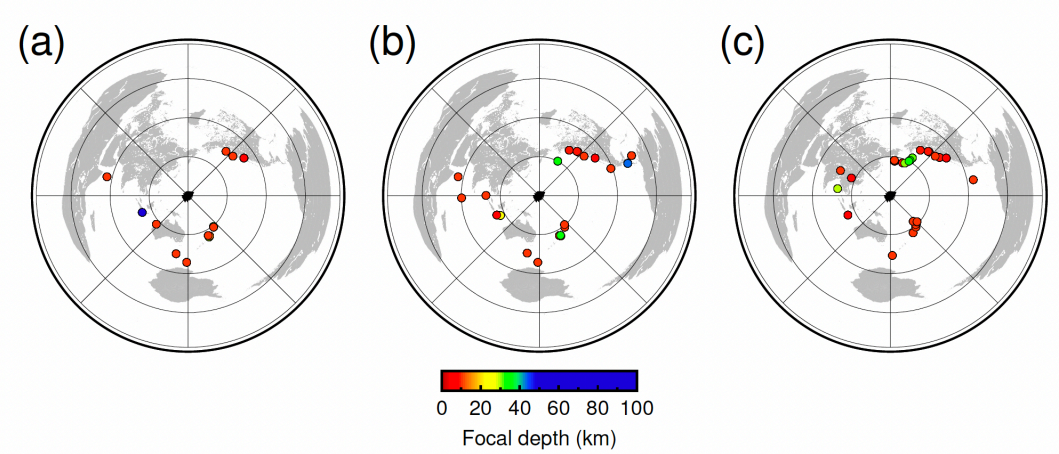

Figure 4.2: Epicentral distribution map of teleseismic events used in this study. The circles show the epicenters. (a) Events used for analysis at (a) 0.005–0.01 Hz, (b) 0.01–0.025 Hz, and (c) 0.025–0.038 Hz.

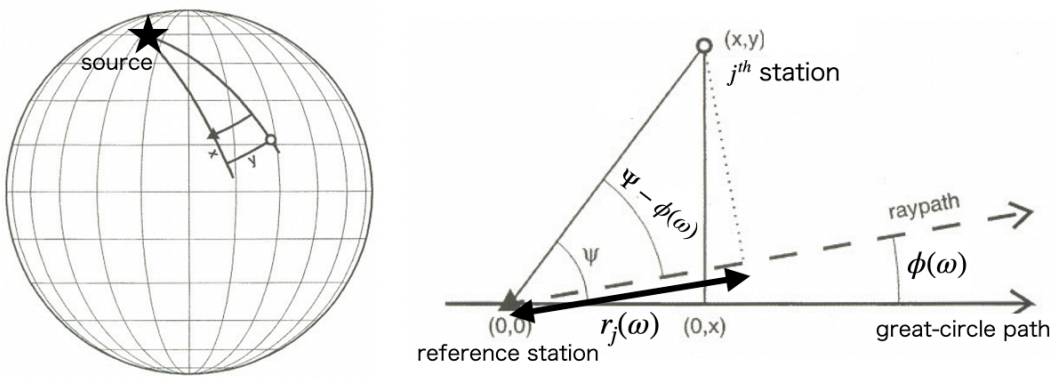

Figure 4.3: The definition of the local coordinate system used in this study. Figure is taken from Forsyth and Li (2005) but some variables are modified to be consistent with the definition in this study.

station j along the ray path is given as

$$r_j(\omega) = \sqrt{x^2 + y^2}\cos\left(\arctan[y/x - \phi(\omega)]\right), \tag{4.1}$$

where $\phi(\omega)$ is the perturbation of surface-wave incident direction from the great-circle path, and ω is angular frequency.

The thresholds for the event selection are different in the three frequency bands and are summarized in Table 4.2. I first select the events having magnitudes larger or equal to 5.5, focal depths shallower or equal to 100 km, and the epicentral distances larger or equal to 4500 or 5000 km. Then the signal with a low signal-to-noise ratio (SNR) is discarded. The SNR thresholds depend on the back azimuth. Low (high) SNR threshold is set for events incident along the long (short) axis of the array. The signal amplitude is estimated from the peak of the envelop function of the 819-s-long Rayleigh wave. The noise amplitude is estimated from the root mean square amplitude

Table 4.2: Summary of the thresholds for the event selection at different frequency bands

Frequency band (Hz)	SNR	min. epicentral distance (km)	min. number of station pairs
(a) 0.005–0.01	12–30	5000	10
(b) 0.01–0.025	12–30	5000	10
(c) 0.025–0.038	3.2–8	4500	8

of 800-s-long waveforms recorded 2 h after the origin time of the event.

I measure the fundamental-mode Rayleigh-wave phase velocity in two steps. In the first step, I estimate the arrival angle of each Rayleigh wave excited by a teleseismic event. The incident angles of Rayleigh waves typically deviate from the great-circle paths due to the heterogeneity outside the array, and the deviations bias the phase velocity in a significant way (Takeo et al., 2013; Foster et al., 2014a). For each Rayleigh wave excited by E^{th} teleseismic event, the arrival angle ($\phi^E(\omega)$) and the average phase velocity ($c^E(\omega)$) are estimated by maximizing the cross-correlation coefficient (E^E) defined as

$$E^E(c^E, \theta^E) = \frac{1}{N_p^E} \sum_{p=1}^{N_p^E} \frac{\sum_\omega \mathfrak{Re}[F_j^E(\omega) F_k^{E*}(\omega) e^{i\Delta\varphi^E(\omega)}]}{\sqrt{\sum_\omega |F_j^E(\omega)^2|} \sqrt{\sum_\omega |F_k^E(\omega)^2|}}, \tag{4.2}$$

where N_p^E is the number of station pairs, ω is the angular frequency, $\mathfrak{Re}$ is the real component, j and k are station indexes, p is station pair (j and k stations) index, F_j^E is the Fourier spectrum observed at the j^{th} station, and $\Delta\varphi^E(c^E, \phi^E, \omega) = \omega[r_j(\omega) - r_k(\omega)]/c^E(\omega)$. The method is similar to the waveform fitting: The phase difference $\Delta\varphi^E$ is given to k^{th} station to synthesize the waveform observed at j^{th} station.

$c^E(\omega)$ and $\phi^E(\omega)$ are calculated from an S-wave velocity structure which has an ocean layer, three crustal layers, and 14 layers in the Moho to a depth of 400 km. Method of estimating phase velocity is the same as that described in Section 3.3.4, but here I fix the sensitivity kernels to that of the initial structure to save the calculation time cost. The arrival angle is also linearized as $\phi(\omega) = \int K_\beta(z, \omega)\phi(z)dz$, where $K_\beta(z, \omega)$ is phase velocity sensitivity kernel to S-wave velocity, and $\phi(z)$ is the apparent parameter of arrival angle. This equation is an empirical one rather than having a clear physical meaning. Mathematically, the sensitivity kernel is a basis function that introduces smoothing in the frequency domain. By using the same basis functions, I can constrain the smoothness effect to be the same for different parameters.

After the measurements for each event, I again perform an event selection with two requirements: (1) the cross-correlation coefficient for each station pair calculated using obtained $c^E(\omega)$ and $\phi^E(\omega)$ has to be larger or equal to 0.9, and (2) the number of station pairs that meet the first criteria has to be larger or equal to 8 or 10 (Table 4.2).

I discard the phase velocity estimated for each E^{th} event in the first step and retain only estimated arrival angles ($\phi^E(\omega)$). Then in the second step of measurement, I re-estimate phase velocity using all the events and station pairs accepted in the first step. I simultaneously estimate

average phase velocity ($c^{ave}(\omega)$) and azimuthal anisotropy which is given by

$$\hat{c}(\omega,\theta) = c^{ave}(\omega)[1 + A_{c2}(\omega)\cos(2\theta) + A_{s2}(\omega)\sin(2\theta)], \tag{4.3}$$

where θ is propagation azimuth, $A_{c2}(\omega)$ and $A_{s2}(\omega)$ are coefficients describing azimuthal anisotropy in Rayleigh waves and defined as

$$A_{c2}(\omega) = \int K_\beta(z,\omega)A_{c2}(z)dz,$$
$$A_{s2}(\omega) = \int K_\beta(z,\omega)A_{s2}(z)dz,$$

where $A_{c2}(z)$ and $A_{s2}(z)$ are depth profile of anisotropic parameters. $c^{ave}(\omega)$, $A_{c2}(\omega)$, and $A_{s2}(\omega)$ are estimated by maximizing the cross-correlation coefficient (E_{all}) defined as

$$E_{all}(c^{ave}, A_{c2}, A_{s2}) = \sum_{E=1}^{N_E} N_p^E E^E(\hat{c}, \phi^E), \tag{4.4}$$

where N_E is the number of events. $c^{ave}(\omega)$, $A_{c2}(\omega)$, and $A_{s2}(\omega)$ are calculated from S-wave velocity structure which has the same layering in the first step.

The phase velocities and anisotropic parameters, as well as their standard errors, are further estimated using the bootstrap method (Efron, 1979) using 100 bootstrap samples: A bootstrap sample consists of randomly selected teleseismic events of the same data size as the original with duplicates allowed. The average of bootstrapped phase velocities and anisotropic parameters are written as $\bar{c}_{0S}^{ave}(\omega)$, $\bar{A}_{c2}^{0S}(\omega)$, and $\bar{A}_{s2}^{0S}(\omega)$. Their uncertainties are defined as the standard deviation of those 100 bootstrap samples ($\Delta c_{0S}(\omega)$, $\Delta A_{c2}^{0S}(\omega)$, and $\Delta A_{s2}^{0S}(\omega)$).

4.4 Results: Azimuthally anisotropic phase velocity

Figure 4.4 shows the obtained phase velocity and azimuthal anisotropy as a function of frequency and Figure 4.5 shows the azimuthal variations of phase velocities. The peak-to-peak amplitude of azimuthal anisotropy, $2A_2(\omega) = 2\sqrt{[\bar{A}_{c2}^{0S}(\omega)]^2 + [\bar{A}_{s2}^{0S}(\omega)]^2}$, is $\sim$1 % at a broad frequency range (Figures 4.4b and 4.5). The fastest direction, $\theta_{max}(\omega) = 0.5\arctan[\bar{A}_{s2}^{0S}(\omega)/\bar{A}_{c2}^{0S}(\omega)]$, is in the east-west direction (90°), oblique from the current absolute plate motion (Figure 4.4c). The measurement was performed by dividing the frequency band into three, and average phase velocities at different bands show excellent connections (Figure 4.4a), whereas the connectivity at 0.025 Hz, especially the fastest direction ($\theta_{max}(\omega)$), is poor (Figure 4.4c). At this frequency band, the azimuthal anisotropy is small ($\sim$0.5 %) and it is difficult to measure the fastest direction with the poor azimuthal coverage (Figure 4.5). The uncertainties for the fastest direction around 0.025 Hz are larger than those at different frequency bands (Figure 4.4c).

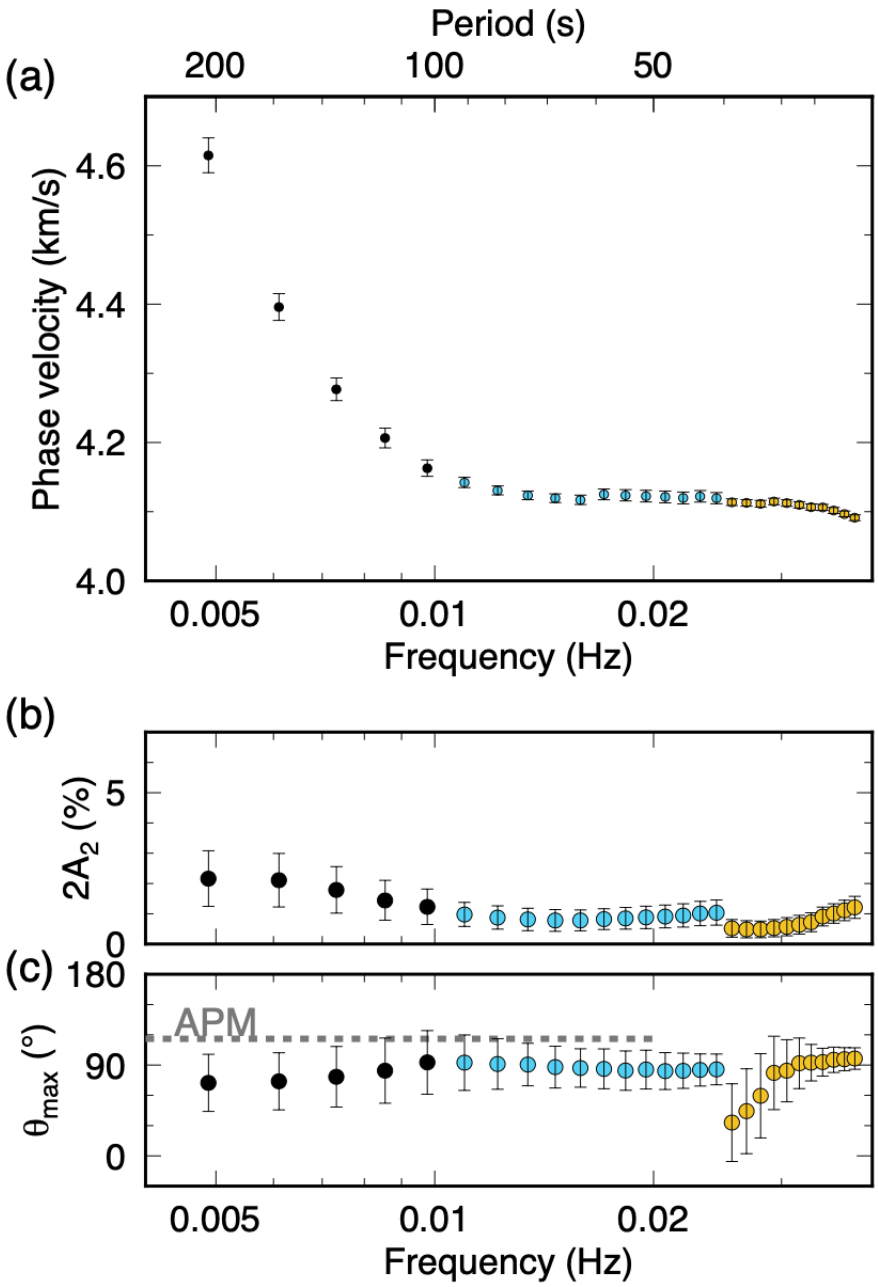

Figure 4.4: The obtained fundamental-mode Rayleigh-wave phase velocities. (a) Average phase velocities ($\bar{c}_{0S}^{ave}(\omega)$). (b) The peak-to-peak intensities of azimuthal anisotropy ($2A_2 = 2\sqrt{[\bar{A}_{c2}^{0S}(\omega)]^2 + [\bar{A}_{s2}^{0S}(\omega)]^2}$). (c) The fastest directions of azimuthal anisotropy ($\theta_{max} = 0.5\arctan[\bar{A}_{s2}^{0S}(\omega)/\bar{A}_{c2}^{0S}(\omega)]$). Different colors indicate the measurements at the different frequency bands (Table 4.1). Their 1σ errors are represented with black solid bars. The gray dashed line represents absolute plate motion (APM).

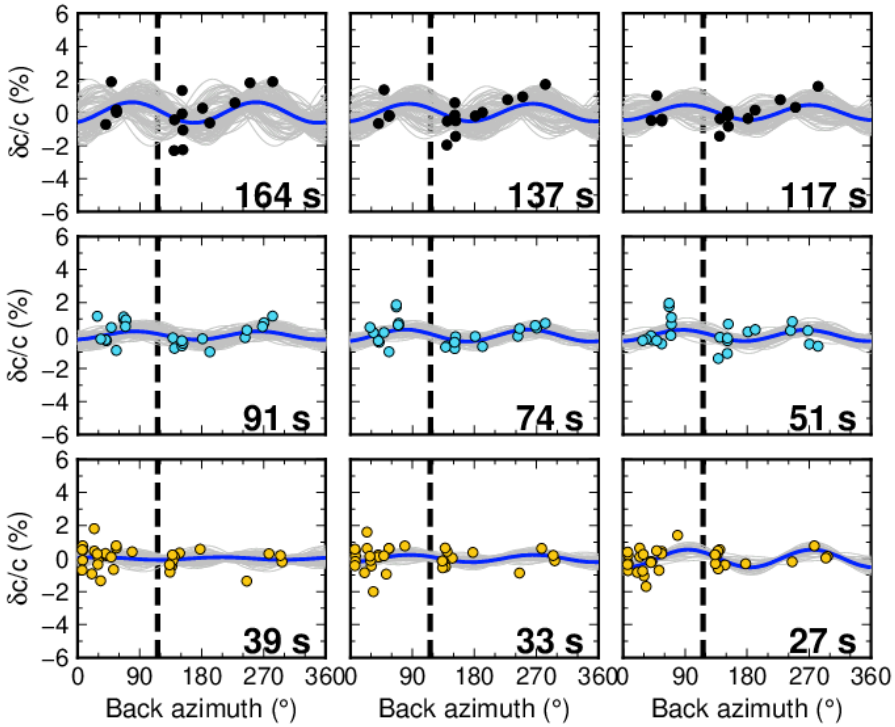

Figure 4.5: Azimuthal variations of phase velocities relative to their average values (see Figure 4.4a for average values). The dots are measurements and different colors indicate the measurements at the different frequency bands (Figure 4.4a and Table 4.1). 2θ-sinusoidal fits are shown in blue and gray lines. Blue lines represent 2θ-sinusoidal fits using the anisotropy parameters ($2A_2$ and θ_{max}) in Figures 4.4b,c. Gray lines represents 2θ-sinusoidal fits obtained from 100 bootstrap samples. The black dashed lines represent the absolute plate motion direction.

Chapter 5

Measurement of Love-wave phase velocity via teleseismic waveform analysis

This chapter is currently non-disclosure as it is scheduled to be published in a journal within five years.

Chapter 6

1D radially and azimuthally anisotropic shear-wave velocity structure

6.1 Introduction

In this chapter, the previously obtained broadband surface-wave phase velocities (Figure 6.1) are inverted to one-dimensional radially and azimuthally anisotropic structures beneath the Oldest-1 Array (Figure 1.7). In Section 6.2, I summarize the phase velocities obtained in Chapters 3–5. In Section 6.3, I obtain radially anisotropic structure using Rayleigh- and Love-wave phase velocities. I first invert for isotropic shear-wave (S-wave) velocity structure using only Rayleigh-wave measurements. Then, I invert for radially anisotropic structure using both Rayleigh- and Love-wave measurements. In Sections 6.4 and 6.5, the azimuthally anisotropic structure is estimated using Rayleigh-wave measurements. Finally, in Section 6.6, these structures will be used to infer (1) the asthenospheric dynamics by comparing to a plate evolution model, (2) the early dynamics of the Pacific plate evolution, and (3) LPO fabric types in the lithosphere and the asthenosphere beneath the Oldest-1 Array.

6.2 Summary of phase velocities measured at 170-Ma seafloor

Figure 6.1 summarizes phase velocities that are measured in Chapters 3–5. The phase velocities of the fundamental-mode Rayleigh waves (0S modes), first higher-mode Rayleigh waves (1S modes), and the fundamental-mode Love waves (0T modes) are measured. Using ambient noise (Chapter 3), I measured phase velocities of the 0S mode (0.04–0.065 Hz), 1S mode (0.1–0.2 Hz), and 0T mode (0.1–0.2 Hz). Using teleseismic waveforms (Chapters 4 and 5), I measured phase velocities of the 0S mode (0.005-0.04 Hz) and 0T mode (0.01-0.03 Hz). At frequencies higher than 0.04 Hz, I divide the array into two (the eastern and western arrays) and determine the structure beneath each array. At frequencies lower than 0.04 Hz, I measured phase velocities using all stations. Rayleigh-wave phase velocities were measured by using noise-reduced data processed in Chapter

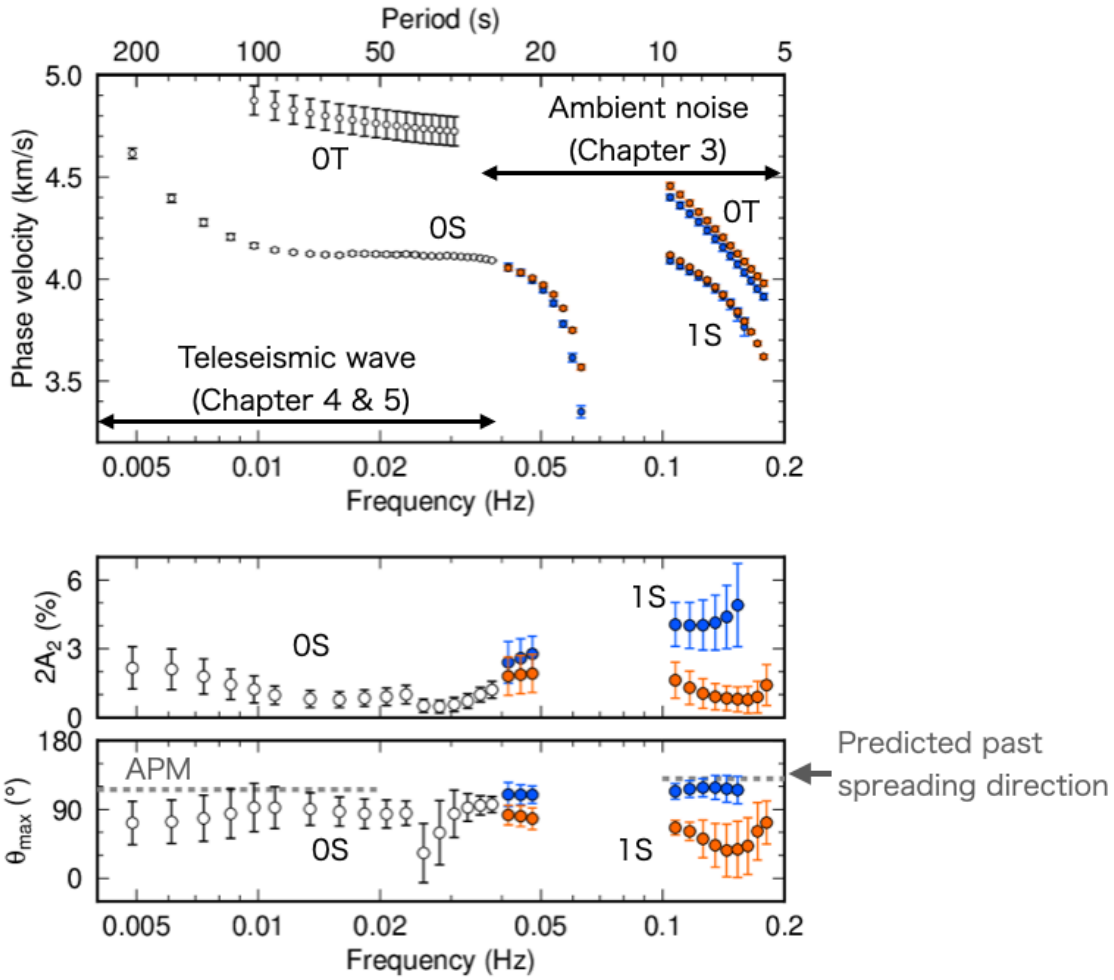

Figure 6.1: Average phase velocities and azimuthal anisotropy in terms of peak-to-peak direction ($2A_2$) and the fastest direction (θ_{max}) that are obtained in previous chapters. 0T: fundamental-mode Love, 0S: fundamental-mode Rayleigh, 1S: first higher-mode Rayleigh.

2.

6.3 Radially anisotropic structure

Parameters to describe radially anisotropic media

Radially anisotropic media, or a transversely isotropic media with the vertical axis of rotational symmetry, can be described by eight parameters: P-wave velocity (V_{PH}), S-wave velocity (V_{SV}), density, attenuation coefficients for P and S waves, and three anisotropic parameters (ϕ, ξ, and η) (Takeuchi and Saito, 1972). The anisotropic parameters are defined as

$$\phi = (V_{PV}/V_{PH})^2\,, \qquad \xi = (V_{SH}/V_{SV})^2\,, \qquad \eta = \frac{F}{A-2L}, \tag{6.1}$$

where V_{PV} and V_{PH} are the velocities of vertically and horizontally propagating P wave, respectively, V_{SH} and V_{SV} are the velocities of horizontally propagating and horizontally or vertically polarized S wave, respectively, η characterizes the P- and S-wave incident angle dependence relative to the vertical symmetric axis, A, F, and L are Love's elastic constants (Takeuchi and Saito, 1972).

6.3.1 Isotropic structure

Model parameters and scaling laws

Rayleigh waves are sensitive to V_{SV} (Figures 1.3 and 1.6). Phase velocities at a frequency higher than 0.1 Hz provide a good constrain in crustal and uppermost mantle structure (<30 km) (Figures 1.3a,c). Rayleigh-wave phase velocities measured at a frequency range of 0.005 to 0.04 Hz provide a good constrain on the structure at a depth range of 30 to 300 km (Figure 1.3b). I, therefore, estimate the depth profile of V_{SV} in a depth range of the seafloor to 300 km. I prepare an ocean layer, three crustal layers, and 13 mantle layers for V_{SV}. Because parameters other than V_{SV} are difficult to constrain only using Rayleigh waves, I scale the other parameters to V_{SV}. S- and P-wave velocities are defined as $V_S = (V_{SV} + V_{SH})/2$ and $V_P = (V_{PV} + V_{PH})/2$, respectively. In crustal layers, P-wave velocity and density are scaled to S-wave velocity using the relationship given by Christensen and Salisbury (1975):

$$
\begin{aligned}
V_{PV}\ \mathrm{km/s} &= 1.75\ \times V_{SV} + 0.375\ \mathrm{km/s}, \\
V_{PH}\ \mathrm{km/s} &= 1.75\ \times V_{SH} + 0.375\ \mathrm{km/s}, \\
\rho\ \mathrm{kg/m^3} &= 0.5(\mathrm{kg/m^3})/(\mathrm{km/s}) \times\ V_S + 1.25\ \mathrm{kg/m^3}.
\end{aligned}
$$

In mantle layers, V_P is constrained to be $\sqrt{3}$ times larger than V_S. Mantle density, attenuation coefficients for P and S waves, and the structure deeper than 400 km are fixed to the values of the PREM (Dziewonski and Anderson, 1981) with a 1-Hz reference frequency. The structure from 300 to 400 km is linearly connected. Thicknesses of crustal layers follow the refraction and reflections results of Abrams et al. (1993), and the total crustal thicknesses are 7.6 km and 7.9 km in the eastern and western array, respectively.

Inversion method

I first invert for the isotropic S-wave velocity structure using only Rayleigh waves under the assumption of $V_{SH} = V_{SV}$. Since I assume isotropic structure, anisotropic parameters are equal to one ($\xi = \phi = \eta = 1$). The inversion method follows Takeo et al. (2018). I use the simulated annealing method (Appendix C; Nam et al., 2004) to search for model parameters that minimize a cost function that is comprised of two terms: a misfit term and a vertical smoothing term. The

misfit term is given by

$$E_{SV} = \sqrt{\sum_{\omega,n} \left[\frac{\bar{c}_n^{ave}(\omega) - c_n^{model}(\omega)}{\Delta c_n(\omega)} \right]^2 / \sum_n N_n}, \tag{6.2}$$

where $\bar{c}_n^{ave}(\omega)$ is the measured n^{th}-mode average phase velocity, $\Delta c_n(\omega)$ is the measurement uncertainty, $c_n^{model}(\omega)$ is the model phase velocity calculated by DISPER80 (Saito, 1988) using model parameters, and N_n is the number of measurements for each n^{th} mode. The model uncertainty will be large if I only use the misfit term to search model parameters. Therefore, to reduce the uncertainty, I introduce the vertical smoothing term to evaluate the model smoothness:

$$R_{SV} = \sum_{i=1}^{N-1} (V_{SV}^{i+1} - V_{SV}^{i})^2, \tag{6.3}$$

where V_{SV}^i is the V_{SV} in i^{th} layer, and N is the number of layers. Combining equations (6.2) and (6.3) the total cost function is defined as

$$E'_{SV} = E_{SV} + \epsilon_{SV} R_{SV}, \tag{6.4}$$

where ϵ_{SV} is a constant determining the weight of the vertical smoothing term and $\epsilon_{SV} = 10$ so as to balance the model uncertainty and the RMS misfit (Figure 6.2).

I prepare 30 000 iterations for the simulated annealing method (Appendix C; Nam et al., 2004) to search optimal model parameters. During the first 100 iterations, the n^{th}-mode phase velocity is calculated by DISPER80 (Saito, 1988) using model parameters. Then, I linearly approximate phase velocity using the perturbation in model parameters and the sensitivity kernels (equation 1.1). Once every 500 iterations, I update the sensitivity kernels if an RMS value of V_{SV} ($\sqrt{(\sum_i^N (V_{SV}^i)^2)/N}$, where N is the number of layers) has changed by more than 2 % compared to that of the previous annealing step. The model uncertainty is evaluated using the 100 sets of dispersion curves obtained by the bootstrap method (Efron, 1979). Each set of dispersion curves is comprised of the bootstrapped 0S- and 1S-mode phase velocities that are obtained from ambient noise and/or teleseismic waveform analyses in Chapters 3 and 4. I substitute j^{th} set of dispersion curves ($c_{0S}^j(\omega)$ and $c_{1S}^j(\omega)$) in equation (6.2) in place of $\bar{c}_n^{ave}$ to estimate j^{th} V_{SV} structure and obtain 100 V_{SV} structures. At each layer, I define the one standard deviation of those 100 models as the model uncertainty.

Figure 6.3 shows the estimated isotropic V_{SV} structures in the eastern and the western arrays. Model phase velocities calculated from the final structures fit the observed data well (Figure 6.3c). V_{SV} of the second layer of the crust (∼6–9 km) is significantly faster in the eastern array than that of the western array, while the third layer (∼9–13 km) is significantly slower in the eastern array than that of the western array (Figure 6.3a). There is no significant difference in the mantle since the dispersion curve is common at frequencies lower than 0.04 Hz, which is measured using

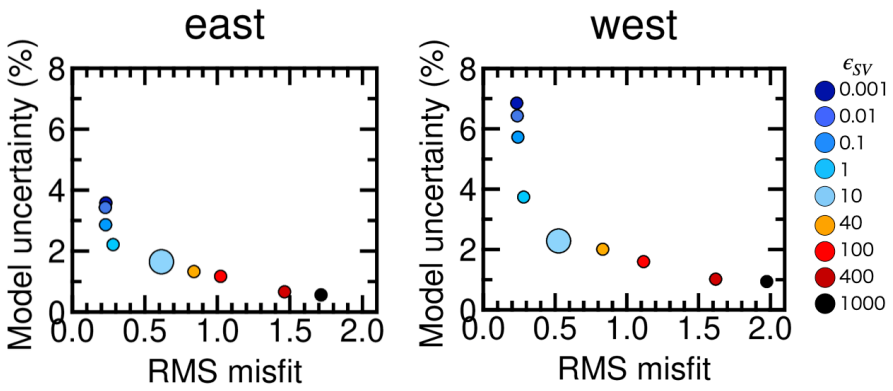

Figure 6.2: Examples of trade-offs between the model uncertainties and the RMS misfit that are averaged for all layers. The different colors represent different ϵ_{SV}. $\epsilon_{SV} = 10$ (light blue) is used for the final structure in Figure 6.3 which is highlighted with large circles.

all stations in the Oldest-1 Array. The velocities at a shallow depth range (<60 km) are about 4.68 km/s. The velocity drops at depths below 80 km, reaching below 4.5 km/s in a depth range of 100–240 km. Deeper than a depth of 180 km, the velocity gets higher and recovers to 4.58 km/s in a depth range of 240–300 km. I define the high-velocity part in a depth range of Moho to 60 km as the Lid and the low-velocity part in a depth range of 80–240 km as the low-velocity zone (LVZ). Same as previous studies, I interpret the Lid and LVZ as corresponding to the lithosphere and asthenosphere, respectively.

6.3.2 Radial anisotropy

Next, I invert for a radially anisotropic structure using both Rayleigh- and Love-wave phase velocities. Love-wave phase velocities at a frequency higher than 0.1 Hz are significantly different between the eastern and western arrays, suggesting there exist differences in a depth range shallower than ∼50 km. The resolution in depth is higher in Rayleigh-wave phase velocity than that of Love waves due to the different shapes in the sensitivity kernels (Figure 1.6). I, therefore, estimate the depth profile of V_{SV} and radial anisotropy (RA_S), where $RA_S = (\sqrt{\xi} - 1) \times 100 = (V_{SH}/V_{SV} - 1) \times 100$, in a depth range of the seafloor to 300 km. The structure layering for V_{SV} and model parameters follow the previous section. I set two mantle layers (Moho–60 km and 60–240 km) for RA_S. The sensitivity of Love waves is almost zero at 50 km (Figure 1.5b), but instead of employing a discontinuity at 50 km, I follow the definition of the Lid estimated by Rayleigh waves and set a discontinuity at the depth of 60 km. At each layer, constant V_{SV} and RA_S are assigned.

The inversion process is the same as that described in Section 6.3.1, except the estimation of ξ is involved and there is no vertical smoothing between two layers in ξ structure. Crust and structures deeper than 240 km are set to be isotropic. In order to estimate radially anisotropic structures, the estimation of anisotropic parameters is needed. Since I cannot constrain ϕ and η (equation 6.1) from the data set, I use the scaling laws of mantle LPO given by Montagner and

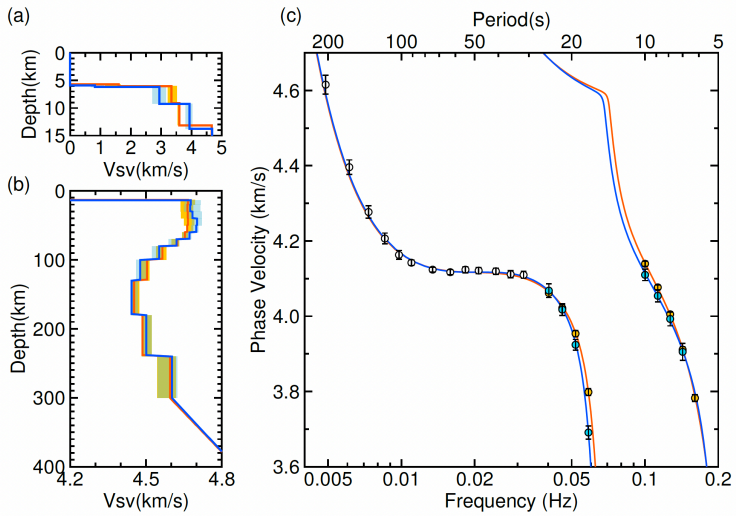

Figure 6.3: The final isotropic V_{SV} structures for the western (blue) and eastern (orange) arrays. (a) Crustal structure. (b) Mantle structure. The shaded areas represent the model uncertainty. (c) Model (solid lines) and measured (dots with error bars) phase velocities.

Anderson (1989) as

$$\phi = \xi^{-1.5}, \qquad \eta = \xi^{-2.5}.$$

The uncertainty of the average phase velocity of the 0T mode measured by teleseismic waveforms is defined in a different way from the other modes, and I cannot determine the model uncertainty by the bootstrap method (Efron, 1979) in the same way as in the previous section. Therefore, I calculate the lower and upper bound of the 0T-mode phase velocity ($\bar{c}^{ave}_{0T}(\omega) - \Delta c_{0T}(\omega)$ and $\bar{c}^{ave}_{0T}(\omega) + \Delta c_{0T}(\omega)$) and estimate lower and upper bounds of radial anisotropy structure. Rayleigh-wave phase velocities are fixed to the average values ($\bar{c}^{ave}_{0S}(\omega)$ and $\bar{c}^{ave}_{1S}(\omega)$). Figures 6.4 and 6.5 show the estimated V_{SV} and radial anisotropy structure in the eastern and western arrays, respectively. Because of the small uncertainties in measured phase velocities, all estimated models show similar values in the shallow structure (<60 km).

Figure 6.6 compares the estimated radial anisotropy in both arrays. The shades in Figure 6.6 represent the model uncertainties. The model uncertainties in the depths of 60–240 km (Figure 6.6) correspond to the upper and lower limits in Figures 6.4 and 6.5. The model uncertainties at the depth range of Moho–60 km (Figure 6.6) are evaluated using the 100 sets of dispersion curves obtained by the bootstrap method (Efron, 1979). Each set of dispersion curves is comprised of the bootstrapped 0T-, 0S-, and 1S-mode phase velocities that are obtained from ambient noise and/or teleseismic waveform analyses in Chapters 3–4, while the 0T-mode phase velocities at a frequency range of 0.01–0.03 Hz, which is estimated in Chapter 5 is fixed to the average values ($\bar{c}^{ave}_{0T}(\omega)$). The j^{th} set of dispersion curves is used to estimate the j^{th} structure. I define the one standard deviation of those 100 models as the model uncertainties at the depth range of Moho–60 km.

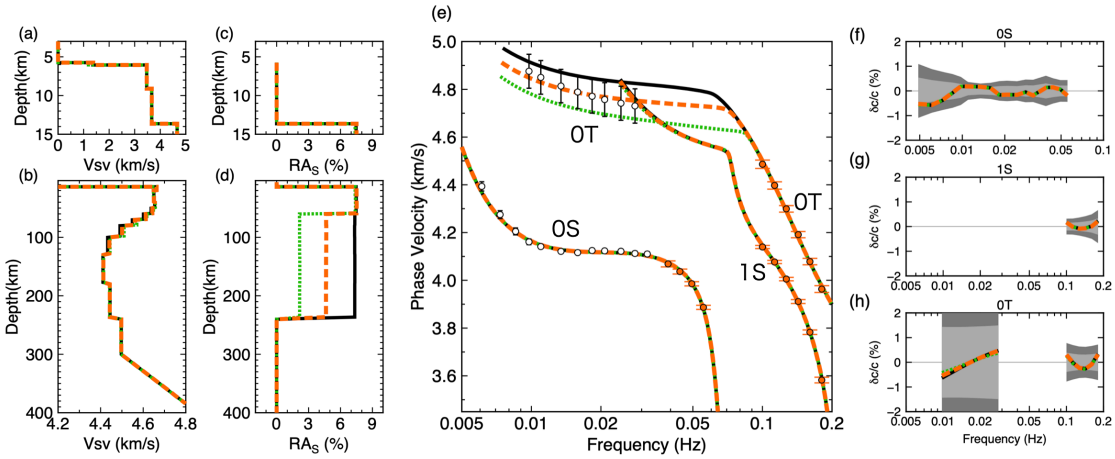

Figure 6.4: Radially anisotropic structure in the eastern array. (a–b) Crustal and mantle V_{SV} structure. The orange dashed line represents the model estimated by average measurement values (circles in e), the green dotted and black solid lines represent the lower and upper bound of radial anisotropy structures. (c–d) Two-layer radial anisotropy (RA_S) structure of crust and mantle, where $RA_S = (V_{SH}/V_{SV} - 1) \times 100$ %. (e) Model (lines) and measured (circles with error bars) phase velocities. (f-h) The 0S-, 1S-, and 0T-mode phase velocity residuals with the 1σ and 2σ measurement errors represented by lighter and darker gray shaded areas, respectively.

In a depth range from Moho to 60 km, $RA_S = 7.5 \pm 1.0$ % in the eastern array and $RA_S = 3.4 \pm 1.1$ % in the western array. The shallow structure (<60 km) is constrained by phase velocities at frequencies higher than 0.1 Hz, and the significant difference in radial anisotropy between the two arrays (Figure 6.6) reflects the significant difference in measured phase velocity (Figure 6.1). In a depth range from 60 to 240 km, RA_S=2–7 % in the eastern array (Figure 6.4) and RA_S=3–8 % in the western array (Figure 6.5). All models fit the measured phase velocities well (Figures 6.4f-h and 6.5f-h). Russell et al. (2019) estimated radial anisotropy within the lower crust and the uppermost mantle (<35 km) beneath the 70-Ma seafloor. Their measured phase velocities could not be fitted by only assuming radial anisotropy within the Lid but required strong radial anisotropy with RA_S=4–5 % within the lower crust. On the other hand, the measured phase velocity in this study did not require radial anisotropy within the crust.

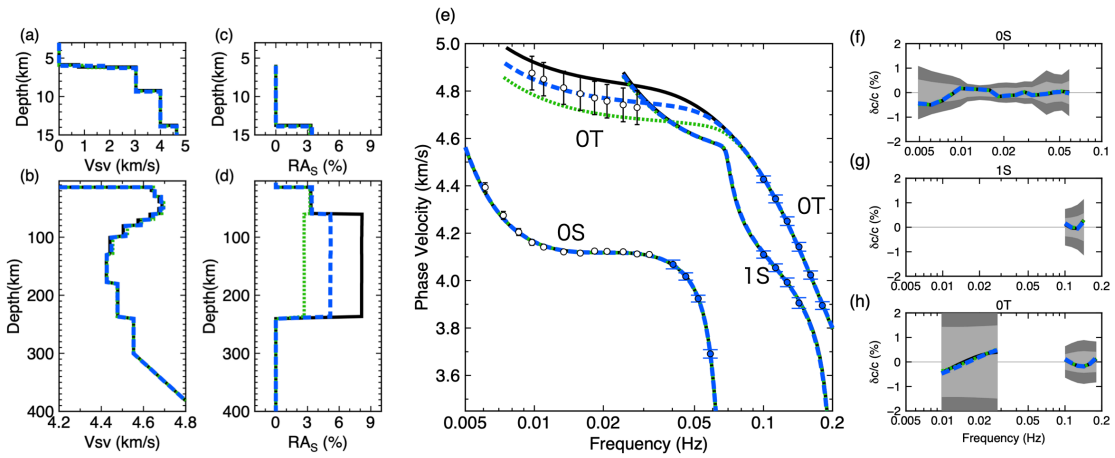

Figure 6.5: Same as Figure 6.4 but for the western array.

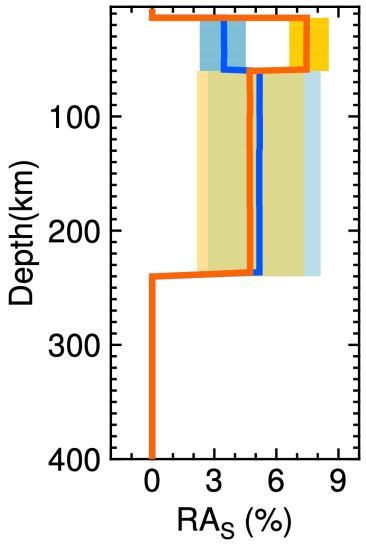

Figure 6.6: The estimated RA_S structures in the eastern (blue) and western (orange) arrays.

6.4 Azimuthally anisotropic structure

Azimuthal anisotropy of V_{SV} can be described by 2θ-sinusoidal pattern. Because Rayleigh waves are mainly sensitive to V_{SV}, if azimuthal anisotropy exists in V_{SV}, Rayleigh waves also display a 2θ-sinusoidal pattern (Montagner and Nataf, 1986). In Chapters 3 and 4, the azimuthal variability of measured phase velocities was fitted by 2θ-sinusoidal pattern both for the 0S and 1S modes which are obtained from ambient noise and/or teleseismic waveform analyses. Therefore, I invert for the 2θ pattern in azimuthal anisotropy of V_{SV} in this section.

6.4.1 Model parameters and inversion method

I describe the azimuthal dependence of V_{SV} as a function of depth z as

$$V_{SV}(z,\theta) = V^0_{SV}(z)[1 + A_{c2}(z)\cos2\theta + A_{s2}(z)\sin2\theta], \tag{6.5}$$

where θ is wave propagation azimuth, $V^0_{SV}(z)$ is isotropic V_{SV}, $A_{c2}(z)$ and $A_{s2}(z)$ are coefficients. I estimate $A_{c2}(z)$ and $A_{s2}(z)$ in each layer of a structure that has 13 layers from Moho to a depth of 300 km. The crust and the structure deeper than 300 km is constrained to be isotropic. The peak-to-peak intensities of anisotropy is given by $2A_2(z) = 2\sqrt{[A_{c2}(z)]^2 + [A_{s2}(z)]^2}$ and the fastest direction of azimuthal anisotropy is given by $\theta_{max}(z) = 0.5\arctan[A_{s2}(z)/A_{c2}(z)]$.

The model azimuthal anisotropy of n^{th}-mode phase velocity ($n = 0S, 1S$) can be given by

$$c^{model}_n(\omega) = c^{ave}_n(\omega)[1 + A^n_{c2}(\omega)\cos2\theta + A^n_{s2}(\omega)\sin2\theta], \tag{6.6}$$

where $A^n_{c2}(\omega)$ and $A^n_{s2}(\omega)$ are given by

$$A^n_{c2}(\omega) = \int_z K^n_\beta(z,\omega)A^n_{c2}(z)dz, \tag{6.7}$$

$$A^n_{s2}(\omega) = \int_z K^n_\beta(z,\omega)A^n_{s2}(z)dz, \tag{6.8}$$

where $K^n_\beta(z,\omega)$ is n^{th}-mode phase velocity sensitivity kernel to S-wave velocity (Figure 1.3). The sensitivity kernels are fixed to the ones obtained from the isotropic V_{SV} structure in Section 6.3.1.

I again use the simulated annealing method (Appendix C; Nam et al., 2004) to estimate the azimuthal anisotropy structure following the method of Takeo et al. (2018). I search for model parameters in each of 13 layers that minimize a cost function which is defined by two terms: a misfit term and a vertical smoothing term. The misfit term is given by

$$E_{AA} = \sqrt{\sum_{n,\omega}\left[\left\{\frac{\bar{A^n_{c2}}(\omega) - A_{c2}(\omega)}{\Delta A^n_{c2}(\omega)}\right\}^2 + \left\{\frac{\bar{A^n_{s2}}(\omega) - A_{s2}(\omega)}{\Delta A^n_{s2}(\omega)}\right\}^2\right] / \sum_n 2N_n}, \tag{6.9}$$

where N_n is the number of measurement points of the n^{th} mode (n=0S, 1S), $\bar{A^n_{c2}}(\omega)$ and $\bar{A^n_{s2}}(\omega)$ are the bootstrap average of the estimated azimuthal anisotropy of the 0S- and 1S-mode phase velocity obtained from ambient noise and/or teleseismic waveforms in Chapters 3 and 4, $\Delta A^n_{c2}(\omega)$ and $\Delta A^n_{s2}(\omega)$ are the uncertainties of $\bar{A^n_{c2}}(\omega)$ and $\bar{A^n_{s2}}(\omega)$, respectively. The vertical smoothing term is given by

$$R_{AA} = \sum_{i=1}^{N}[\left\{A^{i+1}_{c2} - A^i_{c2}\right\}^2 + \left\{A^{i+1}_{s2} - A^i_{s2}\right\}^2]/2, \tag{6.10}$$

where N is the number of layers, A^i_{c2} and A^i_{s2} are $A_{c2}(z)$ and $A_{s2}(z)$ in the i^{th} layer, respectively.

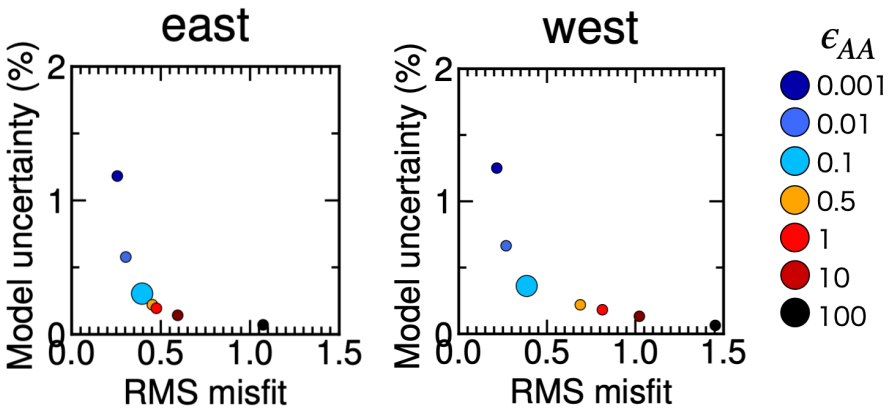

Figure 6.7: Examples of trade-offs between the model uncertainties and the RMS misfits that are averaged over all layers. The different colors represent different ϵ_{AA}. $\epsilon_{AA} = 0.1$ (light blue) is used for the final structure which is highlighted with larger circles.

The total cost function is given by

$$E'_{AA} = E_{AA} + \epsilon_{AA} R_{AA}, \tag{6.11}$$

where ϵ_{AA} determines the weight of the vertical smoothing term. Figure 6.7 shows the trade-off between the model uncertainty and the RMS misfit. I choose $\epsilon_{AA} = 0.1$, which gives moderate values for both the model uncertainty and the RMS misfit.

The model uncertainty is evaluated by the bootstrap method (Efron, 1979) in the same manner as that of Section 6.3.1. I invert the 100 sets of $A^n_{c2}(\omega)$ and $A^n_{s2}(\omega)$ which obtained by the bootstrap method from ambient noise and/or teleseismic waveform analyses in Chapters 3 and 4. Each bootstrap sample is consisted of four anisotropic parameters ($A^{0S}_{c2}(\omega)$, $A^{0S}_{s2}(\omega)$, $A^{1S}_{c2}(\omega)$, and $A^{1S}_{s2}(\omega)$). I invert j^{th} set of parameters to estimate j^{th} $A_{c2}(z)$ and $A_{s2}(z)$ structures. At each layer, I define the one standard deviation of those 100 models as the model uncertainty.

6.4.2 Results

Figure 6.8 shows the peak-to-peak intensity and the fastest direction structures of mantle V_{SV} beneath the Oldest-1 Array. The left two figures show the fitting between the measured and the model azimuthal anisotropy. Both the model intensities and the fastest directions fit the data well except for the intensities at frequencies lower than 0.01 Hz. At those frequencies, the 2θ patterns of phase velocities are not well constrained due to the poor azimuthal coverage (Figure 4.5), and apparent intensities associated with incomplete azimuthal coverage appeared. At frequencies higher than 0.1 Hz, both the measured peak-to-peak intensities and the fastest directions are significantly different between the eastern and western arrays (Figure 6.8 left), resulting in a difference at a depth shallower than 50 km (Figure 6.8 right).

At depths shallower than 50 km, the intensities in the east are 1.6 ± 0.8 % on average, while

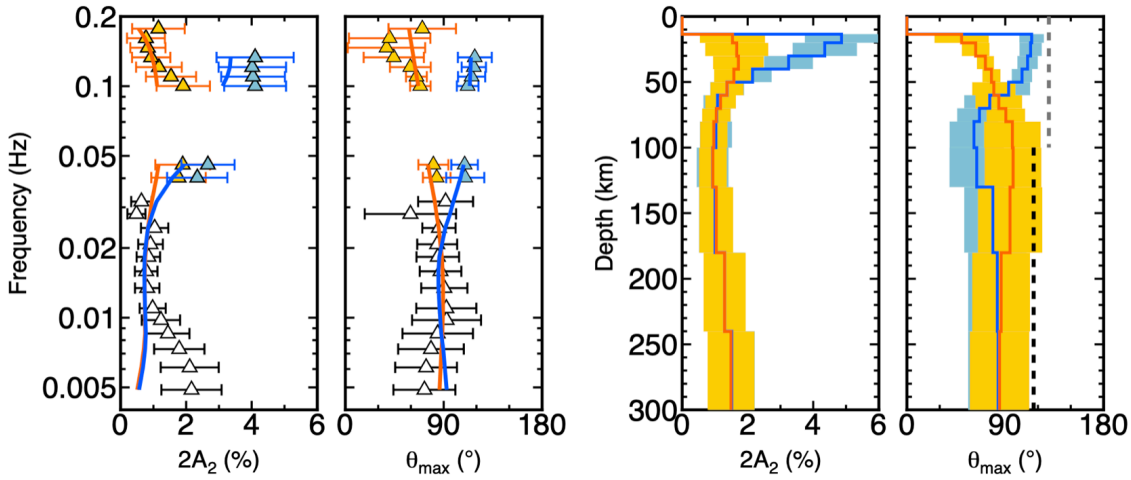

Figure 6.8: The final azimuthally anisotropic V_{SV} structures and model fit of the western (blue) and eastern (orange) arrays. Two figures on the left: Model (solid lines) and measured (triangles with error bars) azimuthal anisotropy as a function of frequency in terms of the peak-to-peak intensities ($2A_2$) and the fastest direction (θ_{max}). Two figures on the right: The final azimuthally anisotropic V_{SV} structures. The shaded areas represent the model uncertainty. The gray broken line represents the direction perpendicular to the 170-Ma isochrone of Seton et al. (2020). The black broken line represents the current absolute plate motion direction.

it is 3.7 ± 0.9 % in the west (Figure 6.8 right). The intensities in the western array change from 4.9 % at Moho to 2.1 % at 50 km (Figure 6.8 right), reflecting the change in measured intensities at a frequency higher than 0.1 Hz and between 0.03–0.05 Hz (Figure 6.8 left). The structure of the fastest directions is also significantly different between the eastern and the western arrays: changing from 50° (NE-SW) and 114°(ESE-WNW) at Moho to 77° (ENE-WSW) and 105° (E-W) at 50 km depth in the eastern and western arrays, respectively. On average, the fastest direction is $111° \pm 10°$ in the west and $66° \pm 13°$ in the east. Since the direction perpendicular to the 170-Ma isochrones is 130°N (Seton et al., 2020), the fastest directions in both areas deviate from the predicted past seafloor spreading direction, in particular in the eastern array.

At depths deeper than 50 km, measurements are common for the eastern and western arrays, hence resulting in similar structures between the two. Although the fastest direction at depths of 60–150 km appears to be different, the difference is not significant since the intensities are weak (∼1 %) at this depth range (Figure 6.9). The intensity is about 1 % at a depth range of 80–240 km, where I defined the LVZ in Section 6.3.1. Within the LVZ, the fastest direction is $93° \pm 27°$ in the east and $72° \pm 25°$ in the west, which deviate from the absolute plate motion (116°) by Gripp and Gordon (2002), but the difference is not significant if I take the two-sigma uncertainty range (plotted range represents one-sigma range).

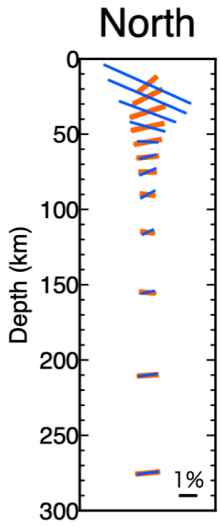

Figure 6.9: A comparison of azimuthal anisotropy depth profile in the western (blue) and the eastern (orange) arrays. The upward direction on the paper is north, and the bars indicate the peak-to-peak intensities at the plotted depth and the fastest direction clockwise from north. The black line at the bottom right represents 1 % peak-to-peak intensity.

6.5 Effect of P-wave anisotropy

Although in the previous section, only azimuthal anisotropy of V_{SV} has been considered for inverting Rayleigh-wave azimuthal anisotropy, P-wave azimuthal anisotropy can also affect Rayleigh-wave azimuthal anisotropy. The pattern of P-wave azimuthal anisotropy shows dominant 2θ patterns for the case of LPO with the horizontal alignment of a-axes of olivine crystals (Montagner and Nataf, 1986). It is V_{PH}, horizontally propagating P-wave velocity, that results in such azimuthal anisotropy. There is no azimuthal anisotropy on V_{PV} since it is vertically propagating and vertically oscillating P-wave velocity. V_{PH} azimuthal anisotropy corresponds to Pn-wave azimuthal anisotropy observed by refraction studies (Shinohara et al., 2008; Shintaku et al., 2014). The 0S-mode phase velocity sensitivity to V_{PH} and V_{SV} are plotted in Figure 6.10a. It can be seen that although the sensitivity to V_{SV} is dominant, the sensitivity to V_{PH} is also non-negligible.

I constrain V_{PH} anisotropy to be 1.3 times larger than V_{SV} anisotropy by referring to observations in previous refraction study in northwestern Pacific basin (Shinohara et al., 2008). Instead of equations (6.7–6.8), I use the following equations to predict Rayleigh-wave azimuthal anisotropy ($A^n_{c2}(\omega)$ and $A^n_{s2}(\omega)$):

$$A^n_{c2}(\omega) = \int_z \left[K^n_{V_{SV}}(z,\omega)A^n_{c2}(z) + 1.3K^n_{V_{PH}}(z,\omega)A^n_{c2}(z)\right] dz, \tag{6.12}$$

$$A^n_{s2}(\omega) = \int_z \left[K^n_{V_{SV}}(z,\omega)A^n_{s2}(z) + 1.3K^n_{V_{PH}}(z,\omega)A^n_{s2}(z)\right] dz, \tag{6.13}$$

where $K^n_{V_{SV}}(z,\omega)$ and $K^n_{V_{PH}}(z,\omega)$ are n^{th}-mode phase velocity sensitivity kernels to V_{SV} and V_{PH},

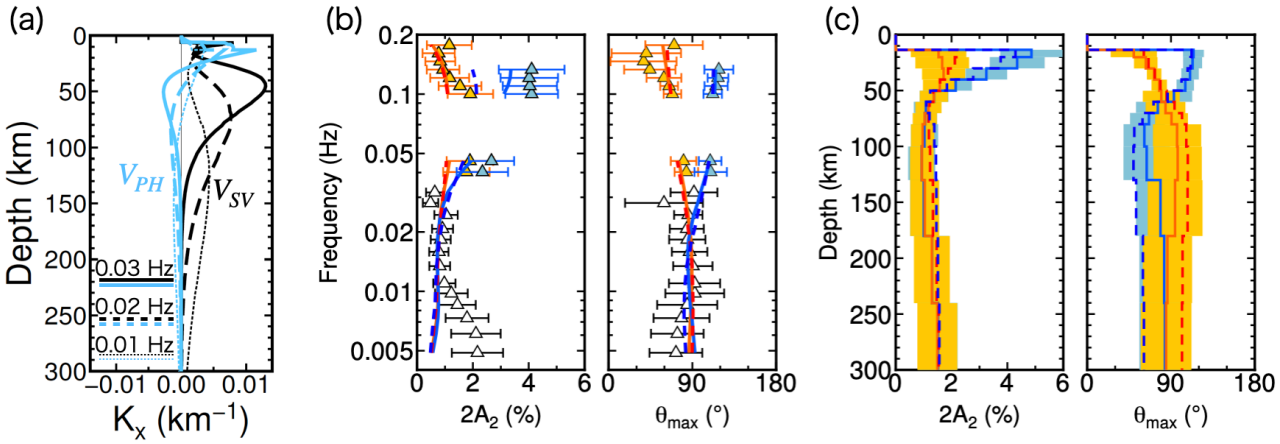

Figure 6.10: (a): 0S-mode phase velocity sensitivity kernels to parameter x. The sensitivity kernels are calculated for structure in Figure 1.1. (b) and (c) are same as Figure 6.8 but azimuthal anisotropy estimated with V_{PH} anisotropy are plotted. Red and deep blue dashed lines represent the model for the eastern and western arrays, respectively, with V_{PH} anisotropy. Orange and blue solid lines represent the model for the eastern and western arrays, respectively, without V_{PH} anisotropy (same as Figure 6.8).

respectively. The sensitivity kernels are fixed to the ones obtained from the isotropic structure in Section 6.3.1.

Figures 6.10b shows a comparison of the model and observed Rayleigh-wave azimuthal anisotropy, and Figures 6.10c shows the corresponding structure. The model uncertainties for the azimuthal anisotropy structure estimated with V_{PH} anisotropy are not shown to simplify the plot, but the values are comparable to that estimated without V_{PH} anisotropy: about 0.7 % in the peak-to-peak intensity and about 20° in the fastest direction.

Both the peak-to-peak intensity and the fastest direction are robust (Figure 6.10c), and the difference in structures between including or not including V_{PH} anisotropy in the estimation falls within the range of uncertainties. However, some differences do exist. In the shallow depths (<50 km), the fastest directions are similar between the V_{PH} anisotropy included and not included structures, but the peak-to-peak intensity changes, and the difference in anisotropy between the eastern and western arrays becomes small: without V_{PH} anisotropy, they were 1.6 % and 3.7 % in the eastern and western arrays, respectively, white with V_{PH} anisotropy, they become 2.0 % and 3.2 %, respectively. The modeled Rayleigh-wave peak-to-peak intensity in the western array predicted by the structure including V_{PH} anisotropy is somehow underestimated (Figure 6.10b), indicating the requirement of the stronger peak-to-peak intensity at shallow depths. At depths of 70–180 km, the peak-to-peak intensity changes from 1.0 % to 1.2 % and 1.4 % for eastern and western arrays, respectively. The fastest direction at depths deeper than 60 km changed by 10–15 degrees in an opposite sense for the eastern and western arrays. All structures provide similar predictions of Rayleigh-wave fastest directions (Figure 6.10b).

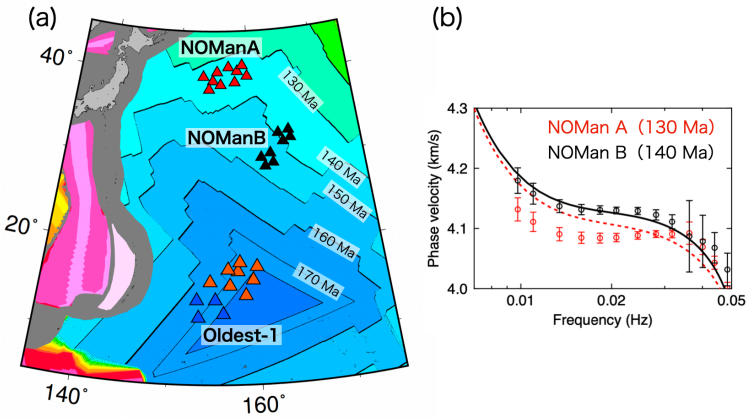

Figure 6.11: (a) Location map of the arrays. The red triangles represent BBOBS stations of NOMan A. The black triangles represent BBOBS stations of NOMan B. The orange and blue triangles represent the BBOBS stations of Oldest-1. The orange stations belong to the eastern array, and the blue stations belong to the western array. (b) Comparison of measured and HSC model predicted phase velocity by Takeo et al. (2018). Circles with error bars are measurements. The black solid line is the model dispersion curve for 140-Ma seafloor, and the red dashed line is that predicted for the 130-Ma seafloor.

6.6 Discussions

6.6.1 Comparison to the previous studies at 130- and 140-Ma seafloor

Takeo et al. (2018) estimated V_{SV} structures beneath two BBOBS arrays deployed in the north-western Pacific Ocean under the Normal Oceanic Mantle (NOMan) project[1] (Figure 6.11a). The NOMan project was designed to understand the "normal" oceanic lithosphere-asthenosphere system, and the arrays were ∼1000 km apart and situated in the old normal seafloor (NOMan A at 130 Ma and NOMan B at 140 Ma). Nevertheless, they found that the differences in shear-wave velocities of the LVZ between the two arrays cannot be explained by the cooling due to their age differences. Figure 6.11b shows their key result. They found that the dispersion curve (phase velocities) measured at NOMan B is consistent with a half-space cooling (HSC) model assuming typical parameters. However, the dispersion curve measured at NOMan A is not consistent with the same HSC model but parameterized with 130 Ma. Combined with the azimuthal anisotropy profile, they interpreted that the bottom of the plate beneath NOMan A is reheated by small-scale convection and there may be downwelling beneath NOMan B.

Here I compare the isotropic V_{SV} structure beneath the Oldest-1 Array to that of Takeo et al. (2018) (Figure 6.12). Only the result in the western array are overlaid. In all three regions, structures at a depth range of Moho to 60 km and structures deeper than 80 km are interpreted as the lithosphere (Lid) and the asthenosphere (80–150 km in Takeo et al. (2018) and 80–240 km in this study), respectively. Utilizing noise-reduced seismograms (Chapter 2), I measured the phase

[1]http://ohpdmc.eri.u-tokyo.ac.jp/dataset/campaign/obs/nomantle/station/index.html

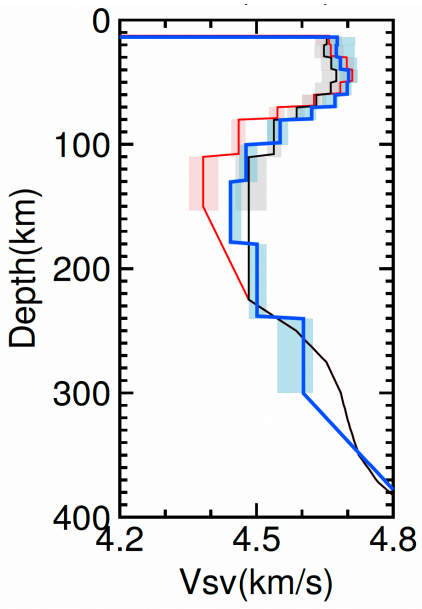

Figure 6.12: A comparison of isotropic V_{SV} structures estimated at the old Pacific seafloor; 170 Ma (Oldest-1 Array; blue line obtained in this study), 140 Ma (NOMan B; black line obtained in Takeo et al., 2018), and 130 Ma (NOMan A; red line obtained in Takeo et al., 2018). The shaded areas represent uncertainties. In Takeo et al. (2018), the structure at the depth range of 225–400 km is fixed to that of the ORM (Maggi et al., 2006) which is a one-dimensional V_{SV} model averaged over 30- to 70-Ma Pacific seafloors. In both studies, the structure deeper than 400 km is fixed to that of the PREM (Dziewonski and Anderson, 1981) with a 1-Hz reference frequency. The velocities at the depth range of 150–225 km and 300–400 km are linearly interpolated in Takeo et al. (2018) and in this study, respectively.

velocities up to the frequency of 0.005 Hz (Figure 6.1). Consequently, I resolved structures deeper than that of Takeo et al. (2018) and constrained the bottom of the LVZ that is recognizable as the velocity recovery at depths deeper than 200 km (Figure 6.12). The lithospheric structures are similar among the three regions, and V_{SV} is 4.65–4.70 km/s. The velocity reduction at the LVZ is the most prominent in the NOMan A (130 Ma), and the velocity reaches a value of 4.38 km/s at the depth range of 110–150 km. At the same or similar depth range in the Oldest-1 and NOMan B, the velocities are about 4.44 km/s and 4.48 km/s, respectively, meaning that the velocity in the LVZ in the NOMan A is about 1–2 % slower than the other regions.

In order to verify whether the difference or similarity of structures among the three regions can be explained by their age differences, I compare those structures in terms of the HSC model by directly comparing their dispersion curves following the method of Takeo et al. (2018). To calculate the synthetic dispersion curve, I first construct a temperature profile of an HSC model assuming a 170-Myr-old seafloor. The potential temperature is set to 1350 °C with an adiabatic temperature gradient of 0.3 °C/km. Then, I convert the temperature profile to an S-wave velocity depth profile assuming a pyrolite model (Stixrude and Lithgow-Bertelloni, 2005, 2011). With this S-wave velocity model, I further calculate the fundamental-mode Rayleigh-wave dispersion curve.

The pyrolite model only provides V_S profile ($V_S = (V_{SH} + V_{SV})/2$) not V_{SV} profile, so one needs the information of RA_S to calculate the dispersion curve. To evaluate RA_S, measurement of the Love-wave dispersion curve is required but Takeo et al. (2018) assumed RA_S=4 % from Moho to a depth of 225 km without obtaining Love-wave measurement. Since the estimated RA_S takes a value between 2–8 % in the Oldest-1 Array, I also assume RA_S=4 % in this study.

I interpret that the NOMan B (140 Ma) follows an HSC model and evaluate whether the 30-Myr age difference can explain the measured phase velocities at the Oldest-1 Array. The age difference of 30 Myr gives a temperature difference of ∼60°C at a depth of 100 km (Figure 6.13a). This results in ∼0.5 % faster S-wave velocities at a depth of 100 km in the 170-Ma seafloor (Oldest-1 Array) compared to that of the 140-Ma seafloor (NOMan B) (Figure 6.13b), and thus the dispersion curve at the Oldest-1 Array should be ∼0.5 % faster than that of the NOMan B if the Oldest-1 mantle follows an HSC model (Figure 6.13c). However, the observed Oldest-1 phase velocities do not follow the HSC model predictions. The phase velocities observed at the Oldest-1 Array are ∼1 % slower than that of the NOMan B at a frequency range of ∼0.01–0.02 Hz, indicating that additional thermal mechanisms might be needed within the LVZ in the Oldest-1 Array.

One possible explanation for the required additional mechanism within the LVZ beneath the Oldest-1 Array is the occurrence of small-scale convection (SSC) (e.g., Richter and Parsons, 1975; Huang and Zhong, 2005). The estimated azimuthal anisotropy depth profile at the depth range of 100–240 km shows the small peak-to-peak intensities ($1.1 \pm 0.5\%$) and the fastest direction ($84° \pm 27°$) which deviate from the APM (116°) (Gripp and Gordon, 2002) for $32° \pm 27°$. van Hunen and Čadek (2009) numerically modeled how SSC perturbs the APM-induced LPO pattern. They showed that well-developed SSC could randomly disturb the amplitude and the direction of the APM-induced LPO, but when the LPO pattern is spatially smoothed, the amplitude of the LPO has reduced by a factor of two, while the orientation does not significantly deviate from the APM ($< 20°$). Since surface-wave sensitivity has a spatial extent, observations in this study should reflect a smoothed LPO pattern. Therefore, observations in this study are consistent with their prediction, supporting the occurrence of SSC. Combined with the previous study in the NOMan A and B, the LVZ in the old Pacific seafloor is variable and does not follow an HSC model.

6.6.2 Implications for the early Pacific evolution

Oceanic plates are formed at and spread apart from mid-ocean ridges. The shearing associated with the seafloor spreading produces an LPO with the intrinsically and seismically fast a-axis of olivine crystals orient in the spreading directions. Thus, lithospheric azimuthal anisotropy is conventionally interpreted as a proxy of mantle shearing due to the seafloor spreading (Nicolas and Christensen, 1987) and used to infer the past seafloor spreading directions. Seismic azimuthal anisotropy with its fastest direction perpendicular to magnetic lineation is frequently observed for both body and surface waves (e.g., Hess et al., 1964; Forsyth, 1975; Takeo et al., 2014; Lin et al., 2016; Mark et al., 2019). Whereas there are also observations of the fastest directions that are

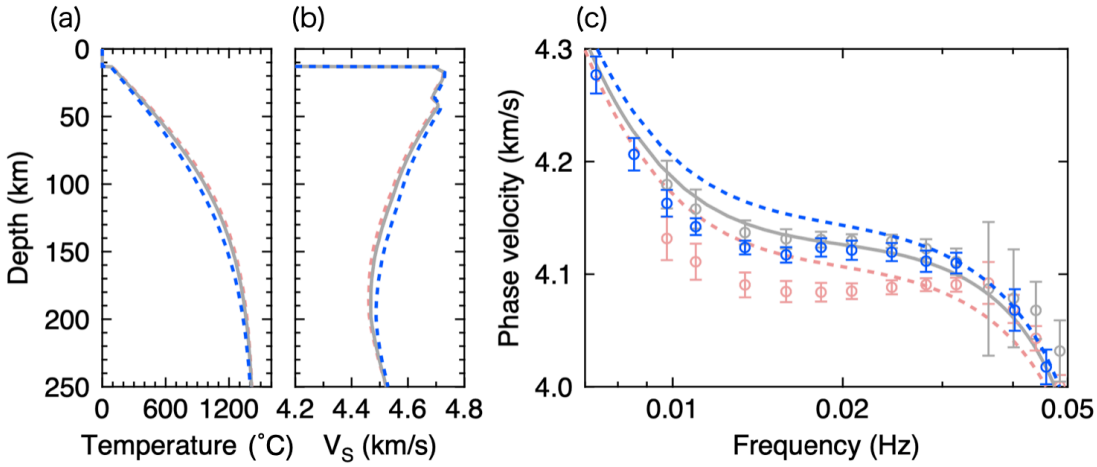

Figure 6.13: (a) Temperature profiles of the half-space cooling model for 170-Ma (blue), 140-Ma (gray), and 130-Ma (red) seafloor. (b) The S-wave velocity depth profiles that correspond to the temperature profiles in (a). (c) Model (lines) and observed (circles with error bars) fundamental-mode Rayleigh-wave phase velocities in each region. The model phase velocities correspond to three structures in (b).

oblique to the magnetic lineations which challenge the conventional notion (e.g., Toomey et al., 2007; Shintaku et al., 2014; Takeo et al., 2016, 2018).

This study observed a significant difference in azimuthal anisotropy between the eastern and western arrays. The fastest direction in the west is quasi-perpendicular to the predicted 170-Ma isochrone while the fastest direction in the east is not (Figure 6.14). The peak-to-peak intensity of V_{SV} azimuthal anisotropy of the shallowest mantle beneath the western array is 4.8±1.1 %. Assuming that Pn anisotropy is 1.3 times larger than Sn anisotropy based on the refraction survey in the northwestern Pacific Ocean (Shinohara et al., 2008), the P-wave anisotropy is 6.3±1.4 % at the top of the upper mantle. This is consistent with the global compilation of the linear relationship between the P-wave azimuthal anisotropy and half-spreading rates (Song and Kim, 2012) if I assume the half-spreading rate at the Oldest-1 Array is 80 mm/year (Abrams et al., 1993; also see Section 1.5.3). In contrast, the V_{SV} anisotropy of the shallowest mantle beneath the eastern array is 1.5±1.0 % which can be converted to P-wave anisotropy as 2.0±1.3 %. The peak-to-peak intensity in the eastern array is anomalously small and is small compared to previous studies in the Pacific basin (e.g., Takeo et al., 2014, 2016, 2018; Russell et al., 2019; Russell, 2021).

The difference between the shallow western and eastern anisotropy may reflect the evolution process of the early Pacific plate. Although there are no available direct observations of geomagnetic lineations at this oldest region, based on the analyses of magnetic lineations on the younger seafloor at norther Pacific (Larson and Chase, 1972; Nakanishi et al., 1992), the Pacific plate is believed to be formed at the Phoenix–Izanagi–Farallon triple junction and thus to have been a triangular shape during its early state (e.g., Seton et al., 2012) (more details are in Section 1.5.3). As can be seen from Figure 6.14, the eastern and western arrays have different distances from

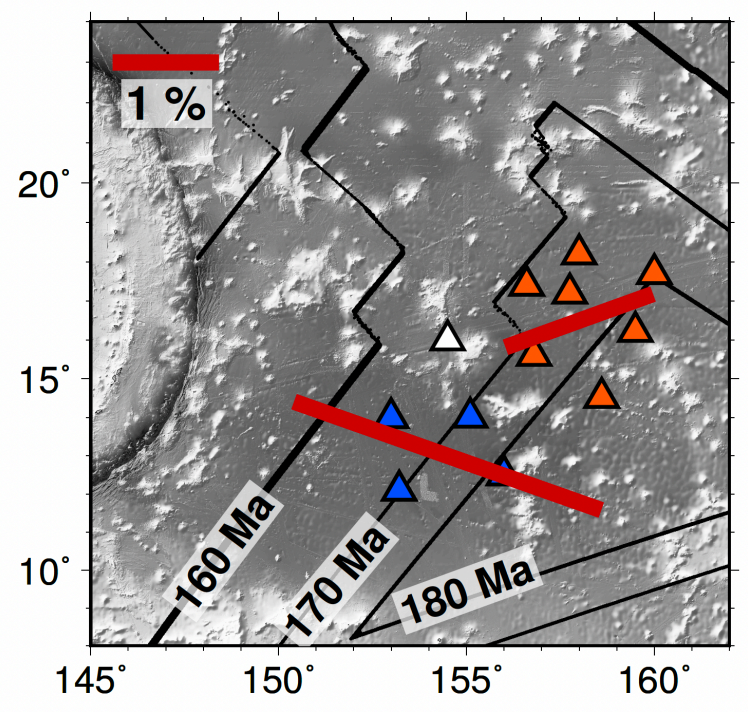

Figure 6.14: The red solid bars represent the average of the fastest directions from Moho to a depth of 50 km in each sub-array. The length of the bars represents the magnitude of peak-to-peak intensities and the 1 % scale is shown in the upper right.

the ancient ridge-ridge-ridge triple junction which can be recognized as a corner, located at 160°E and 18°N, of a triangle formed by the 180-Ma isochrone. The western array is located ∼500 km away from the ancient triple junction whereas the eastern array is very close to or even overlaps with the ancient junction. This difference in locations might be the reason for the different azimuthal anisotropy. The seafloor away from the junction may be formed by relatively simple plate divergence, whereas the seafloor close to the junction may have undergone disturbances by mantle upwelling at the junction.

In order to test the above hypothesis, a mantle-flow simulation is performed to examine the seismic azimuthal anisotropy pattern due to olivine LPO assuming that the three plates divergent away at an equal rate from a ridge-ridge-ridge triple junction (Figure 6.15). This corresponds to the ancient Pacific-Farallon-Izanagi triple junction (Figure 1.9): the southern plate represents the Pacific plate, the western plate represents the Izanagi plate, and the eastern plate represents the Farallon plate. Note that the upper side of the figure is north. The three ridge axes intersect at a point, the triple junction, and passive upwelling is assumed there. The angle between the ridge axes is 120°. The model space is a uniform media, having 200 km in depth and 1500×1500 km horizontally. The spreading rate of the three plates is constant as 1 cm/year. The simulation method and rheological parameters follow Morishige and Honda (2011). A-type olivine fabric is assumed, and the volume fractions of olivine and enstatite are set as 70 % and 30 %, respectively. The crystals initially have random orientations at the base of the model region. As material flows,

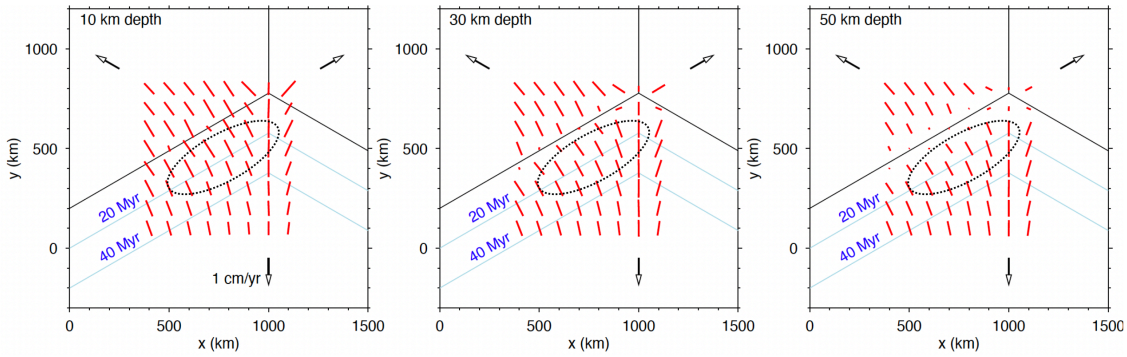

Figure 6.15: Simulation results of seismic azimuthal anisotropy. Figures from left to right correspond to the cross-section at a depth of 10 km, 30 km, and 50 km. Black solid lines represent the ridge axes, black open arrows represent plate-spreading directions, red solid bars represent azimuthal anisotropy, black dotted circles indicate the approximate location of the Oldest-1 Array. The old ridge axes are shown as blue solid lines with age indicated.

the time changes in LPO of aggregates of crystals are traced along a streamline from the base to a target position (Kaminski et al., 2004). Then, using the obtained LPO at the target position and the experimentally-derived elastic tensor of single olivine and enstatite crystals at the pressure of 3 GPa and the temperature of 1400 °C, the elastic tensor of a polycrystalline is obtained by applying Voigt average. Assuming vertically incident and horizontally polarized S-waves, which is equivalent to azimuthal anisotropy of V_{SV} within a horizontal plane, the polarization direction and propagation velocity of the fast and slow S-waves ($V_{S,fast}$ and $V_{S,slow}$) are calculated from the elastic tensor of the polycrystalline by solving the Christoffel equation, and the azimuthal anisotropy is obtained as $(V_{S,fast} - V_{S,slow})/(V_{S,fast} + V_{S,slow})$ with the fastest direction along the polarization direction of fast S-waves. No viscosity change within the model space is assumed. The result has not changed significantly even when the viscosity was given a temperature dependence which assumes a plate model (Parsons and Schlater, 1977) with a potential temperature of 1350 °C and a plate thickness of 95 km.

Figure 6.15 shows results of the simulated azimuthal anisotropy. The black dotted circle indicates the approximate location of the Oldest-1 Array, and according to the simulation results, the azimuthal anisotropy within the array should be almost uniform. This prediction differs from the observations (Figure 6.14), suggesting the early dynamics of the Pacific Plate may have been more complex than the assumed simple model. For example, several fracture zones exist around and within the observation area. Ogasawara Fracture Zone is recognizable as a sudden large jump of 160-Ma isochrones around 19°N in Figure 6.14. This suggests a possibility that there is a variation in the spreading rate along the past ridge axis. Some studies predict somewhat complex evolutionary processes which involve the change from a ridge-ridge-transform to a ridge-ridge-ridge triple junction (Handschum et al., 1988; Boschman and van Hinsbergen, 2016) rather than the simplest and an end-member-like model assumed in this study. However, since those complexities have not yet been well-constrained, I do not further complicate the model to explain the observations.

Future analysis of geophysical data from an array, the Oldest-2 Array, which will cover the ancient Pacific-Farallon ridge and the large portion of the Pacific triangle, will help to reveal the entire picture of the early stages of the Pacific plate evolution.

Alternatively, the observed azimuthal anisotropy may not completely represent the early Pacific evolution history but a result of disturbances associated with subsequent volcanic activities (Section 1.5.3). As summarized in Section 1.5.3, the large portion of the oldest Pacific seafloor has experienced Cretaceous volcanic activities. LIP products covering the EMB and PB are formed by ocean basin flood basalt (Coffin and Eldholm, 1994), which less alters the pre-existing crust compared to the formation of off-axis oceanic plateaus (Coffin et al., 2006). This is supported by the observations of Jurassic oceanic crust at ODP Site 801 and the crustal structures with the thickness of 7–8 km (Abrams et al., 1993; Kaneda et al., 2010; Stadler and Tominaga, 2015). The mantle plumelets that formed the seamounts and other volcanic features (Kopper et al., 2003; Stadler and Tominaga, 2015) could have existed beneath the Oldest-1 Array and have altered the pre-existing crustal and mantle structures. However, the crustal structure beneath the Oldest-1 Array was consistent with that of normal oceanic crust (Abrams et al., 1993). It is unlikely that only the mantle was affected by the Cretaceous volcanism and the crustal structure was unaffected. Therefore, the disturbance due to the plumelets might be not significant in the lithosphere, although the disturbance may largely depend on the spatial distribution geometry of the stems of plumelets originating from the main magma body in the mantle.

6.6.3 Implications from radial anisotropy

Table 6.1 shows a summary of the estimated radial and azimuthal anisotropy. Radial anisotropy is strong beneath the Oldest-1 Array. Radial anisotropy, combined with azimuthal anisotropy, is a key to addressing mantle shearing. Depending on the mantle condition such as temperature, stress, water content, and partial melt, crystal deformation occurs in a different slip system, which is defined by a combination of a slip plane and a slip direction (e.g., Karato et al., 2008). Different slip systems of olivine result in six different and characteristic LPO: A-, B-, C-, D-, E-, and AG-type LPOs (e.g., Mainprice, 2010; Karato et al., 2008; Michibayashi, 2008). In a conventional view, A-type olivine is believed to be dominant in the upper mantle, but a recent seismic study in the 70-Ma seafloor suggests that the upper 7 km mantle is likely to be D-type rather than A-type (Russell, 2021). It is also proposed that fabric-type transition will be induced by high water contents and results in C- or E-type fabrics distributed within the asthenosphere (Karato et al, 2008). Therefore, identifying the LPO type is key to understanding the mantle properties.

Seismic anisotropy provides the most direct and feasible estimations in the LPO types of the real mantle. Different LPO types will result in different magnitudes of radial and azimuthal anisotropy (Figure 6.16). For example, according to Karato et al. (2008) and/or Russell (2021), under horizontal shearing, A-type olivine fabric shows strong radial anisotropy ($RA_S > 0$) with weak azimuthal anisotropy, C-type olivine fabric shows weak radial anisotropy with V_{SH} larger than V_{SV}

($RA_S < 0$), D-type olivine fabric shows moderate radial ($RA_S > 0$) and azimuthal anisotropy, and E-type olivine fabric shows weak radial anisotropy ($RA_S > 0$) with strong azimuthal anisotropy. Karato et al. (2008) and Russell (2021) have complied the relation between azimuthal and radial anisotropy associated with different LPO under horizontal shearing using laboratory experiment deformation and natural samples (Figure 6.16). Compared to their results, the Lid and LVZ beneath the Oldest-1 Array are likely to be comprised of A-type LPO, except the Lid beneath the western array is consistent with both A- and D-type LPO. Water-induced C- and E-type LPO only results in ξ that is smaller than one or larger than one with a small fraction (Figure 6.16), which is not consistent with the observations. Therefore, the LVZ beneath the Oldest-1 Array supports the conventional view of LPO type rather than the water-rich asthenosphere-related C- or E-type LPO (Karato et al., 2008).

The above discussion assumed horizontal shearing. The eastern array is close to the past triple junction, thus the past flow field might have been complicated, and the axis of the LPO may be not confined in a horizontal plane but it may have an oblique axis. As a result, it may result in apparently weak azimuthal anisotropy and strong radial anisotropy. Since the two arrays are close to each other, the observed difference between the two arrays may only be confined to the shallow part which reflects the early evolution process of the Pacific plate. By combining the results from azimuthal anisotropy, mantle simulation, and rheological considerations, as well as the results of the Oldest-2 Array, the dynamics of the birth of the Pacific plate is expected to be unraveled.

Table 6.1: Comparison of estimated magnitudes of radial (ξ) and azimuthal ($2A_2$) anisotropy

	western array		eastern array	
	RA_S (%)	$2A_2$ (%)	RA_S (%)	$2A_2$ (%)
Lid (Moho-60 km)	3.4±1.1	3.2±0.8	7.5±1.0	1.6±0.8
LVZ (60-240 km)	3-8	1.1±0.5	2-7	1.1±0.5

$RA_S = (V_{SH}/V_{SV} - 1) \times 100$
$2A_2$: Peak-to-peak intensity of azimuthal anisotropy

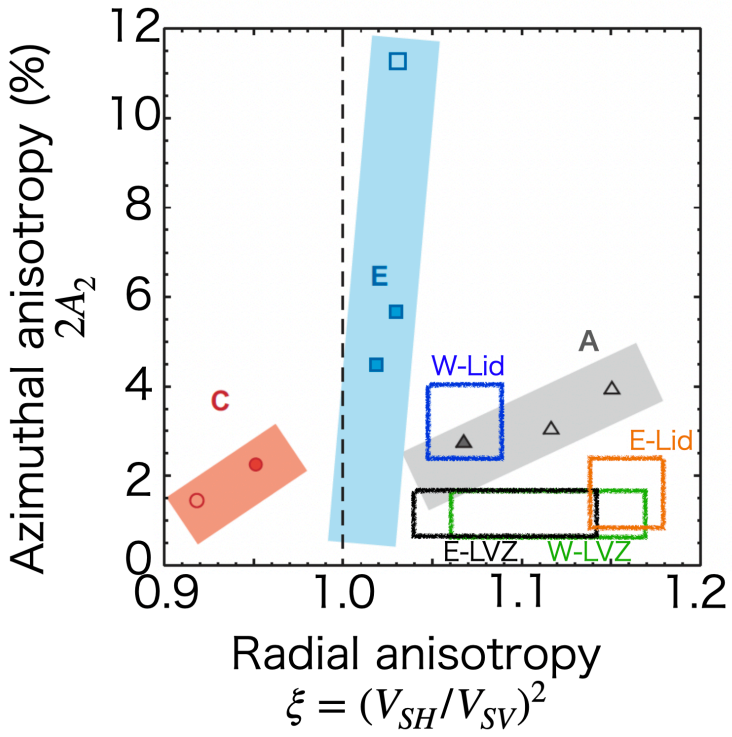

Figure 6.16: Seismic anisotropy of A- (gray), C- (orange), and E-type (blue) olivine LPO. Figure is taken from Karato et al. (2008) with some modifications. ξ is related to RA_S as $RA_S = (\sqrt{\xi} - 1) \times 100$. The anisotropy estimated in the Oldest-1 Array is shown as four open boxes: E-Lid and W-Lid indicate the Lid anisotropy in the eastern and western arrays, respectively, and E-LVZ and W-LVZ indicate the LVZ anisotropy in the eastern and western arrays, respectively.

Chapter 7

Conclusions and future directions

7.1 Summary of this thesis

This thesis first improved the broadband surface-wave array analysis technique by overcoming three technical challenges: (1) high-noise levels at low-frequency BBOBS records, (2) unstable high-frequency phase velocity measurement via seismic interferometry, and (3) mode interference in low-frequency Love waves. Then, I applied the improved method to the seismic data recorded by an array of broadband ocean bottom seismometers (BBOBSs) deployed on the oldest Pacific seafloor (Oldest-1 Array).

The Oldest-1 Array is comprised of 12 seismic stations and seven electro-magnetic stations. It is designed to unravel the lithosphere-asthenosphere system beneath the oldest Pacific seafloor to advance understanding of the evolution process of the Pacific plate and the sub-lithospheric dynamics. In order to achieve the goals of the Oldest-1 Array, it is necessary to constrain the shear-wave velocity structure from the crust to the depth of 300 km where the bottom of the low-velocity zone (LVZ) exists, as well as constraining the azimuthal and radial anisotropy to investigate the past and current mantle flow field. Broadband surface-wave array analysis which combines seismic interferometry and teleseismic waveform analysis is a strong tool to achieve the goals of the Oldest-1 Array because it provides broadband surface-wave phase velocities and quantitatively constrains a continuous structure from the crust to the depths within the asthenosphere directly beneath the focused BBOBS array with a higher spatial resolution compared to the global tomography.

There, however, remains several technical challenges, and I focused on three of them in this thesis. (1) Due to the significant low-frequency noise in the BBOBS records, surface-wave phase velocities can be measured only up to a frequency of 0.01 Hz and can only constrain the structure to depths of 150–200 km in previous studies conducted by the Japanese group (e.g., Takeo et a., 2018). Although Crawford and Webb (2000) established the noise reduction procedure, it has not yet been established to BBOBS developed in Japan. (2) In order to reveal the early evolution process of the Pacific plate, it is necessary to constrain the structural variations quantitatively within the array at shallow depths (<50 km), meaning that phase velocities have to be measured with a small

number of stations. Thus, a more stable phase-velocity measurement is required compared to the previous study. (3) The measurement of low-frequency (<0.03 Hz) Love-wave phase velocities has typically been avoided due to technical difficulties associated with mode interference, so the radially anisotropic structure has rarely been constrained. However, radial anisotropy is essential for understanding mantle convection and mantle temperature structure.

Therefore, it is required to (1) reduce low-frequency noise from the BBOBS seismograms and extract low-frequency (0.005–0.01 Hz) teleseismic waveforms to constrain structure at the depth range of 200–300 km, (2) improving the high-frequency dispersion array measurement technique to resolve the structural variation within the array at shallow depths (<50 km) where the early evolution process of the Pacific plate is recorded, and (3) developing the method of low-frequency Love-wave dispersion array measurement to constrain the radial anisotropy within the Moho to the depths within the asthenosphere.

In Chapter 2, I established the procedure to remove the tilt and compliance noise from the low-frequency vertical component seismograms recorded by BBOBSs developed in Earthquake Research Institute by modifying pre-existing noise reduction method developed by Crawford and Webb (2000) and Bell et al. (2015). The tilt noise originates from the seafloor current and imperfect leveling of seismic sensors (i.e., the discrepancy between the sensor's vertical axis and the gravitational direction; θ), resulting in high coherence between the vertical and horizontal component seismograms. I estimated the θ by calculating the noise transfer function from the horizontal to vertical component records and removed coherent horizontal noise from the vertical component seismograms by aligning the sensor's vertical axis along the gravitational direction. Then, I removed compliance noise that originates from the loading on the seafloor due to the seafloor pressure perturbation. Similar to the tilt noise, using the noise transfer function from the pressure to vertical component records, the compliance noise in the vertical component seismograms was estimated and removed. Noise-reduced vertical component seismograms were about 20 dB quieter than original seismograms at frequencies lower than ∼0.03 Hz. I successfully extracted low-frequency (<0.01 Hz) teleseismic Rayleigh waves, which are essential to infer the shear-wave velocity structure at depths deeper than ∼200 km.

In Chapter 3, I measured Rayleigh- and Love-wave phase velocities (including azimuthal anisotropy) at a frequency range of 0.04–0.2 Hz and 0.1–0.2 Hz, respectively, via ambient noise cross-correlation analysis. In the previous study (Takeo et al., 2014), a dispersion curve was smoothed by expressing it as a series of spline functions to stabilize the measurement. However, when spline functions are used as basis functions, unrealistic peaks and troughs are likely to appear due to the dependence of dispersion curves on the knot intervals of the spline functions. In this study, the multi-mode dispersion curves were directly calculated from a shear-wave velocity structure and measured via waveform fittings. Consequently, more physically appropriate dispersion curves were obtained, and more stable measurements were realized with a small data set compared to the previous study.

The phase-velocity measurements using ambient noise cross-correlation functions typically as-

sume homogeneously and randomly distributed noise sources around stations. The existence of a localized source that generates persistent signals, such as a volcano, may bias the phase-velocity measurement, thus it is essential to understand the origin of the signal. Therefore, in this chapter, I introduced not only the phase-velocity measurement as described above but also showed an example of analysis of a localized source that generates persistent long-period (18 s and 25 s) signals. I conclusively estimated the multiple signal sources located beneath a volcano about 1000 km away from a BBOBS array deployed at the south of the Oldest-1 Array.

In Chapter 4, I measured low-frequency (0.005–0.04 Hz) Rayleigh-wave phase velocities (including azimuthal anisotropy) via teleseismic waveform analysis using the noise-reduced vertical component BBOBS seismograms obtained in Chapter 2. The propagation of low-frequency (0.005–$\sim$0.015 Hz) Rayleigh waves are much clearer in the noise-reduced seismograms since the noise level had been about 20 dB quieter than the original seismograms. Hence, I was able to measure the phase velocity in a broader frequency range (0.005–0.04 Hz) compared to that of the previous study, which measured only at frequencies higher than 0.01 Hz (Takeo et al., 2018). Rayleigh-wave phase velocities at a frequency range of 0.005–0.01 Hz are essential to resolve the V_{SV} structure to a depth of 300 km to constrain the bottom of the LVZ.

In Chapter 5, I developed a method to measure fundamental-mode Love-wave (0T-mode) phase velocities at a frequency range of 0.01–0.03 Hz via teleseismic waveform array analysis using seafloor records. Although there are several well-established array analysis methods of measuring Rayleigh-wave phase velocity, the measurement of Love-wave phase velocity has been avoided due to technical difficulties. Due to the characteristics of the oceanic crust and mantle structure (thin crust and the well-developed LVZ), different modes of Love waves arrive at the observation points with similar travel times and overlap with each other, causing mode interference. Thus, if Love waves are analyzed in the same manner as Rayleigh waves without any special care, which assumes the observed waveforms as the 0T mode, the higher modes may bias the measured 0T-mode phase velocity. In this study, I attempt to reduce the bias in the 0T-mode phase-velocity measurement by regarding the observed Love waves as a summed-wave of the fundamental and the first higher modes, which have relatively large amplitudes compared to the other modes. The bias in the 0T-mode phase velocities due to the presence of the higher modes was successfully reduced from $\sim$3 % to $\sim$1 % for the synthetic data, confirming the effectiveness of the method. The developed method was applied to the teleseismic Love waves recorded by the Oldest-1 Array. I measured the average 0T-mode phase velocities at a frequency range of 0.01–0.03 Hz. The total measurement uncertainty was about 1.5%, which accounts for the bias ($\sim$1 %) due to the presence of unaccounted second and higher modes and the measurement errors ($\sim$0.5 %).

Overall, I measured Rayleigh- and Love-wave phase velocities at a frequency range of 0.005–0.2 Hz and 0.01–0.2 Hz, respectively. In Chapter 6, I inverted the broadband phase velocities into one-dimensional isotropic, azimuthally, and radially anisotropic shear-wave velocity structures to discuss the lithosphere-asthenosphere structure beneath the oldest Pacific seafloor. The isotropic structures were estimated from the crust to the depth of 300 km using only Rayleigh-wave phase

velocities. The high-velocity Lid and the underlying LVZ are well-resolved. In particular, the bottom of the LVZ at depths of 200–300 km is well-constrained because the usable low-frequency teleseismic signals were extracted in Chapter 2. The azimuthally anisotropic structure was estimated from the Moho to the depth of 300 km using Rayleigh-wave phase velocities. In particular, the difference between the western and the eastern arrays of the Oldest-1 Array at depths shallower than 50 km is well-resolved: the peak-to-peak intensity is ∼3.7 % and the fastest direction is quasi-perpendicular to the predicted past seafloor spreading direction in the western array, whereas the peak-to-peak intensity is ∼1.6 % and the fastest direction largely deviates from the predicted past seafloor spreading direction in the western array. The difference is dominantly constrained by the high-frequency phase velocities measured in Chapter 3. At depths deeper than 50 km, the peak-to-peak intensities of azimuthal anisotropy are weak (∼1 %), and the fastest direction is oblique from the absolute plate motion. I used both Rayleigh- and Love-wave phase velocities measured in Chapters 4 and 5 to constrain the radially anisotropic structure, which has two layers (Moho–60 km and 60–240 km) that correspond to the Lid and the LVZ. Within the Lid, the difference between the western and the eastern arrays is again well-resolved: the radial anisotropy ($RA_S = (V_{SH}/V_{SV} - 1) \times 100$) is 3.4±1.1 % in the west and 7.5±1.0 % in the east. Due to the large measurement uncertainties, the estimated radial anisotropy has large uncertainties with the average value of RA_S to be 4–5 %.

The estimated isotropic shear-wave velocity ($V_{SV} = V_{SH}$) structure, as well as Rayleigh-wave phase velocities, are compared to the previous study (Takeo et al., 2018), which investigated 130- and 140-Ma mantle beneath the 'normal' seafloor in the northwestern Pacific. The comparison revealed that velocity difference among three different ages (130, 140, and 170 Ma) in the LVZ could not be solely explained by the cooling associated with the age differences. Assuming that the 140-Ma mantle follows a half-space cooling (HSC) model (Takeo et al., 2018), the observed Oldest-1 phase velocity is about 1 % slower than the 170-Ma HSC model at a frequency range of about 0.01–0.02 Hz. The discrepancy from the HSC model prediction suggests that additional thermal mechanisms such as small-scale convection (Richter and Parsons, 1975) may be required within the LVZ beneath the oldest Pacific seafloor.

The azimuthal anisotropy in depths shallower than 50 km was significantly different between the western and eastern arrays, which may reflect the dynamics of the birth of the Pacific plate. By mantle simulation, I estimated spatial variations in azimuthal anisotropy due to lattice-preferred orientation of mantle materials resulting from the spreading of three plates involving a ridge-ridge-ridge triple junction. The azimuthal anisotropy in shallow depths within the Oldest-1 Array obtained in the simulation are parallel to the spreading direction, and there was no variation in azimuthal anisotropy that would explain the observed differences within the array. The result means that the early evolution process of the Pacific plate is more complicated than the assumed simple model. Although further constraints are difficult due to the limited observations, the deployment of the Oldest-2 Array, which covers a large portion of the oldest seafloor at the east of the Oldest-1 Array, will help to reveal the dynamics of the birth process of the Pacific plate

in more details. The constraints may make the global plate reconstruction more accurate and/or shed light on the evolution process of other oceanic plates.

The azimuthal and radial anisotropy is used to constrain the olivine fabric types beneath the Oldest-1 Array. The strong radial anisotropy with weak azimuthal anisotropy is observed within the LVZ, which is likely to be consistent with A-type olivine fabric assuming the horizontal shearing. The Lid in the western array is likely to be consistent with both A- and D-type olivine fabrics. The radial anisotropy in the eastern array is anomalously strong with $V_{SH} > V_{SV}$, and the azimuthal anisotropy is also anomalously weak compared to the previous studies. The observed anisotropy may not result from the horizontal shearing but an apparent anisotropy of the tilted LPO axis fixed under the disturbance of upwelling associated with the ridge-ridge-ridge triple junction.

7.2 Possible future improvements

Although this thesis has largely improved the broadband surface-wave array analysis, there is still room for improvement. I discuss the potential improvements below.

In Chapter 2, I fitted a cubic function to the pressure-to-vertical transfer function to obtain a smooth transfer function which was used for compliance-noise removal. In the future, instead of the cubic function, I may estimate the smoothed transfer function by directly calculating from a structure. The pressure-to-vertical transfer function, the seafloor compliance, depends on the sediment and crustal structure. Using a structure, I can put a natural *a priori* constraint on the transfer function, where the concept is the same as Chapters 3–5. The seafloor compliance should also be used to infer the structure (Ruan et al., 2014; Bell et al., 2015). It can provide complementary information to surface waves because the seafloor compliance is more sensitive to sediments and upper crust than the first higher-mode Rayleigh waves at a frequency range of 0.1–0.2 Hz analyzed in this study.

Furthermore, in the future, it will be more and more important to reduce the low-frequency noise on horizontal component seismograms recorded by BBOBSs. The success in noise reduction is useful for array analysis and has a broad impact in other analyses such as seismic tomography and receiver function analysis. The development of instruments such as BBOBS-NX has reduced the horizontal component noise level by more than 20 dB at frequencies lower than 0.05 Hz (Shiobara et al., 2013). At the present stage, an ROV is needed for the deployment and recovery of BBOBS-NX and thus BBOBS-NX is not suitable for observations requiring 10–20 stations, but BBOBS-NX will become more common with future automation. The seafloor current is believed to be the dominant noise source on horizontal component seismograms, but the nature and origin of the horizontal noise are still not yet clear. There may be not only tilt noise but also horizontal compliance noise in the horizontal component seismograms, which is observed in offshore California and near Hawaii (Doran et al., 2016). A better understaing of noise on horizontal component seismograms may be important for future noise reduction. Recently, methods to reduce random noise from vertical and horizontal component BBOBS seismograms have been developed and about 10–20 dB reduction

is achieved at all frequencies (Negi et al., 2020). However, the noise level is still much higher than that of the vertical component, and it will be necessary to achieve a more drastic noise reduction in the future.

In Chapter 5, in order to measure array-averaged fundamental-mode Love-wave phase velocity, I simultaneously determined phase velocity outside the array, which was averaged along the source-array path, and phase velocity inside the array. However, these phase velocities have a significant trade-off. In the future, I may utilize results of global tomography, which is expected to be less influenced by the mode interference (Nettles and Dziewonski, 2011), as a reference for the source-array phase velocity to narrow the search range of the global search. In addition, after the investigation of how many overtones impact the measurement, second and higher modes should be included in the analysis and hopefully measured. Since the fundamental mode is mainly sensitive to shallow structures (crust and uppermost mantle), higher-mode phase velocity, which is more sensitive to deeper structures, would provide complementary information and allow us to determine the structure in more detail. Since I used the structure, the inclusion of second and higher modes may be achieved with a relatively small increase in the number of parameters.

Additionally, it was found that phase-velocity measurement is likely to be easier if mode-interference patterns (i.e., amplitude variations within the array) are visible and/or various combinations of interstation distances are used. In future observations, the mode-interference patterns may be more detectable by adding land observation points near the BBOBS array. Furthermore, the station distribution and array size may be important factors and should be investigated in future observations.

It is also important to jointly analyze surface waves extracted from the ambient noise cross-correlation functions and teleseismic waveforms. Transverse-transverse component NCFs have a sharp amplitude reduction at a frequency range of 0.05–0.1 Hz. The amplitude reduction is thought to reflect the energy deficiency of the fundamental mode due to the oceanic crustal and LVZ structure (Takeo et al., 2015 SSJ). Thus, joint analysis of the amplitude changes of NCFs and teleseismic waveforms will provide better constraints on the crust and mantle structure than that of this study.

In the future, if sufficient noise reduction for the horizontal component BBOBS seismograms is achieved, it is possible to select the teleseismic waveforms with various thresholds. The relative amplitude of higher modes varies with the source depth, and the events used in this study whose focal depths are 10–20 km are particularly prone to excite higher modes. If the events can be selected according to their focal depths, it will be easier to avoid the contamination of undesired modes. Moreover, if the number of events is sufficient, the Love-wave azimuthal anisotropy can also be determined.

7.3 Broader contributions of this thesis

This thesis improved broadband surface-wave array analysis by overcoming three technical challenges and estimated isotropic, azimuthally and radially anisotropic shear-wave velocity structures, which are all essential to elucidate the nature of the lithosphere-asthenosphere system. I not only extended the limitation of the resolution in the depth of the V_{SV} structure by extracting useful low-frequency teleseismic waveforms, but I also estimated radially anisotropic structure from the Moho to a depth of 240 km, which was previously rarely investigated at focused BBOBS arrays. In the future, comparisons between seismological observations and laboratory rheological experiments can be made by using three types of structures. Hence, a bridge between seismology and rheology has been established. In addition, we are now ready to test the hypothesized mantle structure that could not be verified due to a lack of Love-wave observations. More BBOBS arrays will be deployed in the Pacific Ocean under international cooperation. By estimating isotropic, azimuthally and radially anisotropic structures at each of the arrays, the oceanic lithosphere-asthenosphere system will be comprehensively constrained, and the variety of mantle dynamics will be unraveled.

In the future, by further combining the technical improvement of the Love-wave phase-velocity measurement and the noise reduction for horizontal component seismograms, the radial anisotropy will be determined in much higher resolution both vertically and horizontally. Then, the unknown nature of the lithosphere-asthenosphere system will be revealed, and those will unquestionably have a game-changing impact on Earth science. This thesis might be the first step to achieving it.

Appendix A

Chapter 2 Supplementary Material

A.1 Station information at offshore Miyagi

The locations of instruments deployed at offshore Miyagi (cruise report for KR15-14) are shown in Table A.1 and Figure A.1. The BBOBS is the one developed by Earthquake Research Institute.

Table A.1: Summary of the station information

	Latidute	Longitude	Depth
BBOBS	38°15.035'N	143°34.983'E	3394 (m)
Current meter	38°15.065'N	143°35.094'E	3405 (m)

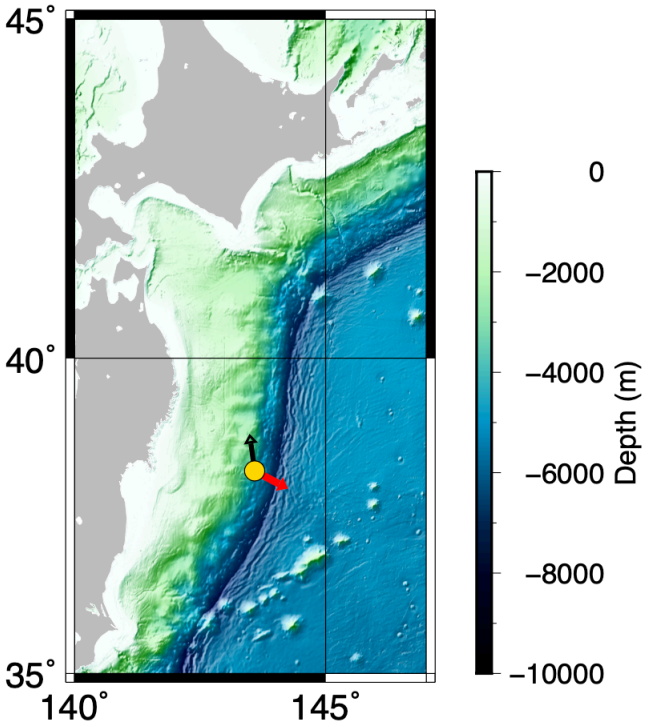

Figure A.1: Station map of the BBOBS and the current meter deployed at offshore Miyagi. The yellow circles are the locations of the BBOBS and the current meter. Two instruments are only 300 m apart and cannot be distinguished in the plotted scale. The black arrow indicates the coherent orientation. The red arrow indicates the flow direction. Both coherent orientations and the flow directions are measured from the north.

A.2 Comparison of noise power-spectral densities recorded at offshore Miyagi and the Oldest-1 Array

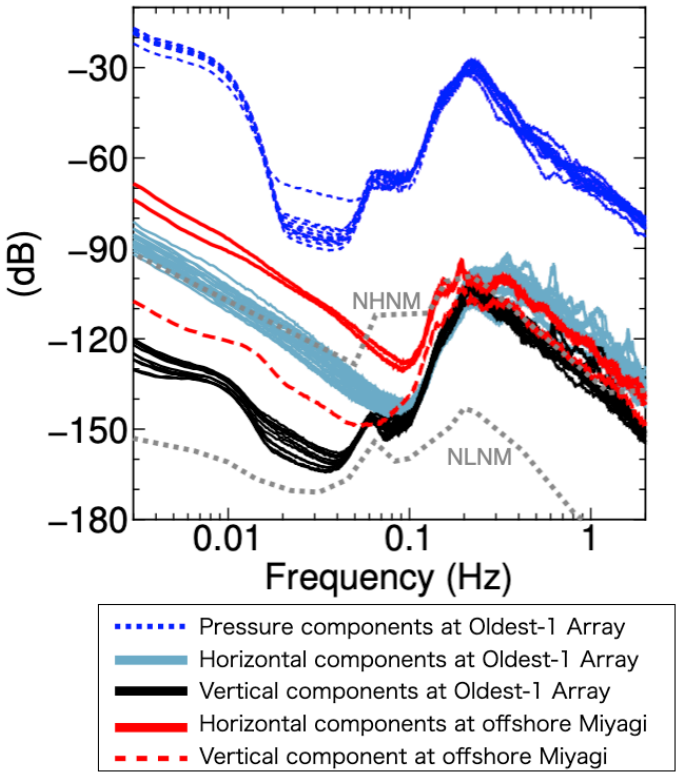

Figure A.2: Noise power-spectral densities of each station within the Oldest-1 Array and at offshore Miyagi. The dashed gray lines are new high and low noise models that represent the upper (NHNM) and lower (NLNM) bounds of noise levels recorded on the land (Peterson, 1993). I first obtain Fourier-transformed 2000-s long section ($H_i(\omega)$ and $Z_i(\omega)$ in equation 2.1) and calculate daily averaged power spectra. Then at each frequency, the median is obtained from the aggregate of daily calculated values.

A.3 Coherence between the horizontal and vertical components at Oldest-1 Array

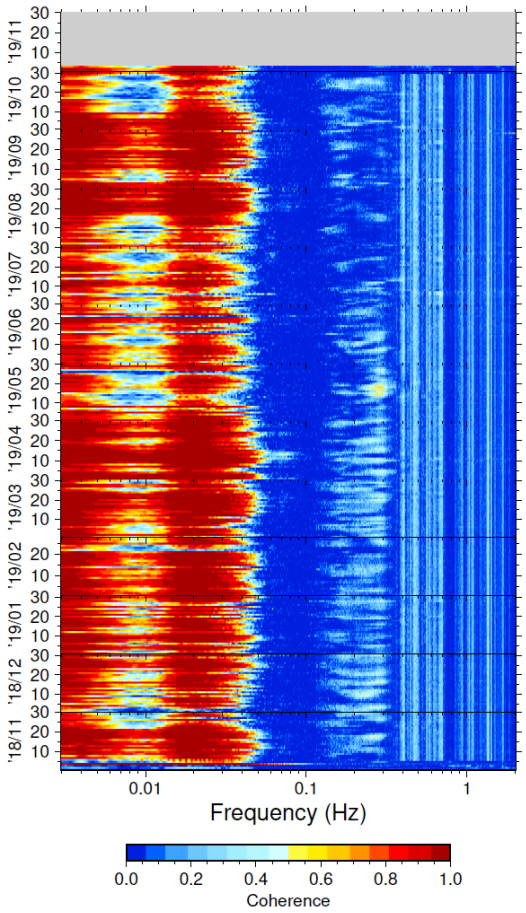

Figure A.3: Squared coherence between the horizontal and vertical component seismograms as a function of time and frequency recorded at OL08 in the Oldest-1 Array.

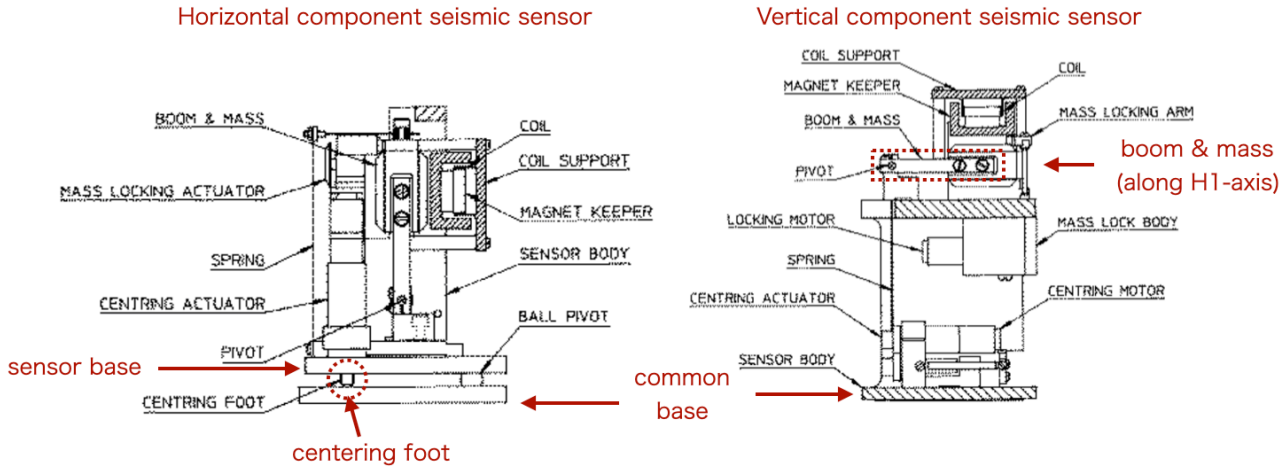

Figure A.4: Horizontal and vertical component CMG-3T sensors. Figure is taken from https://www.guralp.com/documents/MAN-030-0001.pdf with some modifications colored in red.

A.4 Difference between the horizontal and vertical components in BBOBSs used in this study

Here I describe the difference in the accuracy of the axis for each component relative to the axis defined by the gravitational direction. I detail the performance of the CMG-3T installed in BBOBSs developed by Earthquake Research Institute (Japanese-type BBOBS), which was used in the Oldest-1 Array. CMG-3T has three independent seismic sensors (H1, H2, and, Z components) set on a common base (Figure A.4). When CMG-3T starts to operate, the Gimbal system, which has been developed by Earthquake Research Institute, will first adjust the level of the common base of CMG-3T sensors (Levelling). However, a small misalignment (θ) between the gravitational axis and the leveling-defined sensor vertical axis will remain. Then, each component of CMG-3T adjusts its mass position to the center (Centering). The accuracy of the Centering is the same for all three components (3×10^{-3} degrees), but the process of Centering is different between the vertical and horizontal components. In the case of the H1 and H2 components, Centering is achieved by leveling the sensor base of each component by moving the centering foot at the sensor base (Figure A.4). Thus, after leveling, the misalignment felt by H1 and H2 components are sufficiently small, as same as the accuracy of the Centering. On the other hand, in the case of the Z component, the Z component does not adjust the sensor base but takes the sensor vertical axis, which is tilted from the gravitational axis, as a reference axis and Centering occurs along that axis. Therefore, unlike H1 and H2 components, the misalignment between the gravitational axis and the sensor vertical axis is the same as that defined by Levelling, that is θ.

A.5 Estimation of the pressure-to-vertical transfer function

This section introduces the different methods of calculating the pressure-to-vertical (P-to-Z) transfer function. In the main text, the amplitude and phase of the transfer function with small errors are averaged at each frequency to obtain the average amplitude and phase. Then the average amplitude and phase are fitted by cubic functions ($A^{rep}(\omega)$ and $\phi^{rep}(\omega)$) to obtain a representative transfer function ($D^{rep}(\omega)$). Since the transfer function is a complex number, it can also be divided into real and imaginary components. In this section, I calculate the transfer function using the real and imaginary components to see whether the different combination of data results in any differences in the transfer function. The estimation is done similarly to that in the main text. I first extract real and imaginary components whose fractional uncertainties are smaller than 7 % ($R^d(\omega)$ and $I^d(\omega)$, respectively, where d denotes for a day). If there are more than 30 of such data points at a frequency, I obtain average of the aggregates of the real and/or imaginary component data ($R(\omega) = \sum_{d=1}^{N} R^d(\omega)$ and $I(\omega) = \sum_{d=1}^{N} I^d(\omega)$, respectively, where N is the number of days). Then, I fit the average transfer function using cubic functions and obtain the representative P-to-Z transfer function ($R^{rep}(\omega)$ and $I^{rep}(\omega)$).

Figure A.5 shows the comparison between the transfer function estimated using amplitudes and phases (black) and the transfer function estimated using real and imaginary components (blue). The real and imaginary components are converted to amplitude and phase. The amplitude of the two differently estimated transfer functions agrees well. Contrarily, the phase is different at frequencies lower than 0.003 Hz and between 0.02–0.03 Hz. Those differences may arise because data used for fitting only exists in the frequency range of about 0.003–0.015 Hz, and the transfer function has been extrapolated at the rest of the frequency range. Thus, the slight differences in 0.003–0.015 Hz may affect the results at frequencies where extrapolated. I believe that these differences do not significantly influence the results. This study only analyzed data up to 0.005 Hz, so the difference at frequencies lower than 0.003 Hz does not affect the results. At the frequency range of 0.02–0.03 Hz, a cosine taper is applied to the admittance and the amplitude is suppressed. Additionally, at this frequency range, the wavelength of water waves becomes short and does not reach the seafloor, and thus the amplitude of compliance noise becomes small. Therefore, the difference between two differently estimated transfer functions may not be significant.

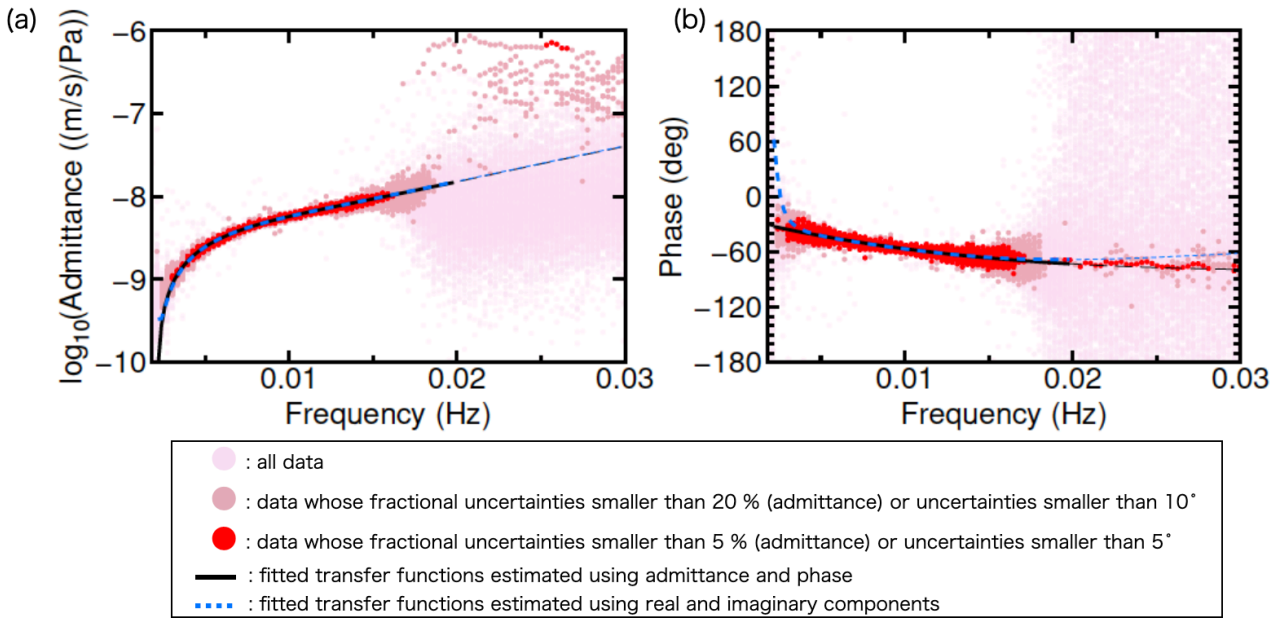

Figure A.5: Same as Figure 2.11. Amplitude and phase converted from the transfer functions estimated using real and imaginary components (blue dashed line) are added.

Appendix B

Chapter 3 Supplementary Material

B.1 List of seismic stations used in Section 3.2

OJP Array was deployed on and around the Ontong Java Plateau, which is the most voluminous Large Igneous Provinces in the ocean to investigate the crust and mantle structure beneath the plateau (Suetsugu et al., 2018). The array comprised of 23 ocean bottom seismometers and 20 ocean bottom electromagnetometers deployed between November 2014 to September 2017. Table B.1 summarises the station location of the OJP Array, which is used in Section 3.2. In addition, I analyzed some land recorded data downloaded from IRIS and OHP DMC. Those data are shown in Table B.2. Data are downloaded from ANSN, GEOSCOPE (https://doi.org/10.18715/GEOSCOPE. G), IRIS/IDA (https://doi.org/10.7914/SN/II), IRIS/USGS (https://doi.org/10.7914/SN/IU), Pacific 21, and Vanuatu Seismic Network.

Table B.1: Summary of the stations in the OJP Array

Station code	Latitude (°)	Longitude (°)	Depth (m)	
seafloor stations				
OJ01	4.996	147.005	4275	×
OJ02	2.038	146.991	4486	○
OJ03	0.059	147.035	4486	○
OJ04	4.450	150.383	3987	○
OJ05	-0.615	153.002	4337	○
OJ06	-4.973	156.045	1491	○
OJ07	-1.971	155.997	1743	△
OJ08	0.036	156.000	1959	○
OJ09	2.022	156.007	2583	○
OJ10	5.009	156.013	3608	×
OJ11	8.013	156.024	4875	○
OJ12	4.002	159.918	3756	○
OJ13	1.926	160.016	2948	○
OJ14	-2.148	159.927	2491	○
OJ15	-5.965	160.041	1813	○
OJ16	-6.417	163.417	3558	○
OJ17	-0.985	164.009	4435	×
OJ18	-3.889	166.708	3441	△
OJ19	-8.012	170.053	4860	○
OJ20	-2.946	174.991	5077	○
OJ21	0.026	170.005	4458	×
OJ22	2.871	166.026	4309	○
OJ23	6.954	164.497	5117	×
land stations				
CHUK	7.464	151.855		○
KOSR	5.287	163.017		○

○: stations used in this study
△: stations not used because electrical noise are observed during the entire observation period
×: stations not available because of hardware malfunctions

Table B.2: Summary of the land stations downloaded from the IRIS DMC and OHP DMC

Station code	Latitude (°)	Longitude (°)	Network code	DMC
ARMA	-30.418	151.629	AU	IRIS
COEN	-13.957	143.175	AU	IRIS
EIDS	-25.369	151.082	AU	IRIS
NFK	-29.043	167.939	AU	IRIS
NIUE	-19.076	-169.927	AU	IRIS
KDU	-12.687	132.473	AU	IRIS
LHI	-31.520	159.061	AU	IRIS
QIS	-20.558	139.605	AU	IRIS
QLP	-26.584	144.235	AU	IRIS
YNG	-34.298	148.396	AU	IRIS
FUTU	-14.308	-178.121	G	IRIS
NOUC	-22.099	166.307	G	IRIS
CAN	-35.319	148.996	G	IRIS
DZM	-22.072	166.444	G	IRIS
MBO	14.392	-16.955	G	IRIS
MSVF	-17.745	178.053	II	IRIS
CTAO	-20.088	146.255	IU	IRIS
KNTN	-2.774	-171.719	IU	IRIS
HNR	-9.439	159.948	IU	IRIS
PMG	-9.405	147.160	IU	IRIS
RAO	-29.245	-177.929	IU	IRIS
SNZO	-41.309	174.704	IU	IRIS
TARA	1.355	172.923	IU	IRIS
PATS	6.837	158.315	PS	IRIS
SANV	-15.447	167.203	VE	IRIS
AMB1	-16.283	168.124	VU	IRIS
MJR	7.060	171.212		OHP

B.2 Locating a local earthquake near the Ambrym island

In order to assess the robustness of the inferred source location of the persistent sources in the Ambrym island (Figures 3.2b,c), I perform the same source location estimation process for a local earthquake near the Ambrym island (Mw 5.8, 167.14°E, 16.29°S, a depth of 13.5 km on April 30, 2016, 8:35:48.5 UTC; the global CMT project). I define the time window for the earthquake starting at 1000 s before and ending at 2276.8 s after the origin time, and then cross-correlate the waveforms for each station pair. The estimated source location is 168.29°E, 16.46°S, showing about one-degree bias to the eastern direction. This bias may be caused by the lateral heterogeneity since the stations west of the estimated source location situate on the Australian Continent while the stations east of the estimated source location situate on the oceanic islands, resulting in the slower propagation on the western region compared to that of the eastern region. If I take this bias into account for the estimated source location of the 25 s signal, the location is 168.03°E, 16.48°S, which is close to the location of the station AMB1 (168.12°E, 16.28°S) in the Ambrym island.

B.3 Comparison of the power spectrogram for the 25 s signal in the Vanuatu Arc and the 26 s signal in the Gulf of Guinea

Based on the comparison of the power spectrogram for the 25 s signal obtained from SANVU, on the Vanuatu Arc, and the 26 s signal obtained from MBO, a part of the GEOSCOPE network situated on the African Continent, I believe the possible contamination on the 25 s signal by the 26 s signal is small. The strength of the 25 s signal is more time-variable compared to that of the 26 s signal (Figures 3.3a and S1a). For example, the power of the 25 s signal is intensified at the end of March 2016 while the 26 s signal does not show any similar intensifications (Figure B.1b). The result is consistent with Zeng and Ni (2014) which concluded that the two signal sources are independent. Considering that the estimated source in Vanuatu Arc is 18,500 km away from the previously estimated source in the Gulf of Guinea (Xia et al., 2013; Xia and Chen, 2020), the power of 26 s signal that should be observed at the Vanuatu Arc would be orders smaller than that of MBO. Besides, I believe that the antipodal focusing effect would not significantly affect the above discussion since the exact antipodal area of the Gulf of Guinea (Figure 5 in Shapiro et al., 2006) is deviated from our estimated source region (Figure 3.2a).

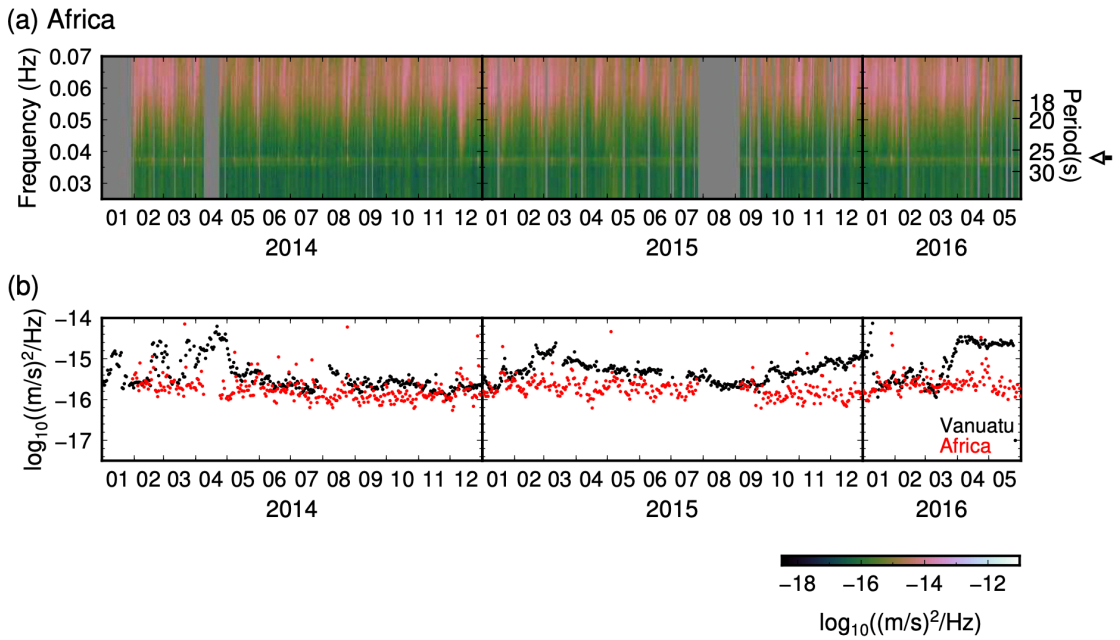

Figure B.1: (a) Power spectrogram of MBO on the African Continent. The black arrow indicates the position of 0.038 Hz (26 s). (b) A comparison of power spectral densities of 25 s signal observed at SANVU on the Vanuatu Arc (averaged in a frequency range of 0.038–0.042 Hz) and 26 s signal observed at MBO (averaged in a frequency range of 0.037–0.039 Hz).

B.4 Calibration of the instrument response for the station AMB1 using distant earthquakes

A comparison of the amplitude of distant earthquakes recorded at SANVU and AMB1 suggests that the instrument response of Guralp CMG-40T sensor at AMB1 provided by the IRIS DMC is likely to be incorrect. According to the IRIS DMC, the frequency response for AMB1 is flat to velocity from 1 Hz to 100 Hz. However, if I use the response to remove the instrument response, the amplitude of distant earthquakes, which are recorded at AMB1 and band-pass filtered between 0.01–0.02 Hz, is about two orders larger than that of SANVU located about 135 km away from AMB1 (Figure B.2a). Since a CMG-40T sensor is provided with several options for the lower-corner frequency, I try to find a more reasonable frequency response by adjusting it: If I assume the lower-corner frequency to be 0.1 Hz (10 s) (Figure B.2b and Table S1), the comparison of the amplitudes of distant earthquakes become reasonable (Figure B.2a). Besides, the Fourier spectra of ambient noise recorded at AMB1 become more consistent with that of SANVU at a frequency range of 0.1–0.3 Hz, where the secondary microseism exists (Figure B.2c). Even using the revised instrument response, the power at AMB1 is still orders larger than that of SANVU at the frequency lower than 0.1 Hz because the instrumental noise is enhanced by the instrument response correction.

As the above response calibration is done at a frequency range of 0.01–0.02 Hz, it is possible

that there exists some discrepancy between the real ground motion and response-corrected ground motion due to employed incorrect response correction and/or the physical site amplification/dis-amplification due to the difference in the local structure. I estimate this effect for a frequency range of 0.03–0.05 Hz, where our target signals reside at AMB1 and SANVU. Ten teleseismic earthquakes are selected based on the following criteria: (1) the epicentral distance is between 3,000–10,000 km, (2) the focal depth is shallower than 100 km, and (3) the magnitude is larger than or equal to 6.0. The selected seismograms are band-pass filtered between 0.03–0.05 Hz, and an 800 s-long seismogram that starts at a travel time for a group speed of 4.5 km/s, is prepared. For each earthquake-generated signal, a time-lag that maximizes the cross-correlation coefficient between AMB1 and SANVU is computed. The signals recorded by AMB1 and SANVU are shifted with the time-lag, and the amplitude ratio between two seismograms is computed. The average amplitude ratio is 0.33 that should be kept in mind whenever I discuss the amplitude for the two stations (Figures B.3a,b).

B.5 Comparison of the secondary microseism with the 25 s and 18 s signals

Figure B.4 shows the power spectrogram of AMB1 at the frequency range of 0.025–0.25 Hz. The time variation of power spectral densities for the 25 s and 18 s signals are not consistent with that of the secondary microseism (5–10 s). For example, the power at 0.2 Hz during the middle of July is higher than the rest of the days in July, whereas the power of the 25 s and 18 s signals in July does not show associated time variation.

B.6 Intensification of the 25 s signal associated with the 2015 eruption

A power spectrogram of the vertical component seismogram recorded at SANVU shows that the intensification of the 25 s signal power corresponds to the minor eruption on February 20, 2015 (Hamling and Kilgour, 2020). The 25 s signal power gets stronger and the dominant period becomes longer after the eruption (at about 30 hours after the Mw 6.4 earthquake). The 18 s signal seems to hide behind the primary microseism that is dominant at around 15 s. The spectrogram is computed using a 409.6 s-long time window with a 50 % overlap (Figure B.5).

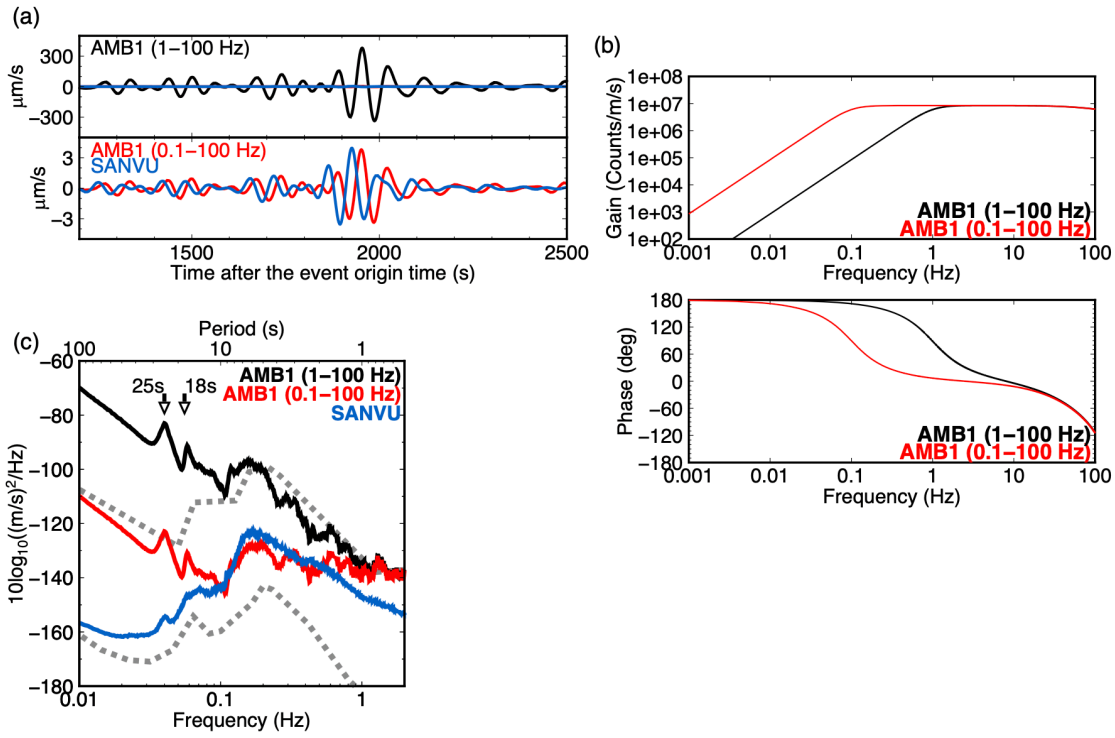

Figure B.2: Comparison of instrument response corrected velocity seismograms recorded by AMB1 and SANVU using two different frequency responses for AMB1. (a) Vertical component records of a distant earthquake (Mw 7.0 in the Aleutian Islands, August 30, 2013, at an epicentral distance of 61.9°) band-pass filtered between 0.01–0.02 Hz. The black and red seismograms represent records from AMB1 assuming the 1–100 Hz response and 0.1–100 Hz velocity flat responses, respectively. The blue seismograms represent the same waveform for SANVU. (b) The response curves of 0.1–100 Hz (red) and 1–100 Hz (black) velocity flat responses: gain (top) and phase (bottom) with total sensitivity referenced at 5 Hz, where the total sensitivity of AMB1 reported by IRIS (the 1-100 Hz response) is used for both cases. (c) The power-spectral density of ambient noise for SANVU (blue) and AMB1 with 1–100 Hz response (black) and 0.1–100 Hz response (red). The gray lines show New Low and High Noise Models (Peterson, 1993).

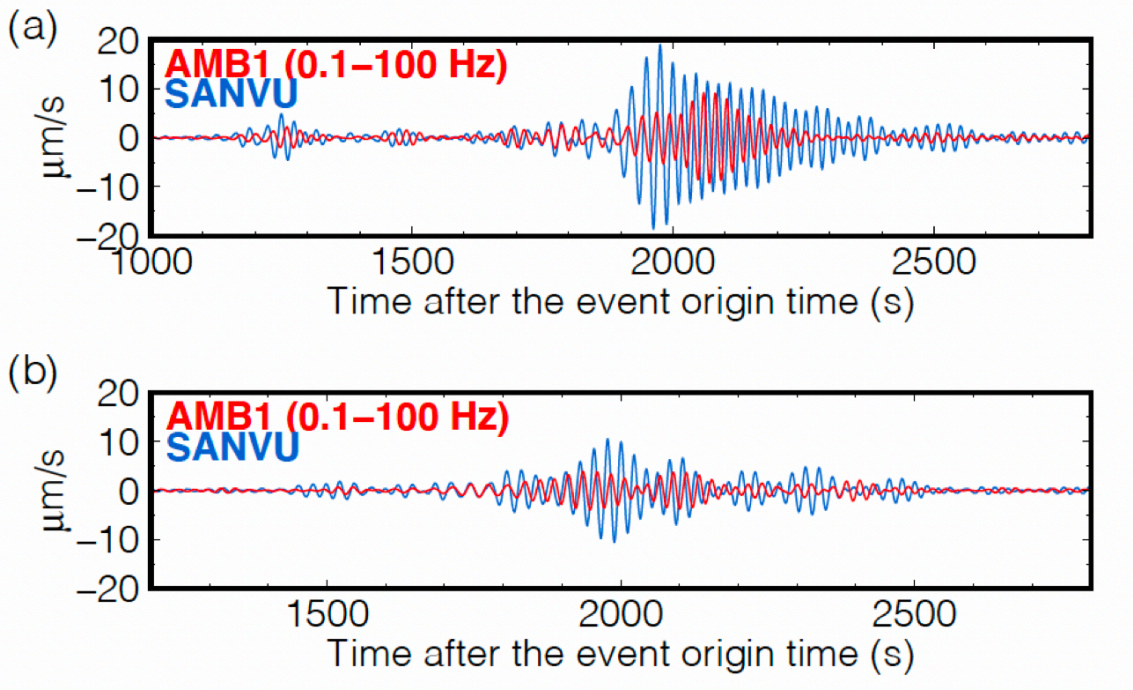

Figure B.3: Comparison of earthquake-generated signals recorded at AMB1 (red) and SANVU (blue). Seismograms are band-pass filtered between 0.03–0.05 Hz. (a) for the same earthquake in Figure B.2a, (b) for an Mw 6.6 earthquake (in South of Java Islands, June 13, 2013, 59.4°).

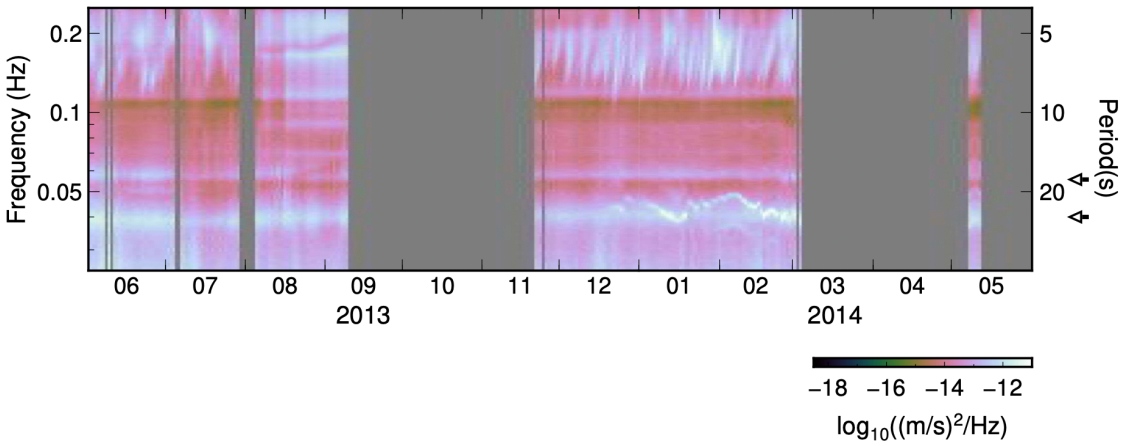

Figure B.4: Power spectrogram (0.025–0.25 Hz) of vertical component recorded at AMB1. Black arrows indicate positions of 25 s and 18 s.

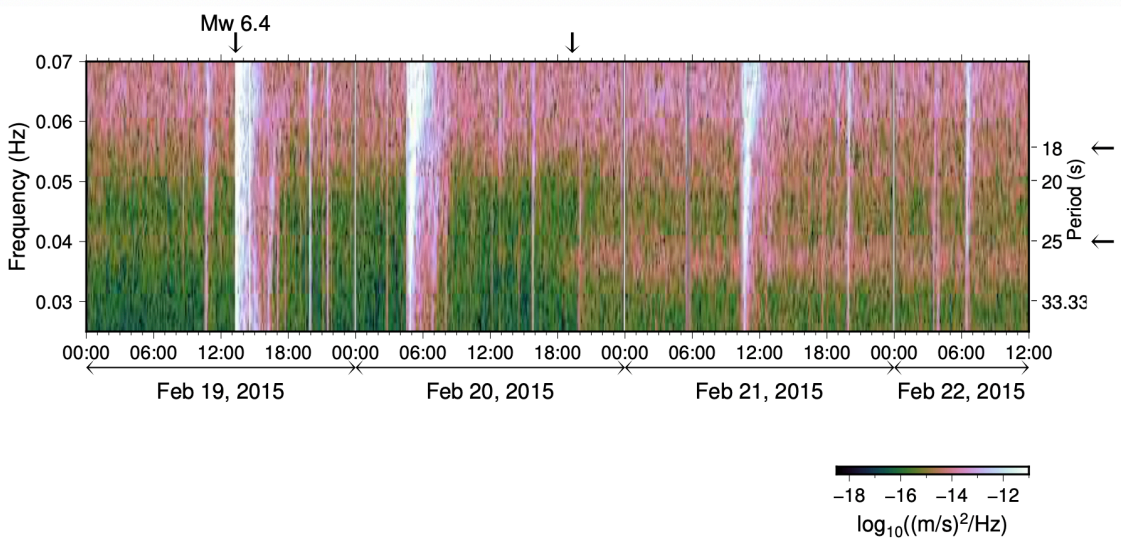

Figure B.5: Power spectrogram of vertical component recorded at SANVU around the time of the 2015 eruption (closed-up of Figure 3a). Black arrows on the top represent the timing of the Mw 6.4 local earthquake and the time 30 hours after the earthquake occurrence that corresponds the onset of the eruption according to Hamling and Kilgour (2020). Black arrows on the right axis represent the position of 18 s and 25 s.

Appendix C

Simulated annealing method

The simulated annealing method is a stochastic global optimization method for a given cost function at a large search space (Kirkpatrick et al., 1983; Szu and Hartley, 1986; Nam et al., 2004). Like a hill-climbing method, at each iteration step, it keeps modifying the current solution to a better solution which gives a smaller cost. However, unlike hill-climbing, during the search process, it stochastically accepts a worse solution which makes the cost larger. The acceptance of a worse solution helps to escape from a local minimum. The likelihood of accepting worse solutions is high at the beginning of the search, and it gets lower toward the end of the search. Acceptance of the worse solution helps to get out of the local minimum and converge towards the global minimum.

There are four steps in the simulated annealing method. In the first step, I define an initial temperature (T_0) and initial solutions ($\mathbf{x}_0 = x_1, x_2, ..., x_i, ..., x_n$, where n is the dimension of $\mathbf{x}_0$). The temperature will be decreased with each iteration, and at m^{th} step it will be given as

$$T_m = \frac{T_0}{1+m}. \tag{C.1}$$

Then, neighborhood solutions (neighbors) of m^{th} step ($\mathbf{x}_m$) will be generated around the solutions of $(m-1)^{th}$ step ($\mathbf{x}_{m-1}$) following a probability density function g. I use the n-dimensional Cauchy distribution proposed by Nam et al. (2004), which is more resistant to trade-offs among parameters compared to the dimension-wise Cauchy distribution or Gaussian distribution. The dimension-wise Cauchy distribution generates neighbors that are in the orthogonal axial direction, and the Gaussian distribution has no broad distribution of neighbors, which means that both restrict the search range. In contrast, the n-dimensional Cauchy distribution shows an omni-directional generation of the neighbors and a broad distribution of neighbors. $x_{m,i}$ and $x_{m-1,i}$ can be related as follows

$$x_{m,i} = x_{m-1,i} + \Delta x_i \tag{C.2}$$

where Δx_i is random variables generated by the n-dimensional Cauchy distribution as

$$g(\Delta \mathbf{x}_m, T_m, k) = \frac{T_m}{(||\Delta \mathbf{x}_m^2|| + T_m^2)^{(n+1)/2}}, \tag{C.3}$$

which is calculated by the method of Nam et al. (2004). In the third step, I evaluate neighbors. If the cost function $E(\mathbf{x}_m)$ is smaller than $E(\mathbf{x}_{m-1})$, $\mathbf{x}_m$ will be accepted. If $E(\mathbf{x}_m)$ is larger than $E(\mathbf{x}_{m-1})$, the neighbors $(\mathbf{x}_m)$ will be accepted with a probability given by

$$\exp\left[-\frac{E(\mathbf{x}_m) - E(\mathbf{x}_{m-1})}{kT_m}\right]. \tag{C.4}$$

Assuming that u is a random variable following a uniform distribution between 0 and 1 ($u \in [0, 1]$), if u is larger than the value of equation (C.4), I accept the neighbors. The likelihood of acceptance gets lower as the temperature decreases. I iterate steps 2 and 3 until T_m reaches a final temperature.

Appendix D

Lists of teleseismic events

Here I show the teleseismic events which are used in surface-wave dispersion measurement in Chapters 4 and 5. Tables D.1–D.3 show the events used in Chapter 4, and Table D.4 shows the events used in Chapter 5. The event lists are taken from USGS catalog[1].

[1] https://earthquake.usgs.gov/fdsnws/event/1/[METHOD[?PARAMETERS]]

Table D.1: A list of teleseismic events that are used for Rayleigh-wave phase velocity measurement at a frequency range of 0.005–0.01 Hz in Chapter 4

Origin date and time (UTC)	Latitude (°)	Longitude (°)	Depth (km)	Magnitude (Mw)
2018/11/30 17:29:29.33	61.346	210.045	46.7	7.1
2019/03/06 15:46:14.90	-32.024	182.115	29.0	6.4
2019/04/18 14:46:01.73	-51.127	139.321	10.0	6.3
2019/04/29 14:19:52.49	10.865	57.228	10.0	6.3
2019/06/02 10:36:29.67	-21.207	186.090	10.0	6.0
2019/06/17 06:02:04.09	-30.839	182.519	12.0	6.1
2019/06/21 08:37:16.94	-30.859	182.532	14.0	6.2
2019/06/27 11:04:56.34	-30.396	180.818	10.0	6.3
2019/07/04 04:30:44.42	51.237	229.500	10.0	6.2
2019/07/04 17:33:49.00	35.705	242.496	10.5	6.4
2019/07/06 03:19:53.04	35.770	242.401	8.0	7.1
2019/07/14 05:39:23.42	-18.224	120.358	10.0	6.6
2019/07/23 10:33:24.05	-61.287	154.114	10.0	6.0
2019/08/02 12:03:27.00	-7.282	104.791	49.0	6.9
2019/09/05 15:02:45.25	43.718	232.181	10.0	5.9

Table D.2: A list of teleseismic events that are used for Rayleigh-wave phase velocity measurement at a frequency range of 0.01–0.025 Hz in Chapter 4

Origin date and time (UTC)	Latitude (°)	Longitude (°)	Depth (km)	Moment magnitude
2018/11/25 03:40:50.81	13.182	278.907	10.0	6.0
2018/11/25 20:56:36.49	13.165	278.954	10.0	5.7
2019/02/18 19:30:22.90	-9.509	112.861	23.0	5.7
2019/04/01 08:11:32.41	7.578	94.337	10.0	5.5
2019/04/22 21:44:41.97	50.222	229.827	10.0	5.5
2019/04/29 14:19:52.49	10.865	57.228	10.0	6.3
2019/05/18 01:51:29.83	-9.508	108.597	8.0	5.6
2019/05/30 09:03:32.33	13.199	270.694	57.9	6.6
2019/06/02 10:36:29.67	-21.207	186.090	10.0	6.0
2019/06/17 06:02:04.09	-30.839	182.519	12.0	6.1
2019/06/21 08:37:16.94	-30.859	182.532	14.0	6.2
2019/06/27 11:04:56.34	-30.396	180.818	10.0	6.3
2019/07/02 09:44:33.24	-1.519	67.606	10.0	5.8
2019/07/05 12:58:27.98	51.344	229.426	9.0	5.6
2019/07/06 03:19:53.04	35.770	242.401	8.0	7.1
2019/07/23 10:33:24.05	-61.287	154.114	10.0	6.0
2019/07/31 05:54:53.15	13.148	270.605	43.0	5.9
2019/08/05 09:01:00.67	-18.379	185.627	10.0	5.7
2019/08/14 21:35:18.45	20.502	250.712	10.0	5.9
2019/08/21 14:28:25.65	-50.330	139.324	10.0	6.0
2019/09/05 15:02:45.25	43.718	232.181	10.0	5.9
2019/09/10 20:32:12.17	57.019	220.471	9.9	5.7
2019/09/27 12:05:02.54	-30.173	182.137	34.0	6.1
2019/10/26 00:41:25.51	52.308	189.861	35.0	5.8

Table D.3: A list of teleseismic events that are used for Rayleigh-wave phase velocity measurement at a frequency range of 0.025–0.038 Hz in Chapter 4

Origin date and time (UTC)	Latitude (°)	Longitude (°)	Depth (km)	Moment magnitude
2018/12/21 18:19:36.10	55.264	164.462	18.1	5.5
2018/12/22 13:29:46.98	55.193	164.629	10.0	5.6
2018/12/23 19:32:22.06	30.408	87.620	10.0	5.8
2018/12/24 12:41:19.25	55.344	164.510	10.0	6.1
2018/12/31 02:35:37.67	54.427	198.487	31.0	6.0
2019/01/05 18:47:11.74	51.335	181.882	30.0	5.9
2019/01/18 16:40:43.57	8.430	256.772	10.0	5.9
2019/03/01 01:02:12.28	-53.417	159.574	10.0	5.9
2019/03/15 17:53:34.01	-27.459	183.538	10.0	5.6
2019/04/02 21:35:30.04	52.170	178.071	8.0	6.4
2019/04/22 21:44:41.97	50.222	229.827	10.0	5.5
2019/05/18 01:51:29.83	-9.508	108.597	8.0	5.6
2019/05/22 00:39:34.96	13.892	92.992	29.0	5.6
2019/05/23 08:45:17.74	51.308	181.761	30.0	6.0
2019/06/02 10:36:29.67	-21.207	186.090	10.0	6.0
2019/06/17 14:55:44.87	28.406	104.933	6.0	5.8
2019/06/20 07:32:57.85	-17.665	186.284	47.7	5.5
2019/06/23 03:53:02.89	40.273	235.700	9.4	5.6
2019/06/26 02:18:07.84	56.182	164.088	10.0	6.3
2019/06/27 04:20:48.11	56.219	164.303	10.0	5.7
2019/07/04 04:30:44.42	51.237	229.500	10.0	6.2
2019/07/04 17:33:49.00	35.705	242.496	10.5	6.4
2019/07/05 12:58:27.98	51.344	229.426	9.0	5.6
2019/07/06 03:19:53.04	35.770	242.401	8.0	7.1
2019/07/09 18:43:43.42	52.899	192.517	33.1	5.5
2019/08/05 09:01:00.67	-18.379	185.627	10.0	5.7
2019/08/22 19:27:11.91	-14.667	182.587	10.0	5.9
2019/09/05 15:02:45.25	43.718	232.181	10.0	5.9
2019/09/10 20:32:12.17	57.019	220.471	9.9	5.7
2019/09/13 22:53:31.34	-15.353	186.830	10.0	5.7
2019/09/22 07:32:33.53	-15.554	186.860	10.0	5.6
2019/10/22 04:18:38.74	-15.198	186.950	10.0	5.8
2019/10/26 00:41:25.51	52.308	189.861	35.0	5.8

Table D.4: A list of teleseismic events that are used for Love-wave phase velocity measurement at a frequency range of 0.01–0.03 Hz in Chapter 5

Origin date and time (UTC)	Latitude (°)	Longitude (°)	Depth (km)	Moment magnitude
2018/11/09 01:49:40.05	71.631	348.757	10.0	6.7
2018/11/30 17:29:29.33	61.346	210.045	46.7	7.1
2018/12/05 04:18:08.42	-21.950	169.427	10.0	7.5
2018/12/05 06:43:04.13	-22.063	169.733	10.0	6.6
2019/06/18 13:22:19.01	38.639	139.477	12.0	6.4
2019/06/25 09:05:40.47	56.202	164.233	10.0	6.4
2019/07/04 04:30:44.42	51.237	229.500	10.0	6.2
2019/07/07 15:08:40.52	0.513	126.189	35.0	6.9
2019/07/14 05:39:23.42	-18.224	120.358	10.0	6.6
2019/07/14 09:10:51.52	-0.586	128.034	19.0	7.2
2019/08/29 15:07:58.64	43.542	232.118	10.0	6.3
2019/09/25 23:46:43.54	-3.453	128.370	12.3	6.5

Acknowledgement

I first would like to express my deepest appreciation to Hitoshi Kawakatsu for his continuous support and so much advice on the research over the past five years. I am also very grateful to Takehi Isse and Akiko Takeo. I have been fortunate to have weekly discussions with these three experts. Much of the parts of this research have arisen from the inspiring discussion with these three wonderful researchers.

I am also grateful to my supervisor, Nozomu Takeuchi. In particular, during the seminar presentations, his insightful questions helped me move forward with my research. I would like to thank Hajime Shiohara for his discussion on the noise reduction process. I enjoyed the discussion, feeling his passion for developing the ocean bottom seismometers. I also thank him for providing data recorded at offshore Miyagi. I thank Manabu Morishige for his discussion and for performing the mantle simulation in Section 6.6.2. I thank Kazunori Yoshizawa for kindly providing me with his WKBJ code. I would also like to thank Kiwamu Nishida for his discussion on ambient noise.

I appreciate for the dissertation committee, Kiyoshi Baba, Kenji Kawai, Kimihiro Mochizuki, Kiwamu Nishida, Kyoko Okino, and Takao Ominato, to review and give me many constructive comments on this thesis. Their comments largely improved the thesis.

I also would like to thank my co-authors who collaborated in Section 3.2: Daisuke Suetsugu, Hiroko Sugioka, Aki Ito, Yasushi Ishihara, Satoru Tanaka, Masayuki Obayashi, Takashi Tonegawa, and Junko Yoshimitsu. Many of them did insightful discussions at conferences and other occasions for my research.

I was fortunate to have chances to participate in research cruises, and the cruises were one of the most exciting events during my past five years. I thank Hitoshi Kawakatsu, James Gaherty, and Zachary Eilon for giving me the opportunity to participate in the deployment cruise of the Young ORCA. I thank Hajime Shiohara, Takehi Isse, Kiyoshi Baba, Hisashi Utada, YoungHee Kim, and Sang-Mook Lee for giving me the opportunity to join the recovery cruise of the Oldest-1 Array. I thank all the members who were involved in the cruise.

I spent five years at Earthquake Research Institute (ERI) and met many wonderful people. I would like to thank all of them. In particular, I thank the members of the Ocean Hemisphere Research Center who supported and guided me and my work. I also thank the fellow graduate students who made my days in graduate school much more fun and exciting. In particular, I thank Jumpei Maruyama, Satoru Baba, and Osamu Sandanbata. ERI was at first an unfamiliar place for me when I started graduate school. I really appreciate their kindness and help over the past

five years. I thank HyeJeong Kim. I was stimulated by her diligence, as well as a lot of impromptu enjoyable chats. I thank Xiaoli Wan. I miss the times that we cooked together and ate about four servings by the two of us. We could hardly move.

Before starting my graduate days, I spent my undergraduate years at Kobe University. I also met so many wonderful people there. In particular, I thank Nobukazu Seama who first guided me to this academic field. His lectures on solid Earth science drew my attention to the lithosphere-asthenosphere system and motivated me to start my journey in science in ERI. I also want to thank Rob Evans, whom I met at Kobe University and went to hot springs together. He has always cared about me and been a good friend.

Finally, I want to thank my family who gave unwavering support all those years. In particular, during the worldwide COVID-19 pandemic, I was reminded of how much support they are giving me. My cheerful and happy family gave me relaxing times during the busiest time of writing this thesis.

Bibliography

Abrams, L. (1992). The seismic stratigraphy and sedimentary history of the east mariana and pigafetta basins of the western pacific. *Proc ODP, Sci Result*, *129*, 551–569.

Abrams, L., Larson, R., Shipley, T., & Lancelot, Y. (1993). Cretaceous volcanic sequences and jurassic oceanic crust in the east mariana and pigafetta basins of the western pacific. *Washington DC American Geophysical Union Geophysical Monograph Series*, *77*, 77–101.

Aki, K. (1957). Space and time spectra of stationary stochastic waves, with special reference to microtremors. *Bulletin of the Earthquake Research Institute*, *35*, 415–456.

Aki, K., & Kaminuma, K. (1963). Phase velocity of low waves in japan (part 1): Love waves from the aleutian shock of march 9, 1957. *Bulletin of the Earthquake Research Institute, University of Tokyo*, *41*(1), 243–259.

Aki, K., & Richards, P. G. (2002). *Quantitative seismology*.

Araki, E. (2009). Calibration of deep sea differential pressure gauge. *JAMSTEC-R*, *9*, 141–148.

Backus, G. E. (1962). Long-wave elastic anisotropy produced by horizontal layering. *Journal of Geophysical Research*, *67*(11), 4427–4440.

Beauduin, R., & Montagner, J. (1997). Time evolution of broadband seismic noise during the french pilot experiment ofm/sismobs. *Oceanographic Literature Review*, *7*(44), 688.

Becker, T. W., Conrad, C. P., Schaeffer, A. J., & Lebedev, S. (2014). Origin of azimuthal seismic anisotropy in oceanic plates and mantle. *Earth and Planetary Science Letters*, *401*, 236–250.

Bell, S. W., Forsyth, D. W., & Ruan, Y. (2015). Removing noise from the vertical component records of ocean-bottom seismometers: Results from year one of the cascadia initiative. *Bulletin of the Seismological Society of America*, *105*(1), 300–313.

Bendat, J. S., & Piersol, A. G. (2011). *Random data: Analysis and measurement procedures* (Vol. 729). John Wiley & Sons.

Bensen, G., Ritzwoller, M., Barmin, M., Levshin, A. L., Lin, F., Moschetti, M., Shapiro, N., & Yang, Y. (2007). Processing seismic ambient noise data to obtain reliable broad-band surface wave dispersion measurements. *Geophysical Journal International*, *169*(3), 1239–1260.

Boschman, L. M., & Van Hinsbergen, D. J. (2016). On the enigmatic birth of the pacific plate within the panthalassa ocean. *Science advances*, *2*(7), e1600022.

Buck, W. R., & Parmentier, E. (1986). Convection beneath young oceanic lithosphere: Implications for thermal structure and gravity. *Journal of Geophysical Research: Solid Earth*, *91*(B2), 1961–1974.

Burgos, G., Montagner, J.-P., Beucler, E., Capdeville, Y., Mocquet, A., & Drilleau, M. (2014). Oceanic lithosphere-asthenosphere boundary from surface wave dispersion data. *Journal of Geophysical Research: Solid Earth*, *119*(2), 1079–1093.

Christensen, N. I., & Salisbury, M. H. (1975). Structure and constitution of the lower oceanic crust. *Reviews of Geophysics*, *13*(1), 57–86.

Coffin, M. F., Duncan, R. A., Eldholm, O., Fitton, J. G., Frey, F. A., Larsen, H. C., Mahoney, J. J., Saunders, A. D., Schlich, R., & Wallace, P. J. (2006). Large igneous provinces and scientific ocean drilling: Status quo and a look ahead. *Oceanography*, *19*(4), 150–160.

Coffin, M. F., & Eldholm, O. (1994). Large igneous provinces: Crustal structure, dimensions, and external consequences. *Reviews of Geophysics*, *32*(1), 1–36.

Cox, C., Deaton, T., & Webb, S. (1984). A deep-sea differential pressure gauge. *Journal of Atmospheric and Oceanic Technology*, *1*(3), 237–246.

Cox, H. (1973). Spatial correlation in arbitrary noise fields with application to ambient sea noise. *The Journal of the Acoustical Society of America*, *54*(5), 1289–1301.

Crawford, W. C., & Webb, S. C. (2000). Identifying and removing tilt noise from low-frequency (< 0.1 hz) seafloor vertical seismic data. *Bulletin of the Seismological Society of America*, *90*(4), 952–963.

Crawford, W. C., Webb, S. C., & Hildebrand, J. A. (1991). Seafloor compliance observed by long-period pressure and displacement measurements. *Journal of Geophysical Research: Solid Earth*, *96*(B10), 16151–16160.

Dahlen, F., & Tromp, J. (1998). Theoretical global seismology.

Debayle, E., Bodin, T., Durand, S., & Ricard, Y. (2020). Seismic evidence for partial melt below tectonic plates. *Nature*, *586*(7830), 555–559.

Deen, M., Wielandt, E., Stutzmann, E., Crawford, W., Barruol, G., & Sigloch, K. (2017). First observation of the earth's permanent free oscillations on ocean bottom seismometers. *Geophysical Research Letters*, *44*(21), 10–988.

Doran, A. K., & Laske, G. (2016). Infragravity waves and horizontal seafloor compliance. *Journal of Geophysical Research: Solid Earth*, *121*(1), 260–278.

Dorman, J., Ewing, M., & Oliver, J. (1960). Study of shear-velocity distribution in the upper mantle by mantle rayleigh waves. *Bulletin of the Seismological Society of America*, *50*(1), 87–115.

Dziewonski, A. M., & Anderson, D. L. (1981). Preliminary reference earth model. *Physics of the earth and planetary interiors*, *25*(4), 297–356.

Efron, B. (1979). Bootstrap methods: Another look at the jackknife: Annual statistics.

Eilon, Z. C., Gaherty, J. B., Zhang, L., Russell, J., McPeak, S., Phillips, J., Forsyth, D. W., & Ekström, G. (2021). The pacific obs research into convecting asthenosphere (orca) experiment. *Seismological Research Letters*.

Ekström, G., Nettles, M., & Dziewoński, A. (2012). The global cmt project 2004–2010: Centroid-moment tensors for 13,017 earthquakes. *Physics of the Earth and Planetary Interiors*, *200*, 1–9.

Ekström, G., Tromp, J., & Larson, E. W. (1997). Measurements and global models of surface wave propagation. *Journal of Geophysical Research: Solid Earth*, *102*(B4), 8137–8157.

Fischer, K. M., Rychert, C. A., Dalton, C. A., Miller, M. S., Beghein, C., & Schutt, D. L. (2020). A comparison of oceanic and continental mantle lithosphere. *Physics of the Earth and Planetary Interiors*, 106600.

Forsyth, D. W. (1975). The early structural evolution and anisotropy of the oceanic upper mantle. *Geophysical Journal International*, *43*(1), 103–162.

Forsyth, D. W., & Li, A. (2005). Array analysis of two-dimensional variations in surface wave phase velocity and azimuthal anisotropy in the presence of multipathing interference. *Seismic Earth: Array Analysis of Broadband Seismograms*, *157*, 81–97.

Forsyth, D. W., Webb, S. C., Dorman, L. M., & Shen, Y. (1998). Phase velocities of rayleigh waves in the melt experiment on the east pacific rise. *Science*, *280*(5367), 1235–1238.

Foster, A., Ekström, G., & Hjörleifsdóttir, V. (2014). Arrival-angle anomalies across the usarray transportable array. *Earth and Planetary Science Letters*, *402*, 58–68.

Foster, A., Nettles, M., & Ekström, G. (2014). Overtone interference in array-based love-wave phase measurements. *Bulletin of the Seismological Society of America*, *104*(5), 2266–2277.

Furumura, T., & Kennett, B. (2005). Subduction zone guided waves and the heterogeneity structure of the subducted plate: Intensity anomalies in northern japan. *Journal of Geophysical Research: Solid Earth*, *110*(B10).

Gaherty, J. B., Jordan, T. H., & Gee, L. S. (1996). Seismic structure of the upper mantle in a central pacific corridor. *Journal of Geophysical Research: Solid Earth*, *101*(B10), 22291–22309.

Gripp, A. E., & Gordon, R. G. (2002). Young tracks of hotspots and current plate velocities. *Geophysical Journal International*, *150*(2), 321–361.

Gutenberg, B. (1948). On the layer of relatively low wave velocity at a depth of about 80 kilometers. *Bulletin of the Seismological Society of America*, *38*(2), 121–148.

Gutenberg, B., & Richter, C. F. (1939). New evidence for a change in physical conditions at depths near 100 kilometers. *Bulletin of the Seismological Society of America*, *29*(4), 531–537.

Hamling, I. J., Cevuard, S., & Garaebiti, E. (2019). Large-scale drainage of a complex magmatic system: Observations from the 2018 eruption of ambrym volcano, vanuatu. *Geophysical Research Letters*, *46*(9), 4609–4617.

Hamling, I., & Kilgour, G. (2020). Goldilocks conditions required for earthquakes to trigger basaltic eruptions: Evidence from the 2015 ambrym eruption. *Science advances*, *6*(14), eaaz5261.

Handschumacher, D. W., Sager, W. W., Hilde, T. W., & Bracey, D. R. (1988). Pre-cretaceous tectonic evolution of the pacific plate and extension of the geomagnetic polarity reversal

time scale with implications for the origin of the jurassic "quiet zone". *Tectonophysics*, *155*(1-4), 365–380.

Haney, M. M., Mikesell, T. D., van Wijk, K., & Nakahara, H. (2012). Extension of the spatial autocorrelation (spac) method to mixed-component correlations of surface waves. *Geophysical Journal International*, *191*(1), 189–206.

Harkrider, D. G., & Anderson, D. L. (1966). Surface wave energy from point sources in plane layered earth models. *Journal of Geophysical Research*, *71*(12), 2967–2980.

Harmon, N., Forsyth, D., & Webb, S. (2007). Using ambient seismic noise to determine short-period phase velocities and shallow shear velocities in young oceanic lithosphere. *Bulletin of the Seismological Society of America*, *97*(6), 2009–2023.

Harmon, N., Rychert, C. A., Kendall, J. M., Agius, M., Bogiatzis, P., & Tharimena, S. (2020). Evolution of the oceanic lithosphere in the equatorial atlantic from rayleigh wave tomography, evidence for small-scale convection from the pi-lab experiment. *Geochemistry, Geophysics, Geosystems*, *21*(9), e2020GC009174.

Hess, H. (1964). Seismic anisotropy of the uppermost mantle under oceans. *Nature*, *203*(4945), 629–631.

Holcomb, L. G. (1980). Microseisms: A twenty-six-second spectral line in long-period earth motion. *Bulletin of the Seismological Society of America*, *70*(4), 1055–1070.

Holcomb, L. G. (1998). Spectral structure in the earth's microseismic background between 20 and 40 seconds. *Bulletin of the Seismological Society of America*, *88*(3), 744–757.

Huang, J., & Zhong, S. (2005). Sublithospheric small-scale convection and its implications for the residual topography at old ocean basins and the plate model. *Journal of Geophysical Research: Solid Earth*, *110*(B5).

Isse, T., Suetsugu, D., Ishikawa, A., Shiobara, H., Sugioka, H., Ito, A., Kawano, Y., Yoshizawa, K., Ishihara, Y., Tanaka, S., et al. (2021). Seismic evidence for a thermochemical mantle plume underplating the lithosphere of the ontong java plateau. *Communications Earth & Environment*, *2*(1), 1–7.

Janiszewski, H. A., Gaherty, J. B., Abers, G. A., Gao, H., & Eilon, Z. C. (2019). Amphibious surface-wave phase-velocity measurements of the cascadia subduction zone. *Geophysical Journal International*, *217*(3), 1929–1948.

Jurkevics, A. (1988). Polarization analysis of three-component array data. *Bulletin of the seismological society of America*, *78*(5), 1725–1743.

Kaminski, E., Ribe, N. M., & Browaeys, J. T. (2004). D-rex, a program for calculation of seismic anisotropy due to crystal lattice preferred orientation in the convective upper mantle. *Geophysical Journal International*, *158*(2), 744–752.

Kanazawa, T., Mochizuki, M., & Shiobara, H. (2001). Broadband seismometer for a long-term observation on the sea floor. *Proceedings of the OHP/ION Joint Symposium on Long-term Observations in the Oceans: Current Status and Perspectives for the Future*, S11–06.

Kaneda, K., Kodaira, S., Nishizawa, A., Morishita, T., & Takahashi, N. (2010). Structural evolution of preexisting oceanic crust through intraplate igneous activities in the marcus-wake seamount chain. *Geochemistry, Geophysics, Geosystems*, *11*(10).

Kaneshima, S., Kawakatsu, H., Matsubayashi, H., Sudo, Y., Tsutsui, T., Ohminato, T., Ito, H., Uhira, K., Yamasato, H., Oikawa, J., et al. (1996). Mechanism of phreatic eruptions at aso volcano inferred from near-field broadband seismic observations. *Science*, 642–645.

Karato, S.-i., Jung, H., Katayama, I., & Skemer, P. (2008). Geodynamic significance of seismic anisotropy of the upper mantle: New insights from laboratory studies. *Annu. Rev. Earth Planet. Sci.*, *36*, 59–95.

Kawakatsu, H., Kaneshima, S., Matsubayashi, H., Ohminato, T., Sudo, Y., Tsutsui, T., Uhira, K., Yamasato, H., Ito, H., & Legrand, D. (2000). Aso94: Aso seismic observation with broadband instruments. *Journal of Volcanology and Geothermal Research*, *101*(1-2), 129–154.

Kawakatsu, H., & Yamamoto, M. (2015). Volcano seismology. *Earthquake Seismology*, 389–419.

Kawakatsu, H., Kumar, P., Takei, Y., Shinohara, M., Kanazawa, T., Araki, E., & Suyehiro, K. (2009). Seismic evidence for sharp lithosphere-asthenosphere boundaries of oceanic plates. *science*, *324*(5926), 499–502.

Kawakatsu, H., Ohminato, T., & Ito, H. (1994). 10s-period volcanic tremors observed over a wide area in southwestern japan. *Geophysical Research Letters*, *21*(18), 1963–1966.

Kawakatsu, H., & Utada, H. (2017). Seismic and electrical signatures of the lithosphere–asthenosphere system of the normal oceanic mantle. *Annual Review of Earth and Planetary Sciences*, *45*, 139–167.

Kawano, Y., Isse, T., Takeo, A., Kawakatsu, H., Shiobara, H., Takeuchi, N., Sugioka, H., Kim, Y., Utada, H., & Lee, S. (2020). Seismic structure of the lithosphere-asthenosphere system beneath the oldest seafloor-the broadband dispersion analysis of the oldest-1 (pacific array) data. *AGU Fall Meeting Abstracts*, *2020*, DI013–03.

Kawano, Y., Isse, T., Kawakatsu, H., Takeo, A., & Shiobara, H. (2019a). Noise reduction and surface wave array dispersion measurements applied to noman's broadband obs data. *JpGU Meeting Abstracts*, *2019*, SCG56–P28.

Kawano, Y., Isse, T., Takeo, A., Kawakatsu, H., Suetsugu, D., Shiobara, H., Sugioka, H., Ito, A., Ishihara, Y., Tanaka, S., et al. (2020). Persistent long-period signals recorded by an obs array in the western-central pacific: Activity of ambrym volcano in vanuatu. *Geophysical Research Letters*, *47*(19), e2020GL089108.

Kawano, Y., Isse, T., Takeo, A., Kawakatsu, H., Suetsugu, D., Shiobara, H., Sugioka, H., Ito, A., Ishihara, Y., Tanaka, S., et al. (2019b). Array analysis of obs recordings at ontong java plateau: Preliminary analysis via seismic interferometry. *AGU Fall Meeting Abstracts*, *2019*, DI13C–0023.

Kennett, B., & Furumura, T. (2015). Toward the reconciliation of seismological and petrological perspectives on oceanic lithosphere heterogeneity. *Geochemistry, Geophysics, Geosystems*, *16*(9), 3129–3141.

Kirkpatrick, S., Gelatt Jr, C. D., & Vecchi, M. P. (1983). Optimization by simulated annealing. *science*, *220*(4598), 671–680.

Koppers, A. A., Staudigel, H., Pringle, M. S., & Wijbrans, J. R. (2003). Short-lived and discontinuous intraplate volcanism in the south pacific: Hot spots or extensional volcanism? *Geochemistry, Geophysics, Geosystems*, *4*(10).

Larson, R. L., & Chase, C. G. (1972). Late mesozoic evolution of the western pacific ocean. *Geological Society of America Bulletin*, *83*(12), 3627–3644.

Legrand, D., Kaneshima, S., & Kawakatsu, H. (2000). Moment tensor analysis of near-field broadband waveforms observed at aso volcano, japan. *Journal of volcanology and geothermal research*, *101*(1-2), 155–169.

Legrand, D., Rouland, D., Frogneux, M., Carniel, R., Charley, D., Roult, G., & Robin, C. (2005). Interpretation of very long period tremors at ambrym volcano, vanuatu, as quasi-static displacement field related to two distinct magmatic sources. *Geophysical research letters*, *32*(6).

Lin, P.-Y. P., Gaherty, J. B., Jin, G., Collins, J. A., Lizarralde, D., Evans, R. L., & Hirth, G. (2016). High-resolution seismic constraints on flow dynamics in the oceanic asthenosphere. *Nature*, *535*(7613), 538–541.

Luo, Y., Yang, Y., Zhao, K., Xu, Y., & Xia, J. (2015). Unraveling overtone interferences in love-wave phase velocity measurements by radon transform. *Geophysical Journal International*, *203*(1), 327–333.

Ma, Y., Clayton, R. W., Tsai, V. C., & Zhan, Z. (2013). Locating a scatterer in the active volcanic area of southern peru from ambient noise cross-correlation. *Geophysical Journal International*, *192*(3), 1332–1341.

Ma, Z., & Dalton, C. A. (2019). Evidence for dehydration-modulated small-scale convection in the oceanic upper mantle from seafloor bathymetry and rayleigh wave phase velocity. *Earth and Planetary Science Letters*, *510*, 12–25.

Maggi, A., Debayle, E., Priestley, K., & Barruol, G. (2006a). Azimuthal anisotropy of the pacific region. *Earth and Planetary Science Letters*, *250*(1-2), 53–71.

Maggi, A., Debayle, E., Priestley, K., & Barruol, G. (2006b). Multimode surface waveform tomography of the pacific ocean: A closer look at the lithospheric cooling signature. *Geophysical Journal International*, *166*(3), 1384–1397.

Mainprice, D. (2010). 2.16 seismic anisotropy of the deep earth from a mineral and rock physics perspective. *Treatise on Geophysics, Volume 2: Mineral Physics*, 437.

Mark, H., Collins, J., Lizarralde, D., Hirth, G., Gaherty, J., Evans, R., & Behn, M. (2021). Constraints on the depth, thickness, and strength of the g discontinuity in the central

pacific from s receiver functions. *Journal of Geophysical Research: Solid Earth*, *126*(4), e2019JB019256.

Mark, H., Lizarralde, D., Collins, J., Miller, N. C., Hirth, G., Gaherty, J., & Evans, R. (2019). Azimuthal seismic anisotropy of 70-ma pacific-plate upper mantle. *Journal of Geophysical Research: Solid Earth*, *124*(2), 1889–1909.

Matthews, K. J., Müller, R. D., Wessel, P., & Whittaker, J. M. (2011). The tectonic fabric of the ocean basins. *Journal of Geophysical Research: Solid Earth*, *116*(B12).

Michibayashi, K. (2008). Structure sensitivity and elastic anisotropy within peridotites. *JOURNAL OF GEOGRAPHY-CHIGAKU ZASSHI*, *117*(1), 93–109.

Montagner, J.-P., & Anderson, D. L. (1989). Petrological constraints on seismic anisotropy. *Physics of the earth and planetary interiors*, *54*(1-2), 82–105.

Montagner, J.-P., & Nataf, H.-C. (1986). A simple method for inverting the azimuthal anisotropy of surface waves. *Journal of Geophysical Research: Solid Earth*, *91*(B1), 511–520.

Montagner, J.-P., & Tanimoto, T. (1991). Global upper mantle tomography of seismic velocities and anisotropies. *Journal of Geophysical Research: Solid Earth*, *96*(B12), 20337–20351.

Morishige, M., & Honda, S. (2011). Three-dimensional structure of p-wave anisotropy in the presence of small-scale convection in the mantle wedge. *Geochemistry, Geophysics, Geosystems*, *12*(12).

Nakanishi, M., Tamaki, K., & Kobayashi, K. (1992). Magnetic anomaly lineations from late jurassic to early cretaceous in the west-central pacific ocean. *Geophysical Journal International*, *109*(3), 701–719.

Nam, D., Lee, J.-S., & Park, C. H. (2004). N-dimensional cauchy neighbor generation for the fast simulated annealing. *IEICE TRANSACTIONS on Information and Systems*, *87*(11), 2499–2502.

Nataf, H.-C., & Ricard, Y. (1996). 3smac: An a priori tomographic model of the upper mantle based on geophysical modeling. *Physics of the Earth and Planetary Interiors*, *95*(1-2), 101–122.

Negi, S. S., Kumar, A., Ningthoujam, L. S., & Pandey, D. K. (2021). An efficient approach of data adaptive polarization filter to extract teleseismic phases from the ocean-bottom seismograms. *Seismological Society of America*, *92*(1), 528–542.

Nettles, M., & Dziewoński, A. M. (2011). Effect of higher-mode interference on measurements and models of fundamental-mode surface-wave dispersion. *Bulletin of the Seismological Society of America*, *101*(5), 2270–2280.

Nicolas, A., & Christensen, N. I. (1987). Formation of anisotropy in upper mantle peridotites-a review. *Composition, structure and dynamics of the lithosphere-asthenosphere system*, *16*, 111–123.

Nishida, K., Kawakatsu, H., & Obara, K. (2008). Three-dimensional crustal s wave velocity structure in japan using microseismic data recorded by hi-net tiltmeters. *Journal of Geophysical Research: Solid Earth*, *113*(B10).

Nishimura, C. E., & Forsyth, D. W. (1989). The anisotropic structure of the upper mantle in the pacific. *Geophysical Journal International*, *96*(2), 203–229.

Ohira, A., Kodaira, S., Nakamura, Y., Fujie, G., Arai, R., & Miura, S. (2017). Evidence for frozen melts in the mid-lithosphere detected from active-source seismic data. *Scientific reports*, *7*(1), 1–8.

Oliver, J. (1962). A worldwide storm of microseisms with periods of about 27 seconds. *Bulletin of the Seismological Society of America*, *52*(3), 507–517.

Oliver, J. (1963). Additional evidence relating to "a worldwide storm of microseisms with periods of about 27 seconds". *Bulletin of the Seismological Society of America*, *53*(3), 681–685.

Parker, R., & Oldenburg, D. (1973). Thermal model of ocean ridges. *Nature Physical Science*, *242*(122), 137–139.

Parsons, B., & McKenzie, D. (1978). Mantle convection and the thermal structure of the plates. *Journal of Geophysical Research: Solid Earth*, *83*(B9), 4485–4496.

Parsons, B., & Sclater, J. G. (1977). An analysis of the variation of ocean floor bathymetry and heat flow with age. *Journal of geophysical research*, *82*(5), 803–827.

Peterson, J. et al. (1993). Observations and modeling of seismic background noise.

Richter, F. M., & Parsons, B. (1975). On the interaction of two scales of convection in the mantle. *Journal of Geophysical Research*, *80*(17), 2529–2541.

Ruan, Y., Forsyth, D. W., & Bell, S. W. (2014). Marine sediment shear velocity structure from the ratio of displacement to pressure of rayleigh waves at seafloor. *Journal of Geophysical Research: Solid Earth*, *119*(8), 6357–6371.

Russell, J. B., Gaherty, J. B., Lin, P.-Y. P., Lizarralde, D., Collins, J. A., Hirth, G., & Evans, R. L. (2019). High-resolution constraints on pacific upper mantle petrofabric inferred from surface-wave anisotropy. *Journal of Geophysical Research: Solid Earth*, *124*(1), 631–657.

Russell, J. B. (2021). *Structure and evolution of the oceanic lithosphere-asthenosphere system from high-resolution surface-wave imaging* (Doctoral dissertation). Columbia University.

Saito, M. (1988). Disper80: A subroutine package for the calculation of seismic normal-mode solutions. *Seismological algorithms*, 293–319.

Schaeffer, A., Lebedev, S., & Becker, T. (2016). Azimuthal seismic anisotropy in the earth's upper mantle and the thickness of tectonic plates. *Geophysical Supplements to the Monthly Notices of the Royal Astronomical Society*, *207*(2), 901–933.

Schmerr, N. (2012). The gutenberg discontinuity: Melt at the lithosphere-asthenosphere boundary. *Science*, *335*(6075), 1480–1483.

Seton, M., Müller, R. D., Zahirovic, S., Williams, S., Wright, N. M., Cannon, J., Whittaker, J. M., Matthews, K. J., & McGirr, R. (2020). A global data set of present-day oceanic crustal age and seafloor spreading parameters. *Geochemistry, Geophysics, Geosystems*, *21*(10), e2020GC009214.

Seton, M., Whittaker, J. M., Wessel, P., Müller, R. D., DeMets, C., Merkouriev, S., Cande, S., Gaina, C., Eagles, G., Granot, R., et al. (2014). Community infrastructure and repository

for marine magnetic identifications. *Geochemistry, Geophysics, Geosystems*, *15*(4), 1629–1641.

Seton, M., Müller, R. D., Zahirovic, S., Gaina, C., Torsvik, T., Shephard, G., Talsma, A., Gurnis, M., Turner, M., Maus, S., et al. (2012). Global continental and ocean basin reconstructions since 200 ma. *Earth-Science Reviews*, *113*(3-4), 212–270.

Seydoux, L., de Rosny, J., & Shapiro, N. M. (2017). Pre-processing ambient noise cross-correlations with equalizing the covariance matrix eigenspectrum. *Geophysical Journal International*, *210*(3), 1432–1449.

Shapiro, N. M., & Campillo, M. (2004). Emergence of broadband rayleigh waves from correlations of the ambient seismic noise. *Geophysical Research Letters*, *31*(7).

Shapiro, N. M., Campillo, M., Stehly, L., & Ritzwoller, M. H. (2005). High-resolution surface-wave tomography from ambient seismic noise. *Science*, *307*(5715), 1615–1618.

Shapiro, N. M., Ritzwoller, M., & Bensen, G. (2006). Source location of the 26 sec microseism from cross-correlations of ambient seismic noise. *Geophysical research letters*, *33*(18).

Shinohara, M., Araki, E., Kanazawa, T., Suyehiro, K., Mochizuki, M., Yamada, T., Nakahigashi, K., Kaiho, Y., Fukao, Y., et al. (2006). Deep-sea borehole seismological observatories in the western pacific: Temporal variation of seismic noise level and event detection. *Annals of geophysic*.

Shinohara, M., Fukano, T., Kanazawa, T., Araki, E., Suyehiro, K., Mochizuki, M., Nakahigashi, K., Yamada, T., & Mochizuki, K. (2008). Upper mantle and crustal seismic structure beneath the northwestern pacific basin using a seafloor borehole broadband seismometer and ocean bottom seismometers. *Physics of the Earth and Planetary Interiors*, *170*(1-2), 95–106.

Shinohara, M., Kanazawa, T., & Shiobara, H. (2011). Recent progress in ocean bottom seismic observation and new results of marine seismology. *2011 IEEE Symposium on Underwater Technology and Workshop on Scientific Use of Submarine Cables and Related Technologies*, 1–7.

Shintaku, N., Forsyth, D. W., Hajewski, C. J., & Weeraratne, D. S. (2014). Pn anisotropy in mesozoic western pacific lithosphere. *Journal of Geophysical Research: Solid Earth*, *119*(4), 3050–3063.

Shiobara, H., Kanazawa, T., & Isse, T. (2012). New step for broadband seismic observation on the seafloor: Bbobs-nx. *IEEE Journal of Oceanic Engineering*, *38*(2), 396–405.

Shito, A., Suetsugu, D., Furumura, T., Sugioka, H., & Ito, A. (2013). Small-scale heterogeneities in the oceanic lithosphere inferred from guided waves. *Geophysical Research Letters*, *40*(9), 1708–1712.

Song, T.-R. A., & Kim, Y. (2012). Anisotropic uppermost mantle in young subducted slab underplating central mexico. *Nature Geoscience*, *5*(1), 55–59.

Stadler, T. J., & Tominaga, M. (2015). Intraplate volcanism of the western pacific: New insights from geological and geophysical observations in the pigafetta basin. *Geochemistry, Geophysics, Geosystems*, *16*(9), 3015–3033.

Stein, C. A., & Stein, S. (1992). A model for the global variation in oceanic depth and heat flow with lithospheric age. *Nature*, *359*(6391), 123–129.

Stixrude, L., & Lithgow-Bertelloni, C. (2005). Mineralogy and elasticity of the oceanic upper mantle: Origin of the low-velocity zone. *Journal of Geophysical Research: Solid Earth*, *110*(B3).

Stixrude, L., & Lithgow-Bertelloni, C. (2011). Thermodynamics of mantle minerals-ii. phase equilibria. *Geophysical Journal International*, *184*(3), 1180–1213.

Suetsugu, D., & Shiobara, H. (2014). Broadband ocean-bottom seismology. *Annual Review of Earth and Planetary Sciences*, *42*, 27–43.

Suetsugu, D., Shiobara, H., Sugioka, H., Tada, N., Ito, A., Isse, T., Baba, K., Ichihara, H., Ota, T., Ishihara, Y., et al. (2018). The ojp array: Seismological and electromagnetic observation on seafloor and islands in the ontong java plateau. *JAMSTEC Report of Research and Development*, *26*, 54–64.

Szu, H., & Hartley, R. (1987). Fast simulated annealing. *Physics letters A*, *122*(3-4), 157–162.

Takeo, A., Kawakatsu, H., Isse, T., Nishida, K., Sugioka, H., Ito, A., Shiobara, H., & Suetsugu, D. (2016). Seismic azimuthal anisotropy in the oceanic lithosphere and asthenosphere from broadband surface wave analysis of obs array records at 60 ma seafloor. *Journal of Geophysical Research: Solid Earth*, *121*(3), 1927–1947.

Takeo, A., Nishida, K., Isse, T., Kawakatsu, H., Shiobara, H., Sugioka, H., & Kanazawa, T. (2013). Radially anisotropic structure beneath the shikoku basin from broadband surface wave analysis of ocean bottom seismometer records. *Journal of Geophysical Research: Solid Earth*, *118*(6), 2878–2892.

Takeo, A. (2020). Practical developments of ambient noise cross-correlation analysis in the oceanic basin regions. *JpGU Meeting Abstracts*, *2020*, SSS12–12.

Takeo, A., Forsyth, D. W., Weeraratne, D. S., & Nishida, K. (2014). Estimation of azimuthal anisotropy in the nw pacific from seismic ambient noise in seafloor records. *Geophysical Journal International*, *199*(1), 11–22.

Takeo, A., Kawakatsu, H., Isse, T., Nishida, K., Shiobara, H., Sugioka, H., Ito, A., & Utada, H. (2018). In situ characterization of the lithosphere-asthenosphere system beneath nw pacific ocean via broadband dispersion survey with two obs arrays. *Geochemistry, Geophysics, Geosystems*, *19*(9), 3529–3539.

Takeo, A., Kawakatsu, H., Nishida, K., & Isse, T. (2015). Difference in the excitation efficiency of fundamental and first higher modes of love wave between oceanic and continental regions (s07-p03)(poster session)(abs.) *Programme and Abstracts, the Seismological Society of Japan, Fall Meeting*, *2015*, 232–232.

Takeuchi, H., & Saito, M. (1972). Seismic surface waves. *Methods in computational physics*, *11*, 217–295.

Tanimoto, T., & Anderson, D. L. (1984). Mapping convection in the mantle. *Geophysical Research Letters*, *11*(4), 287–290.

Tharimena, S., Rychert, C., Harmon, N., & White, P. (2017). Imaging pacific lithosphere seismic discontinuities—insights from ss precursor modeling. *Journal of Geophysical Research: Solid Earth*, *122*(3), 2131–2152.

Thatcher, W., & Brune, J. N. (1969). Higher mode interference and observed anomalous apparent love wave phase velocities. *Journal of Geophysical Research*, *74*(27), 6603–6611.

Tian, Y., & Ritzwoller, M. H. (2017). Improving ambient noise cross-correlations in the noisy ocean bottom environment of the juan de fuca plate. *Geophysical Journal International*, *210*(3), 1787–1805.

Tivey, M. A., Sager, W. W., Lee, S.-M., & Tominaga, M. (2006). Origin of the pacific jurassic quiet zone. *Geology*, *34*(9), 789–792.

Tominaga, M., Sager, W. W., Tivey, M. A., & Lee, S.-M. (2008). Deep-tow magnetic anomaly study of the pacific jurassic quiet zone and implications for the geomagnetic polarity reversal timescale and geomagnetic field behavior. *Journal of Geophysical Research: Solid Earth*, *113*(B7).

Tominaga, M., Tivey, M. A., & Sager, W. W. (2021). A new middle to late jurassic geomagnetic polarity time scale (gpts) from a multiscale marine magnetic anomaly survey of the pacific jurassic quiet zone. *Journal of Geophysical Research: Solid Earth*, *126*(3), e2020JB021136.

Toomey, D. R., Jousselin, D., Dunn, R. A., Wilcock, W. S., & Detrick, R. (2007). Skew of mantle upwelling beneath the east pacific rise governs segmentation. *Nature*, *446*(7134), 409–414.

van Hunen, J., & Čadek, O. (2009). Reduced oceanic seismic anisotropy by small-scale convection. *Earth and Planetary Science Letters*, *284*(3-4), 622–629.

Wapenaar, K., Draganov, D., Snieder, R., Campman, X., & Verdel, A. (2010a). Tutorial on seismic interferometry: Part 1—basic principles and applications. *Geophysics*, *75*(5), 75A195–75A209.

Wapenaar, K., Slob, E., Snieder, R., & Curtis, A. (2010b). Tutorial on seismic interferometry: Part 2—underlying theory and new advances. *Geophysics*, *75*(5), 75A211–75A227.

Weaver, R., Froment, B., & Campillo, M. (2009). On the correlation of non-isotropically distributed ballistic scalar diffuse waves. *The Journal of the Acoustical Society of America*, *126*(4), 1817–1826.

Webb, S. C., & Crawford, W. C. (1999). Long-period seafloor seismology and deformation under ocean waves. *Bulletin of the Seismological Society of America*, *89*(6), 1535–1542.

Webb, S. C., Deaton, T. K., & Lemire, J. C. (2001). A broadband ocean-bottom seismometer system based on a 1-hz natural period geophone. *Bulletin of the Seismological Society of America*, *91*(2), 304–312.

Webb, S. C., Zhang, X., & Crawford, W. (1991). Infragravity waves in the deep ocean. *Journal of Geophysical Research: Oceans*, *96*(C2), 2723–2736.

Weeraratne, D. S., Forsyth, D. W., Yang, Y., & Webb, S. C. (2007). Rayleigh wave tomography beneath intraplate volcanic ridges in the south pacific. *Journal of Geophysical Research: Solid Earth*, *112*(B6).

Wessel, P., Matthews, K. J., Müller, R. D., Mazzoni, A., Whittaker, J. M., Myhill, R., & Chandler, M. T. (2015). *Semiautomatic fracture zone tracking* (tech. rep.). Wiley Online Library.

White, R. S., McKenzie, D., & O'Nions, R. K. (1992). Oceanic crustal thickness from seismic measurements and rare earth element inversions. *Journal of Geophysical Research: Solid Earth*, *97*(B13), 19683–19715.

Winterer, E. L., Natland, J. H., Van Waasbergen, R. J., Duncan, R. A., Mcnutt, M. K., Wolfe, C. J., Silva, I. P., Sager, W. W., & Sliter, W. V. (1993). Cretaceous guyots in the northwest pacific: An overview of their geology and geophysics. *The Mesozoic Pacific: Geology, Tectonics, and Volcanism*, *77*, 307–334.

Xia, Y., & Chen, X. (2020). Observation of a new long-period (16-s) persistent tremor originating in the gulf of guinea. *Geophysical Research Letters*, *47*(15), e2020GL088137.

Xia, Y., Ni, S., & Zeng, X. (2013). Twin enigmatic microseismic sources in the gulf of guinea observed on intercontinental seismic stations. *Geophysical Journal International*, *194*(1), 362–366.

Yamamoto, M., Kawakatsu, H., Kaneshima, S., Mori, T., Tsutsui, T., Sudo, Y., & Morita, Y. (1999). Detection of a crack-like conduit beneath the active crater at aso volcano japan. *Geophysical research letters*, *26*(24), 3677–3680.

Yang, X., Luo, Y., Xu, H., & Zhao, K. (2020). Shear wave velocity and radial anisotropy structures beneath the central pacific from surface wave analysis of obs records. *Earth and Planetary Science Letters*, *534*, 116086.

Yoshizawa, K., & Kennett, B. (2002). Non-linear waveform inversion for surface waves with a neighbourhood algorithm—application to multimode dispersion measurements. *Geophysical Journal International*, *149*(1), 118–133.

Zeng, X., & Ni, S. (2010). A persistent localized microseismic source near the kyushu island, japan. *Geophysical Research Letters*, *37*(24).

Zeng, X., & Ni, S. (2011). Correction to a persistent localized microseismic source near the kyushu island, japan. *Geophysical Research Letters*, *38*(16).

Zeng, X., & Ni, S. (2014). Evidence for an independent 26-s microseismic source near the vanuatu islands. *Pure and Applied Geophysics*, *171*(9), 2155–2163.